MOTOR VALLEY UNIVERSITY OF EMILIA ROMAGNA

Master's Degree in Advanced Automotive Engineering

Master's Degree Thesis

Experimental Electrothermal Characterization and Modelling of Li-Ion Battery Cells for Automotive Applications

Supervisor:
Prof. Davide BARATER

Candidate:
Luca TRUSSARDI

Academic Year 2024/2025
Graduation Date: April, 2026

Master’s Degree in Advanced Automotive Engineering
Motor Valley University of Emilia Romagna, Italy

"You can do anything, but not everything"

— **David Allen**

Sommario

Questa tesi tratta la caratterizzazione elettrotermica di celle a ioni di litio per applicazioni automotive.

Contesto e Motivazione

La transizione verso la mobilità elettrica e l'adozione di sistemi di accumulo dell'energia richiedono tecnologie di stoccaggio energetico sempre più performanti. Le celle agli ioni di litio dominano questo settore grazie alla loro elevata densità energetica; tuttavia, la loro gestione termica rappresenta una sfida importante. L'accumulo eccessivo di calore non solo degrada le prestazioni della batteria, ma pone anche seri rischi per la sicurezza. In questo contesto, una caratterizzazione elettrotermica accurata diventa uno strumento fondamentale per ottimizzare rapidamente il design del sistema e sviluppare strategie di controllo sicure ed efficienti, in quanto un modello affidabile e preciso permette di simulare il sistema in maniera dettagliata, ottenendo informazioni che richiederebbero altrimenti lunghe e costose campagne sperimentali.

Obiettivi e Oggetto di Studio

Il presente lavoro di tesi si pone l'obiettivo di analizzare e modellare il comportamento elettrotermico di una specifica cella agli ioni di litio: la Molicel P45B, una cella cilindrica formato 21700 sviluppata per applicazioni automotive e commerciali ad alte prestazioni. L'approccio adottato mira a fornire una visione completa del componente e del suo comportamento operativo, integrando la risposta elettrica con quella termica sia in condizioni statiche che dinamiche.

Metodologia e Strumentazione

Per il raggiungimento degli obiettivi, è stata progettata da zero un'architettura di test dedicata. Sfruttando un ciclatore per batterie, un sistema di acquisizione dati e una camera climatica, sono stati condotti test sperimentali mirati. Il monitoraggio della tensione, della corrente, della temperatura e del flusso di calore ha permesso

di estrarre i parametri fondamentali per la costruzione di un modello elettrotermico equivalente. La caratterizzazione elettrica ha estratto i parametri di circuito equivalente di Thevenin del secondo ordine (resistenze e capacità), mentre quella termica ha caratterizzato un circuito termico equivalente del primo ordine (capacità termica, resistenza termica ambiente e coefficiente di calore entropico). Inoltre, per facilitare l'analisi della grande mole di dati raccolti, è stato sviluppato uno script di elaborazione personalizzato dotato di un'interfaccia grafica intuitiva, concepito per rendere le future campagne di test più rapide e accessibili. Questa tesi fornisce anche, in Appendice, accesso agli script che sono stati creati e una breve guida all'utilizzo.

Validazione e Risultati

I parametri fisici calcolati sono stati integrati all'interno di un modello matematico elettrotermico, successivamente implementato in un ambiente di simulazione avanzato. La bontà del modello è stata verificata validando i risultati della simulazione confrontandoli direttamente con i dati sperimentali, confermando l'applicabilità della metodologia proposta per scenari di utilizzo del campo automotive.

Limiti e Sviluppi Futuri

L'analisi critica dei risultati ha evidenziato alcune limitazioni metodologiche: il test Hybrid Pulse Power Characterization (HPPC) ha mostrato dei limiti nell'estrazione ottimale dei parametri circuitali, e l'accuratezza del modello termico del primo ordine si è rivelata inferiore alle aspettative. Questi aspetti, uniti alle fondamenta poste da questo lavoro, aprono la strada a possibili sviluppi futuri, tra cui l'estensione dell'analisi all'intero range di tensione, l'integrazione della dipendenza termica nel modello, l'adozione di algoritmi di stima dello State of Charge (SOC) più avanzati e la futura implementazione su sistemi Battery Management System (BMS) in scenari operativi reali.

Abstract

The increasing demand for Electric Vehicles (EVs) and Energy Storage Systems (ESSs) relies heavily on the advancement of Lithium-ion (Li-ion) battery technology. Because excessive heat generation can lead to severe performance degradation and safety risks, effective thermal management is one of the primary challenges in battery system design. Thus, accurate electrothermal characterization and modelling are essential for developing precise control strategies and ensuring safe operation. This thesis focuses on the experimental electrothermal characterization and modelling of the Molicel P45B, a 21700 cylindrical Li-ion cell designed for advanced automotive applications.

A comprehensive testing methodology was designed and executed using a battery tester, Data Acquisition (DAQ) system, and thermal chamber. Tests were conducted under both static and dynamic charge and discharge conditions to capture the cell's coupled electrical and thermal responses. Voltage and current measurements were utilized to extract electrical Equivalent Circuit Model (ECM) parameters, while surface temperature and heat flux were precisely monitored to extract thermal ECM parameters, including thermal capacity and Entropic Heat Coefficient (EHC). A custom data elaboration script featuring a graphical user interface was developed, significantly reducing the effort required for future characterization work.

Finally, a mathematical electrothermal model integrating both the electrical and thermal aspects was implemented in advanced simulation software. The developed model was successfully validated against experimental data, confirming its applicability for realistic scenario simulation. While the study demonstrates the viability of this holistic characterization approach, it also identifies limitations in using Hybrid Pulse Power Characterization (HPPC) for ECM parameter estimation and notes constraints in first order thermal model accuracy. Ultimately, this work provides a robust foundational framework for electrothermal battery analysis, paving the way for future research into temperature dependent modelling, advanced State of Charge (SOC) estimation, and full integration into Battery Management System (BMS).

Keywords: Lithium-Ion Batteries, Electrothermal Characterization, Equivalent Circuit Modelling, Battery Management System, Electric Vehicles.

Table of Contents

List of Figures

List of Tables

List of Scripts

List of Acronyms

AC	Alternating Current
BMS	Battery Management System
BTS	Battery Testing System
CARMA	Controlled Autoregressive Moving Average
CC	Constant Current
CRM	Component-Resolved Model
CV	Constant Voltage
DAQ	Data Acquisition
DC	Direct Current
DFN	Doyle-Fuller-Newman
DOD	Depth of Discharge
ECM	Equivalent Circuit Model
EHC	Entropic Heat Coefficient
EIS	Electrochemical Impedance Spectroscopy
EKF	Extended Kalman Filter
ESS	Energy Storage System
EV	Electric Vehicle
eVTOL	Electric Vertical Take-Off and Landing
GHP	Guarded Hot Plate
GITT	Galvanostatic Intermittent Titration Technique
GNL	General Nonlinear
HPPC	Hybrid Pulse Power Characterization
LCO	Lithium Cobalt Oxide
LFP	Lithium Iron Phosphate
Li-ion	Lithium-ion
LMO	Lithium Manganese Oxide
LRM	Layer-Resolved Model
LTO	Lithium Titanate Oxide
MSMD	Multi-Scale Multi-Dimensional
NCA	Lithium Nickel Cobalt Aluminum Oxide
NMC	Lithium Nickel Manganese Cobalt Oxide
OCV	Open Circuit Voltage
ODE	Ordinary Differential Equation
OLS	Ordinary Least Squares
PDE	Partial Differential Equation
PNGV	Partnership for a New Generation of Vehicles
RC	Resistor-Capacitor
RMS	Root Mean Square

RW	Random Walk
SDM	Single-Domain Model
SEI	Solid Electrolyte Interphase
SOC	State of Charge
SOE	State of Energy
SPM	Single Particle Model
SSE	Sum of Squared Errors
TIS	Thermal Impedance Spectroscopy
UKF	Unscented Kalman Filter
VCC	Variant Convective Cooling

List of Symbols

Symbol	**Description**	**Unit**
A	Area	m^2
Bi	Biot Number	-
c	Specific Heat Capacity	$J/(kg\,K)$
C	Battery Capacity	Ah
C	Electrical Capacitance	F
C_{th}	Thermal Capacitance	J/K
d	Thickness	m
E	Electrical Energy	J
f	Frequency	Hz
h	Heat Transfer coefficient	$W/(m^2\,K)$
I	Electrical Current	A
k	Thermal Conductivity	$W/(m\,K)$
L	Length	m
m	Mass	kg
P	Electrical Power	W
Q	Heat	J
$\dot{Q}$	Heat Generation/Transfer Rate	W
$\dot{Q}''$	Heat Flux Density	W/m^2
R	Electrical Resistance	Ω
R_{th}	Thermal Resistance (Absolute)	K/W
R''_{th}	Thermal Resistance (Specific)	$K\,m^2/W$
S	Heat Flux Sensor Sensitivity	$V\,m^2/W$
t	Time	s
T	Temperature	K
V	Electrical Voltage	V
X	Electrical Reactance	Ω
Z	Electrical Impedance	Ω
Z_{th}	Thermal Impedance	K/W
η	Efficiency	-
ω	Angular Frequency	rad/s
τ	Time Constant	s

Introduction

In this chapter, the background and motivation, purpose and objectives, scope, and outline of the thesis are presented.

0.1 Background and Motivation

The increasing demand for Electric Vehicles (EVs) and Energy Storage Systems (ESSs) has driven significant advancements in battery technology. In particular, Lithium-ion (Li-ion) cells are widely used due to their high energy density and efficiency. However, thermal management of the battery cells is one of the main challenges, as excessive heat can lead to performance degradation and safety risks. Accurate characterization and modelling of Li-ion cells are crucial for effective temperature management, performance optimization, and safe system operation. In fact, a deeper understanding of the electrothermal behavior enables more precise control strategies, leading to improved system design and enhanced safety. For this reason, this thesis focuses on the experimental electrothermal characterization and modelling of Li-ion cells specifically selected for advanced automotive applications.

0.2 Purpose and Objectives

The purpose of this thesis is to develop a comprehensive understanding of the electrothermal behavior of Li-ion cells under various operating conditions. The primary objectives of this thesis are:

- To conduct experimental tests to characterize the response of Li-ion cells during charge and discharge cycles
- To develop a mathematical model that accurately predicts the electrothermal behavior of Li-ion cells both in static and dynamic operating conditions
- To validate the developed model against experimental data and assess its applicability in realistic scenarios

0.3 Scope

This study focuses on the P45B, a 21700 cylindrical Li-ion cell produced by Molicel, developed for automotive and commercial applications. In any case, the approach, methodologies and findings used in this thesis can be extended to other cell formats and chemistries with appropriate adjustments.

- The electrical characterization will include measurements of voltage and current during various charge and discharge cycles, performed both in static and dynamic conditions, with the purpose of extracting the electrical Equivalent Circuit Model (ECM) parameters (equivalent resistances and capacitances)
- The thermal characterization will involve monitoring the temperature distribution across the cell surface using thermocouples and the heat flux using a heat flux sensor, providing an estimation of the thermal ECM parameters (thermal capacity and Entropic Heat Coefficient (EHC))
- The developed electrothermal model will integrate both electrical and thermal aspects to simulate the cell's behavior under various operating conditions, and will be implemented in a simulation software to evaluate the cell's performance in multiple scenarios, validating the model accuracy against experimental results

0.4 Thesis Structure

The thesis is organized into the following chapters:

- **Chapter 1:** ***Theoretical Overview*** - Recap of the theory of operation of battery cells and summary of the existing research on Li-ion cell electrothermal characterization and modelling
- **Chapter 2:** ***Experimental Setup and Test Methodology*** - Description of the investigated cell specifications, experimental apparatus, test procedures, and data acquisition methods used for the characterization
- **Chapter 3:** ***Electrical Characterization Approach and Results*** - Presentation and discussion of the electrical characterization approach and results
- **Chapter 4:** ***Thermal Characterization Approach and Results*** - Presentation and discussion of the thermal characterization approach and results

- **Chapter 5:** ***Model Development and Validation*** - Implementation of the electrothermal model in the simulation environment and validation against experimental data
- **Conclusion** - Summary of key findings and suggestions for future research

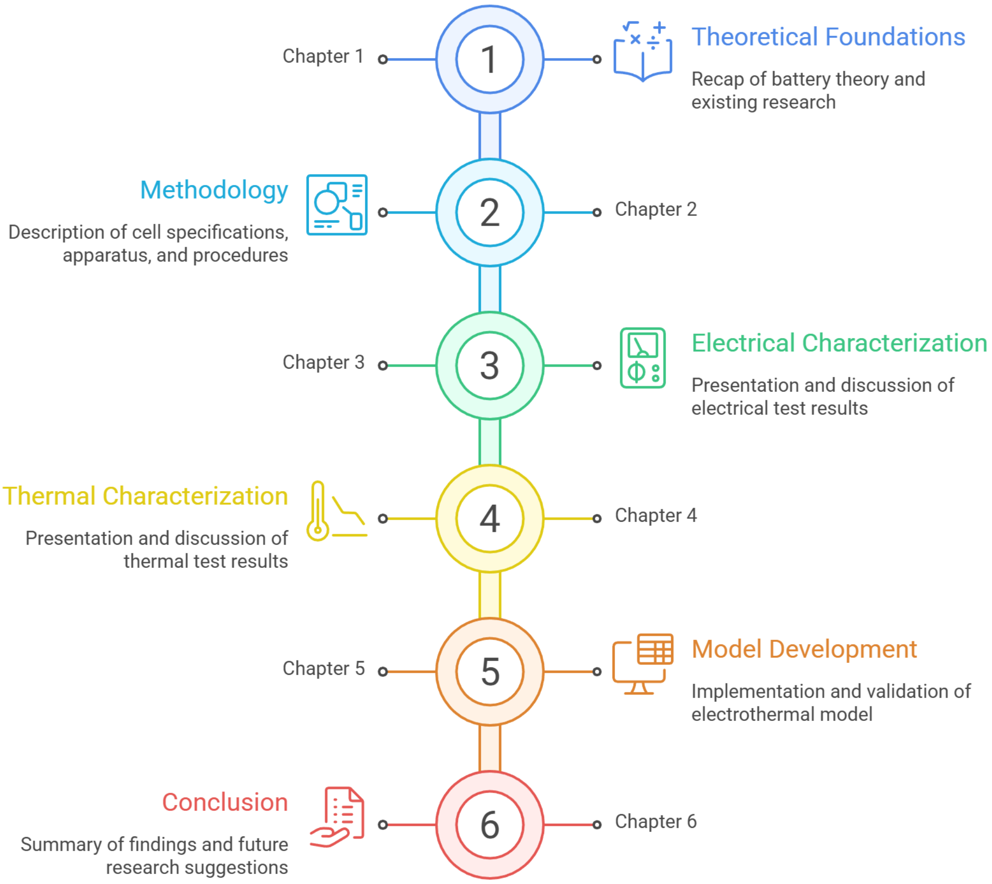

Figure 1: Thesis outline

1

Theoretical Overview

In this chapter, the fundamentals of battery cells physics, operation and manufacturing are presented, together with a review of the main characterization techniques and modelling approaches.

1.1 Li-ion Cells Basics

Batteries are energy storage devices that convert chemical energy into electrical energy through electrochemical reactions. They become essential components in various applications, including portable electronics, EVs, and renewable ESSs due to their ability to accumulate and deliver energy efficiently. As a matter of fact, global Li-ion battery demand is projected to reach more than 5 Terawatt-hours by 2050, thirty times the 2020 level [1]. This almost exponential growth is driven by the increasing adoption of electric devices, which require efficient and reliable energy storage solutions.

A battery system is usually composed of a battery pack and an electronic control system, the Battery Management System (BMS), that handles the charging and discharging processes, monitors the state of the battery, and ensures safety during operation. The battery pack consists of multiple cells, usually arranged in modules and typically connected in series and/or parallel to achieve the desired voltage, capacity and power ratings.

1.1.1 Li-ion Cell Construction and Materials

A battery cell is made up of four parts[1]:

---

[1] The convention used for naming the terminals comes from chemical Red-Ox reactions: reduction occurs at the cathode and oxidation at the anode. In the context of batteries, the naming is typically referred to the discharge process

- **Cathode**: The positive electrode during discharge, where reduction occurs, accepting electrons from the external circuit
- **Anode**: The negative electrode during discharge, where oxidation occurs, releasing electrons to the external circuit
- **Electrolyte**: A chemical medium that allows the flow of ions between the anode and cathode
- **Separator**: A porous membrane that physically separates the anode and cathode, allowing ion flow but impeding electron passage, thus preventing short circuits between the electrodes

The cathode, separator and anode are usually overlapped one over the other in a layered sandwich structure, often referred to as a jelly roll, to maximize the surface area and thus the electrochemical performance. Depending on the cell form factor (see Section 1.1.3), the jelly roll can be rolled (cylindrical cells) or stacked (prismatic and pouch cells) to fit within the cell casing. The electrolyte is then filled into the cell as the last step of the manufacturing process. The construction of a typical Li-ion cell is illustrated in Figure 1.1.

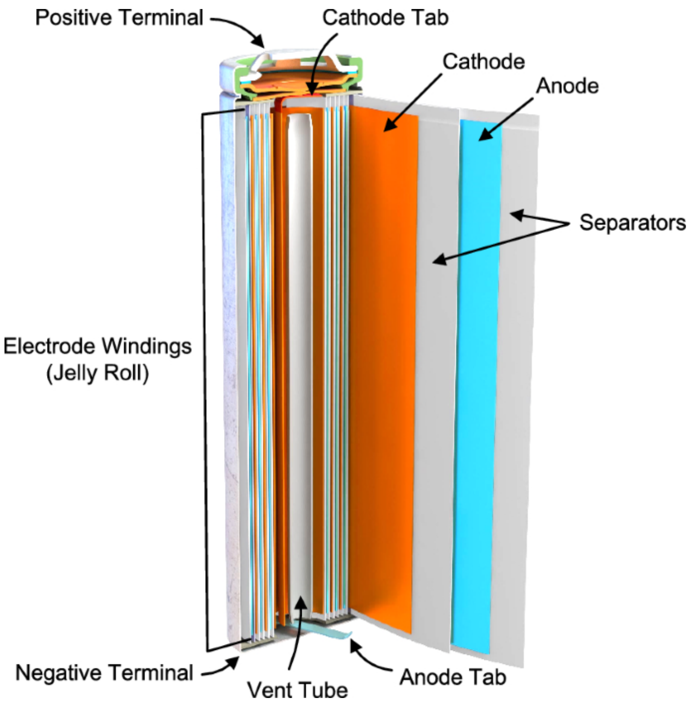

Figure 1.1: Lithium-ion cell Construction

Among various battery technologies, Li-ion chemistries are widely used due to their high energy density, long cycle life, and relatively low self-discharge rates.

Unlike traditional batteries that rely on chemical breakdown (like lead-acid), the physical operation of Li-ion batteries relies on a mechanism called intercalation. The intercalation process involves the reversible insertion and extraction of lithium ions into and from the electrode materials during charging and discharging cycles, as opposite to plating or alloying mechanisms found in other battery types. This process allows for efficient energy storage and release while maintaining the structural integrity of the electrode materials over time.

Li-ion battery cell electrodes are thus typically made of materials that present a chemical structure that can easily accommodate lithium ions through intercalation:

- **Cathode materials**: The cathodes are usually made of lithium metal oxides, that are the source of lithium ions in the cell. Common cathode materials are Lithium Cobalt Oxide (LCO), Lithium Manganese Oxide (LMO), Lithium Iron Phosphate (LFP), Lithium Nickel Manganese Cobalt Oxide (NMC), and Lithium Nickel Cobalt Aluminum Oxide (NCA). These materials are chosen for their high energy density, stability, and ability to reversibly intercalate lithium ions. A summary of cathode materials' main properties is reported in Table 1.1

- **Anode materials**: Graphite is the most commonly used anode material due to its excellent Li-ion intercalation properties, good electrical conductivity and low cost. Other materials, such as hard carbon, silicon and Lithium Titanate Oxide (LTO) are also adopted in some applications for their higher capacity or faster charging capabilities. A summary of anode materials' main properties is reported in Table 1.2

- **Electrolyte**: The electrolyte is typically a lithium salt (e.g., $LiPF_6$) dissolved in a mixture of organic solvents, which provides high ionic conductivity and stability over a wide temperature range

- **Separator**: Separators are usually made of microporous polymers, such as polyethylene (PE) or polypropylene (PP), which provide mechanical strength and chemical stability while allowing ion flow

The cathode material is usually deposited onto a thin aluminum foil that acts as a current collector. The anode material is usually deposited onto a thin copper foil that acts as a current collector. The current collectors are welded to the cell terminals, allowing the flow of electrons to the external circuit.

Table 1.1: Comparison of Li-ion battery cathode materials [2] [3] [4]

Material	**LCO**	**LMO**	**LFP**	**NMC**	**NCA**
Formula	$LiCoO_2$	$LiMn_2O_4$	$LiFePO_4$	$LiNiMnCoO_2$	$LiNiCoAlO_2$
Structure	Layered	Spinel	Olivine	Layered	Layered
Energy (Wh/kg)	150–200	100–150	90–160	150–220	200–260
Voltage (V)	3,6–3,7	3,7–3,8	3,2–3,3	3,6–3,7	3,60
Cycle Life (cycles)	500–1000	300–700	1000–2000	1000–2000	500–1000
Runaway (°C)	≈ 150	≈ 250	≈ 270	≈ 210	≈ 150
Safety	Low	Mod/High	Very High	Moderate	Low/Mod
Cost	High	Low	Very Low	Moderate	High

Table 1.2: Comparison of Li-ion battery anode materials [2] [3] [4]

Material	**Graphite**	**LTO**	**Silicon**	**Hard Carbon**
Formula	C_6	$Li_4Ti_5O_{12}$	Si	C
Structure	Layered	Spinel	Diamond/Amorphus	Turbostratic
Capacity (mAh/g)	350–372	160–175	3500–4200	200–400
Voltage (V)	0,05–0,2	1,5–1,6	0,3–0,5	0,1–1,0
Cycle Life	1000–5000+	10000+	< 500	1000+
Safety	Moderate	Very High	Moderate	Mod/High
Cost	Low	High	High	Low

1.1.2 Li-ion Cell Operation

The process of Li-ions intercalation is illustrated in Figure 1.2:

- During discharge, lithium ions move from the anode to the cathode through the electrolyte, while electrons flow through an external circuit providing electrical energy to the powered device. The anode undergoes oxidation, releasing lithium ions and electrons

  $$\textbf{Anode Reaction: } \mathrm{Li}_x\mathrm{C}_6 \longrightarrow x\mathrm{Li}^+ + x\mathrm{e}^- + \mathrm{C}_6 \tag{1.1}$$

  while the cathode undergoes reduction, accepting lithium ions and electrons

  $$\textbf{Cathode Reaction: } \mathrm{Li}_{1-x}\mathrm{CoO}_2 + x\mathrm{Li}^+ + x\mathrm{e}^- \longrightarrow \mathrm{LiCoO}_2 \tag{1.2}$$

- During charging, the external power source forces electrodes, and thus the lithium ions, to move back from the cathode to the anode. As for the charging process, the electrons are forced to flow through the external circuit, while the lithium ions travel through the electrolyte and separator within the battery cell (the two semi-reactions are the same, but the verse is opposite to the discharge one)

The overall cell reaction can be summarized as

$$\mathrm{Li}_x\mathrm{C}_6 + \mathrm{Li}_{1-x}\mathrm{CoO}_2 \rightleftharpoons \mathrm{C}_6 + \mathrm{LiCoO}_2 \tag{1.3}$$

where

- during discharge the reaction proceeds from left to right (→)
- during charge the reaction proceeds from right to left (←)

Note that $\mathrm{Li}_x\mathrm{C}_6$ and C_6 represent the anode material (e.g. graphite) in the lithiated and delithiated states, respectively, while $\mathrm{Li}_{1-x}\mathrm{CoO}_2$ and LiCoO_2 represent the cathode material (e.g. lithium cobalt oxide) in the delithiated and lithiated states. Remember that, when the cell is fully charged, the anode is fully lithiated and the cathode is fully delithiated. Vice versa occurs when the cell is fully discharged.

1.1.3 Li-ion Cell Form Factors

Battery cells come in various form factors, each with its own advantages and disadvantages in terms of energy density, thermal management, manufacturing complexity, and cost. Figure 1.3 shows the three most common battery cell form factors:

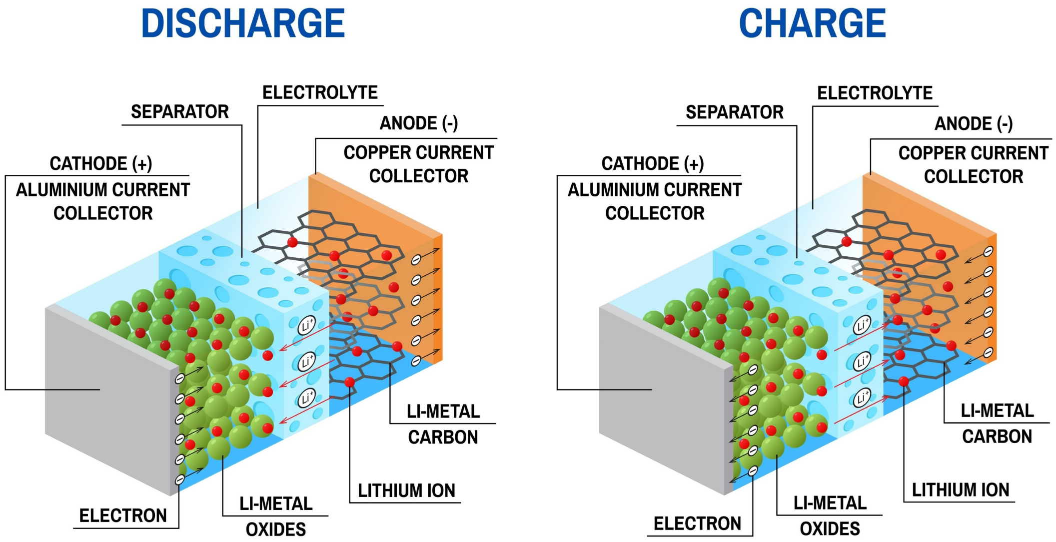

Figure 1.2: Lithium-ion cell operation

- **Cylindrical cells**: These cells have a cylindrical shape and are widely used in automotive applications due to their high manufacturability, optimal mechanical robustness and good thermal managment compatibility. They are available in different form factors, such as 18650, 21700, and 46800 where the numbers indicate the dimensions of the cell (e.g., 46 mm diameter and 80 mm length for 46800 cells)

- **Prismatic cells**: These cells have a rectangular shape and are often preferred due to their higher energy density at pack level and easier packability. On the downside, they can present challenges in thermal management and mechanical stability compared to cylindrical cells (e.g., swelling issues). They are commonly used in EVs and stationary ESSs

- **Pouch cells**: These cells have a flexible, pouch-like structure that allows for lightweight and compact designs. They are commonly used in portable electronics and advanced EVe applications, offering high energy density and design flexibility, but they may require additional protective measures to prevent swelling and damage due to their lack of a rigid casing

Table 1.3 provides an overview of the battery cell form factors adopted by major automotive manufacturers in their EVs, along with the specific cell variants and chemistries used.

Table 1.3: Overview of battery cell form factors in automotive applications [5]

Manufacturer	Vehicle Model	Form Factor	Chemistry
Tesla	Model 3/Y (LR)	Cylindrical 21700	NMC/NCA
Tesla	Model 3/Y (SR)	Prismatic	LFP
Tesla	Cybertruck	Cylindrical 46800	NMC
Tesla	Model S/X (Plaid)	Cylindrical 18650	NCA
BYD	Seal/Han/Atto 3	Prismatic	LFP
Ford	Mustang Mach-E (ER)	Pouch	NMC
Ford	Mustang Mach-E (SR)	Prismatic	LFP
Ford	F-150 Lightning	Pouch	NMC
General Motors	Hummer EV/Lyriq	Pouch	NCMA
Volkswagen	ID.4/ID. Buzz	Prismatic	NMC
Hyundai/Kia	Ioniq 5/EV6	Pouch	NMC
BMW	i4/iX	Prismatic	NMC
Rivian	R1T/R1S	Cylindrical 21700	NMC/LFP
Lucid	Air/Gravity	Cylindrical 21700	NMC/NCA
Toyota	bZ4X	Prismatic	NMC
Porsche	Taycan	Pouch	NMC
Porsche	Macan	Prismatic	NMC
Rimac	Nevera	Cylindrical 21700	NMC
Ferrari	Elettrica	Pouch	NMC

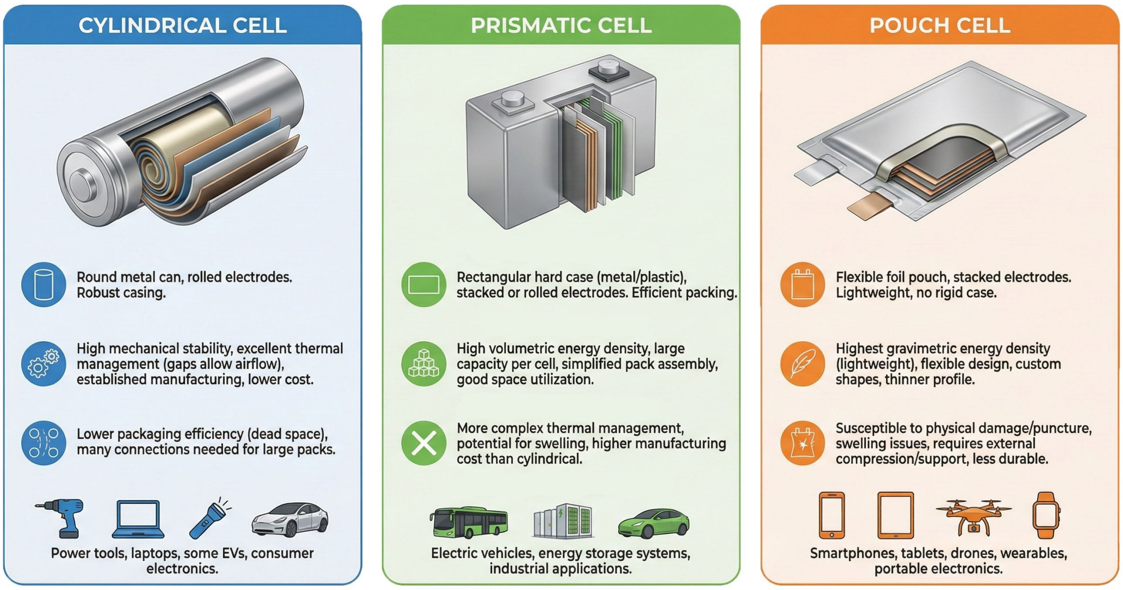

Round metal can, rolled electrodes. Robust casing.

High mechanical stability, excellent thermal management (gaps allow airflow), established manufacturing, lower cost.

Lower packaging efficiency (dead space), many connections needed for large packs.

Power tools, laptops, some EVs, consumer electronics.

Rectangular hard case (metal/plastic), stacked or rolled electrodes. Efficient packing.

High volumetric energy density, large capacity per cell, simplified pack assembly, good space utilization.

More complex thermal management, potential for swelling, higher manufacturing cost than cylindrical.

Electric vehicles, energy storage systems, industrial applications.

Flexible foil pouch, stacked electrodes. Lightweight, no rigid case.

Highest gravimetric energy density (lightweight), flexible design, custom shapes, thinner profile.

Susceptible to physical damage/puncture, swelling issues, requires external compression/support, less durable.

Smartphones, tablets, drones, wearables, portable electronics.

Figure 1.3: Battery cell form factors

1.1.4 Li-ion Cell Operating Parameters

The simplest representation of a battery cell is shown in Figure 1.4. The cell is modelled as an ideal voltage source V_{OC} and an internal series resistor R_i. The resistor R represents an external load connected to the battery terminals.

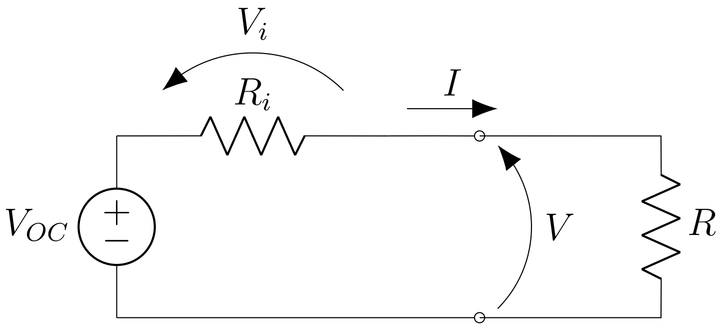

Figure 1.4: Simplified battery equivalent circuit model

Key operating parameters that influence the operation of the battery cell include:

1.1.4.1 Voltage

When discussing battery cell operating voltages, it is important to distinguish between:

- **Open Circuit Voltage** V_{OC}: The Open Circuit Voltage (OCV) is the theoretical voltage produced by the battery cell ignoring its internal losses. It corresponds to the voltage at the battery terminals when the battery is fully rested (i.e, no charging nor discharging has occured for a significant amount of time, and chemical equilibrium inside the battery has been reached). It depends on the State of Charge (SOC), temperature and latest current sign (this last dependence is a consequence of hysteresis phenomena, i.e, the OCV at agiven SOC is different depending on whether the battery was last charging or discharging)

$$V_{OC} = f(SOC, T, sgn(I)) \tag{1.4}$$

- **Terminal Voltage** V: The terminal voltage represents the voltage at the battery terminals when a load is applied. It depends on the OCV, internal resistance and load characteristics

$$V = V_{OC} - \underbrace{R_i \cdot I}_{V_i} = f(OCV, R_i, R) \tag{1.5}$$

The OCV is more relevant for estimating the SOC, while the terminal voltage determines the usable power on the load and the overall system behaviour.

1.1.4.2 Internal Resistance

The internal resistance R_i is a lumped parameter that represents all the internal losses within the battery cell. Internal losses can be classified into three contributions:

- **Ohmic (Resistive) Losses**: They are due to the resistance of electrodes, current collectors, electrolyte and separator. They are proportional to current and appear immediately when a load is applied

- **Charge Transfer (Activation) Losses**: They represent the energy barrier that must be overcome for charge transfer to occur at the electrode interface. They are nonlinear with current and dominant at low currents

- **Mass Transport (Concentration) Losses**: They are a consequence of mass transport at the electrode surface, as the reactants are consumed (or produced) faster than they can be replenished (or removed) by diffusion. They are strongly nonlinear with current and dominant at high currents

The different contributions are also showed for clarity in Figure 1.5.

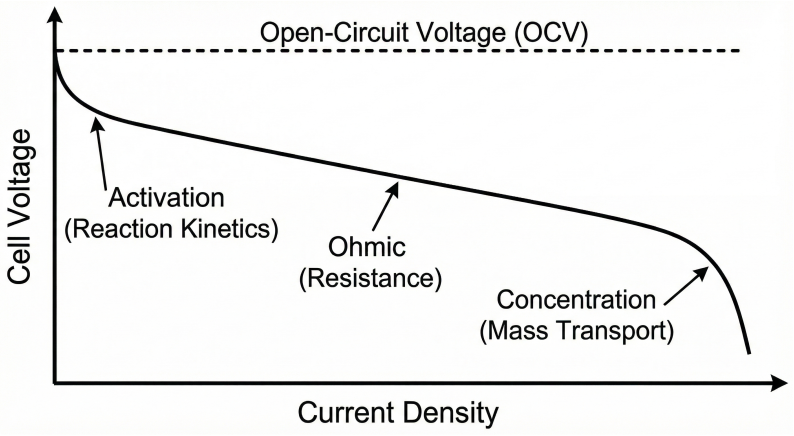

Figure 1.5: Voltage loss contributions

The internal resistance depends on the SOC, temperature, sign of the current (if the cell is charging or discharging) and age of the cell

$$R_i = f(SOC, T, sgn(I), aging) \tag{1.6}$$

1.1.4.3 Current

In the context of battery cells, the current sign convenction is usually such that I is assumed positive when it's discharging the cell (providing power to the load).

Current intensity can also be expressed as a C-rate. The C-rate is defined as the current I (in amperes) given as a multiple or fraction of the battery's rated capacity C (in ampere-hours, Ah).

$$C\text{-}rate = \frac{I}{C} \tag{1.7}$$

1.1.4.4 Capacity

The capacity of a cell C is the total amount of charge that it can store and deliver under specified conditions. Mathematically, the capacity can be just obtained as the integral of the current in time. It is usually expressed in ampere-hours (Ah)

$$C = \int I(t)\, dt \tag{1.8}$$

The rated capacity of a battery cell is referred to a 20 hours discharge process (thus with a current of C/20) performed at 20 °C. The actual capacity generally depends on the discharge conditions (current, temperature) and age of the cell

$$C = f(I, T, aging) \tag{1.9}$$

- **Current**: The actual capacity decreases for increasing discharge current (see Figure 1.6 for an example)
- **Temperature**: The actual capacity decreases for decreasing temperature (see Figure 1.7 for an example)
- **Aging**: The actual capacity decreases (fades) for increasing age (see Figure 1.8 for an example)

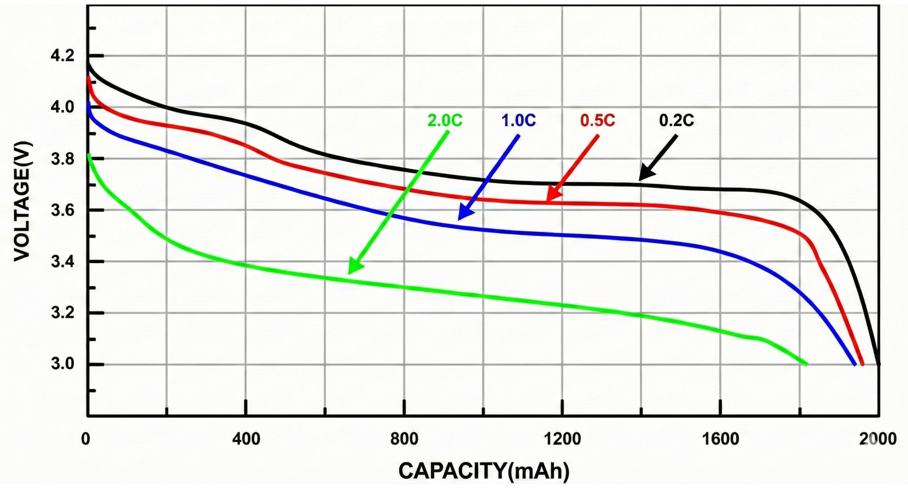

Figure 1.6: Discharge curves of a Li-ion cell at different C-rates [6]

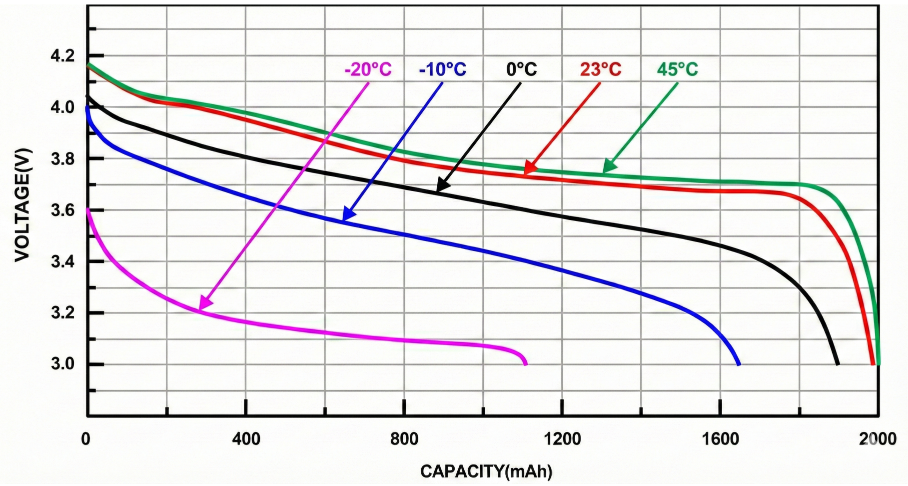

Figure 1.7: Discharge curves of a Li-ion cell at different temperatures [6]

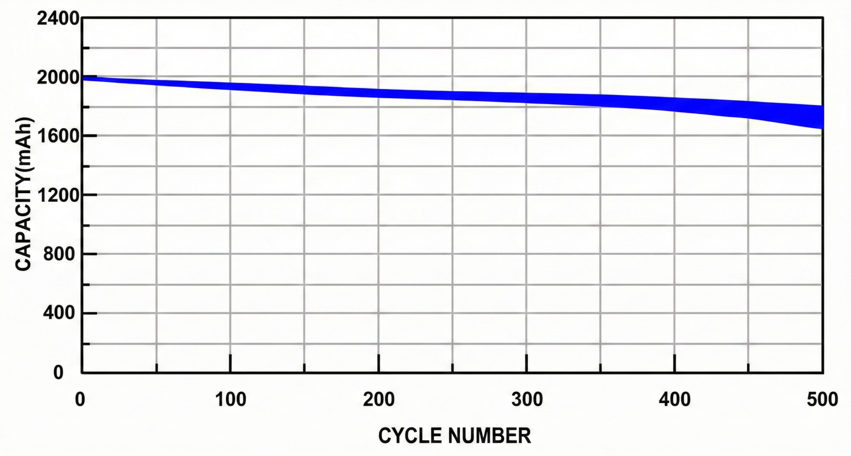

Figure 1.8: Capacity fade of a Li-ion cell with aging [6]

1.1.4.5 State of Charge (SOC)

The State of Charge (SOC) is a dimensionless value describing the amount of usable charge available in the battery expressed as a percentage of the rated capacity

$$SOC(t) = \frac{C(t)}{C_{Rated}} = SOC_0 - \frac{\int I(t)\,dt}{C_{Rated}} \tag{1.10}$$

The typical Li-ion characteristic $V_{OC} = f(SOC)$ curve is shown in Figure 1.9.

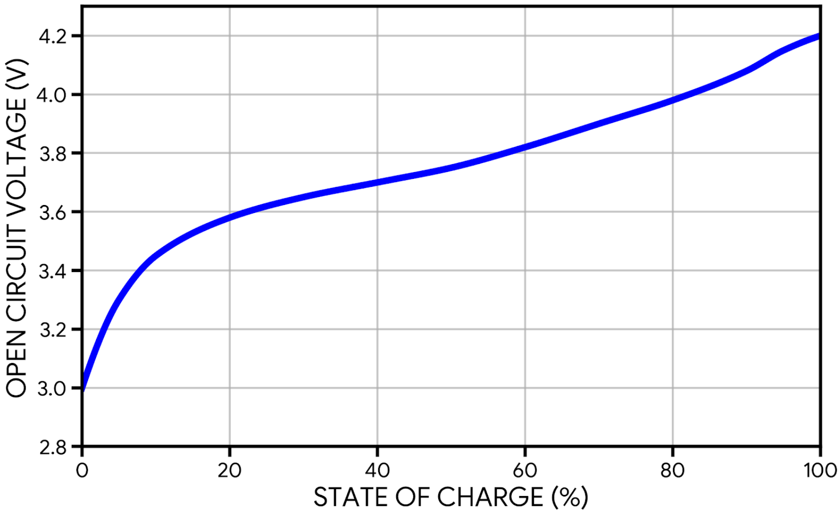

Figure 1.9: Characteristic curve of a Li-ion cell

Sometimes, a parameter called Depth of Discharge (DOD) is used instead of the SOC. It is defined as the complement of the SOC

$$DOD(t) = 1 - SOC(t) \tag{1.11}$$

1.1.4.6 Energy

The energy of a battery cell is the total amount of electrical energy the cell can deliver when discharged from its charged state to its cutoff voltage. Mathematically, the energy can be just obtained as the integral of the voltage with respect to capacity. It is usually expressed in watt-hours (Wh)

$$E = \int V(C)\, dC \tag{1.12}$$

1.1.4.7 State of Energy (SOE)

As for the SOC for capacity, a dimensionless parameter can be defined to describe the effective battery energy content at a given instant. It is called the State of Energy (SOE)

$$SOE(t) = \frac{E(t)}{E_{Rated}} = SOE_0 - \frac{\int P(t)\, dt}{E_{Rated}} \tag{1.13}$$

where $E_{Rated} = C_{Rated} \cdot V_{Rated}$ and $P(t) = V(t) \cdot I(t)$.

1.1.4.8 Heat Generation

Heat generation in a battery cell comes from several physical and electrochemical processes. The fundamental components are the following [7, 8, 9, 10]:

- **Irreversible Heat $\dot{Q}_{irr}$**: This is energy permanently lost as heat due to internal losses. It always heats the battery, regardless of whether it is charged or discharged (irreversible). It incorporates two different contributions:
    - **Joule Heating**: This is the heat generated by Joule effect as a consequence of the flow of electrons and ions through the resistive components of the cell
    - **Polarization Heat**: This heat arises from the energy barriers that must be overcome for the electrochemical reactions to occur. It is due to the activation and concentration polarization phenomena already discussed in Section 1.1.4.2 for internal resistance

  These two terms are typically lumped toghether into

$$\dot{Q}_{irr} = R_i I^2 = I(V_{OC} - V) \tag{1.14}$$

- **Reversible (Entropic) Heat $\dot{Q}_{rev}$**: It represents the energy absorbed or released as a result of entropy changes associated with the electrochemical reactions. Unlike irreversible heat, this can either generate or absorb heat (reversible). It can be expressed using the following equation

  $$\dot{Q}_{rev} = -IT\frac{dV_{OC}}{dT} \tag{1.15}$$

  where the term $\frac{dV_{OC}}{dT}$ is usually referred to as EHC.

  Note that the entropic term has been defined with a negative sign to comply with the chosen current sign convention: a positive EHC indicates endothermic reversible heat generation during discharging, and exothermic during charging (the opposite applies for a negative EHC) [10]. In general, the EHC can be either positive or negative, varying with the battery's SOC and the specific electrochemistry [7, 11].

  At low currents (e.g., C/10), the entropic heat is significant and can actually cause a battery to cool down slightly during parts of the charge/discharge cycle. On the other hand, at high currents the irreversible heat term is usually predominant, and the entropic contribution can be neglected [12]

- **Side Reactions Heat $\dot{Q}_{SideReactions}$**: It is produced as a consequence of parasitic reactions like Solid Electrolyte Interphase[2] (SEI) formation and growth, electrolyte decomposition and lithium plating. However, side reactions typically happen at sufficiently slow rates such that they contribute negligibly to the cell's total heat generation, particularly in their operating temperature range (this contribution becomes non-negligible only at high temperatures, close to thermal runaway[3] conditions)

- **Mixing Heat $\dot{Q}_{Mixing}$**: This heat arises from concentration gradients in the battery due to lithium ions movement through the electrolyte or diffusion inside the electrodes. For electrochemical systems with good transport properties, these concentration gradients are generally negligible

---

[2] The SEI is a thin, passivation layer that forms on the surface of the anode during the first few charge cycles of a Li-ion battery. Being ionically conductive and electronically insulating, it doesn't affect cell operation. It has a protective function, preventing further electrolyte decomposition and shielding the anode from chemical attacks

[3] Thermal runaway is a self-reinforcing failure phenomenon in which an initial abuse or fault (e.g., overheating, overcharging, internal short circuit, or mechanical damage) causes the battery temperature to rise, triggering a sequence of exothermic reactions that generate heat faster than it can be dissipated, leading to an uncontrolled temperature increase that often results in venting of gases, fire, and explosion

Thus, ignoring the side reactions and mixing terms, the overall formula for the heat produced or absorbed by a battery cell can be written as

$$\dot{Q} = \underbrace{I(V_{OC} - V)}_{\text{Irreversible}} - \underbrace{IT\frac{dV_{OC}}{dT}}_{\text{Reversible}} \tag{1.16}$$

Where the sign convention for heat generation is such that $\dot{Q}$ is positive when heat is produced by the battery cell (when discharging, $I > 0$ and $V < V_{OC}$ thus $\dot{Q}_{irr} > 0$, while when charging $I < 0$ and $V > V_{OC}$ thus still $\dot{Q}_{irr} > 0$. As said already, the sign of $\dot{Q}_{rev}$ instead depends on the relative sign of the current and the EHC, that generally varies) and negative when heat is absorbed.

Overall, the heat generated is dependent upon the charge/discharge current, temperature, SOC, and age of the cell

$$\dot{Q} = f(I, T, SOC, aging) \tag{1.17}$$

1.1.4.9 Efficiency

The (round trip energy) efficiency of a battery cell describes how effectively it converts electrical energy between charge and discharge, accounting for losses. It is the ratio of the electrical energy delivered during discharge $E_{Discharge}$ to the electrical energy supplied during charging E_{Charge}

$$\eta = \frac{E_{Discharge}}{E_{Charge}} = \eta_C \cdot \eta_V \tag{1.18}$$

It is given by two contributions:

- **Coulombic (Faradaic) Efficiency** η_C: This is the charge efficiency by which electrons are transferred in a battery. It is the ratio of the total charge extracted from the battery $C_{Discharge}$ to the total charge input to the battery C_{Charge} over a cycle

  $$\eta_C = \frac{C_{Discharge}}{C_{Charge}} \tag{1.19}$$

  The typical columbic efficiencies of Li-ion cells are really high (>99%)

- **Voltaic Efficiency** η_V: This is the ratio of the average discharge voltage $V_{Discharge}$ to the average charge voltage V_{Charge} over a cycle (as introduced in Section 1.1.4.2 when presenting the internal resistance, the "input" charging voltage is always higher than the rated voltage to activate the chemical reaction within the battery, and the "output" discharging voltage is always lower than the rated one due to losses)

$$\eta_V = \frac{V_{Discharge}}{V_{Charge}} = \frac{V_{OC} - R_i \cdot I}{V_{OC} + R_i \cdot I} \tag{1.20}$$

Thus, the voltaic efficiency generally depends (using the super simple model of Figure 1.4) on the OCV, on the internal resistance R_i and especially on the discharge current I. This means that the efficiency of a battery will inevitably decay for increasing discharge (and charge) current rates.

Also note that the calculation of η_V is not really straightforward as typically both V_{OC}, R_i and I are variables that depend on different parameters and vary significantly during the discharge and charge processes

Typical energy efficiencies η of Li-ion cells are between 85 and 99% depending on the discharge conditions [13].

1.2 Characterization Techniques

Battery cell characterization is the systematic process of measuring, testing, and analyzing a battery cell's electrical, thermal, and electrochemical properties to understand its performance, behaviour, and limitations in defined working environments. The objective of battery characterization is generally to retrieve equivalent parameters that describe the cell operation under different operating conditions. The data that is gathered through characterization is then used for the development of battery simulation models. A faithful and reliabe battery model is essential for effective online parameter estimation[4] and robust BMS design [14, 15, 16, 17].

Battery characterization methods can be classified into:

- **Electrical Characterization**: Techniques that focus on characterizing the electrical performance of the battery cell, including voltage, current, capacity, internal resistance, and efficiency under various load conditions. They aim to obtain a simple way or representing the electrical effects related to the complex operation of the battery cell (chemical reaction kinetics and transport phenomena)

---

[4] Online parameter estimation is a real-time identification process that infers and updates battery model parameters from measured quantities during operation, enabling adaptive modelling, state estimation, and health monitoring under changing operating conditions

- **Thermal Characterization**: Techniques that focus on measuring the thermal behaviour of the battery cell, including temperature distribution, heat generation rates, thermal conductivity, and specific heat capacity. They aim to obtain a simple way or representing the thermal effects related to the complex operation of the battery cell (heat generation and dissipation mechanisms)
- **Physical Material Characterization**: Techniques that focus on analyzing the physical and chemical properties of battery materials, such as electrode morphology, electrolyte composition, and structural integrity. They can be performed after cell disassembly (e.g, material spectroscopy, electrode microscopy) of through non-destructive imaging methods (e.g., X-ray tomography)

In the context of this thesis, only the electrical and thermal characterization techniques are reviewed, as they are most relevant for the development of electrothermal battery models and require less specialized equipment compared to physical material characterization methods.

1.2.1 Electrical Characterization Techniques

Electrical characterization determines how a battery cell behaves electrically under different operating conditions. It can be subdivided into static and dynamic techniques:

- **Static techniques**: These techniques apply constant current profiles to the battery cell and measure its response over time. They are useful for determining parameters such as capacity, internal resistance, and OCV. The most common static characterization technique is the constant current charge/discharge test
- **Dynamic techniques**: These techniques utilize current or voltage pulses/sinusoids to evaluate the cell dynamic load response. They are useful for characterizing equivalent parameters that describe the cell's behaviour in response to time varying conditions. They can be further subdivided into Direct Current (DC) and Alternating Current (AC) techniques. Examples of dynamic characterization methods are Hybrid Pulse Power Characterization (HPPC), Galvanostatic Intermittent Titration Technique (GITT) and Electrochemical Impedance Spectroscopy (EIS)

Other specific tests can be developed depending on the specific research interests and application requirements. Manuals [18] and [19] provide comprehensive reviews of battery electrical characterization techniques that are not covered in this thesis, like peak power, self discharge and cycle life tests. One other widely used technique that is not implemented in this thesis but is commonly used in research and in industry is the use of real-world drive cycles [17, 20, 14, 21, 22]. This approach is based on varying current profiles that simulate real-world operating conditions and are inspired on standardized driving cycles. The most common real-world driving profiles are based on the FTP-72 (Federal Test Procedure 1972, common in the United States), WLTP (Worldwide Harmonized Light Vehicles Test Procedure, used especially in Europe) and CLTC (China Light-Duty Vehicle Test Cycle, developed in China) standards. They are designed to replicate everyday driving conditions, including acceleration, deceleration, idling, and cruising phases, to provide a realistic assessment of vehicle energy consumption. These more sofisticated approaches are usually implemented in later stages of battery testing and validation rather than in the initial characterization phase.

The main techniques of interest for the context of this study and typically used for electrical characterization of Li-ion cells are:

1.2.1.1 Constant Current Charge/Discharge Characterization

In this technique, the battery cell is first charged and then discharged with a constant current rate. The quantities that can be derived from this test are:

- **Capacity**: The capacity is calculated by integrating the charge/discharge current over the charge/discharge time, providing a measure of the total charge the battery can store and deliver. The effects of temperature, charge/discharge rate and aging can also be analyzed by performing multiple tests under different conditions. Examples of applications of this technique in research are [17, 14, 23, 16, 15].

- **Open Circuit Voltage (OCV)**: The OCV can be obtained by charging/discharging the cell at a very low current (like C/20 or C/50) to minimize internal resistance effects[5]. The OCV curve is then derived by averaging the charge and discharge voltage profiles (to mitigate hysteresis effects). Examples of research applications of this approach include [17, 14].

- **Internal Resistance**: The internal resistance can be estimated by comparing the OCV to the terminal voltage, and applying Ohm's law

$$R_i = \frac{V_{OC} - V}{I} \tag{1.21}$$

---

[5] The OCV can also be derived using higher current rates, but to exclude the effect of internal losses the battery needs to rest sufficiently before each voltage measurement is performed [24]

The charge and discharge processes are set up according to the Constant Current (CC) and Constant Voltage (CV) strategies:

- **CC-CV Charging**: Initially, the charger supplies a fixed current (usually 1 C), and the voltage of the cell gradually rises as it charges (CC phase). Once the battery voltage reaches the maximum charge voltage threshold (usually 4,2 V for Li-ion chemistries), the charger switches to CV mode. The voltage is held steady while the current gradually decreases as the battery approaches full charge. The charging process is stopped when the current drops below a specific threshold (usually a small fraction of the nominal current, like C/50 or C/100). The charge process is shown in Figure 1.10

- **CC Discharging**: The battery cell is dicharged with a constant current (spanning a large range of values, from C/20 to even 20 C) until the minimum discharge voltage threshold is reached. As this happens discharge is stopped immediately

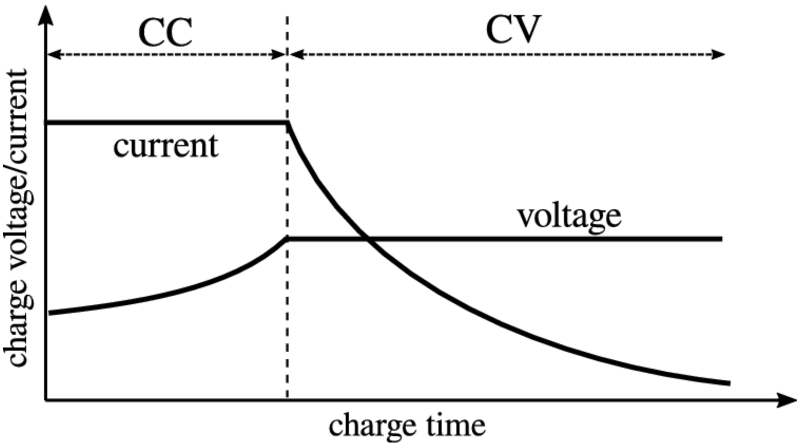

Figure 1.10: CC-CV charge curve [25]

1.2.1.2 Hybrid Pulse Power Characterization (HPPC)

Hybrid Pulse Power Characterization (HPPC) is a standardized test that applies high-current discharge and charge pulses at various SOC levels to determine dynamic power capability. The voltage response, specifically the instantaneous drop and the subsequent exponential recovery is used to build the ECM. The test also allows the estimation of the discharge and regen power capabilities, that are used to estimate the theoretical maximum power that can be provided/recovered at a given SOC (those quantities will not be investigated in this thesis, more information is available in [18] and [19]).

The detailed HPPC test profile is resumed in Table 1.4, and is composed of the following steps:

- **Static Capacity Test**: First of all, the battery cell is fully discharged (Step 0). If the cell was originally fully charged, this CC discharge cycle is often used for obtaining a precise estimation of the actual capacity of the cell (fundamentally performing a static capacity test). The reason why it is important ho have a recent estimation of the cell's capacity is because this value is required to calculate the capacity to be removed at each 10% SOC step of the HPPC
- **HPPC Test Preparation**: Then, the cell is fully charged following a CC-CV charging procedure (Step 1). After that, the cell is let to rest for at least 1 hour for achieving thermal and electrochemical equilibrium (Step 2). This introductory steps are visible in Figure 1.11
- **HPPC Pulses**: Finally, the HPPC pulses are performed:
  - **Discharge Pulse** (Step 3): A 10-second-long CC discharge pulse, having a current intensity of 1 C
  - **Relaxation** (Step 4): A 40-second-long relaxation phase, that allows for measurement of the dynamic cell response
  - **Charge Pulse** (Step 5): A 10-second-long CC charge pulse, having a current intensity of 75% the discharge one (thus 0,75 C)
  - **SOC Discharge** (Step 6): A CC discharge phase, having a current intensity of 1 C, with the purpose of decreasing the SOC by 10%

  The pulses are repeated for 9 times, spanning in the 90 to 10% SOC range at 10% decrements. Between each set of pulses, a 1-hour rest time is present for equilibration purposes. The detail of the pulses is show in Figure 1.12.

  As stated in [19], the HPPC can be either performed at low current (at least 1 C) or high current (75% of the manufacturer's absolute maximum allowable pulse discharge current for 30 seconds). The low current HPPC test is what is found most commonly in the literature.

  For more accurate results, a use-specific tuning of the HPPC pulse parameters (height and length of the discharge and regen pulses, relaxation time duration) can be performed. Article [17] proves that changing the pulse specifications affects the final results, and informs that the chosen profile should be modified for the application. In the context of this thesis, the standard 1 C low pulse discharge current profile will be kept as a reference

The complete test sequence can be seen in Figure 1.13. In this example, an HPPC with subsequent -10% SOC discharging steps has been considered. The same approach can be used with +10% SOC charging steps.

The explanation on how the ECM parameters are retrieved from experimental data is discussed in Section 3.2.2.

Examples of research applications of HPPC include [17, 23, 21, 26, 22].

Table 1.4: HPPC test profile [18]

Step	Mode	Value	Limit	Time	Notes
0	CC Discharge	1 C	2,5 V	-	Discharge to 0% SOC
1	CC-CV Charge	1 C	4,2 V/0,05 A	-	Charge to 100% SOC
2	Rest	-	-	1 h	Equilibrium
3	**CC Discharge**	**1 C**	**2,5 V**	**10 s**	**Discharge Pulse**
4	Rest	-	-	40 s	Relaxation
5	**CC Charge**	**0,75 C**	**4,2 V**	**10 s**	**Regen Pulse**
6	CC Discharge	1 C	2,5 V	-	Remove 10% Capacity
7	Loop	-	-	-	Go to Step 2 (Repeat 9 times)
8	End	-	-	-	Test Complete

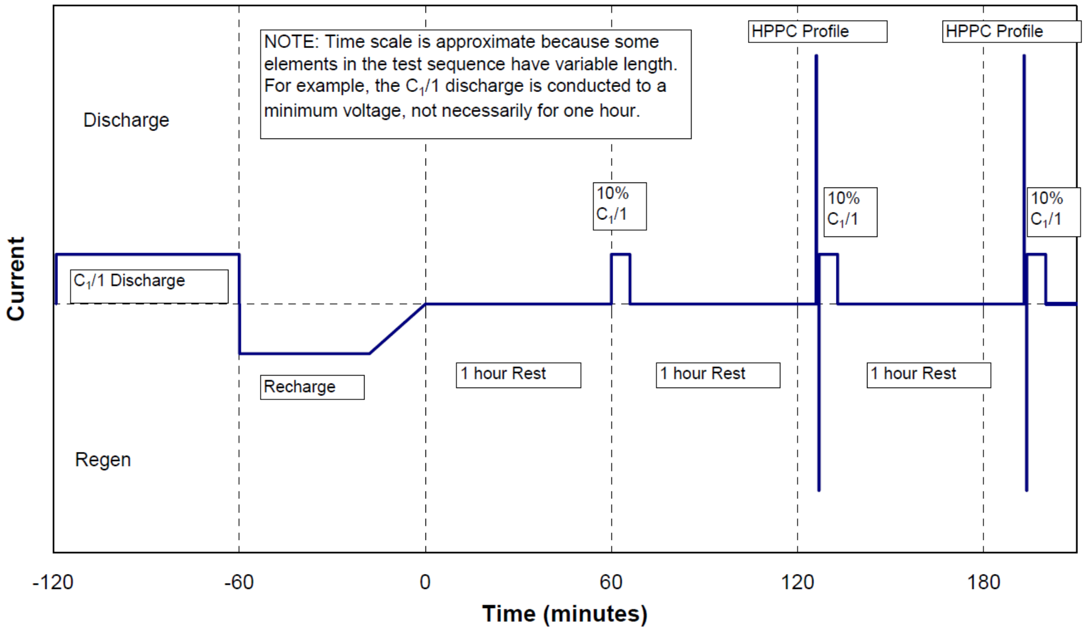

Figure 1.11: HPPC test start [18]

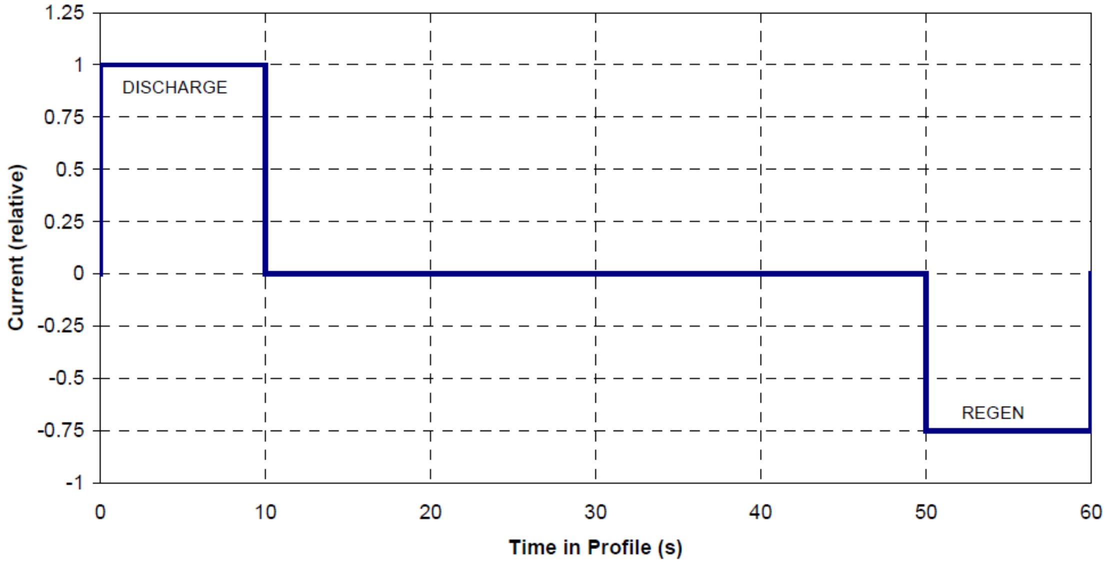

Figure 1.12: HPPC test discharge and regen pulses [18]

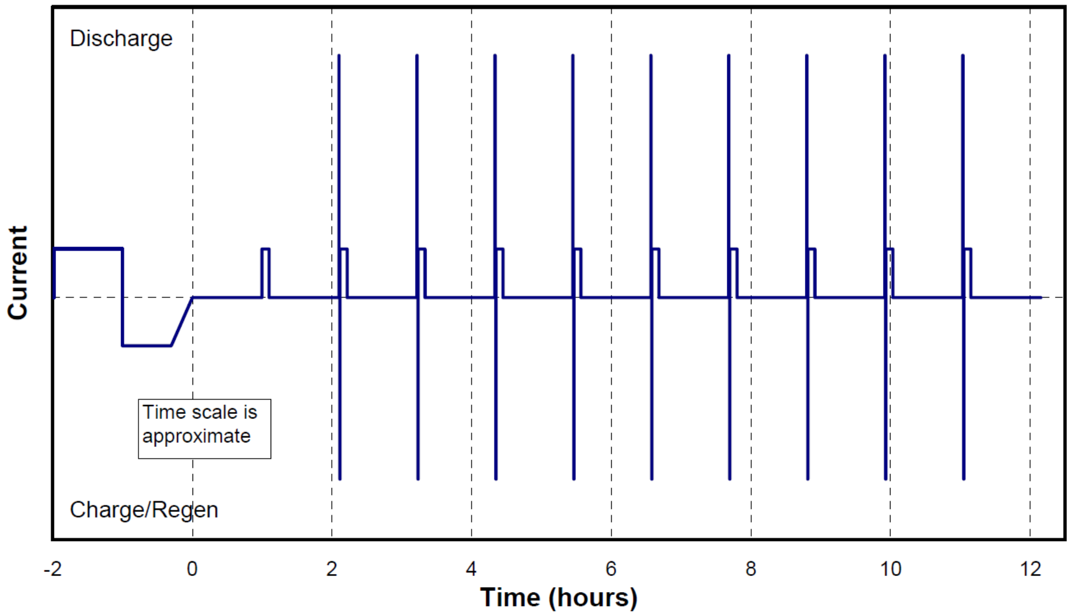

Figure 1.13: HPPC full test sequence [18]

1.2.1.3 Galvanostatic Intermittent Titration Technique (GITT)

Similar to HPPC, Galvanostatic Intermittent Titration Technique (GITT) also uses impulsive loads to characterize battery cells. GITT is a high-precision electrochemical testing method that consists of a series of small current pulses followed by long relaxation periods, repeated across the entire SOC window. Unlike HPPC, which focuses on high-current power capability, GITT focuses on the kinetics of ion movement and thermodynamic equilibrium. The foundational paper that defines GITT and derives the mathematical framework behind it is [27]. In the context of Li-ion batteries, GITT has three main applications: determining the diffusion coefficient of lithium ions within the electrode active materials, analyzing the OCV, and evaluating overpotential and internal resistance.

Different current intensities and durations, together with different relation times, can be used [28]. In Table 1.5 the typical test parameters for GITT are reported. The general GITT test profile, shown in Figure 1.14, is composed by the following steps:

- **GITT Test Preparation**: The cell is fully charged following a CC-CV charging procedure (Step 1). After that, the cell is let to rest for at least 4 hours for achieving thermal and electrochemical equilibrium (Step 2)
- **HPPC Pulses**: The GITT pulses are performed:
    - **Titration Pulse** (Step 3): A constant current pulse, having a low current amplitude (e.g., C/10 or C/20) is applied for an intermediate duration (typically 10 to 30 minutes)
    - **Relaxation** (Step 4): Then, the current is stopped for a long duration (typically 1 to 4 hours)

  This loop is run until the minimum discharge voltage threshold is reached

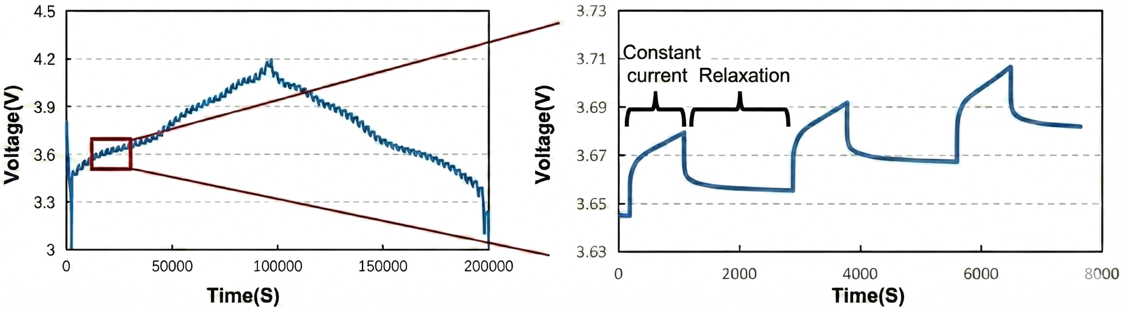

Figure 1.14: GITT test sequence [29]

As for HPPC, GITT can be applied also to consecutive charging steps. This combined charge/discharge approach can be used for the study of hysteresis phenomena.

Table 1.5: GITT test profile

Step	Mode	Value	Limit	Time	Notes
1	CC-CV Charge	1 C	4,2 V/0,05 A	-	Charge to 100% SOC
2	Rest	-	-	4 h	Equilibrium
3	**CC Discharge**	**C/20**	**2,5 V**	**10 m**	**Titration Pulse**
4	**Rest**	**-**	**-**	**1 h**	**Relaxation**
5	Loop	-	-	-	Go to Step 3 (Repeat until $V_{cell} \leq 2,5V$)
6	End	-	-	-	Test Complete

Since the focus of this thesis is more on ECM rather than detailed electrochemical characterization, HPPC has been chosen in place of GITT as the main test methodology for battery cell electrical characterization.

An example of application of GITT in the literature is given by [14]. [15] proposes a “Current pulse test” that shares some similarities with the GITT approach.

1.2.1.4 Electrochemical Impedance Spectroscopy (EIS)

Electrochemical Impedance Spectroscopy (EIS) is a frequency-based electrochemical technique that probes resistance, capacitance, and diffusion processes in electrochemical systems by measuring their impedance response to small AC signals. While HPPC and GITT are time-domain (DC) techniques, EIS is a frequency-domain (AC) technique. It applies a sinusoidal perturbation (voltage or current) sweeped over a range of frequencies, and measures the system response (current or voltage, respectively) so that the electrical impedance $Z(\omega)$, function of angular frequency $\omega = 2\pi f$, can be characterized.

$$Z(\omega) = \frac{V(\omega)}{I(\omega)} \tag{1.22}$$

In the context of Li-ion battey cells, EIS is used to identify and quantify different resistance, capacitance and impedance contributions within the cell: ohmic resistance R_{ohm}, charge transfer resistance R_{ct}, Solid Electrolyte Interphase (SEI) resistance R_{SEI} and capacitance C_{SEI}, double layer capacitance C_{dl}, and diffusion impedance (also called Warburg impedance Z_W). An introductory overview of EIS and its applications is proposed in [30].

The general EIS test profile, shown in Table 1.6, is composed by the following steps:

- **EIS Test Preparation**: The battery is brought to a specific SOC (e.g., 50%) through charging/discharging (Steps 1 and 2) and typically rested for a long period (1-4 hours) to ensure the voltage is stable (Step 3)
- **EIS Frequency Sweep** (Step 4): A small sinusoidal signal is applied. Two different test methodologies exist:
  - **Potentiostatic**: A voltage sine wave (typically 5 mV to 10 mV amplitude) is applied, and current response is measured
  - **Galvanostatic**: A current sine wave is applied, and voltage response is measured

  The frequency of the sine wave is changed over a sweep of frequencies, starting from a high frequency (e.g., 100 kHz) to a low frequency (e.g., 10 mHz)

Table 1.6: EIS test profile

Step	Mode	Value	Limit	Time	Notes
1	CC-CV Charge	1 C	4,2 V	-	Charge to 100% SOC
2	CC Discharge	1 C	-	-	Discharge to target SOC
3	Rest	-	-	4 h	Equilibrium
4	**EIS**	**5-10 mV (Amplitude)**	**-**	**-**	**100 kHz-0.01 Hz (Frequency)**
5	End	-	-	-	Test Complete

The test results are typicall showed as a Nyquist diagram of the complex cell impedance. The plot represents the cell resistance $R = Re(Z)$ on the horizontal axis, and the cell reactance $X = Im(Z)$ on the vertical one. Since battery cells usually have a predominant capacitive behaviour ($X < 0$) the plot typically has the vertical axis inverted. An example of these diagrams is reported in Figure 1.15, and its fundamental characteristics have been highlited with the following numbering:

1. The lower part of the plot, towards positive reactances $X > 0$ corresponds to the high frequency inductive behaviour of the cell

- The intersection of the curve with the horizontal axis represents the frequency at which the battery cell behaves as a resisitive component. The abscissa of the point represents the ohmic resistance of the cell R_{ohm}

2. The first (high frequency) arc represents the SEI layer resistance R_{SEI} and capacitance C_{SEI}
3. The second (mid frequency) arc represents the charge transfer resistance R_{ct} coupled with the double layer capacitance C_{dl}
4. The low frequency tail (usually a 45° line for $\omega \rightarrow 0$) represents the diffusive behaviour, often described by the Warburg impedance Z_W

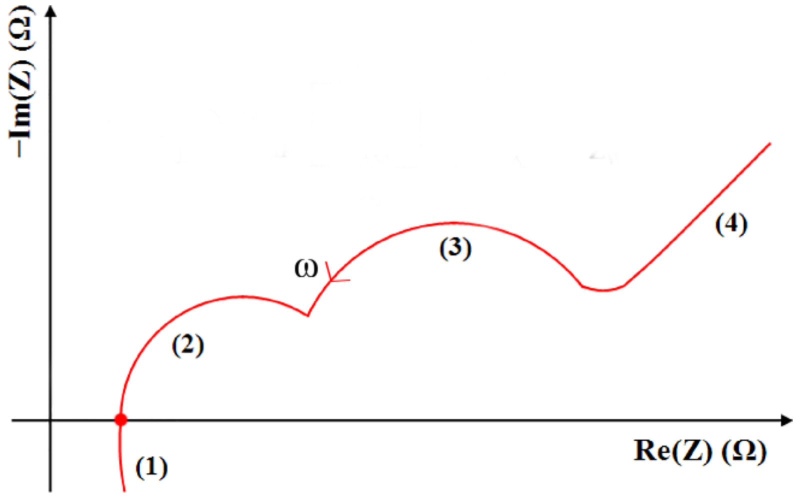

Figure 1.15: EIS cell impedance Nyquist diagram [31]

Due to the cost of the specific equipment required (potentiostat and frequency response analyzer) and the research interest on general cell characterization rather than advanced physical diagnostic, HPPC has been preferred over EIS for the scope of this thesis. This choice has been shared by many others in the literature [15, 26, 14, 22, 20].

1.2.2 Thermal Characterization Techniques

Thermal characterization examines how a battery cell generates, stores, and dissipates heat during operation. While the methodologies for electrical characterization have quite stagnantly settled on conventional standardized methods, the literature on thermal characterization techniques is quite vast and original, including methodologies quite different one from the other. This makes the task of creating a comprehensive classification quite difficult. Anyway, in general, thermal characterization tehcniques can be classified into steady state and transient methods [32] (Figure 1.16 proposes an overview of the advantages and disadvantages of the two approaches):

- **Steady-State Methods**: These techniques are characterized by a constant temperature profile over time ($\partial T/\partial t = 0$). They are ideally suited for measuring the thermal conductivity k. The most common steady state characterization methods are heat guarding, the heat flow comparative method, direct heating and the potentiometric method

- **Transient Methods**: These techniques are characterized by a time-varying temperature response ($\partial T/\partial t \neq 0$). They can measure thermal conductivity k and specific heat capacity c. The most common transient characterization methods are calorimetry, thermal impedance spectroscopy, the heat source method and variant convective cooling

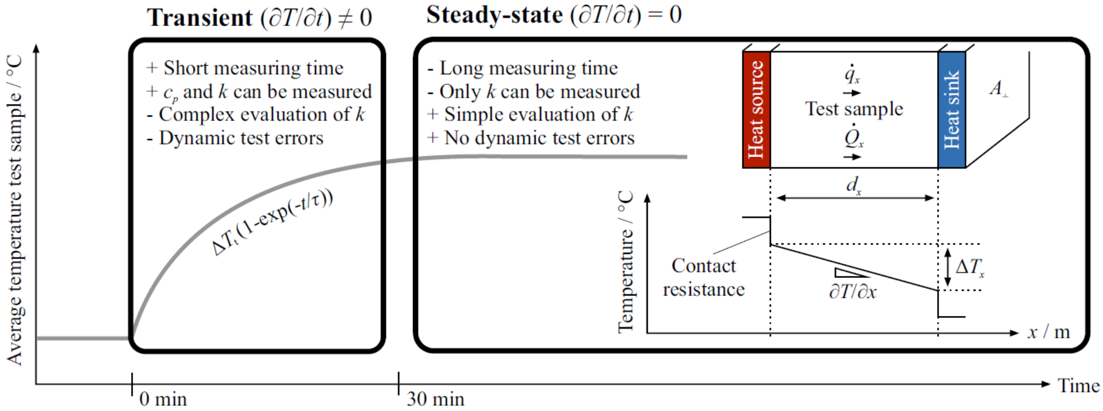

Figure 1.16: Thermal characterization techniques classification [32]

The main techniques of interest for the context of this study and typically used for thermal characterization of Li-ion cells are:

1.2.2.1 Heat Guarding Method

Heat guarding is a steady-state technique for measuring the thermal conductivity of materials by measuring heat flow through a sample. The most common version is the Guarded Hot Plate (GHP) method, that uses a central heater surrounded by a guard heater. The specimen is sandwiched between a central hot plate and one or more cold plates, with the separate guard ring heater surrounding it (Figure 1.17). Since the central and ring heater have the same temperature, the setup guarantees unidirectional heat flow from the hot to the cold plates. The system runs until it reaches thermal equilibrium, and at this point the thermal conductivity k is calculated using Fourier's Law for 1-dimensional heat conduction

$$k = \frac{\dot{Q} \cdot d}{A_c \cdot \Delta T} \tag{1.23}$$

where $\dot{Q}$ is the dissipated heat power, d the thickness of material, A_c the cross-sectional area, and ΔT is the temperature difference between the hot and cold side.

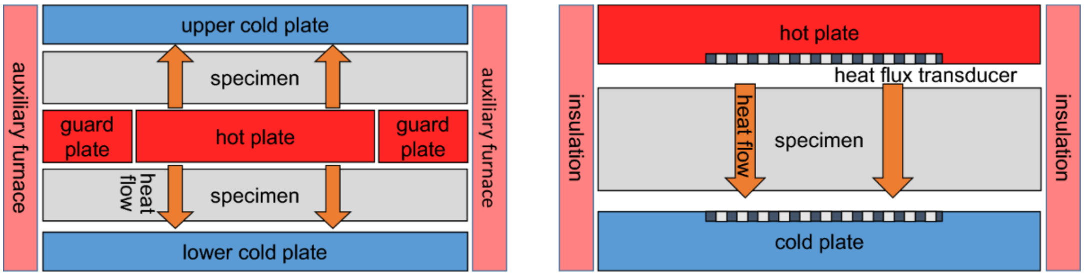

Figure 1.17: Examples of GHP setups [33]

In the context of battery cells, the standard GHP method can be applied only for the characterization of prismatic or pouch cells, as the cylindrical cell form factor difficultly adapts to this test setup [32]. One example of application of the GHP method for the characterization of prismatic Li-ion cells is presented in [34].

For the characterization of cylindrical cells, a novel heat guarding method has been been proposed by [35] (more precisely, this method follows a quasi steady-state approach, as it relies on a constant temperature rise rate rather than a constant absolute temperature). A central test battery is heated from one of the therminals, and to ensure that heat only flows axially and doesn't leak radially out the sides, the test battery is surrounded by "guard batteries" (dummy cells or identical cells) that are heated in the same way (Figure 1.18). This approach allows for a very precise measurement of the axial thermal conductivity k_z and specific heat capacity c simultaneously.

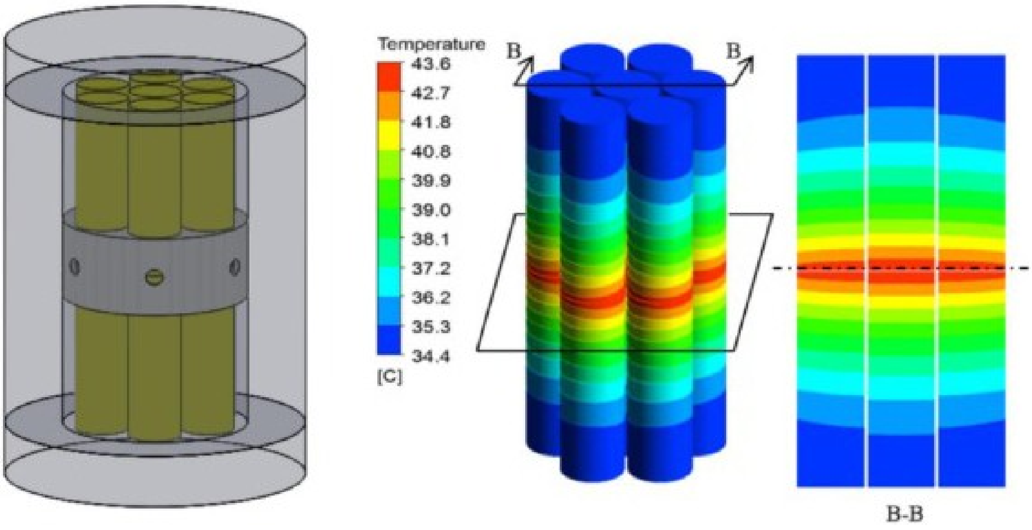

Figure 1.18: Quasi-steady state heat guarding measurement setup [35]

1.2.2.2 Heat Flow Comparative Method

The heat flow comparative method (Figure 1.19) is similar to the GHP, with the only difference that heat flow is determined by a heat flux sensor or by a reference material with known thermal conductivity. When the sample and a reference material (or heat flux sensor) are placed in series and insulated perfectly with respect to the surroundings, the heat flux flowing through them is the same. Thus, by using the heat flux sensor or by measuring the temperature drop on the reference material, the heat flux can be derived (measuring the temperature drop on the sample material allows one to derive the thermal conductivity using Equation 1.23).

In [36], the axial thermal conductivity of cylindrical Li-ion cells is assessed using brass cylinders as the heat flow comparative material.

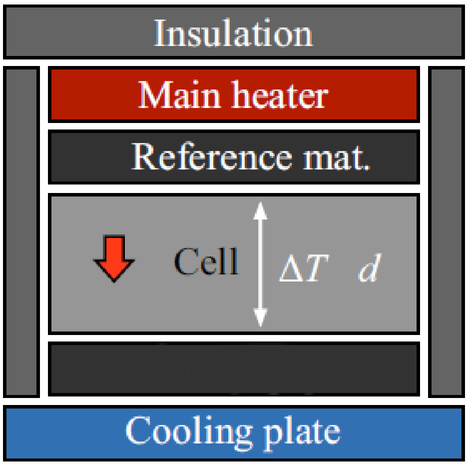

Figure 1.19: Heat flow comparative method setup [32]

1.2.2.3 Direct Heating Method

In the direct heating method (Figure 1.20), the heat used for thermal characterization is produced by powering the battery cells. The heating rate is calculated from the voltage and current of the test cell and the temperature difference is often measured between the inner core and the outer surface (when internal temperature measurements are required, direct heating is a destructive method). Due to the spatial distribution of the heat rate, which is generated volumetrically within the cell, the evaluation is more complex than with the other steady-state methods.

An example of application of direct heating for thermal characterization of Li-ion cells is given by [11].

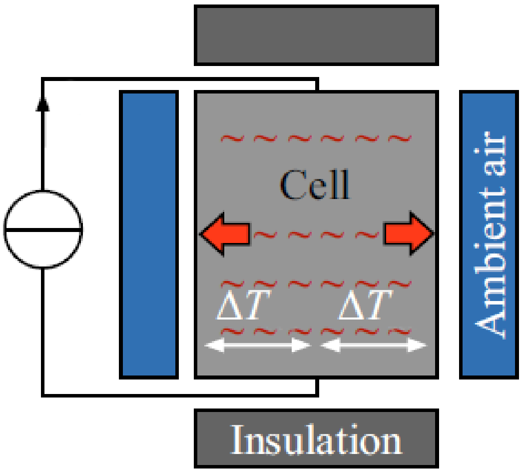

Figure 1.20: Direct heating method setup [32]

1.2.2.4 Potentiometric Method

The potentiometric method is one of the most common approaches used for the determination of the EHC. The method relies on measuring the OCV of the battery at a fixed SOC while varying the ambient temperature. The battery is charged or discharged to a specific SOC and rested for a sufficient time, then the temperature control system (e.g., climatic chamber) set point temperature is changed and hold until the battery reaches thermal equilibrium. At equilibrium, the SOC is measured. Repeating the process for different temperatures and SOCs allows one to characterize the dependency of OCV in function of temperature. The slope of $OCV = f(T)$, that is $\frac{dV_{OC}}{dT}$, is exactly the EHC.

An example of curve of EHC in function of SOC is provided in Figure 1.21. Representative research applications of this technique are in [12, 37]

1.2.2.5 Calorimetry

Calorimetry is the science of measuring the heat exchanged by a system with its surroundings. It employs a calorimeter (Figure 1.22), a device that can measure how much heat is released or absorbed during a physical or chemical process. In battery thermal characterization, it is considered the golden standard for heat capacity determination due to its high accuracy. Two main modes of operation can be defined:

- **Accelerating Rate Calorimetry**: Used for cell-level characterization. The cell is suspended in an adiabatic chamber surrounded by heaters. A known amount of heat is supplied to the cell, and the resulting temperature rise ΔT is measured

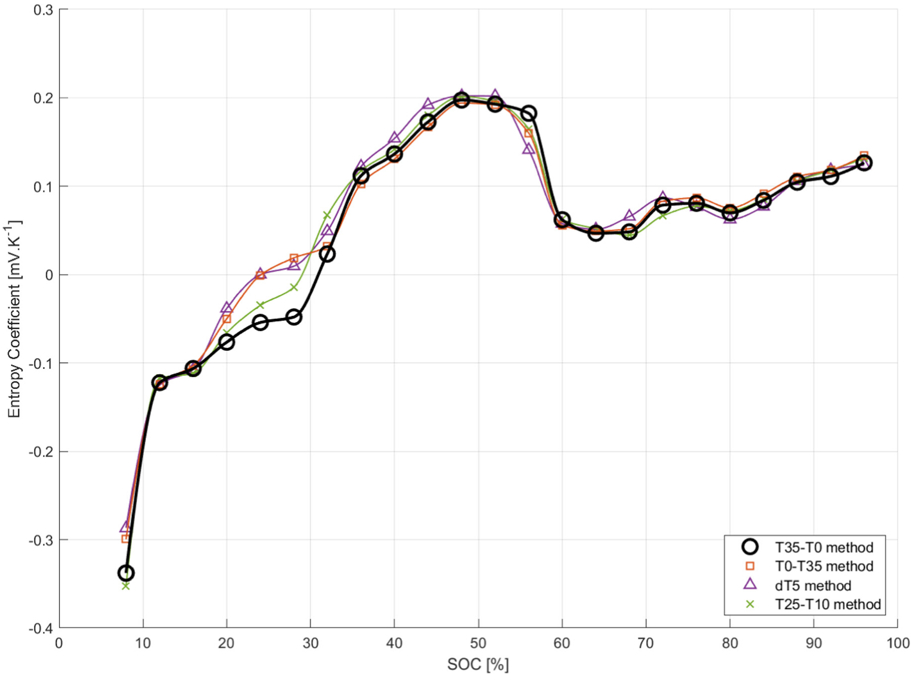

Figure 1.21: Examples of EHC plot obtained using the potentiometric method [37]

- **Differential Scanning Calorimetry**: Used for material-level characterization. Small samples of battery components (anode, cathode, separator, electrolyte) are heated alongside a reference sample. The system measures the difference in heat flow required to increase the temperature of the sample against the reference

For both methods, the specific heat can be determined as

$$c = \frac{Q}{m \cdot \Delta T} \tag{1.24}$$

where Q is the heat provided, and m the mass of the sample.

One example of use of calorimetry for thermal characterization of Li-ion cells is [38]. One other interesting application of calorimetry is the study of thermal runaway, as done in [39]. In the past, calorimetry has also been applied for the determination of the reversible (entropic) heat and the EHC (through the so-called isothermal battery calorimetry strategy), but the approah has shown important accuracy limitations and has consequently not been used in research anymore [37].

It is also quite common to employ thermal characterization techniques that, even if avoid using an expensive calorimeter, try to mimic calorimetry by making use of experimental setups designed to create adiabatic (or near-adiabatic) conditions to function substantially as calorimeters for determining thermal parameters [35, 40].

Most of the research papers that develop this alternative approaches then validate their results using the traditional calorimetry.

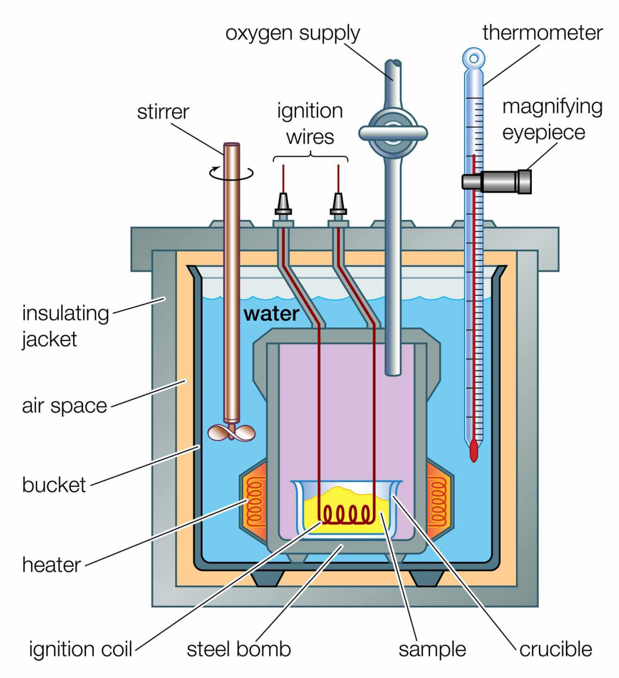

Figure 1.22: Bomb calorimeter

1.2.2.6 Thermal Impedance Spectroscopy (TIS)

Thermal Impedance Spectroscopy (TIS) is a non-destructive analytical method that measures the temperature response of a system to a usually sinusoidal heat input to determine its thermal properties. Just as EIS applies an AC current to measure electrical impedance $Z = V/I$, TIS applies a periodic heat signal to the measure thermal impedance Z_{th}, that is defined as

$$Z_{th}(\omega) = \frac{T(\omega)}{\dot{Q}(\omega)} \tag{1.25}$$

The heat input is provided by the cell itself, that is powered by a battery cycler with a sinusoidal current profile (since heat generation is proportional to the square of current $P = I^2R_i$, a sinusoidal current creates a sinusoidal heat wave) sweeped over a wide range of frequencies, while temperature sensors placed on the cell surface record the temperature response (Figure 1.23).

As for EIS, the output of TIS is a Nyquist plot, whose axes are the real and imaginary components of the complex thermal impedance Z_{th} (Figure 1.24). In particular, different components can be highlited:

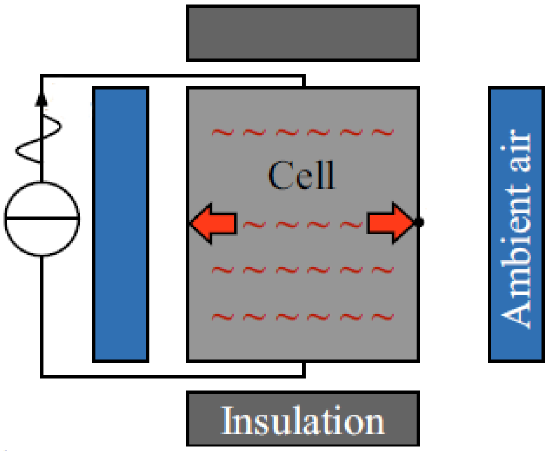

Figure 1.23: Thermal impedance spectroscopy setup [32]

- **Low Frequency**: The low-frequency response corresponds to the static thermal behavior of the battery cell. This region allows for the determination of the thermal resistance with the ambient R_{th}
- **Intermediate Frequency**: Intermediate frequencies describe diffusion phenomena and allow one to characterize the thermal conductivity k
- **High Frequency**: The higher frequency response corresponds to the dynamic thermal behavior of the cell. This region is required to characterize the thermal capacitance and thus obtain the specific heat capacity c

Examples of application of TIS to Li-ion battery cells are [41, 42].

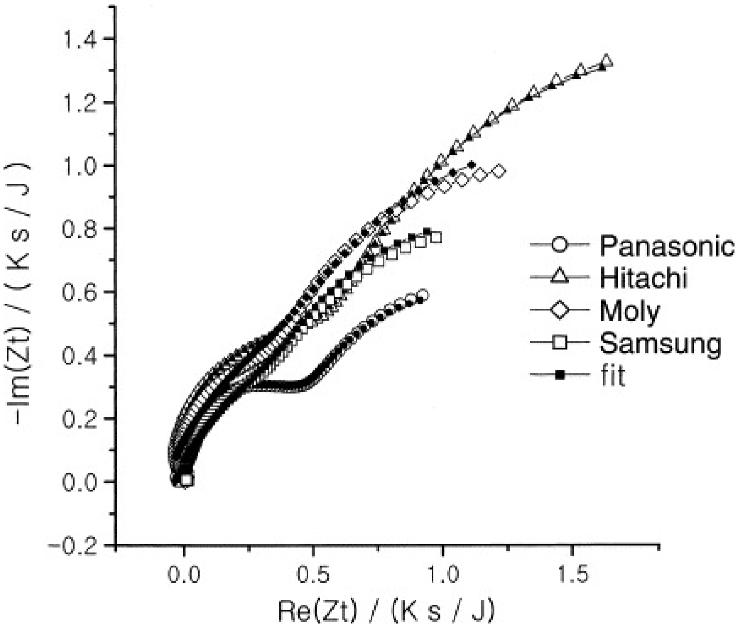

Figure 1.24: Thermal impedance spectrum of Li-ion cells [42]

1.2.2.7 Heat Source Method

This category includes a wide set of methodologies that use heating elements attached to the sample for thermal characterization. The thermal properties are derived from the time-dependent temperature rise that is measured using temperature sensors. Two primary variations of this methodology exist:

- **Transient Line Source**: This method uses a wire inserted in the test cell, that behaves both as a heat source and a temperature sensor. The temperature rise of the wire itself is recorded over time and used to estimate the thermal conductivity k of the surrounding material. An advanced version of this approach includes an additional external thermocouple that measures the temperature field induced by the thin heating element at a distance, allowing for more precise calculations. This method is usually a destructive one since the element need to be placed inside of the battery cell

- **Transient Plane Source**: This method has a similar principle of operation to the transient line source, but uses a planar heater, that is attached to the surface of the battery cell, or sandwitched between two of them (Figure 1.25). The plane source sensor is very often used simultaneously as a heat source and as a resistance temperature sensor, but additional external sensors can also be employed. This approach has a larger measuring range, and it's usually non-destructive

Examples of studies from the literature that apply similar techniques are [43, 44].

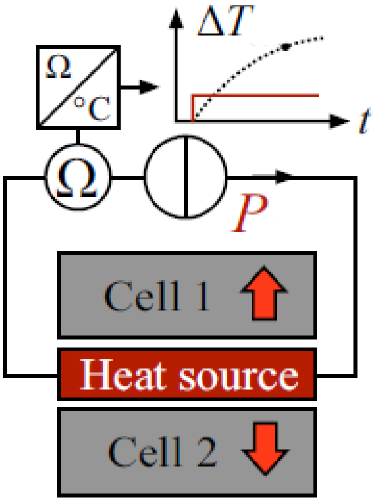

Figure 1.25: Heat source method setup for a plane heater [32]

1.2.2.8 Variant Convective Cooling (VCC)

Variant Convective Cooling (VCC) is a transient characterization technique designed to measure specific heat capacity c and thermal conductivity k. This method characterizes those thermal properties by observing the temperature profile over time during heating and cooling phases under different convective boundary conditions. Since two quantities need to be retrieved, the method is based on subjecting the battery cell to heat generation under at least two different convective boundary conditions (for example, varying air velocities using a controllable fan). By analyzing the temperature response under these different conditions, it is possible to mathematically separate the different heat contributions within the cell thermal balance, allowing for the simultaneous identification of both thermal properties of interest with relatively low experimental effort (Figure 1.26).

Examples of reseach activities on this topic are [11, 45]. One variant of this approach is proposted by [46], that maintains a stable forced convection environment but varies the heating boundary condition by using external heaters.

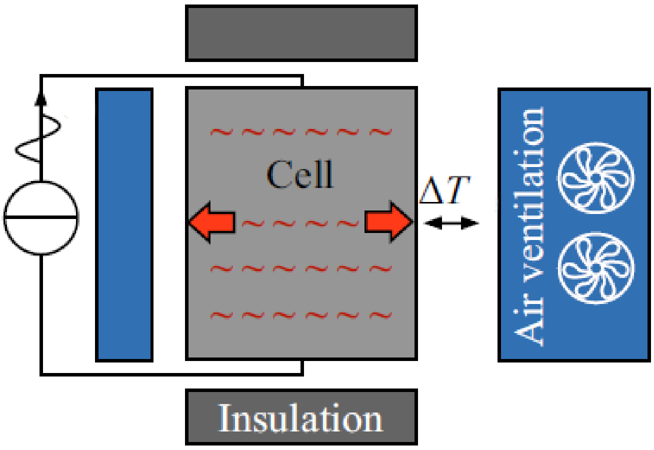

Figure 1.26: Variant convective cooling setup for a plane heater [32]

1.2.3 Characterization Technique Selection

- **Electrical Characterization** In this thesis, a constant current charge/discharge characterization at different current rates has been perfomed for capacity determination, while HPPC has been chosen as the dynamic characterization approach. This decision is validated by the literature, which demonstrates that these techniques are widely used, provide a reliable correlation during modelling and are a fast and effective way to retrieve data [17, 23, 24, 21, 26, 41, 15]

- **Thermal Characterization** In this thesis, the internal heat from the cell has been used as the heating method, and a heat flux sensor has been selected as the thermal characterization instrument. Thermal information has been acquired concurrently with the electrical characterization tests, reducing overall testing time. The use of heat flux sensors for thermal characterization is supported by the literature, which confirms that this approach is simple, cost-efficient, and non-destructive [47, 48, 40, 44]

1.3 Modelling Approaches

Battery modelling is the systematic development and use of mathematical, computational, and algorithmic representations of the electrochemical energy storage system in order to describe, predict, analyze, and control its electrical, thermal, chemical, and mechanical behavior (how it stores energy, delivers power, heats up, ages and degrades) across multiple operating conditions and stages of its life cycle. Battery modelling is important because it enables prediction, safety, control, optimization, lifetime estimation, and cost-effective development of battery systems [22]. A complete and exhaustive battery model needs to represent the electrochemical, electrical, thermal, mechanical and aging domains to predict accurately the cell behaviour.

Depending on the level of complexity, and specifically on how many spatial dimensions are explicitly resolved, modelling approaches can also be classified into 0D (zero-dimensional or lumped-parameter), 1D (one-dimensional), 2D (two-dimensional) and 3D (three-dimensional). In general, the higher the number of spatial coordinates of the model, the higher is its accuracy but lower is its computational efficiency. For the context of real-time battery modelling that is used in BMS applications, 0D models are the most common choice, as they are the best compromise between complexity and accuracy [14].

It is also important to mention that the selected battery model is deeply affected by which spatial and temporal scales are of interest of the specific study:

- **Spatial Scales**: atomic → particle → electrode → cell → module → pack
- **Temporal Scales**: microseconds (charge transfer phenomena) → hours (cycling) → years (aging)

1.3.1 Electrical Models

Electrical models describe how the battery stores and deliveres electrical charge (correlating the different electrical quantities, like voltage and current, and estimating power, energy and SOC in different operating conditions).

Fundamentally, the electrical model receives some quantities in input, elaborates them, and provides some quantities as an output [22, 17, 20, 12]:

- **Input** The primary input of the electrical model is the battery load current I. This is usually measured by current sensors connected to the battery. Secondary inputs to the model are:
  - **SOC** The OCV and internal impedance parameters R, C are highly dependent on the SOC. A primary estimation of the SOC, usually obtained by means of Coulomb counting[6], is thus provided
  - **Temperature** The OCV and internal impedance parameters R, C are also dependent on the temperature T. Battery temperature, measured by proper sensors, is thus also provided

  These secondary inputs to the model are fundamental, so that the correct values of all the model parameters can be exactly defined. This process is usually implemented adopting lookup tables of the variable parameters in function of the inputs OCV, R_i, $C_i = f(SOC, T)$
- **Output** The output of the electrical model is the battery terminal voltage V. The terminal voltage is the fundamental output of the model because it is the primary physical response of the battery to the applied load and serves as the measurable quantity used to validate internal state estimates that cannot be measured directly (basically, the terminal voltage estimation is compared with the real measured voltage at the battery terminals, and this information is used to correct SOC and other internal state quantitites)

The parameters that define the operation of the model (electrical resistances R, electrical capacitances C and the OCV curve) are obtained through the previous characterization stages described in Section 1.2.1 by applying the mathematical derivations that will be described in Chapter 3.

Electrical battery modelling includes different methodological approaches, that span across different domains and applications [24, 26]:

- **Equivalent Circuit Models (ECM)**: These models represent battery cells using electrical circuits. They are computationally very light and easy to parameterize using pulse tests, but they are unable to describe cell aging and

---

[6] Coulomb counting is a state-estimation method used in Li-ion battery models to determine the battery's state of charge by integrating the battery current over time

degradation phenomena. For these reasons, these models are usually employed in the BMS of battery systems for EVs and ESS applications. These models are spatially 0D

- **Data-Driven Models**: These models rely purely on statistical or machine learning correlations between input measured data (current, voltage, temperature) provided in large datasets. They can capture highly non-linear behavior that is hard to model mathematically and do not require precise knowledge of cell chemistry. On the other hand, they require massive amounts of high-quality training data, and have poor generalization (a model trained on a specific cell of a given form factor or manufacturer cannot be used for other cells). These models are of interest when massive amount of data is available, like for example in the case of EV fleet management. These models are usually 0D

- **Physics-Based Models**: These models attempt to simulate the actual internal laws of physics governing the battery, such as mass transport, diffusion dynamics, and intercalation kinetics. They solve partial differential equations representing the movement of lithium ions through the cathode, separator, and anode, as well as the diffusion of solid lithium inside the active material particles. They accurately provide deep insights about cell operation at the electrode level, but are computationally expensive and impossible to use at system level. These models are used for the research and development of new battery cells, allowing to represent into detail advanced aging and degradation mechanisms. These models can be 1D (Single Particle Model (SPM)), 2D (Doyle-Fuller-Newman (DFN)) or 3D (Multi-Scale Multi-Dimensional (MSMD)) depending on the application

In the context of this thesis, only the electrical ECM approaches are reviewed in detail, as they are the most common and relevant for the scope of the project (that is battery electrothermal modelling at cell level) and easy to parametrise starting from the previously chosen characterization methodologies [15]. Regarding spatial complexity, the electrical modelling will be limited to 0D models. Data-driven and physics-based models will not be considered as out of scope for the context of this work.

The most common electrical ECMs for Li-ion battery modelling include the internal resistance, Thevenin, Partnership for a New Generation of Vehicles (PNGV) and General Nonlinear (GNL) models [24]:

1.3.1.1 Internal Resistance Model

As already introduced in Section 1.1.4, the internal resistance model is the simplest possible equivalent circuit representation of a Li-ion battery. It ignores complex dynamic behaviors and treats the battery purely as an ideal voltage source V_{OC} connected in series with a single resistor R_0 (Figure 1.27).

The equations that describe the internal resistance model are

$$\begin{cases} V(t) = V_{OC} - V_0(t) \\ V_0(t) = R_0 \cdot I(t) \end{cases} \tag{1.26}$$

which coupled provide

$$V(t) = V_{OC} - R_0 \cdot I(t) \tag{1.27}$$

The voltage response to a step discharge current of the internal resistance model is an instantaneous voltage drop (Figure 1.28).

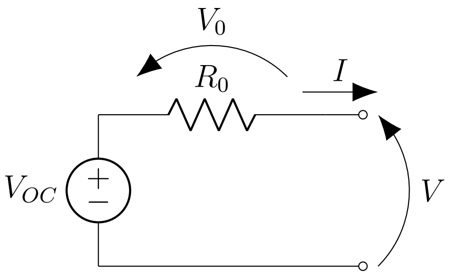

Figure 1.27: Internal resistance model

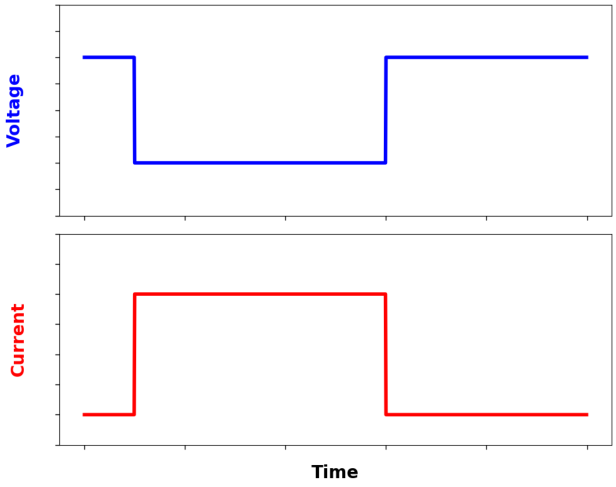

Figure 1.28: Internal resistance model voltage response

1.3.1.2 Thevenin Model

The Thevenin model is the most widely used ECM in practical applications. It extends the simple internal resistance model by adding a number of parallel Resistor-Capacitor (RC) branches. The presence of the RC parallels enables the modelling of the dynamic responses of the system having time constants $\tau_i = R_i \cdot C_i$.

The simplest Thevenin model is the 1RC model, exhibiting only one RC branch (Figure 1.29).

The equations that describe the 1RC model are

$$\begin{cases} V(t) = V_{OC} - V_0(t) - V_1(t) \\ V_0(t) = R_0 \cdot I(t) \\ \dfrac{dV_1(t)}{dt} = \dfrac{I(t)}{C_1} - \dfrac{V_1(t)}{R_1 C_1} \end{cases} \tag{1.28}$$

which coupled provide (for the case of the step response appling a constant discharge current of magnitude I starting at $t = 0$, with initial condition $V_1(t)|_{t=0} = 0$)

$$V(t) = V_{OC} - I \cdot R_0 - I \cdot R_1 \left(1 - e^{-\frac{t}{\tau_1}}\right) \tag{1.29}$$

where $\tau_1 = R_1 \cdot C_1$.

The voltage response to a step discharge current of the 1RC model presents, after the instantaneous voltage drop due to R_0, an additional exponential decay consequence of $R_1 C_1$ (Figure 1.30).

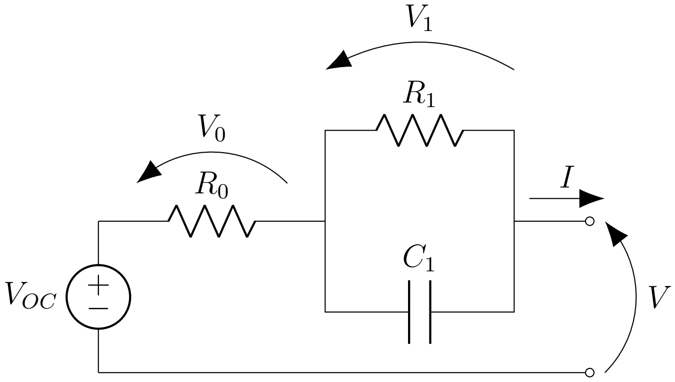

Figure 1.29: Thevenin 1RC model

In general, Thevenin models can have an arbitrary number of RC parallels, but the usual number of those in practical applications is in the range from one to three.

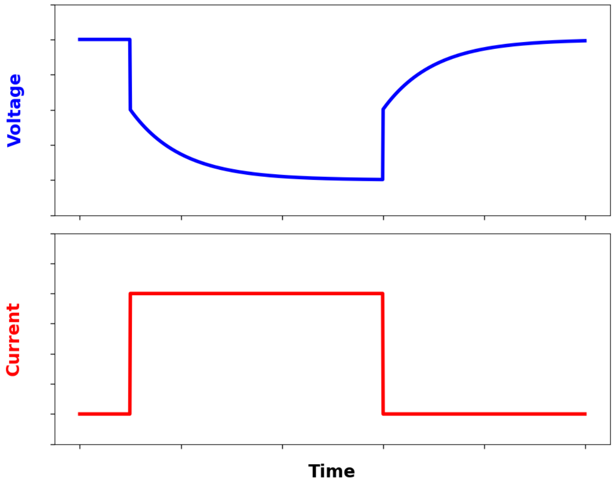

Figure 1.30: Thevenin 1RC model voltage response

Figure 1.31 shows the 2RC model, that is the most common one in Li-ion battery applications.

In the 2RC model:

- R_0 represents the internal ohmic resistance of the battery cell, and produces an instantaneous voltage drop as the current is applied
- R_1 and C_1 represent the electrochemical polarization phenomena that happen as a result of charge transfer kinetics at the surface of the electrode, and produce an exponential decay having a fast dynamic (order of seconds)
- R_2 and C_2 represent the concentration polarization effects that occour with diffusion, and produce an exponential decay having a slow dynamic (order of minutes)

Thus, typically $\tau_1 = R_1 \cdot C_1 << R_2 \cdot C_2 = \tau_2$.

The equations that describe the 2RC model are

$$\begin{cases} V(t) = V_{OC} - V_0(t) - V_1(t) - V_2(t) \\ V_0(t) = R_0 \cdot I(t) \\ \dfrac{dV_1(t)}{dt} = \dfrac{I(t)}{C_1} - \dfrac{V_1(t)}{R_1 C_1} \\ \dfrac{dV_2(t)}{dt} = \dfrac{I(t)}{C_2} - \dfrac{V_2(t)}{R_2 C_2} \end{cases} \tag{1.30}$$

which coupled provide (for the case of the step response appling a constant discharge current of magnitude I starting at $t = 0$, with initial conditions $V_1(t)|_{t=0} = 0$ and

$V_2(t)|_{t=0} = 0$)

$$V(t) = V_{OC} - I \cdot R_0 - I \cdot R_1 \left(1 - e^{-\frac{t}{\tau_1}}\right) - I \cdot R_2 \left(1 - e^{-\frac{t}{\tau_2}}\right) \tag{1.31}$$

where $\tau_1 = R_1 \cdot C_1$ and $\tau_2 = R_2 \cdot C_2$.

The voltage response to a step discharge current of the 2RC model presents a combined exponential response having two separate time constants (Figure 1.32).

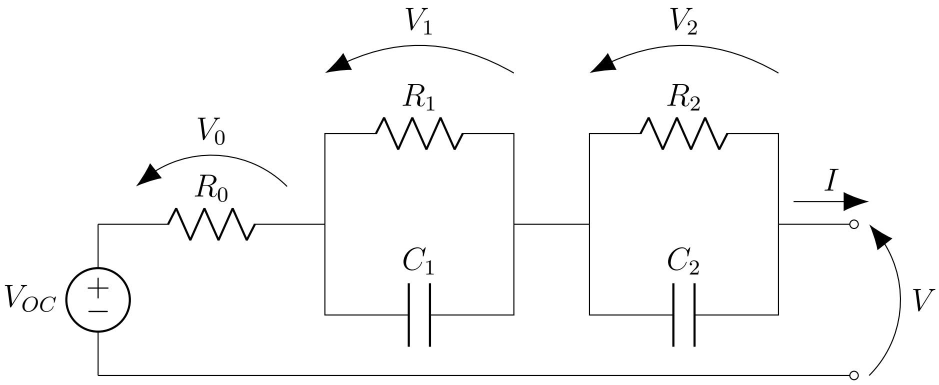

Figure 1.31: Thevenin 2RC model

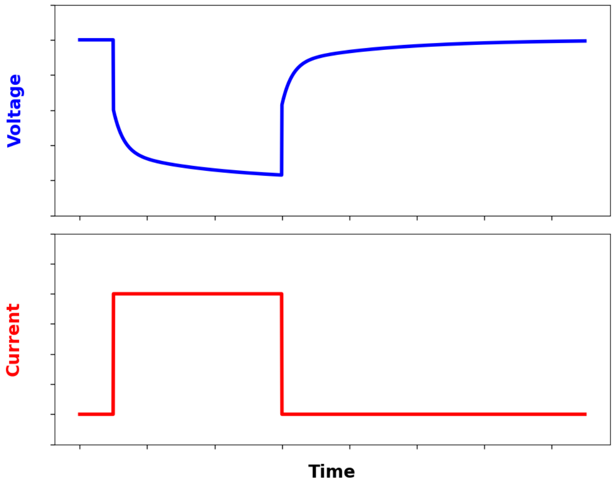

Figure 1.32: Thevenin 2RC model voltage response

1.3.1.3 PNGV Model

The PNGV model is an enhanced version of the standard Thevenin model. It was developed in the 1990s by a consortium of US car manufacturers (Ford, GM, Chrysler) to create a standard model for hybrid electric vehicle simulation. Its defining feature is that it accounts for the change in OCV as the battery discharges. The PNGV model adds a capacitor C_{OC} in series to the standard (in this case 2RC) Thevenin model (Figure 1.33).

The equations that describe the PNGV model are

$$\begin{cases} V(t) = V_{OC} - V_0(t) - V_1(t) - V_2(t) - V_C(t) \\ V_0(t) = R_0 \cdot I(t) \\ \dfrac{dV_1(t)}{dt} = \dfrac{I(t)}{C_1} - \dfrac{V_1(t)}{R_1 C_1} \\ \dfrac{dV_2(t)}{dt} = \dfrac{I(t)}{C_2} - \dfrac{V_2(t)}{R_2 C_2} \\ \dfrac{dV_C(t)}{dt} = \dfrac{I(t)}{C_{OC}} \end{cases} \tag{1.32}$$

which coupled provide (for the case of the step response appling a constant discharge current of magnitude I starting at $t = 0$, with initial conditions $V_1(t)|_{t=0} = 0$, $V_2(t)|_{t=0} = 0$ and $V_C(t)|_{t=0} = 0$)

$$V(t) = V_{OC} - I \cdot R_0 - I \cdot R_1 \left(1 - e^{-\frac{t}{\tau_1}}\right) - I \cdot R_2 \left(1 - e^{-\frac{t}{\tau_2}}\right) - I \frac{t}{C_{OC}} \tag{1.33}$$

where $\tau_1 = R_1 \cdot C_1$ and $\tau_2 = R_2 \cdot C_2$.

The voltage response to a step discharge current of the PNGV model presents a combined exponential response having two separate time constants plus the OCV drop due to the series capacitor, that for the case of a constant current is linear over time (Figure 1.34).

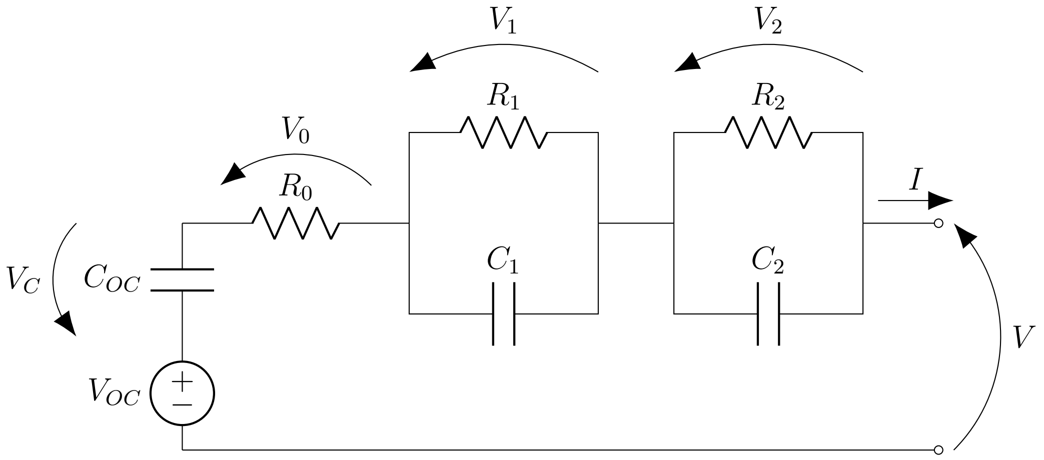

Figure 1.33: PNGV model

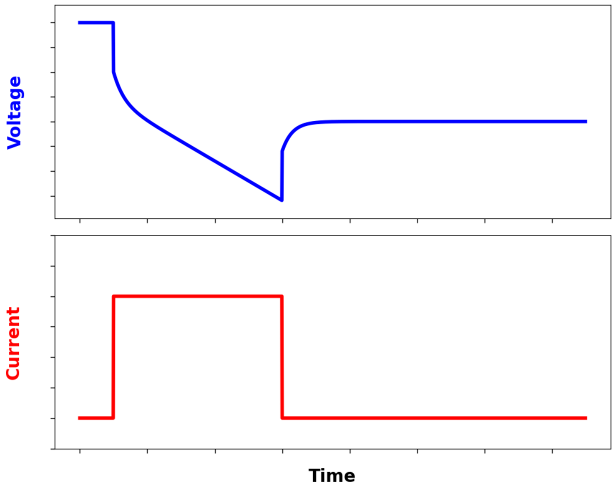

Figure 1.34: PNGV model voltage response

1.3.1.4 GNL Model

The GNL model is an evolution of the PNGV that considers in addition for the presence of self discharge. The effect of self discharge is accounted for by placing an additional resistor, called self discharge resistor R_p, connected to the battery terminals in parallel with the load (Figure 1.35).

The presence of the self discharge resistor produces a leakage current I_p that causes the terminal voltage V to be always lower than the OCV (the leakage current I_p must flow through R_0 and the RC pairs to get to the resistor, creating a permanent voltage drop) and continuously decreasing also when a load is not applied (the leakage current I_p slowly discharges the series capacitor C_{OC}, causing a small but steadily decrease of voltage at the battery terminals).

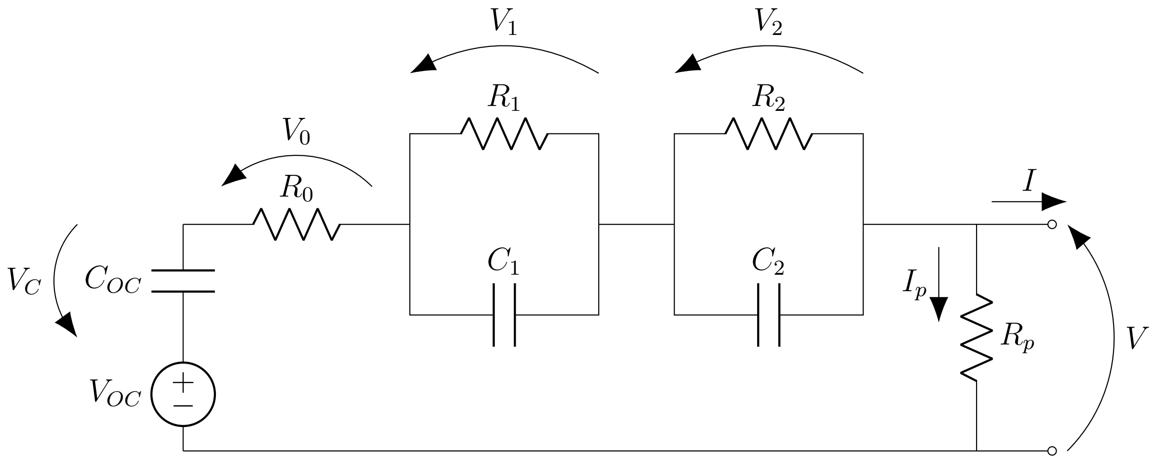

Figure 1.35: GNL model

A rough estimation of the voltage response to a step discharge current of the GNL model is shown in Figure 1.36 (note that the effect of self discharge has been notably magnified).

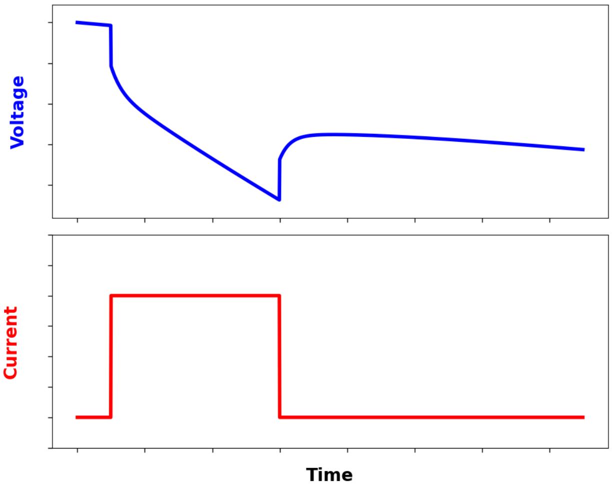

Figure 1.36: GNL model voltage response (estimated)

1.3.1.5 Advanced Models

In advanced Li-ion cell electrical modelling, in addition to the approaches already mentioned, even more complex strategies can be adopted, with the purpose of introducing new elements capable of representing nonlinear phenomena:

- **Variable Parameters**: as already mentioned, the circuit parameters R and C generally vary with the SOC, temperature and also with the current rate. In advanced models, these variables are not treated as constants, and they are multidimensional surfaces that are interpolated for obtaining the values for the specific operating conditions
- **Diodes**: the circuit parameters may also change depending on the sign of the current (different for charging and discharging). This effect can be modelled introducing different branches, having different values of the parameters and having different current sign controlled using diodes (Figure 1.37)
- **Hysteresis**: the OCV for a given SOC can also vary between charging and discharging (this mechanism, briefly mentioned in Section 1.1.4 goes under the name of hysteresis), especially for specific chemistries like LFP. A dynamic hysteresis voltage term can be added to represent this contribution
- **Warburg Impedance**: additional non-linearities can be modelled using the Warburg impedance. Introduced in the context of EIS (Section 1.2.1.4), the Warburg impedance is a complex impedance that is used to model diffusion controlled processes

- **Series Inductor**: to model extremely high frequency behaviour, a series inductor can be added
- **Block-Oriented Nonlinear Models**: state-of-the-art battery models use block-oriented structures that combine dynamic linear modules with static nonlinear modules to create a nonlinear ECM. Several configurations can be used to structure these models (Figure 1.38) [49]:
  - **Wiener Configuration**: Consists of a dynamic linear module followed by a static nonlinear module
  - **Hammerstein Configuration**: Reverses the Wiener approach by placing a static nonlinear module before a dynamic linear module
  - **Hammerstein–Wiener Configuration**: Connects a static nonlinear module in series with the Hammerstein configuration (sandwiching the linear module between two nonlinear ones)
  - **Hammerstein-CARMA Configuration**: It introduces colored noise to the Hammerstein configuration to simulate external noise disturbances alongside the internal nonlinear characteristics (CARMA stands for Controlled Autoregressive Moving Average[7])

  In these configurations, the static nonlinear modules are often represented by polynomial functions, while the dynamic linear modules utilize standard ECM components (like the RC networks that have been thoroughly described in this section)

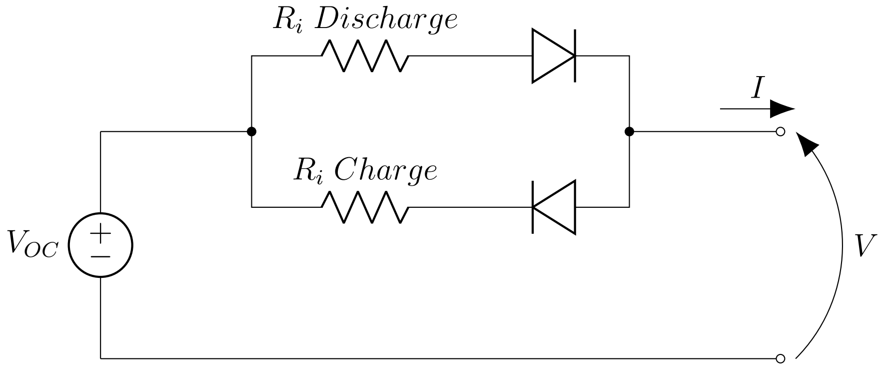

Figure 1.37: Current sign dependant equivalent circuit using diodes [50]

---

[7] CARMA is a system identification model that describes a process output as a function of its own previous values (autoregressive), previous control actions (controlled), and a stochastic error term representing the influence of random noise (moving average)

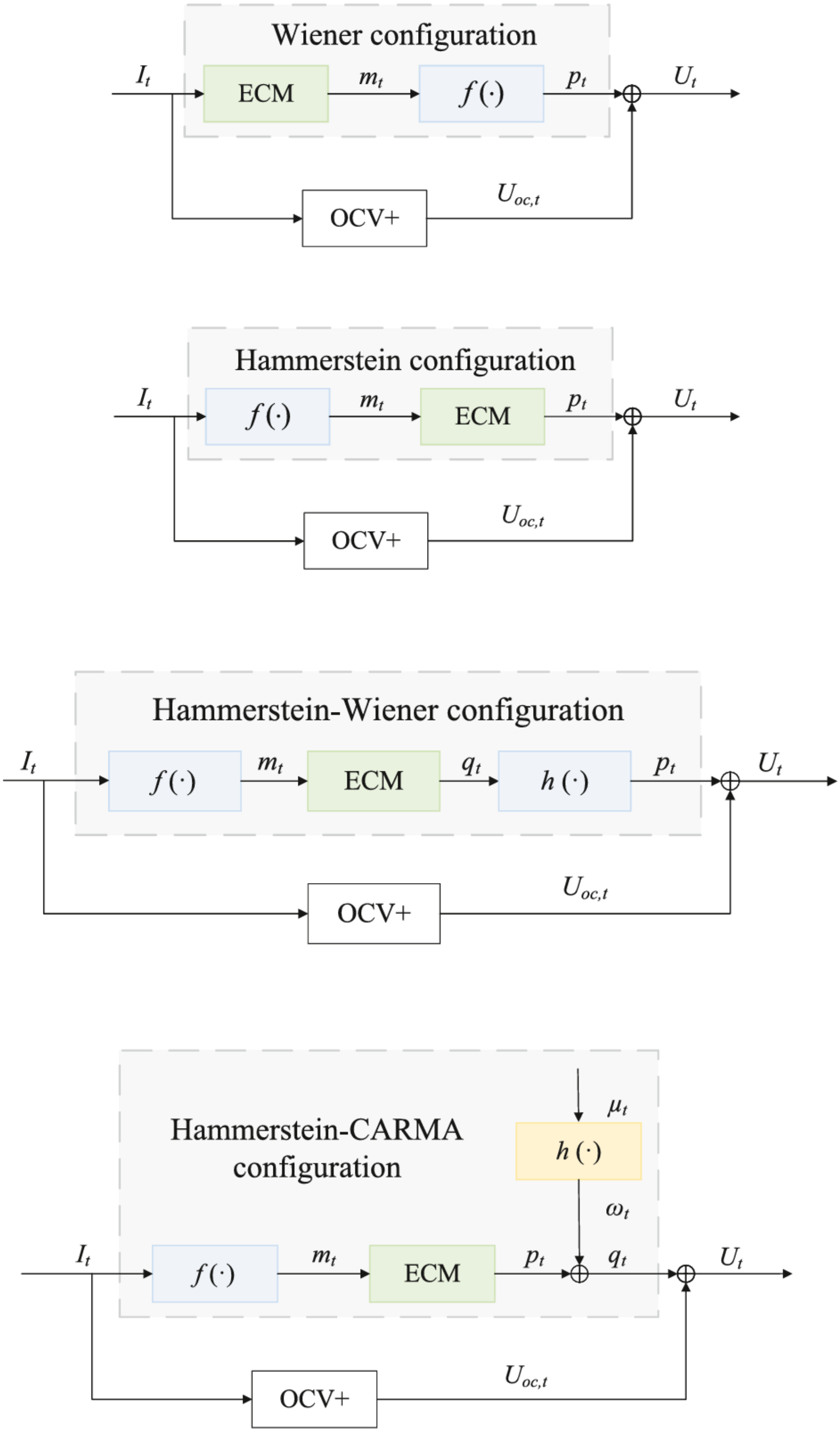

Figure 1.38: Block-oriented nonlinear model examples [49]

1.3.2 Thermal Models

Thermal models describe how electrochemical processes produce heat and how this is exhanged between the system and the surrounding environment (studying heat generation, heat transfer, and temperature evolution).

As for the electrical counterpart, the thermal model receives some quantities in input, elaborates them, and provides some quantities as an output [8, 43, 9, 32]:

- **Input** The primary input of the thermal model is the heat generation rate $\dot{Q}$, that is usually calculated just considering the irreversible term $\dot{Q}_{irr}$, obtained using Equation 1.14 from the measured values of voltage V, current I and from the tabulated values of the OCV or R_i depending on the approach used for the calculation (if the entropic heat is also considered, calculating it using Equation 1.15, also the last cell temperature T and tabulated values of the EHC are required). The ambient temperature T_a is a secondary input, required to determine the heat exchanged by convection with the surroundings
- **Output** The output of the thermal model is the temperature of the cell T, obtained at specific locations and with a level of accuracy dependent on the model complexity (core, surface, or complete spatial temperature distribution)

The parameters that define the operation of the model (thermal resistances R_{th}, thermal capacitances C_{th} and thermal conductivities k) are obtained through the previous characterization stages described in Section 1.2.2 by applying the mathematical derivations that will be described in Chapter 4.

Thermal battery modelling includes different methodological approaches, that span across different levels of accuracy and complexity (Figure 1.39) [32, 9]:

- **Lumped Capacitance Model**: In this model, the entire battery is treated as a single homogeneous mass with a uniform temperature, and the heat exchange problem is solved using a simple energy balance equation. This is a 0D approach, and it is the simplest thermal model that can be used
- **Equivalent Thermal Circuit Models**: These models are based on the electrothermal analogy and adopt Ordinary Differential Equations (ODEs) to solve the problem. They can be first-order (single thermal mass, 0D) or second-order (two temperature nodes, quasi 1D)
- **Single-Domain Models**: In Single-Domain Models (SDMs) all cell components are homogenized into a single domain (e.g., a hollow cylinder) with anisotropic thermal conductivity (axial k_z and radial k_r). This is the simplest (low resolution) 2D/3D model that can be used

- **Component-Resolved Models**: Component-Resolved Models (CRMs) simplify the jelly roll with a homogeneous domain possessing anisotropic thermal properties, while other components like the casing and mandrel[8] remain separate domains. Neglecting the jelly roll geometry significantly reduces simulation time but can introduce temperature errors if not carefully calibrated. It is a medium resolution 2D/3D model (multiple domains)

- **Layer-Resolved Models**: Layer-Resolved Models (LRMs) resolve the detailed geometry of the battery, including individual layers of the electrode-separator stack and accounting for the geometry of the jelly roll (for example spiral in cylindrical cells) and specific thermal contact resistances between the layers. These 2D/3D models are the most precise but also have the highest computational cost, having very high resolution on each of the domains of the real cell

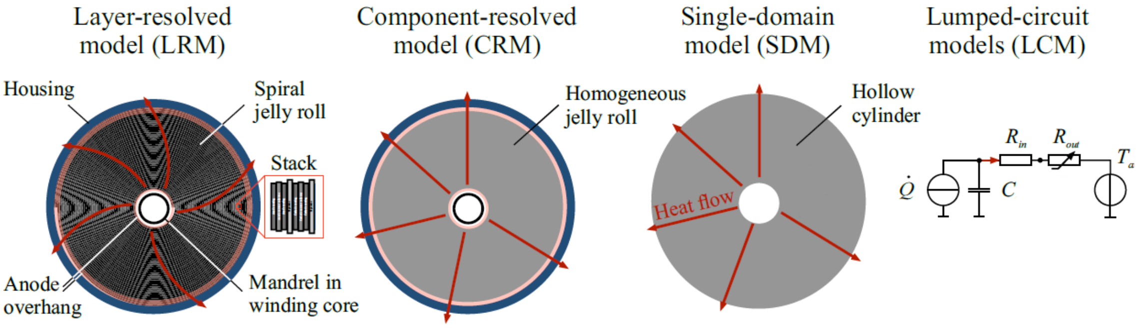

Figure 1.39: Thermal models for cylindrical cells [32]

In the context of this thesis, only the lumped capacitance and thermal ECM approaches are reviewed in detail, as they are the most common and relevant for the scope of the project (that, as said, is battery electrothermal modelling at cell level) and compatible with the tests performed during characterization. Regarding spatial complexity, the thermal modelling will be limited to 0D and quasi-1D models. SDMs, CRMs and LRMs will not be considered as out of scope for the context of this work.

So, the common thermal modelling strategies for Li-ion batteries that are going to be discussed into detail are the lumped capacitance and thermal ECM approaches [9, 46, 43, 8, 12]:

---

[8] A mandrel is a cylindrical core used during electrode winding to define and support the inner diameter of cylindrical battery cells

1.3.2.1 Lumped Capacitance Model

The lumped capacitance model is the simplest method for transient thermal analysis. It treats the battery as a homogeneous body with a uniform temperature, neglecting or simplifying spatial temperature gradients (fundamentally, it assumes that the object has infinite internal thermal resistance compared to the heat transfer capabilities at the boundary surfaces).

The model is derived from the first law of thermodynamics, that is nothing else than an instantaneous energy balance: the rate of change of internal energy is equal to the net heat absorbed by the system (heat generation minus heat exchanged by convection)

$$mc\frac{dT}{dt} = \dot{Q} - hA_{tot}\left(T - T_a\right) \tag{1.34}$$

where m is the mass of the cell, c the specific heat, $\dot{Q}$ the internal heat generation, h the heat transfer coefficient, A_{tot} the total surface area, and T and T_a are the cell and ambient temperatures, respectively.

The validity of this model is typically checked using the dimensionless Biot number, defined as

$$Bi = \frac{\text{Internal Conduction Resistance}}{\text{External Convection Resistance}} = \frac{hL_c}{k_r} \tag{1.35}$$

where for this application k_r is the radial thermal conductivity of the cylindrical battery cell and L_c is the characteristic length, calculated as the ratio of volume over surface area.

In general:

- If $Bi < 0.1$: The error is less than 5%. The lumped model is valid
- If $Bi > 0.1$: Internal gradients are significant. More complex models required

The lumped parameter approach has been applied to thermal modelling of Li-ion batteries by [51, 35, 47].

1.3.2.2 Equivalent Thermal Circuit Models

The equivalent thermal circuit approach is a modelling strategy that simplifies complex heat transfer problems by treating them as electrical circuits. It relies on the electrothermal analogy (Table 1.7), that is the direct mathematical analogy between the diffusion of heat and the flow of electricity.

Table 1.7: Electrothermal analogy

Thermal Quantity	**Unit**	**Electrical Analogy Quantity**	**Unit**
Temperature (T)	K	Voltage (V)	V
Heat Flow Rate ($\dot{Q}$)	W	Current (I)	A
Thermal Resistance (R_{th})	K/W	Resistance (R)	Ω
Thermal Capacitance (C_{th})	J/K	Capacitance (C)	F
Constant Temperature	K	Voltage Source	V
Heat Generation	W	Current Source	A

Thermal networks are usually classified depending on the number of nodes (capacitors) they use to represent the heat transfer problem. In general, two main circuit topologies can be used (Figure 1.40):

- **Foster Networks**: The Foster network is a series connection of parallel RC pairs. It is an abstract mathematical representation that does not correspond to anything physical (the internal nodes do not correspond to real temperatures)
- **Cauer Networks**: The Cauer network is a ladder network where capacitors are connected to the ground. It is considered a physical representation of heat flow because the circuit structure represents a direct mapping of the physical layers of the components under study, and node temperatures are correlated to real temperatures

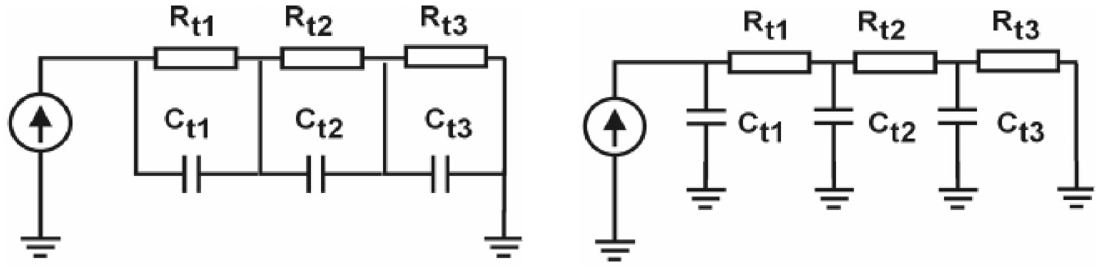

(a) Foster Network Example (b) Cauer Network Example

Figure 1.40: Equivalent Thermal Circuit Networks [52]

In the context of battery modelling, the most common topologies are first and second order Cauer networks:

First Order (1-State) Thermal ECMs

The first-Order (also called 1-state) thermal ECM considers the battery cell as a single thermal mass having a uniform bulk temperature T. The equivalent circuit

(Figure 1.41) is composed of a heat source $\dot{Q}$ that represents the battery internal heat generation, a thermal capacitance C_{th} that represents the battery's ability to store heat and a thermal resistance R_{th} that accounts for the opposition to heat transfer from the battery core to the ambient environment, having temperature T_a.

The equation that defines heat transfer in this scenario is

$$C_{th}\frac{dT}{dt} = \dot{Q} - \frac{T - T_a}{R_{th}} \tag{1.36}$$

that is a first-order ODE.

This approach is physically identical to the lumped capacitance model. In fact, definining in Equation 1.34 the thermal resistance as

$$R_{th} = \frac{1}{h \cdot A_{tot}} \tag{1.37}$$

and the thermal capacity as

$$C_{th} = m \cdot c \tag{1.38}$$

one obtains exactly Equation 1.36.

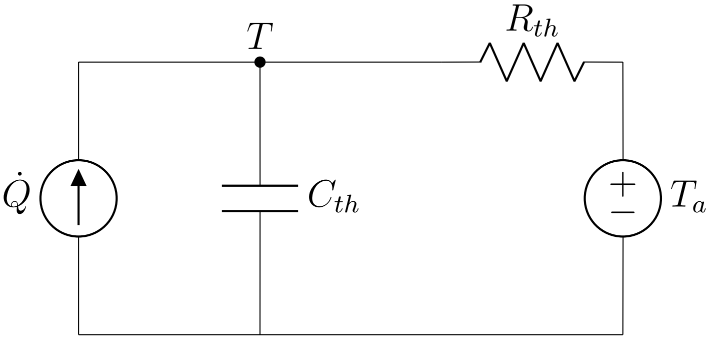

Figure 1.41: First order equivalent thermal circuit model

One other first order approach that is frequently used in the literature is the one that splits the thermal resistance R_{th} in two contributions ($R_{th,c}$, cell component, and $R_{th,a}$, ambient component), adding the effect of internal conduction in the cell, allowing one to have an estimation of both the core and surface temperatures (T_c and T_s) without proceeding with a second order model. This advanced first order approach is found in Figure 1.42, and the equation that describes it is

$$C_{th}\frac{dT_c}{dt} = \dot{Q} - \frac{T_c - T_s}{R_{th,c}} = \dot{Q} - \frac{T_s - T_a}{R_{th,a}} \tag{1.39}$$

that is still a first order ODE.

Examples of reseach activities applying the first order approach are [14, 12, 46, 7, 9].

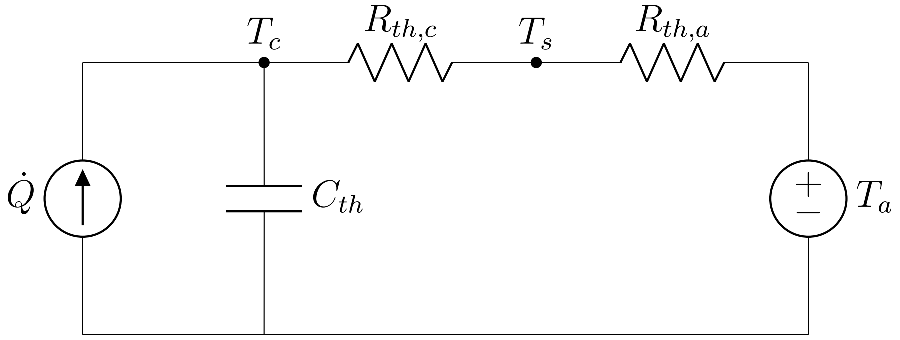

Figure 1.42: Advanced first order equivalent thermal circuit model with core and surface temperature

Second Order (2-State) Thermal ECMs

Second-Order (also called 2-state) thermal ECMs (Figure 1.43) consist of two nodes (core and surface, having a thermal capacity of $C_{th,c}$ and $C_{th,s}$ respectively) connected by an internal (core) thermal resistance $R_{th,c}$. An external (ambient) thermal resistance $R_{th,a}$ connects the cell surface to the environment, having temperature T_a. This strategy captures the core temperature T_c and surface temperature T_s separately.

Because there are two nodes with thermal mass, two coupled ODEs are needed to solve the system (hence second order)

$$\begin{cases} C_{th,c}\dfrac{dT_c}{dt} = \dot{Q} - \dfrac{T_c - T_s}{R_{th,c}} \\ C_{th,s}\dfrac{dT_s}{dt} = \dfrac{T_c - T_s}{R_{th,c}} - \dfrac{T_s - T_a}{R_{th,a}} \end{cases} \tag{1.40}$$

where the core and surface thermal capacities are usually defined as $C_{th,c} = 0,8 \cdot C_{th}$ and $C_{th,s} = 0,2 \cdot C_{th}$ respectively, the external ambient thermal resistance $R_{th,a}$ is defined as per Equation 1.37 and the internal core thermal resistance is written as

$$R_{th,c} = \frac{\ln(r_{out}/r_{in})}{2\pi k_r L} \tag{1.41}$$

where r_{out} is the outer radius of the conduction zone (the casing radius), r_{in} is the inner radius of the heat generation zone (the center pin radius), k_r is the radial thermal conductivity and L the cell length.

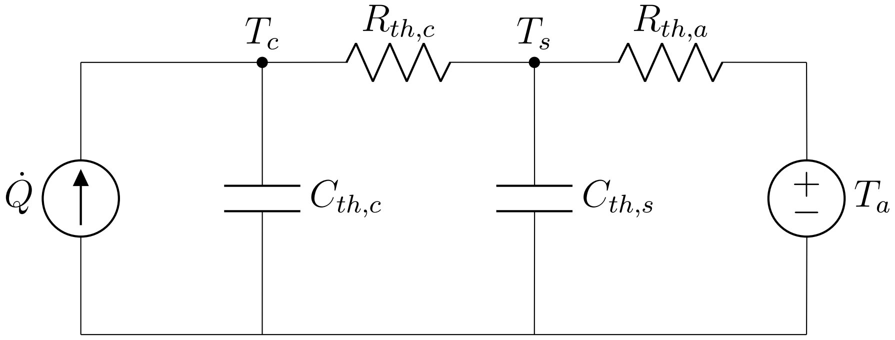

Figure 1.43: Second order equivalent thermal circuit model

Second order models have a higher accuracy, but of course introduce some additional complexity.

Examples of reseach activities exploiting the second order approach are [8, 9, 43].

1.3.3 Electrothermal Model Coupling Strategies

The electrical and thermal model are strictly coupled by a strong non-linear dependency, and they thus both require information one from the other to fully determine their state parameters:

- the electrical model needs the temperature as an input to determine the exact value of the parameters of the model (R, C, OCV)
- the thermal model needs the voltage, current and OCV as an input to derive the heat generation rate $\dot{Q}$

This evidences the relative interdependence between the two models. The approaches that are typically used to solve the issue are the following [53, 8, 54, 55]:

- **One-Way Coupling**: The electrical model calculates heat generation and sends this data to the thermal model. The thermal model calculates the temperature distribution, without further feedback to the electrical model. The limitation of this approach is that the electrical parameters are not updated based on the calculated temperature (they are either assumed constant or set to a static temperature profile), leading to less precise results
- **Two-Way Coupling**: The electrical model calculates power loss and sends the heat generation rate to the thermal model. The thermal model computes the cell temperature and feeds it back to the electrical model. This approach is much more accurate, and it is the industry standard for electrothermal modelling (Figure 1.44)

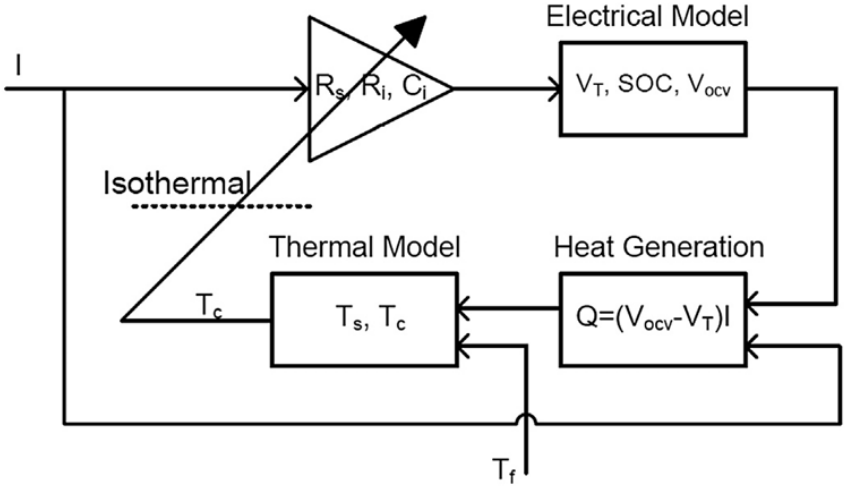

Figure 1.44: Electrothermal model coupling [8]

In this thesis, only the electrical and thermal models have been discussed in detail. As said already, battery modelling is a complex topic and the complete model coupling is much more complex (see Figure 1.45 for an example).

1.3.4 Model Selection

- **Electrical Modelling** The Thevenin 2RC model (Figure 1.31) has been selected as the go-to strategy for electrical modelling in this thesis. This choice is backed by general agreement in the literature, as pointed out by different research activities [24, 17, 22, 12, 16] (3RC model level accuracy has been proven to be required only in really specific applications, like for the case of LFP-chemistry cells [56, 20])

- **Thermal Modelling** The first order thermal ECM (Figure 1.41) has been chosen as the thermal modelling approach, being the simplest but yet effective methodology for temperature estimation. Research in the literature which demonstrates that first order thermal models are fast, easy to implement and still providing a good match with experimental data includes [43, 32, 9, 8]

- **Elctrothermal Model Coupling** To account for the strong interdependence between the electrical and thermal behaviours, a two-way coupling approach is the most reliable and proven solution according to the literature [8, 12, 7]. In this project, the electrothermal characterization has been performed at a single ambient temperature. Therefore, the model parameters depend only on the SOC and not on temperature. Consequently, a one-way coupling has been selected for building the electrothermal model

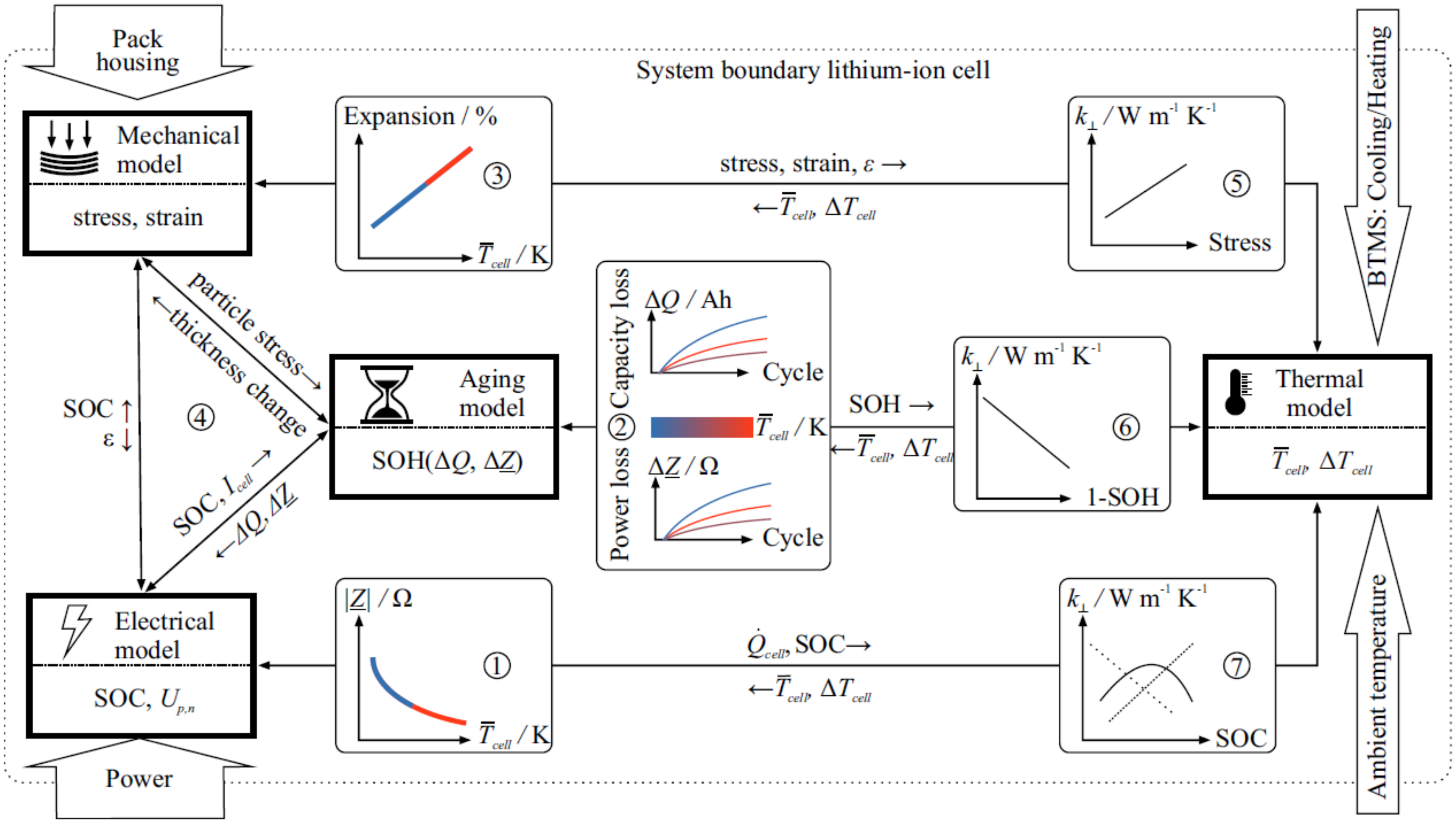

Figure 1.45: Battery full model coupling [32]

2

Experimental Setup and Test Methodology

This chapter describes the specifications of the investigated Li-ion cells, the experimental apparatus used for characterization, the procedures followed during testing, and the data acquisition methods employed to collect data.

2.1 Experimental Setup

The following experimental setup has been designed and built for the electrothermal characterization of Li-ion battery cells [57] (Figure 2.1):

- the **test battery** is a Molicel P45B cylindrical 21700 Li-ion cell
- the **sensing instrumentation** is composed of a Hukseflux FHF05 heat flux sensor and two Pico Technology SE030 Type K thermocouples
- the **data acquisition system** is a Dewesoft DEWE-43A
- the **battery testing system** is a Neware BTS-4008
- the **environmental control system** is a MSL Evolution Clima EC 300CA climatic chamber

The test cells have been put inside the climatical chamber, supported by a test rack having a battery holder with spring-loaded contacts whose terminals are connected to the battery testing system (Figure 2.2). All the sensors wiring has been organized and connected to the data acquisition system using proper adapters (Figure 2.3).

Figure 2.4 shows a summary schematic of the test setup.

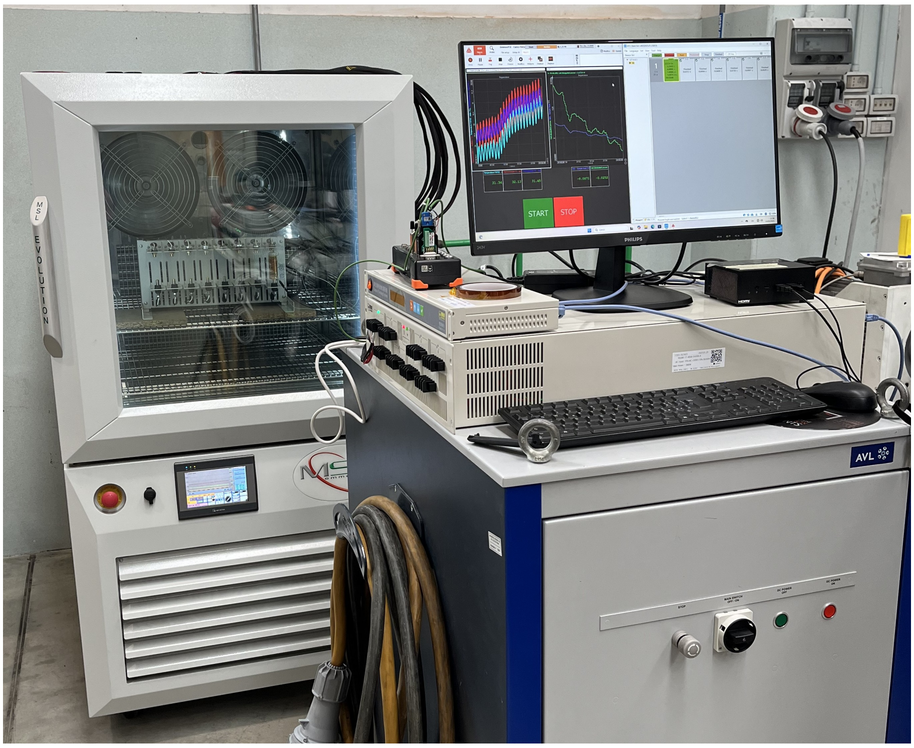

Figure 2.1: Test setup

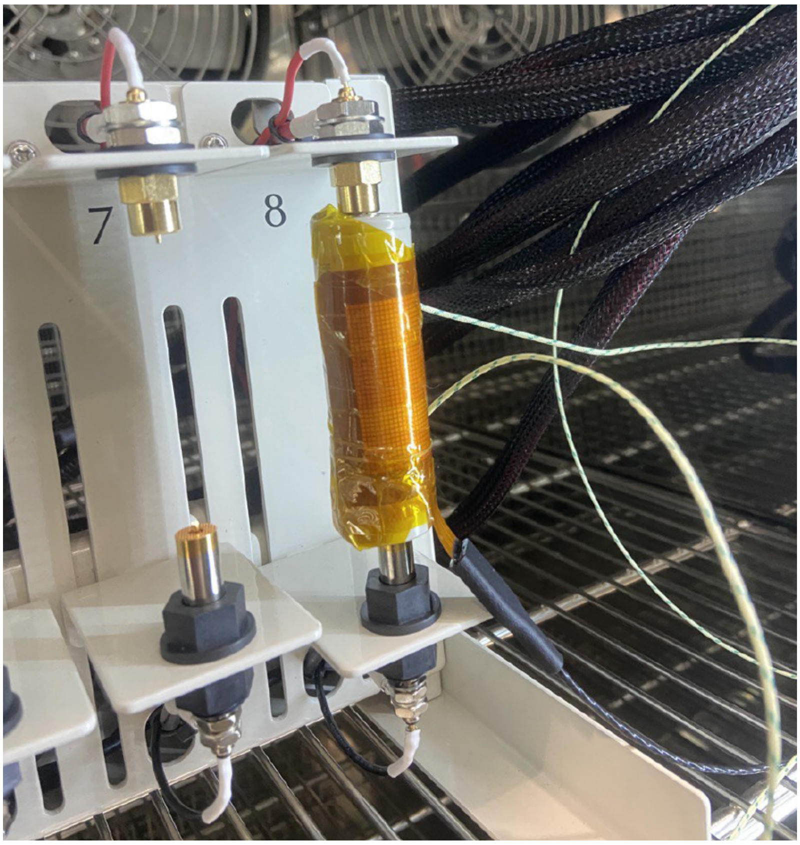

Figure 2.2: Detail of the test battery

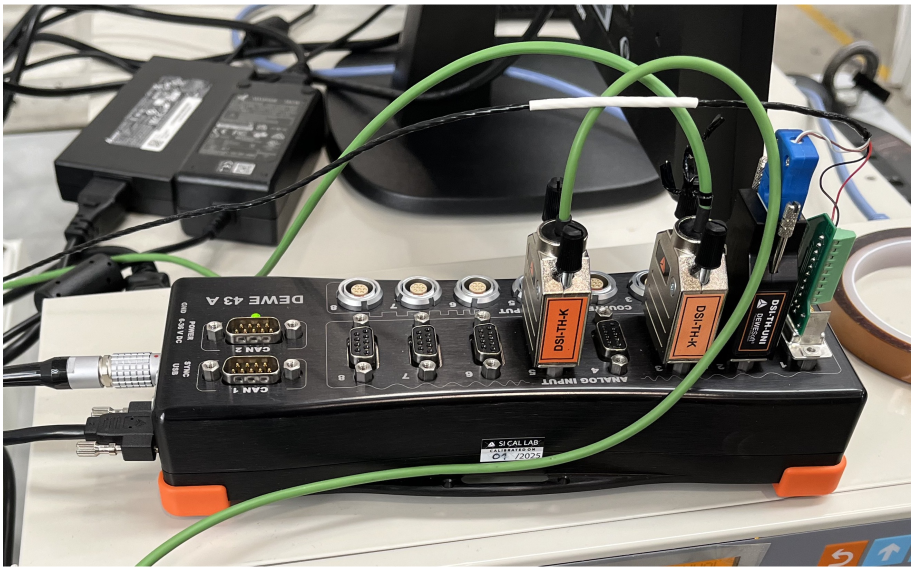

Figure 2.3: Detail of the data acquisition system wiring connections

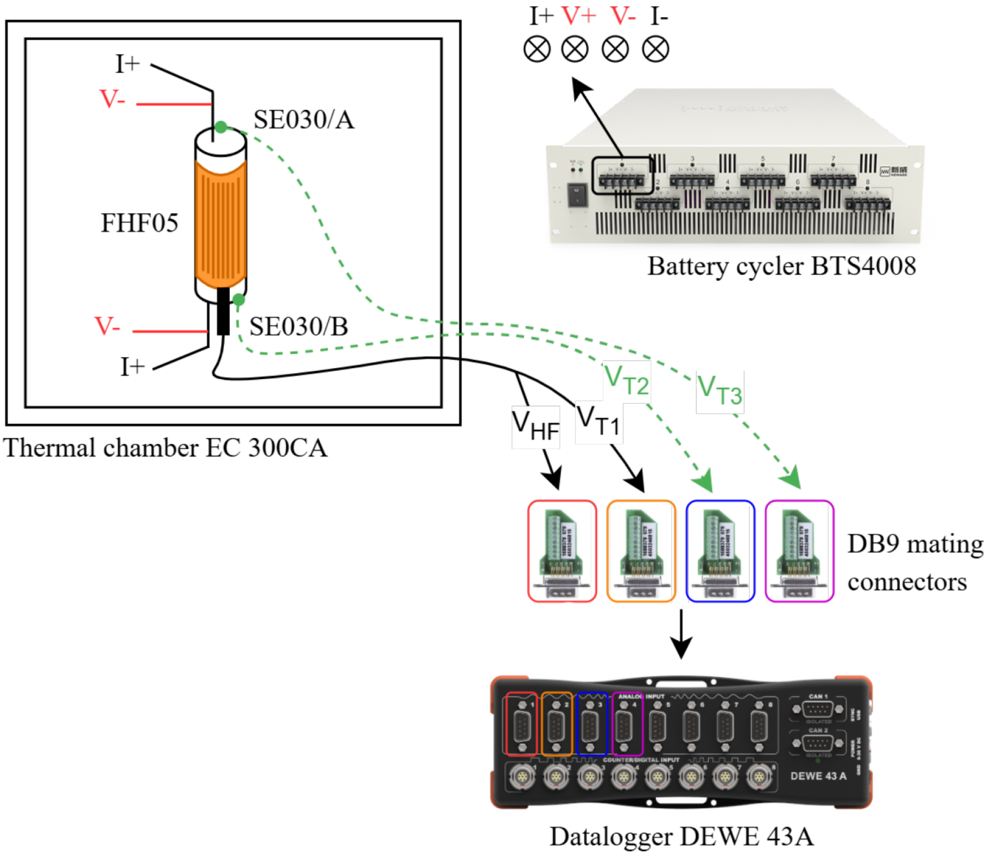

Figure 2.4: Test setup schematic [57]

2.1.1 Test Battery

The battery cell that has been used for characterization and testing in this project is the Molicel P45B (Figure 2.5), a 21700 cylindrical Li-ion cell designed and produced by Molicel, a Taiwan-based Li-ion battery manufacturing company specialized in high-performance battery cells. It is a low impedance cell designed for EV, Electric Vertical Take-Off and Landing (eVTOL) and home appliances applications featuring a NMC cathode chemistry and a Silicon-doped graphitic anode. The high-Nickel cathode structure and Silicon oxide dopant added to the anode enable an increased cell energy density, making it the ideal choice for energy storage in ultra-high power applications. Figure 2.6 showes the typical characteristic curves of the Molicel P45B battery cell. The cell has been selected due to its significant performance and due to its suitability for electric automotive applications. The cell is also in use by the Formula Student teams from University of Modena and Reggio Emilia, that built the battery packs of both the hybrid and full-electric driverless cars starting from this cylindrical cell

- the hybrid race car presents a battery pack with a 14S 3P architecture (42 cells in total)
- the driverless electric race car has a battery pack having a 132S 3P architecture (396 cells in total)

The cell characterization procedure has been done in collaboration with the aforementioned teams to provide them useful data for battery pack design. The complete specifications of the cell, obtained from the manufacturer datasheet [58], can be found in Table 2.1.

Figure 2.5: Molicel P45B battery cell

Table 2.1: Molicel INR-21700-P45B cell specifications [58]

Category	**Parameter**	**Specification**
Capacity	Typical	4500 mAh
	Minimum	4300 mAh
Energy	Typical	16,2 Wh
	Minimum	15,5 Wh
Voltage	Nominal	3,6 V
	Charge	4,2 V
	Discharge	2,5 V
Charge	Standard Current	4,5 A
	Maximum Current	13,5 A (70°C cut-off)
Discharge	Continuous Current	45 A (80°C cut-off)
Temperature	Charge	0°C to 60°C
	Discharge	−40°C to 60°C
Energy Density	Volumetric	643 Wh/l
	Gravimetric	242 Wh/kg
Impedance	AC (30% SOC)	7 mΩ
	DC (50% SOC)	15 mΩ
Physical	Form Factor	Cylindrical
	Dimensions	$21,55 \times 70,15$ mm
	Weight	70 g

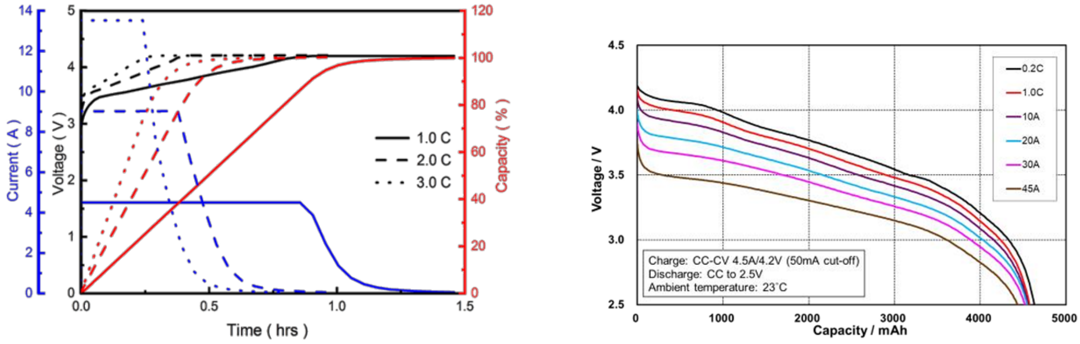

(a) Charge characteristic

(b) Discharge rate characteristic

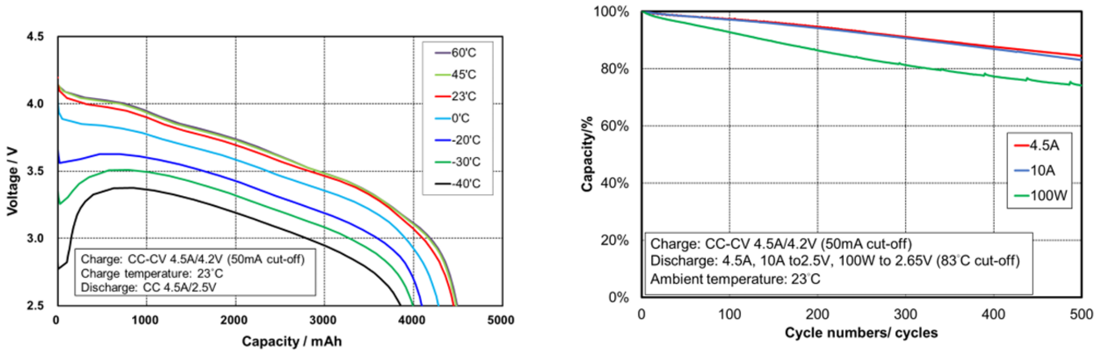

(c) Discharge temperature characteristic

(d) Cycle characteristic

Figure 2.6: Molicel INR-21700-P45B cell characteristic curves [58]

2.1.2 Sensing Instrumentation

The test cell has been intrumented with a heat flux sensor (having an integrated Type T thermocouple) and two Type K thermocouples.

2.1.2.1 Heat Flux Sensor

The adopted heat flux sensor is the Hukseflux FHF05 (Figure 2.7), and it has been wrapped around the cell lateral surface using kapton tape (Figure 2.2). The transducer is based on a thermopile[1], which measures the temperature difference across the sensor body. The thermopile generates a small voltage that is a function of the temperature difference. The heat flux density $\dot{Q}''$ is proportional to the thermal gradient between the two sides ΔT through the thermal conductivity of the heat flux sensor body k

$$\dot{Q}'' = k\frac{\Delta T}{d} \tag{2.1}$$

where d is the sensor thickness and k can be calculated as $k = d/R''_{th} = 0,36\ W/(mK)$, where R''_{th} is the sensor specific thermal resistance.

In practice, the heat flux density is determined starting from the voltage measurement from the thermopile V and the sensitivity of the sensor S. The exact sensitivity of the sensor is determined at the manufacturer by calibration, and can be found on the product certificate that is supplied with each sensor (in this case, the sensitivity at 20°C is $S = 17,39 \cdot 10^{-6} V/(W/m^2)$). Then, the heat flux density value, corrected for sensitivity variations with temperature, can be determined as

$$\dot{Q}'' = \frac{V}{S(1 + 0,002(T - 20))} \tag{2.2}$$

where T is the temperature, measured in °C, determined by the Type T thermocouple that is integrated into the heat flux sensor itself.

The heat transfer rate $\dot{Q}$ through the sensor area A_s can be determined as

$$\dot{Q} = \dot{Q}'' \cdot A_s \tag{2.3}$$

where $A_s = 36\ mm \times 36\ mm = 12,96 \cdot 10^{-4}\ m^2$.

---

[1] A thermopile consists of a number of thermocouples electrically connected in series. A single thermocouple consists of two metal alloys and generates an output voltage that is proportional to the temperature difference between its hot and cold junctions. In a heat flux transducer, the hot and cold junctions are located at the opposite sensor surfaces, and this allows to determine the heat flux through the sensor. Putting thermocouples in series amplifies the signal

The complete heat flux sensor specifications, obtained from the manufacturer manual [59], are provided in Table 2.2.

Table 2.2: Hukseflux FHF05-50X50 heat flux sensor specifications [59]

Category	**Parameter**	**Specification**
General	Model	FHF05-50X50
	Measurand	Heat flux, Temperature
	Sensor Type	Thermopile with thermal spreaders
Measurement	Heat Flux Range	$(-10 \text{ to } +10) \cdot 10^3$ W/m^2
	Sensitivity (Nominal)	$13 \cdot 10^{-6}$ V/(W/m^2)
	Calibration Uncertainty	±5% ($k = 2$)
	Temperature Sensor	Type T Thermocouple (IEC 60584-1 Class2)
Physical	Dimensions	50×50 mm
	Thickness	$0,4$ mm
	Bending Radius	$\geq 7,5$ mm
	Thermal Resistance	$11 \cdot 10^{-4}$ K/(W/m^2)
Environmental	Temperature (Continuous)	−70°C to +120°C
	Temperature (Short term)	−160°C to +150°C
	IP Rating	IP67

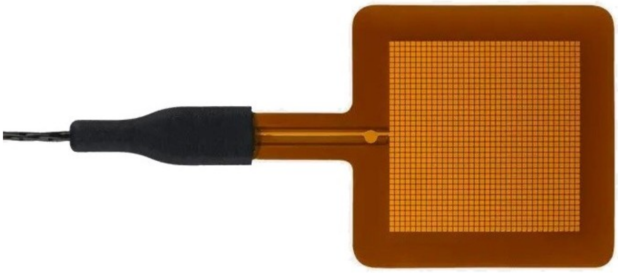

Figure 2.7: Hukseflux FHF05 heat flux sensor

The heat flux sensor is connected to the data logging system using a DSUB adapter (Figure 2.8). The technical specifications of the selected adapter, provided by the manufactured in [60], are summarised in Table 2.3.

Similarly, the integrated Type T thermocouple is connected to the data logger using the Dewsoft DSI-TH-UNI adapter (Figure 2.9), that performs the cold junction compensation and allows to connect the thermocouple to the DSUB analog input. Table 2.4 summarises the technical specifications of the universal adapter as provided by the manufacturer in [61].

Table 2.3: Phoenix Contact VS-09-ST-DSUB/10-MPT-0,5 specifications [60]

Category	**Parameter**	**Specification**
General	Model	VS-09-ST-DSUB/10-MPT-0,5
	Item Number	1688379
	Type	D-SUB Contact Insert (Male)
Electrical	Rated Voltage	60 V
	Rated Current	5 A
	Insulation Resistance	≥ 5000 MΩ
	Contact Resistance	$\leq 2,5$ mΩ
Physical	Dimensions	$31 \times 12,6 \times 49$ mm
	Housing Material	Steel (tin-plated)
	Contact Material	Copper alloy
Environmental	Operating Temperature	-20°C to +80°C
	IP Rating	IP20

Table 2.4: Dewesoft DSI-TH-UNI adapter specifications [61]

Category	**Parameter**	**Specification**
General	Model	DSI-TH-UNI
	Adapter Type	Universal Thermocouple Adapter
	Supported Types	K, J, T, R, S, N, E, B, C
	Host Interface	DSUB-9 (TEDS Automatic Detection)
	Sensor Connector	Mini Thermocouple (Female, Universal)
Performance	Measurement Range	-270°C to +400°C (with Type T)
	Cold Junction Compensation	Integrated (Accuracy: 0.5 °C)
	Input Impedance	> 10 MΩ
	Bias Current	50 nA
	Bandwidth	150 Hz (Host amplifier dependent)
Accuracy	Typical (from 0 to 200°C)	$\pm 1,8$°C (with DEWE-43A, Type T)
Physical	Dimensions	$52 \times 31 \times 15$ mm
	Weight	40 g
Environmental	Operating Temperature	-10°C to +60°C
	IP Rating	IP50

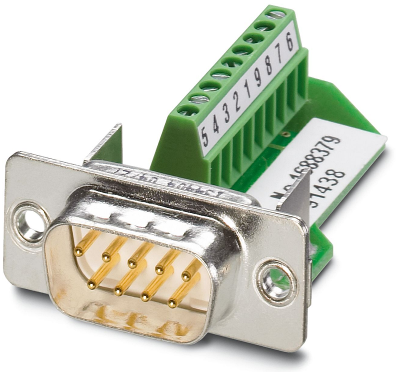

Figure 2.8: Phoenix Contact DSUB adapter

Figure 2.9: Dewesoft DSI-TH-UNI adapter

2.1.2.2 K-Type Thermocouple

The cell has also been instrumented with two Type K thermocouples (Figure 2.10), that have been attached to the two cell terminals using kapton tape. The SE030/A thermocouple is attached under the cell relief valve, close to positive terminal, while SE030/B has been fixed on cell bottom surface (negative terminal), see Figure 2.4. The presence of three different temperature measuring devices allows one to do more accurate considerations on how heat is generated and spatially distributed around the cell surface, other than for measurement reilability. Table 2.5 presents a summary of the technical specifications for the two Type K thermocouples, as provided by the manufacturer in [62].

The two Type K thermocouples have been conncted to the data logging device using two Dewesoft DSI-TH-K adapters (Figure 2.11), that provide cold junction compensation and galvanic isolation. Table 2.6 lists the manufacturer's technical specifications for the two Type K thermocouple adapters [61].

Table 2.5: Pico Technology SE030 Type K thermocouple specifications [62]

Category	**Parameter**	**Specification**
General	Model	SE030
	Sensor Type	Type K Thermocouple
	Insulation	Fiberglass (Twisted Pair)
	Standard	IEC 60584-2:1993 / BS EN 60584-1:2013
Measurement	Temperature Range	−60°C to +350°C
	Conductor Diameter	0,3 mm
Physical	Cable Length	2 m
	Tip Diameter	1,5 mm
	Connection	Molded Flat Pin Mini-Plug

Table 2.6: Dewesoft DSI-TH-K adapter specifications [61]

Category	**Parameter**	**Specification**
General	Model	DSI-TH-K
	Adapter Type	Type K Thermocouple Adapter
	Host Interface	DSUB-9 (TEDS Automatic Detection)
	Sensor Connector	Mini Thermocouple (Female, Green)
Performance	Measurement Range	−200°C to +1370°C
	Cold Junction Compensation	Integrated (Accuracy: 1.0°C)
	Input Impedance	> 10 MΩ
	Bias Current	50 nA
	Bandwidth	70 kHz (Host amplifier dependent)
Accuracy	Typical (from 0 to 200°C)	$\pm 2,3$°C (with DEWE-43A)
Physical	Dimensions	52 × 31 × 15 mm
	Weight	40 g
Environmental	Operating Temperature	−10°C to +60°C
	IP Rating	IP50

Figure 2.10: Pico Technology SE030 Type K thermocouple

Figure 2.11: Dewesoft DSI-TH-K adapter

2.1.3 Data Acquisition System

The Dewesoft DEWE-43A (Figure 2.12) has been used as Data Acquisition (DAQ) system. The four analog inputs (one heat flux sensor, one Type T thermocouple and two Type K thermocouples) were connected and recorded during the tests using the data acquisition software DewesoftX provided with the device. The software was set up to correctly interpret the signal provided by the sensors and to perform the heat flux calculation starting from the sensor output voltage. The manufacturer-provided technical specifications for the DEWE-43A are outlined in Table 2.7 [63].

Figure 2.12: Dewesoft DEWE-43A DAQ

Table 2.7: Dewesoft DEWE-43A technical specifications [63]

Category	Parameter	Specification
Analog Inputs	Channels	8 (Differential, Full Bridge, Voltage)
	ADC Type	24-bit sigma-delta with antialiasing
	Sampling Rate	200 kS/s (Simultaneous)
	Ranges	±10 V, ±1 V, ±100 mV, ±10 mV
Digital/Counters	Channels	8 counters / 24 digital inputs
	Resolution	32-bit
	Timebase	102,4 MHz (10 MHz Max Bandwidth)
CAN Bus	Ports	2 × CAN 2.0B (High Speed)
	Isolation	Galvanic Isolated
Power	Supply Voltage	9–36 V DC
	Consumption	Typical 6 W, Maximum 18 W
	Sensor Supply	12 V, 5 V, ±5 V (Programmable)
Physical	Dimensions	225 × 80 × 45 mm
	Weight	0,72 kg
Environmental	Operating Temp	$-20°$C to 60°C
	IP Rating	IP50
	Shock/Vibration	EN 60068-2-27 / EN 60068-2-6

2.1.4 Battery Testing System

The battery testing system is a Neware BTS-4008 (Figure 2.13), capable of managing charge and discharge of up to eight cells at a time. Each of the eight channel is capable of providing or draining 20 A of current. The device allows for charging and discharging of the battery cell at specified voltages/currents, through the proprietary software Battery Testing System (BTS). The software also allows one to define specific set of charging/discharging cycles that permit to perform advanced testing techniques like HPPC or GITT. An overview of the technical specifications of the cell tester, as provided by the manufacturer in [64], is given in Table 2.8.

Table 2.8: Neware BTS-4008-5V20A-A specifications [64]

Category	**Parameter**	**Specification**
General	Channels	8 independent channels
	Input Power	AC 220V/110V ±10%, 50Hz, 1420W
	Resolution	AD: 24-bit, DA: 16-bit
Voltage	Range	25 mV–5 V
	Accuracy	$\pm 0,1\%$ of FS
Current	Range	0,1 A–20 A
	Accuracy	$\pm 0,1\%$ of FS
	Response Time	$\leq$ 20 ms (10% to 90%)
Power	Per Channel	100 W
	Accuracy	$\pm 0,2\%$ of FS
Modes	Charge	CC, CV, CCCV, CP
	Discharge	CC, CP, CR, CV, CCCV
	Pulse	CC, CP (Min Pulse 500 ms)
Physical	Dimensions	483 × 690 × 130 mm
Environment	Operating Temp	0°C to 40°C
	Humidity	$\leq$ 70% RH

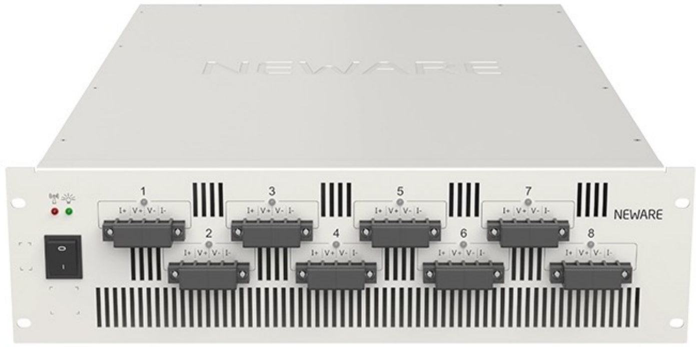

Figure 2.13: Neware BTS-4008 battery tester

2.1.4.1 Wiring Harness

The tester interfaces to the cell through a 4-wire connection ($V+$ and $V-$ for voltage measument, $I+$ and $I-$ for current deployment). Since each of the channels of the battery tester allows for charging/discharging only up to 20 A, and for discharging of the cell at high C-rates higher discharge currents were required, a special wiring has been developed (Figure 2.14). The wiring has been realised using thick copper cables to withstand the higher current, and connects three of the tester channels in parallel, bringing the maximum charge/discharge current to 60 A. The Neware BTS software allows for digital parallelisation up to four different channels, so that the current is automatically shared between the different channels and enabling testing at current rates that would be impossible to reach without this solution.

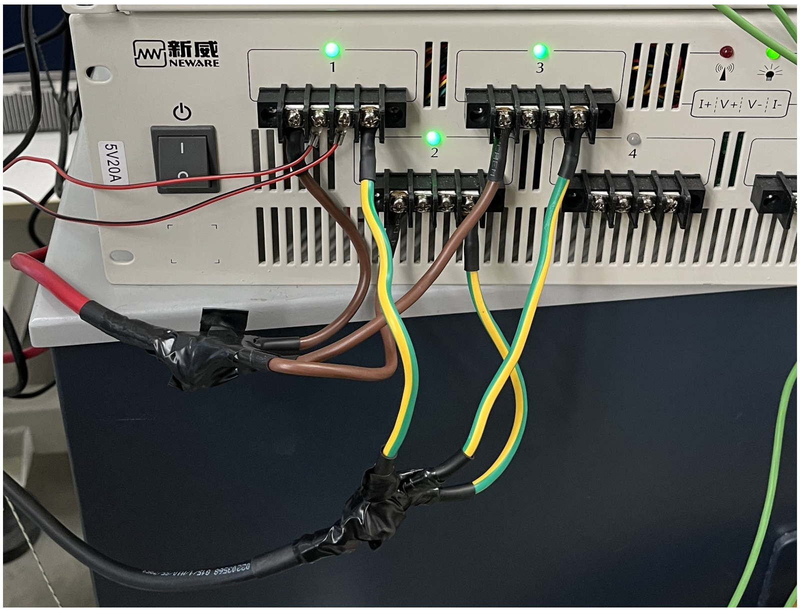

Figure 2.14: High current wiring harness setup

2.1.5 Environmental Control System

Environmental control is realised using an MSL climatic chamber (Figure 2.15). The chamber allows both for temperature and humidity managment, but for the extent of this characterization only temperature has been controlled. All the tests have been carried out at a chamber temperature of 30 °C. Before proceeding with testing, sufficient time was allowed for the temperature in the chamber to be stable and for the cell to reach thermal equilibrium with the chamber environment. Table 2.9 provides the technical specifications for the climatic chamber [65].

Table 2.9: MSL Evolution Clima EC 300CA specifications [65]

Category	**Parameter**	**Specification**
General	Model	EC 300CA (Evolution Clima)
	Volume	300 dm^3
Performance	Temperature Range	$-50°\mathrm{C}$ to $+180°\mathrm{C}$
	Temperature Constancy	$\pm 0,5°\mathrm{C}$
	Humidity Range	5% to 99% RH
	Ramp Up Rate	7 °C/min
	Ramp Down Rate	4 °C/min
	Cooling Capacity	3 HP
	Maximum Total Power	13 kW
	Humidity System Power	1,20 kW
Physical	Internal Dimensions	700 × 700 × 620 mm
	External Dimensions	900 × 1750 × 1200 mm
	Weight	530 kg
Components	Fans	2
	Heaters	2 × 3500 W

Figure 2.15: MSL Evolution Clima EC 300CA

2.2 Test Methodology

The characterization tests that have been performed are constant current discharge at different current rates and HPPC. The charge/dischage procedures have been implemented in the BTS software provided by Neware, that allows for setup of the test profiles, control of the different channels during testing and acquisition, visualization and export of data of the electrical quantitites of interest. In particular, the tests have been set up using the test builder function, that allows to define each specific step using a graphic interface (Figure 2.16).

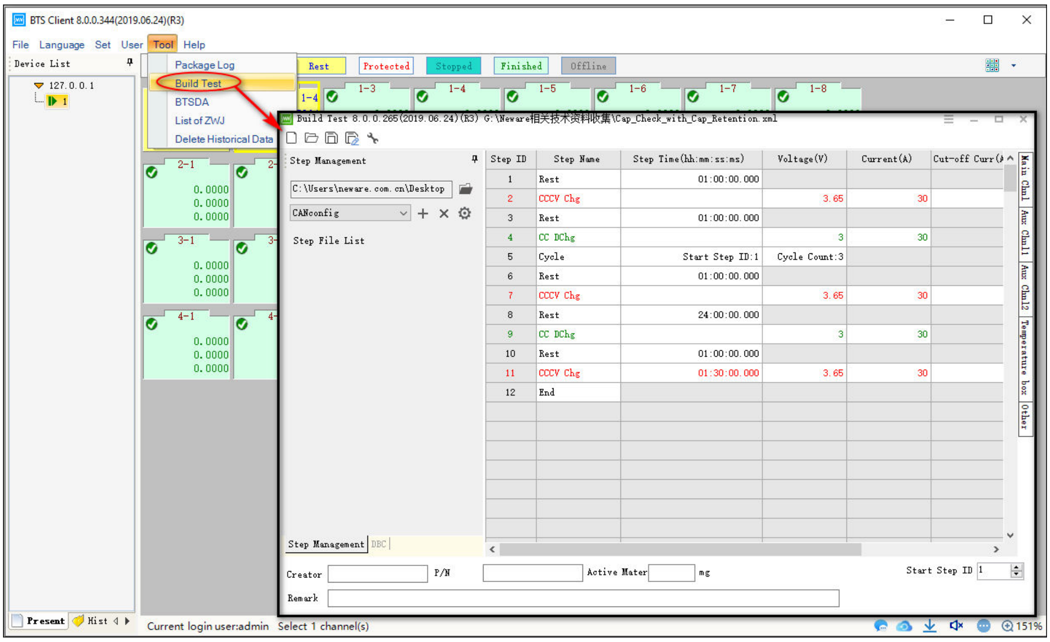

Build Test 8.0.0.265(2019.06.24)(R3) G:\Neware相关技术资料收集\Cap_Check_with_Cap_Retention.xml

C:\Users\neware.com.cn\Desktop

CANconfig

Step ID	Step Name	Step Time(hh:mm:ss:ms)	Voltage(V)	Current(A)	Cut-off Curr(A
1	Rest	01:00:00.000			
2	CCCV Chg		3.65	30	
3	Rest	01:00:00.000			
4	CC DChg		3	30	
5	Cycle	Start Step ID:1	Cycle Count:3		
6	Rest	01:00:00.000			
7	CCCV Chg		3.65	30	
8	Rest	24:00:00.000			
9	CC DChg		3	30	
10	Rest	01:00:00.000			
11	CCCV Chg	01:30:00.000	3.65	30	
12	End				

Creator
P/N
Active Mater mg
Start Step ID 1
Remark

Figure 2.16: Neware test builder interface

2.2.1 Constant Current Discharge Tests

The purpose of constant current discharge tests is to assess the cell performance at various discharge current rates. The implementation of the test profile in the BTS software is summed up in Table 2.10. The battery is charged at 1C and then discharged at a constant current rate; the different current rates that have been tested are described in Table 2.11. The test at 13C (current above the P45B cell maximum discharge rate specifications of 10C, Table 2.1) has been peformed with the scope of assessing the cell capability of discharging at super high discharge rates for very short amount of time, required by the Formula Student teams for designing the powertrain system, and specifically for understanding the maximum acceleration performance the electric drive could provide (that depends on the peak power the battery pack can supply). During this test, the maximum current that the test setup with three parallelized channels can drain has been selected. Temperature has been accurately monitored to avoid the occurrence of thermal runaway phenomenas.

Table 2.10: Constant current discharge implementation (1C discharge example)

			Set Values		Cut-off Limits		
Id	**Step Name**	**Time**	**Voltage**	**Current**	**Voltage**	**Current**	**Notes**
1	Rest	00:00:10	-	-	-	-	
2	CCCV Chg	-	4,1 V	4,5 A	-	0,05 A	Full Chg
3	Rest	00:10:00	-	-	-	-	
4	CC DChg	-	-	4,5 A	2,9 V	-	Full DChg
5	Rest	00:10:00	-	-	-	-	
6	End	-	-	-	-	-	

Table 2.11: Constant current discharge selected current rates

C-rate	Current
C/2	2,25 A
1C	4,5 A
2C	9 A
4C	18 A
10C	45 A
13C	60 A

The test results will be presented and discussed in Chapter 3.

2.2.2 Hybrid Pulse Power Characterization (HPPC) Tests

The purpose of HPPC is to characterize the dynamic performance of the cell, and derive the ECM parameters for the electrothermal model of the battery. The HPPC test profile (Table 2.12) has been implemented in the BTS battery software starting from the examples provided by the software itself and by the literature on the topic. Fundamentally, the cell is first charged and discharged to assess the effective capacity, and then charged again before running the HPPC profile. The charge and discharge pulses are interleaved by brief rest periods that allow to measure the voltage response to the step current. Differently from the test profile described in Section 1.2.1.2, a rest phase following the charge pulse has been added with the purpose of allowing the monitoring of the response also for the charge current pulse. Between each set of pulses, the cell is discharged by 10% of its SOC. The exact amount of capacity to be drained C_{12} (capacity discharged at Step 12, see Table 2.12) to have an exact decrease of 10% of the total capacity is calculated in the BTS software using the following custom function

$$C_{12} = C_4 \cdot 0,1 - C_8 + C_{10} \tag{2.4}$$

where C_4 is the effective capacity measured during the pilot discharge step, C_8 is the amount of charge removed during the discharge pulse, and C_{10} is the amount of charge recovered during the charge pulse. The HPPC pulses are repeated for a total of 11 times, spanning the range from 100 to 0% SOC at -10% increments. The chosen current amplitude for the entire test (current pulses included) has been 1C, symmetrical over charging and discharging, making this a low current HPPC test.

Note that, both for constant current discharge tests and HPPC, the lower and upper voltage limits for charge and discharge have been chosen as $V_{Lower,Limit} = 2,9\ V$ and $V_{Upper,Limit} = 4,1\ V$, respectively. This choise has been done arbitrarily in the interest of safeguarding the battery cell from undue damage (excessively charging or discharging of a battery, techically referred to as overcharging and overdischarging, can damage the cell over time) and preserving it for future tests.

The test results and parameter extrapolation methodology will be presented and discussed in Chapter 3.

Table 2.12: HPPC implementation

			Set Values		**Cut-off Limits**		
Id	**Step Name**	**Time**	**Voltage**	**Current**	**Voltage**	**Current**	**Notes**
1	Rest	00:00:10	-	-	-	-	
2	CCCV Chg	-	4,1 V	4,5 A	-	0,05 A	Full Chg
3	Rest	00:10:00	-	-	-	-	
4	CC DChg	-	-	4,5 A	2,9 V	-	Full DChg
5	Rest	01:00:00	-	-	-	-	
6	CCCV Chg	-	4,1 V	4,5 A	-	0,05 A	Full Chg
7	Rest	01:00:00	-	-	-	-	
8	CCCV DChg	00:00:30	2,9 V	4,5 A	-	0,05 A	DChg Pulse
9	Rest	00:00:40	-	-	-	-	
10	CCCV Chg	00:00:10	4,1 V	4,5 A	-	0,05 A	Chg Pulse
11	Rest	00:00:40	-	-	-	-	
12	CC DChg	-	-	4,5 A	2,9 V	-	10% SOC DChg
13	Rest	01:00:00	-	-	-	-	
14	Cycle	-	-	-	-	-	Start step ID:8, Cycle count:10
15	CC DChg	-	-	4,5 A	2,9 V	-	Final DChg
16	Rest	00:30:00	-	-	-	-	
17	End	-	-	-	-	-	

3

Electrical Characterization Approach and Results

This chapter focuses on the electrical characterization of Li-ion cells. It shows the testing results and describes the methodology that has been followed for the extraction of the electrical equivalent circuit parameters that will be used for deriving the electrical model of the battery cell.

3.1 Constant Current Discharge Results

Constant current discharge testing methodology has been introduced in Section 2.2.1. Figure 3.1 shows the behaviour of voltage and current against time during a constant current discharge at 1C. The charging and discharging phases can be clearly noticed. In particular, one can identify the two charging steps (CC and CV). Note that the current convenction for the battery tester is opposite to the one adopted in the theoretical introduction in Chapter 1, thus in such Figure the current will be assumed to be positive while charging, and negative during discharging.

3.1.1 Capacity Measurement

During constant current discharge testing, the primary output is the variation of the battery cell's capacity with the discharge current rate. In fact, as mentioned in Section 1.1.4.9, the efficiency of a battery cell depends heavily on the discharge current. The most comprehensive way to show this effect is to plot the characteristic curve (voltage versus capacity) of the battery in different discharge conditions. The results of the constant current discharge characterization performed in this study are shown in Figure 3.2. Key observations on these curves are:

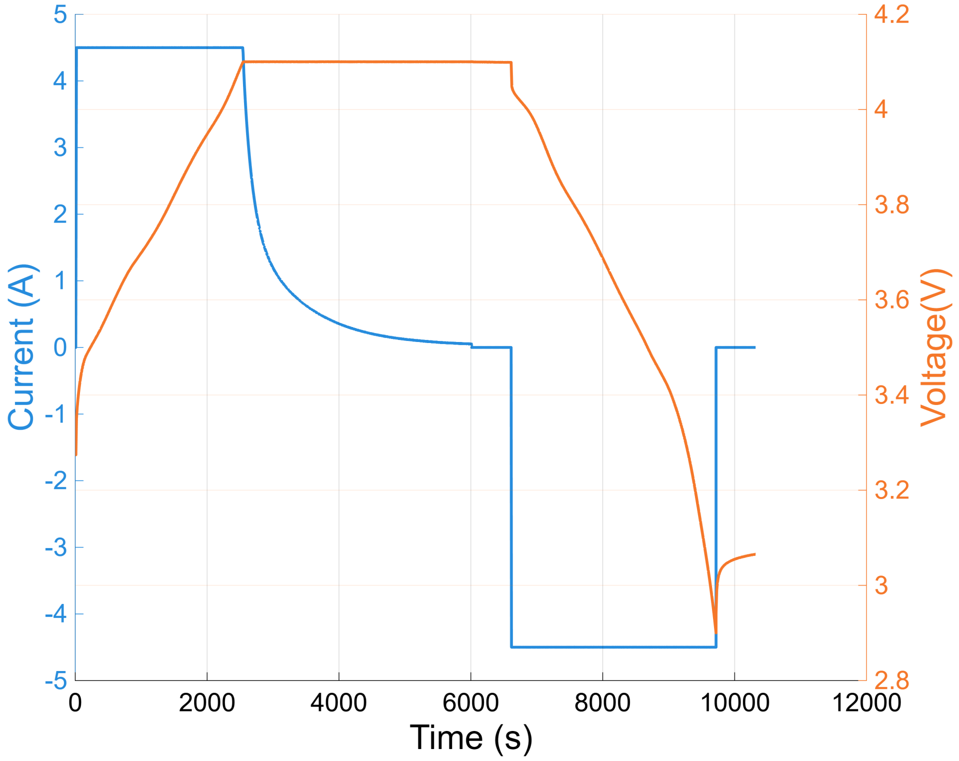

Figure 3.1: Voltage, Current vs. Time (1C current rate)

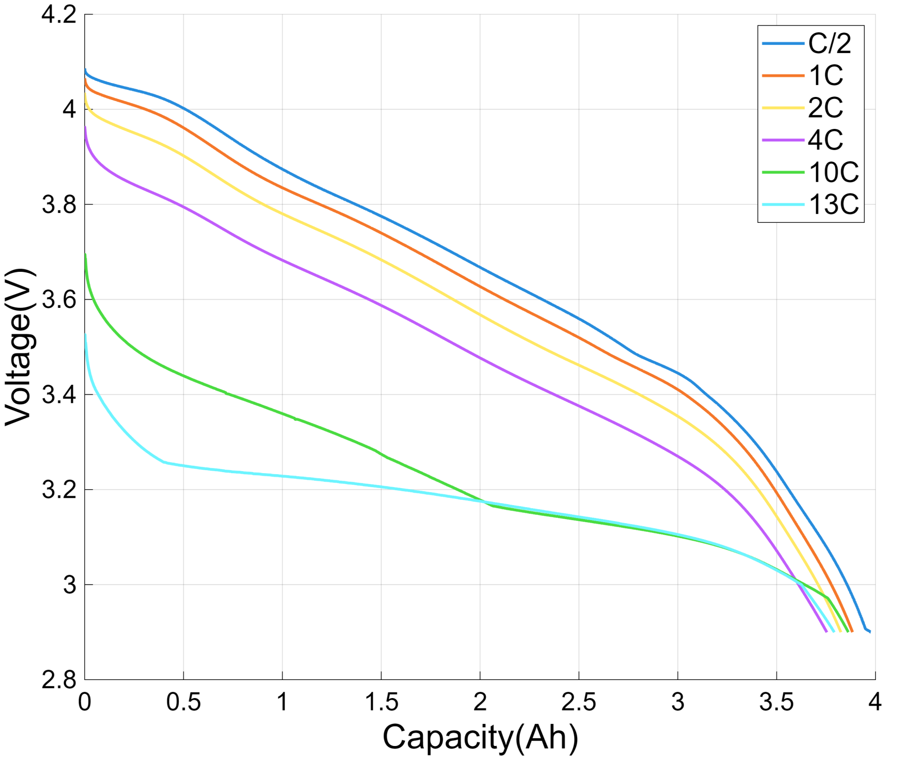

Figure 3.2: Voltage vs. Capacity (different discharge current rates)

- For the case of the Molicel P45B, the rated capacity is 4500 mAh, while the measured one is more of about 4000 mAh (see the ‘Capacity’ column in Table 3.1). This result may be due to the fact that the cell has been discharged in a conservative way, using $V_{Lower,Limit} = 2,9\ V$ and $V_{Upper,Limit} = 4,1\ V$ as lower and upper voltage limits, while the limits proposed by the manufacturer in the datasheet [58] are $V_{Lower,Datasheet} = 2,5\ V$ and $V_{Upper,Datasheet} = 4,2\ V$

- As expected, capacity generally decreases for increasing discharge current rates. This is due to the higher losses experienced within the battery in those high-power discharge conditions. Interestingly, there is an unexpected shift in this pattern while moving from the 4C to the 10C curve. This is a consequence of the change from the low to the high-current wiring harness. As introduced in 2.1.4.1, a different wiring (parallelizing multiple channels of the battery testing system) has been utilized in the tests requiring more than 20 A of current (i.e., the 10C and 13C ones). The high-current wiring has a lower resistance due to the thicker (and shorter) copper wires compared to the standard ones provided by Neware. The lower resistance of the wires, producing lower voltage drop and power losses, is the suspected cause of this inconsistency

- Voltage also decreases for increasing current rates, and this is also due the higher losses that occour at high discharge currents, but compared to the capacity variation (that is a qualitative measure of how the Coulombic efficiency changes) one can notice how the voltage variation (that is a qualitative measure of how the Voltaic efficiency changes) is much more pronounced. In short, the voltage drop is much more significant than the capacity one, and this should be considered when designing an electric powertrain system, as the delivered energy (that is the area below the voltage versus capacity plot) is noticeably affected (see the ‘Energy’ column in Table 3.1)

Table 3.1: Constant current discharge measured capacities and energies

C-rate	**Capacity**	**Energy**
C/2	3975 mAh	14,46 Wh
1C	3884 mAh	14,04 Wh
2C	3825 mAh	13,65 Wh
4C	3754 mAh	13,10 Wh
10C	3862 mAh	12,48 Wh
13C	3792 mAh	12,03 Wh

In addition, considering the cell performance during high-power discharging, it can be seen (Figure 3.3) how at high discharge current rates the battery cannot deliver the requested current continuously. While at 4C the cell steadily delivers 18 A until it's fully discharged, the same doesn't apply at 10C and 13C. The presumed reasons for this effect are:

- the high discharge currents produce excessive heating that trigger the internal safety systems integrated in the battery cell (80 °C cut-off [58]) and cap the maximum power that can be delivered

- the cell, due to the high voltage losses and its internal resistance, cannot physically push the current that is requested, even if the battery tester (that fundamentally behaves as a variable impedance) minimizes the resistance opposed to current flow

During the tests performed, the battery derates after 165 seconds when discharging at 10C (6,94 Wh delivered) and after 24 seconds when delivering 13C (1,34 Wh delivered).

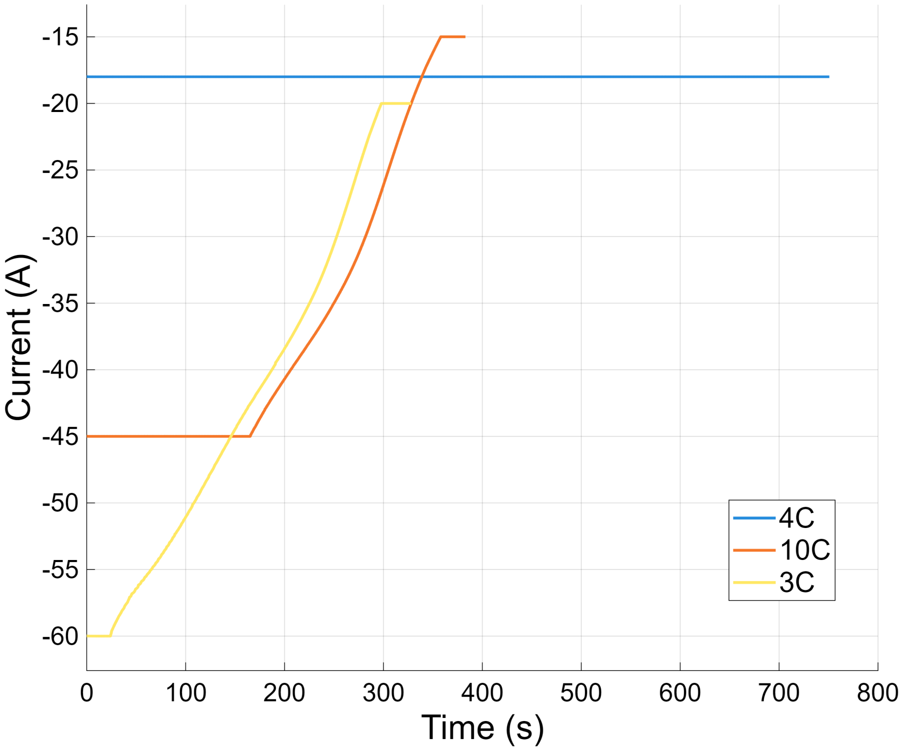

Figure 3.3: Current vs. Time - Discharging Step (different discharge current rates)

3.2 Hybrid Pulse Power Characterization (HPPC) Results

HPPC testing methodology has been introduced in Section 2.2.2. Figure 3.4 shows the behaviour of voltage and current against time during HPPC. The pilot charge and discharge phases (used to assess effective capacity), the final charge in preparation for the test and the different pulse steps can be seen. A detail of one of the pulse events, characterized by the discharge pulse followed by the charge pulse and the 10% SOC discharge is shown for clarity in Figure 3.5.

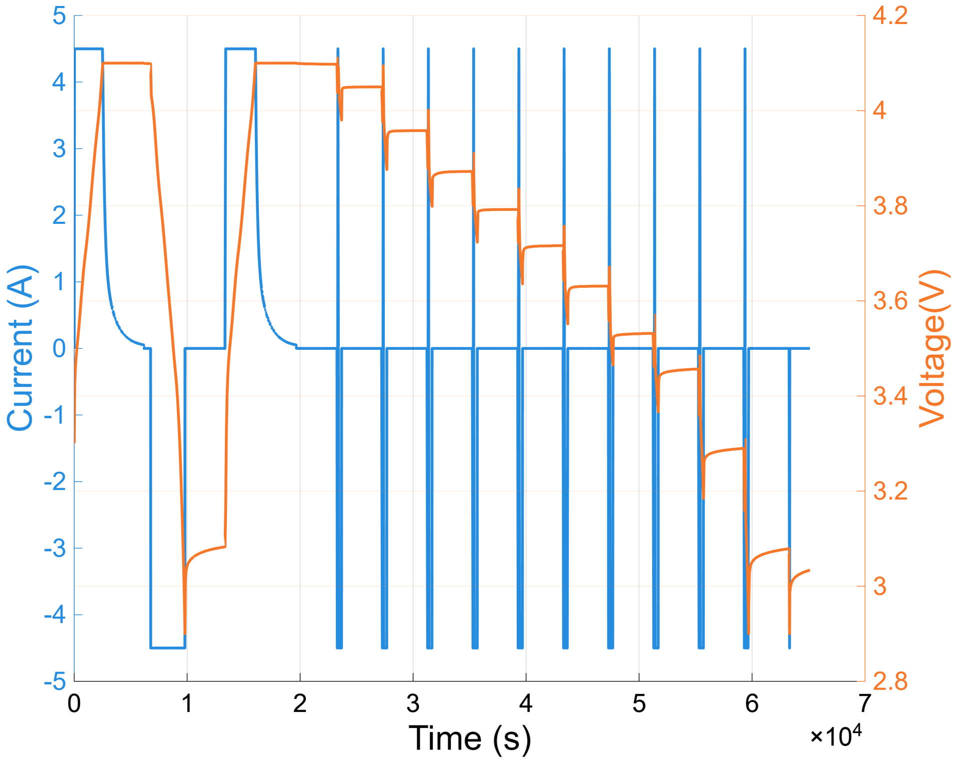

Figure 3.4: Voltage, Current vs. Time (HPPC)

The typical HPPC pulse profile is shown in Figure 3.6. The following characteristic points can be identified:

- A represents the OCV of the battery, as it is the voltage obtained after a sufficient rest time
- AB is the sudden voltage drop that is produced as the discharge current pulse starts, and it can be associated to the series resistance R_0 in the battery models
- BC (discharge pulse) is the exponential decay happening during discharging, due to polarization phenomena, that is modelled using a number of RC blocks

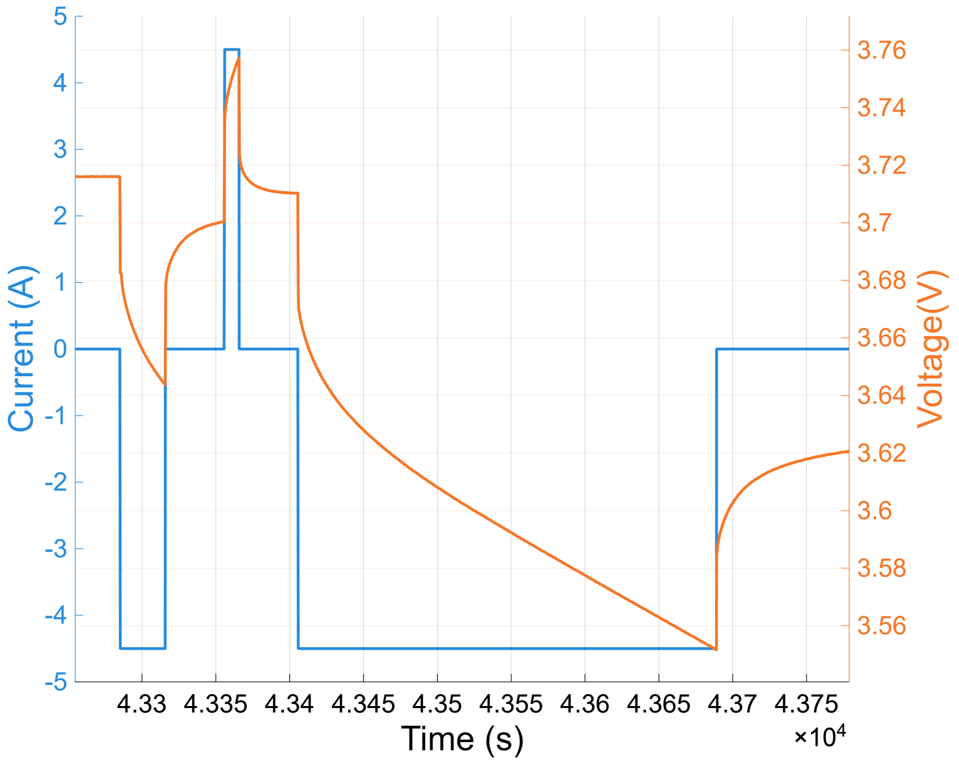

Figure 3.5: Voltage, Current vs. Time (HPPC) - Zoom

in series and can thus be used for characterizing the R, C values by fitting exponential functions

- CD represents the sudden voltage rise that is produced as the discharge current pulse ends, and is also a measure of the series resistance R_0
- DE (discharge relaxation) is the exponential recovery after the discharge event, and can also be used to characterize the RC blocks
- EF is the sudden voltage rise that is produced as the charge current pulse starts, also an indicator of R_0
- FG (charge pulse) is the exponential growth occurring during charging, and can be used as source for fitting of R and C values, too
- GH is the sudden voltage drop that is produced as the charge current pulse ends, and is related to R_0, too
- HI (charge relaxation) is the exponential recovery occurring after the charging pulse end, also function of the R and C values

Thus, the generic approach that has been used for HPPC characterization is:

- A is used to determine the OCV

$$V_{OC}(SOC) = V_A \tag{3.1}$$

- AB, CD, EF and GH are used to derive the series resistance R_0

$$R_0(SOC) = \frac{V_A - V_B}{|I_d|} = \frac{V_D - V_C}{|I_d|} = \frac{V_F - V_E}{|I_c|} = \frac{V_G - V_H}{|I_c|} \tag{3.2}$$

  where $|I_d|$ and $|I_c|$ are the discharge and charge current pulse intensities, respectively

- BC, DE, FG and HI are used to derive the other R, C parameters by exponential functions fitting

This approach is repeated for every SOC value at which the HPPC pulses have been reoccured, allowing to characterize the parameters in function of the battery State of Charge.

The OCV results are shown in Section 3.2.1, while the methodology that has been followed for deriving the equivalent circuit parameters, together with the values obtained, are shown in Section 3.2.2.

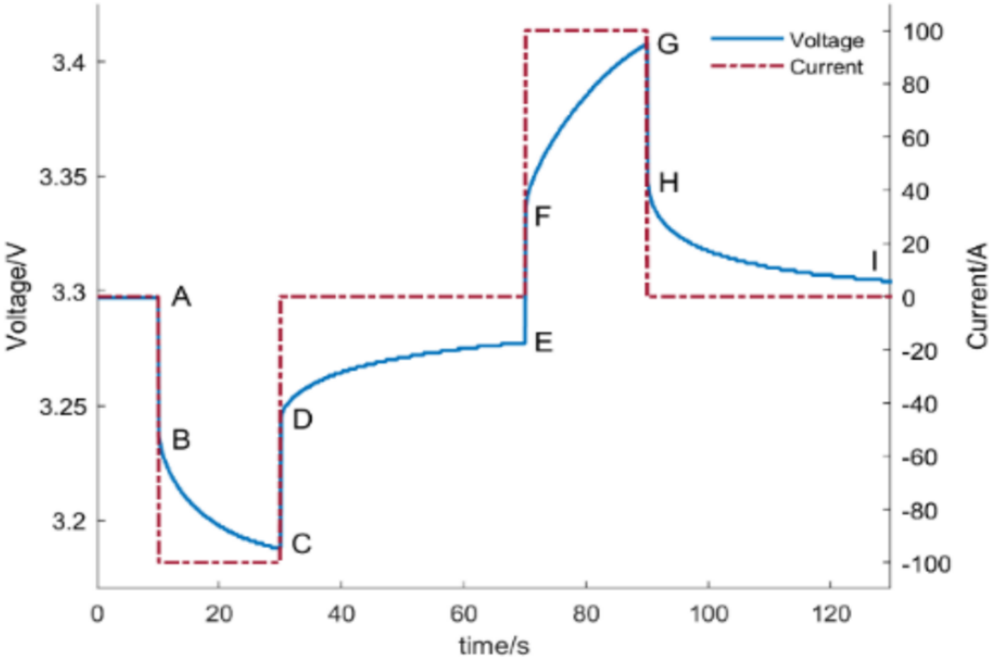

Figure 3.6: Typical HPPC profile [66]

In the context of this work, characterization has been performed in the 10 to 90% SOC range for the following reasons:

- the 100% SOC pulses quality was low due to the set voltage protection limits, and the obtained parameters were unphysical
- the 0% pulse went missing due to an issue with defining the number of pulses to be performed while setting the test program on the Neware BTS software

3.2.1 Open Circuit Voltage (OCV) Measurement

The OCV obtained during testing of Molicel P45B battery cells according to the HPPC test profile described in Section 2.2.2 is shown in Figure 3.7. The curve is surprisingly quite linear, especially in the 20 to 90% SOC range. The reason for this linearity is presumed to be related to the conservativly chosen voltage limits for testing ($V_{Lower,Limit} = 2,9\ V$ and $V_{Upper,Limit} = 4,1\ V$).

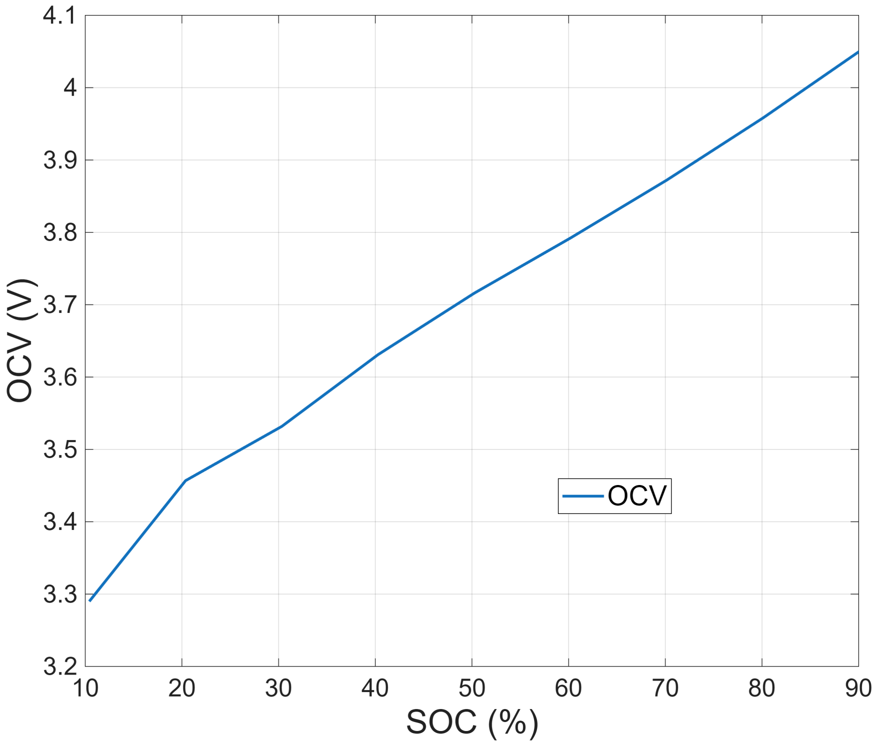

Figure 3.7: OCV vs. SOC

Calculating the OCV by measuring the voltage at the end of the rest phases does not allow for characterization of hysteresis, as HPPC has been performed only for decreasing SOCs. For obtaining a precise estimation of voltage hysteresis, HPPC in both the charging and discharging direction should be made, or proceeding with a low current rate (e.g. C/20) charging/discharging test.

3.2.2 Equivalent Circuit Model (ECM) Parameters Extraction

As introduced in Section 1.3.4, the chosen electrical model is the Thevenin 2RC model described in Section 1.3.1 and reported again for clarity in Figure 3.8.

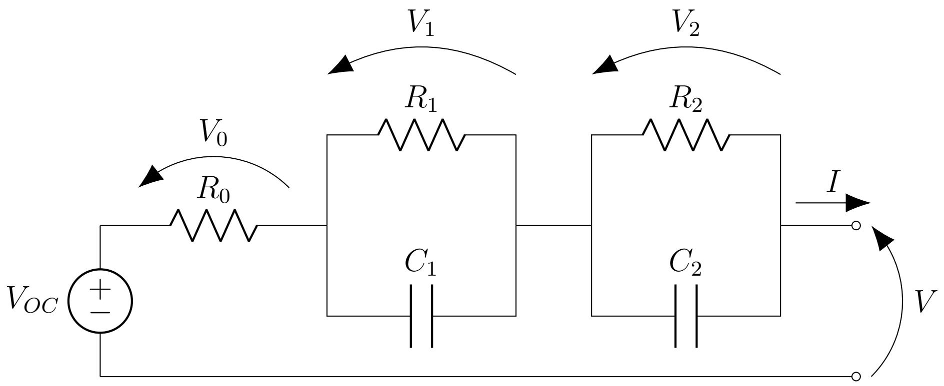

Figure 3.8: Thevenin 2RC model

The model parameters V_{OC}, R_0, R_1, C_1, R_2, C_2 have been defined and calculated as:

3.2.2.1 Open Circuit Voltage (OCV)

The ideal voltage souce V_{OC} is characterized by measuring the voltage at the end of each rest phase. The result is shown in Figure 3.7. The OCV Matlab code is reported in Script 3.1. The code derives the OCV isolating the first rest period at each SOC level, and sampling the voltage at the last data point of this rest period.

Script 3.1: OCV Matlab Script

```
% OCV (voltage at the end of 1h rests, that are the first, fourth, seventh, ...)
% Iterating the -10% SOC increments (variable j)
OCVdata.OCV(j)=Data.('Voltage (V)')(ends(1+(j-1)*3));
```

3.2.2.2 Series Resistance R_0

The series resistance R_0 is calculated as described in Equation 3.2. The calculation is repeated, for increased accuracy, on all the four voltage steps that allow the estimation of this parameter (discharge AB, discharge relaxation CD, charge EF, charge relaxation GH steps of Figure 3.6). The results of this calculation are shown in Figure 3.11. The R_0 Matlab code is shown in Script 3.2. The code uses the rest phases typical of HPPC as reference for identifying the different voltage values.

Script 3.2: R0 Matlab Script

```
% R0 (instantaneous voltage drop divided by current amplitude)
% Iterating the -10% SOC increments (variable j)
R0data.R0Discharge(j)=(OCVdata.OCV(j)-Data.('Voltage (V)')(ends(1+(j-1)*3)+1))/abs(Data
    .('Current (A)')(ends(1+(j-1)*3)+1)); % R0 D=(VA-VB)/Id, where VA=VOC (voltage at
    the end of the first rest) and VB is the voltage sampled immediately after
R0data.R0DischargeRelaxation(j)=(Data.('Voltage (V)')(starts(2+(j-1)*3))-Data.('Voltage
    (V)')(starts(2+(j-1)*3)-1))/abs(Data.('Current (A)')(starts(2+(j-1)*3)-1)); % R0 DR
    =(VD-VC)/Id, where VD is the voltage at the start of the second rest and VC the
    voltage sampled immediately before
R0data.R0Charge(j)=(Data.('Voltage (V)')(ends(2+(j-1)*3)+1)-Data.('Voltage (V)')(ends
    (2+(j-1)*3)))/abs(Data.('Current (A)')(ends(2+(j-1)*3)+1)); % R0 C=(VF-VE)/Ic, where
     VF is the voltage after the end of the second rest and VE the voltage sampled
    immediately before
R0data.R0ChargeRelaxation(j)=(Data.('Voltage (V)')(starts(3+(j-1)*3)-1)-Data.('Voltage (
    V)')(starts(3+(j-1)*3)))/abs(Data.('Current (A)')(starts(3+(j-1)*3)-1)); % R0 CR=(VG
    -VH)/Ic, where VG is the voltage before the start of the third rest and VH the
    voltage sampled immediately after
```

3.2.2.3 Dynamic Parameters R_1, C_1, R_2, C_2

The dynamic parameters R_1, C_1, R_2, C_2 are determined by fitting the experimental curves with exponential functions. The procedure is repeated for the four relevant steps where the dynamic behaviour of the battery cell is exploited (discharge pulse BC, discharge relaxation DE, charge pulse FG, charge relaxation HI steps of Figure 3.6) for increased faithfulness and for reasons of scientific interest.

As introduced in Section 1.3.1.2, the step response of the system when a constant current of magnitude I is applied at $t = 0$, assuming initial conditions $V_1(t)|_{t=0} = 0$ and $V_2(t)|_{t=0} = 0$, is

$$V(t) = V_{OC} - \underbrace{IR_0}_{V_0(t)} - \underbrace{IR_1\left(1 - e^{-\frac{t}{\tau_1}}\right)}_{V_1(t)} - \underbrace{IR_2\left(1 - e^{-\frac{t}{\tau_2}}\right)}_{V_2(t)} \tag{3.3}$$

where $\tau_1 = R_1 \cdot C_1$ and $\tau_2 = R_2 \cdot C_2$.

If the capacitors C_1 and C_2 are assumed to have non-zero initial voltages $V_1(t)|_{t=0} = V_1(0)$ and $V_2(t)|_{t=0} = V_2(0)$, then the expression of the terminal voltage becomes

$$V(t) = V_{OC} - \underbrace{IR_0}_{V_0(t)} - \underbrace{IR_1 - [V_1(0) - IR_1]\, e^{-\frac{t}{\tau_1}}}_{V_1(t)} - \underbrace{IR_2 - [V_2(0) - IR_2]\, e^{-\frac{t}{\tau_2}}}_{V_2(t)} \tag{3.4}$$

Note that in next paragraphs time t is going to be defined relatively to the start of the considered step ($t = 0$ at the start of the current pulse or relaxation phase).

Discharge Pulse (Segment BC)

For the case of the first discharge pulse, that happens after the long rest phase, the initial conditions on the capacitor voltages can be assumed to be zero. The equation that describes the voltage response is Equation 3.3 where $I = I_d > 0$. Isolating the transient terms from the constant OCV and V_0 one obtains

$$V(t) - V_{OC} + I_d R_0 = -I_d R_1 \left(1 - e^{-\frac{t}{\tau_1}}\right) - I_d R_2 \left(1 - e^{-\frac{t}{\tau_2}}\right) \tag{3.5}$$

The right side of Equation 3.5 can be fit by

$$y(t) = -a \cdot (1 - e^{-\frac{t}{\tau_1}}) - b \cdot (1 - e^{-\frac{t}{\tau_2}}) + c \tag{3.6}$$

where a and b represent the maximum voltage drop across each RC pair, τ_1 and τ_2 the time constants of the discharge phase and c is a constant offset term used to correct estimation errors in the OCV. The R, C parameters for the discharge phase can be then obtained by doing

$$\begin{cases} a = I_d \cdot R_1 \implies R_1 = \dfrac{a}{I_d} \\ \tau_1 = R_1 \cdot C_1 \implies C_1 = \dfrac{\tau_1}{R_1} \\ b = I_d \cdot R_2 \implies R_2 = \dfrac{b}{I_d} \\ \tau_2 = R_2 \cdot C_2 \implies C_2 = \dfrac{\tau_2}{R_2} \end{cases} \tag{3.7}$$

The implementation in the code is shown in Script 3.3.

Script 3.3: Discharge Matlab Script

```
% Discharge
% Iterating the -10% SOC increments (variable j)
Dischargedata=Data(ends(1+(j-1)*3)+1:starts(2+(j-1)*3)-1,:);
DischargeArray{j}=Dischargedata;

% Data initialization
Dischargedata.('Voltage (V)')=Dischargedata.('Voltage (V)')-Dischargedata.('Voltage (V)'
    )(1); % V(t)-VOC+V0 (the voltage at the start of the pulse includes the OCV and V0)
Dischargedata.('Time (s)')=Dischargedata.('Time (s)')-Dischargedata.('Time (s)')(1); %
    Relative time

% Fitting
ft=fittype('- a*(1 - exp(-x/tau1)) - b*(1 - exp(-x/tau2)) + c', ...
```

```
             'independent', 'x', ...
             'coefficients', {'a', 'tau1', 'b', 'tau2', 'c'});
opts = fitoptions(ft);
%[a, tau1, b, tau2, c]
opts.Lower=[1e-5, 0.05, 1e-5, 5, -1];
opts.Upper=[1.0, 5, 1.0, 200.0, +1];
opts.StartPoint=[0.05, 0.5, 0.05, 30.0, 0];
Dfit=fit(Dischargedata.('Time (s)'), Dischargedata.('Voltage (V)'), ft, opts);

% Extracting parameters and saving
R1data.R1Discharge(j)=Dfit.a/abs(Data.('Current (A)')(ends(1+(j-1)*3)+1)); % R1=a/Id
C1data.C1Discharge(j)=Dfit.tau1/R1data.R1Discharge(j); % C1=tau1/R1
R2data.R2Discharge(j)=Dfit.b/abs(Data.('Current (A)')(ends(1+(j-1)*3)+1)); % R2=b/Id
C2data.C2Discharge(j)=Dfit.tau2/R2data.R2Discharge(j); % C2=tau2/R2
adata.aDischarge(j)=Dfit.a;
bdata.bDischarge(j)=Dfit.b;
cdata.cDischarge(j)=Dfit.c;
tau1data.tau1Discharge(j)=Dfit.tau1;
tau2data.tau2Discharge(j)=Dfit.tau2;
```

Discharge Relaxation (Segment DE)

For the case of the discharge relaxation, that happens immediately after the discharge pulse, the initial conditions on the capacitor voltages are different from zero. The equation that describes the voltage response is Equation 3.4 where $I = 0$. Isolating the transient terms from the constant OCV one obtains

$$V(t) - V_{OC} = -V_1(0) \cdot e^{-\frac{t}{\tau_1}} - V_2(0) \cdot e^{-\frac{t}{\tau_2}} \tag{3.8}$$

where $V_1(0)$ and $V_2(0)$ are the polarization voltages accumulated across the capacitors during the discharging phase

$$\begin{cases} V_1(0) = I_d \cdot R_1 \cdot (1 - e^{-\frac{T_d}{\tau_{1d}}}) \\ V_2(0) = I_d \cdot R_2 \cdot (1 - e^{-\frac{T_d}{\tau_{2d}}}) \end{cases} \tag{3.9}$$

where $I_d > 0$ is the discharge pulse current amplitude, T_d is the duration of the discharge pulse and τ_{1d}, τ_{2d} are the time constants from the discharge phase.

The right side of Equation 3.8 can be fit by

$$y(t) = -a \cdot e^{-\frac{t}{\tau_1}} - b \cdot e^{-\frac{t}{\tau_2}} + c \tag{3.10}$$

where a and b represent the initial amplitudes of the polarization voltages at the moment relaxation begins, τ_1 and τ_2 the time constants of the discharge relaxation phase and c is a constant offset term used to correct estimation errors in the OCV. The R, C parameters for the discharge relaxation phase can be then obtained by doing

$$\begin{cases} a = I_d \cdot R_1 \cdot (1 - e^{-\frac{T_d}{\tau_{1d}}}) \implies R_1 = \dfrac{a}{I_d \cdot (1 - e^{-\frac{T_d}{\tau_{1d}}})} \\ \tau_1 = R_1 \cdot C_1 \implies C_1 = \dfrac{\tau_1}{R_1} \\ b = I_d \cdot R_2 \cdot (1 - e^{-\frac{T_d}{\tau_{2d}}}) \implies R_2 = \dfrac{b}{I_d \cdot (1 - e^{-\frac{T_d}{\tau_{2d}}})} \\ \tau_2 = R_2 \cdot C_2 \implies C_2 = \dfrac{\tau_2}{R_2} \end{cases} \tag{3.11}$$

The implementation in the code is shown in Script 3.4.

Script 3.4: Discharge Relaxation Matlab Script

```matlab
% Discharge Relaxation
% Iterating the -10% SOC increments (variable j)
DischargeRelaxationdata=Data(starts(2+(j-1)*3):ends(2+(j-1)*3),:);
DischargeRelaxationArray{j}=DischargeRelaxationdata;

% Data initialization
InstantOCV=interp1(OCVdata.SOC, OCVdata.OCV, DischargeRelaxationdata.SOC(1), 'linear', '
    extrap'); % OCV interpolation
DischargeRelaxationdata.('Voltage (V)')=DischargeRelaxationdata.('Voltage (V)')-
    InstantOCV; % V(t)-VOC
DischargeRelaxationdata.('Time (s)')=DischargeRelaxationdata.('Time (s)')-
    DischargeRelaxationdata.('Time (s)')(1); % Relative time

% Fitting
ft = fittype('- a*exp(-x/tau1) - b*exp(-x/tau2) + c', ...
             'independent', 'x', ...
             'coefficients', {'a', 'tau1', 'b', 'tau2', 'c'});
opts = fitoptions(ft);
%[a, tau1, b, tau2, c]
opts.Lower=[1e-5, 0.05, 1e-5, 5, -1];
opts.Upper=[1.0, 5, 1.0, 200.0, +1];
opts.StartPoint=[0.05, 0.5, 0.05, 30.0, 0];
DRfit=fit(DischargeRelaxationdata.('Time (s)'), DischargeRelaxationdata.('Voltage (V)'),
     ft, opts);

% Extracting parameters and saving
```

```
R1data.R1DischargeRelaxation(j)=DRfit.a/abs(Data.('Current (A)')(ends(1+(j-1)*3)+1))/(1-
    exp(-Dischargedata.('Time (s)')(end)/Dfit.tau1)); % R1=a/Id/(1-exp(-Td/tau1d))
C1data.C1DischargeRelaxation(j)=DRfit.tau1/R1data.R1DischargeRelaxation(j); % C1=tau1/R1
R2data.R2DischargeRelaxation(j)=DRfit.b/abs(Data.('Current (A)')(ends(1+(j-1)*3)+1))/(1-
    exp(-Dischargedata.('Time (s)')(end)/Dfit.tau2)); % R2=b/Id/(1-exp(-Td/tau2d))
C2data.C2DischargeRelaxation(j)=DRfit.tau2/R2data.R2DischargeRelaxation(j); % C2=tau2/R2
adata.aDischargeRelaxation(j)=DRfit.a;
bdata.bDischargeRelaxation(j)=DRfit.b;
cdata.cDischargeRelaxation(j)=DRfit.c;
tau1data.tau1DischargeRelaxation(j)=DRfit.tau1;
tau2data.tau2DischargeRelaxation(j)=DRfit.tau2;
```

Charge Pulse (Segment FG)

For the case of the charge pulse, that happens after the short rest phase following the discharge pulse, the initial conditions on the capacitor voltages cannot be assumed to be zero (the rest phase is not long enough for reaching equilibrium). The equation that describes the voltage response is Equation 3.4 where $|I| = I_c > 0$. Isolating the transient terms from the constant OCV and V_0 one obtains

$$\begin{aligned} V(t) - V_{OC} - I_c R_0 &= I_c R_1 - [V_1(0) + I_c R_1]\, e^{-\frac{t}{\tau_1}} + I_c R_2 - [V_2(0) + I_c R_2]\, e^{-\frac{t}{\tau_2}} \\ &= I_c R_1 \left(1 - e^{-\frac{t}{\tau_1}}\right) - V_1(0) \cdot e^{-\frac{t}{\tau_1}} + I_c R_2 \left(1 - e^{-\frac{t}{\tau_2}}\right) - V_2(0) \cdot e^{-\frac{t}{\tau_2}} \end{aligned} \tag{3.12}$$

where $V_1(0)$ and $V_2(0)$ are the residual polarization voltages across the capacitors at the start of the charge phase

$$\begin{cases} V_1(0) = V_{1dr}(0) \cdot e^{-\frac{T_{dr}}{\tau_{1dr}}} \\ V_2(0) = V_{2dr}(0) \cdot e^{-\frac{T_{dr}}{\tau_{2dr}}} \end{cases} \tag{3.13}$$

where $V_{1dr}(0) = a_{dr} = I_d R_1 (1 - e^{-\frac{T_d}{\tau_{1d}}})$, $V_{2dr}(0) = b_{dr} = I_d R_2 (1 - e^{-\frac{T_d}{\tau_{2d}}})$ are the voltages on the capacitors at the start of the discharge relaxation phase, T_{dr} is the duration of the discharge relaxation and τ_{1dr}, τ_{2dr} are the time constants from the discharge relaxation phase.

The right side of Equation 3.12 can be fit by

$$y(t) = a \cdot (1 - e^{-\frac{t}{\tau_1}}) - V_1(0) \cdot e^{-\frac{t}{\tau_1}} + b \cdot (1 - e^{-\frac{t}{\tau_2}}) - V_2(0) \cdot e^{-\frac{t}{\tau_2}} + c \tag{3.14}$$

where a and b represent the magnitude of the polarization caused by the charging current across each RC pair, τ_1 and τ_2 the time constants of the charge phase and c is a constant offset term used to correct estimation errors in the OCV. $V_1(0)$ and $V_2(0)$ are constants, passed to the solver as problem coefficients. The R, C parameters for the charge phase can be then obtained by doing

$$\begin{cases} a = I_c \cdot R_1 \implies R_1 = \dfrac{a}{I_c} \\ \tau_1 = R_1 \cdot C_1 \implies C_1 = \dfrac{\tau_1}{R_1} \\ b = I_c \cdot R_2 \implies R_2 = \dfrac{b}{I_c} \\ \tau_2 = R_2 \cdot C_2 \implies C_2 = \dfrac{\tau_2}{R_2} \end{cases} \tag{3.15}$$

The implementation in the code is shown in Script 3.5.

Script 3.5: Charge Matlab Script

```
% Charge
% Iterating the -10% SOC increments (variable j)
Chargedata=Data(ends(2+(j-1)*3)+1:starts(3+(j-1)*3)-1,:);
ChargeArray{j}=Chargedata;

% Data initialization
V1_res=DRfit.a*exp(-DischargeRelaxationdata.('Time (s)')(end)/DRfit.tau1); % V1(0)=V1dr
    (0)*exp(-Tdr/tau1dr)
V2_res=DRfit.b*exp(-DischargeRelaxationdata.('Time (s)')(end)/DRfit.tau2); % V2(0)=V2dr
    (0)*exp(-Tdr/tau1dr)
InstantOCV=interp1(OCVdata.SOC, OCVdata.OCV, Chargedata.SOC(1), 'linear', 'extrap'); %
    OCV interpolation
Chargedata.('Voltage (V)')=Chargedata.('Voltage (V)')-InstantOCV-R0data.R0Charge(j)*abs(
    Data.('Current (A)')(ends(2+(j-1)*3)+1)); % V(t)-VOC-V0
Chargedata.('Time (s)')=Chargedata.('Time (s)')-Chargedata.('Time (s)')(1); % Relative
    time

% Fitting
ft=fittype('+ a*(1 - exp(-x/tau1)) + b*(1 - exp(-x/tau2)) - V1*exp(-x/tau1) - V2*exp(-x/
    tau2) +c', ...
            'independent', 'x', ...
            'coefficients', {'a', 'tau1', 'b', 'tau2', 'c'}, ...
            'problem', {'V1', 'V2'});
opts = fitoptions(ft);
%[a, tau1, b, tau2, c]
opts.Lower=[1e-5, 0.05, 1e-5, 5, -1];
```

```
opts.Upper=[1.0, 5, 1.0, 200.0, +1];
opts.StartPoint=[0.05, 0.5, 0.05, 30.0, 0];
Cfit=fit(Chargedata.('Time (s)'), Chargedata.('Voltage (V)'), ft, opts,'problem', {
    V1_res, V2_res});

% Extracting parameters and saving
R1data.R1Charge(j)=Cfit.a/abs(Data.('Current (A)')(ends(2+(j-1)*3)+1)); % R1=a/Ic
C1data.C1Charge(j)=Cfit.tau1/R1data.R1Charge(j); % C1=tau1/R1
R2data.R2Charge(j)=Cfit.b/abs(Data.('Current (A)')(ends(2+(j-1)*3)+1)); % R2=b/Ic
C2data.C2Charge(j)=Cfit.tau2/R2data.R2Charge(j); % C2=tau2/R2
adata.aCharge(j)=Cfit.a;
bdata.bCharge(j)=Cfit.b;
cdata.cCharge(j)=Cfit.c;
tau1data.tau1Charge(j)=Cfit.tau1;
tau2data.tau2Charge(j)=Cfit.tau2;
V1data.V1Charge(j)=V1_res;
V2data.V2Charge(j)=V2_res;
```

Charge Relaxation (Segment HI)

For the case of the charge relaxation, that happens immediately after the charge pulse, the initial conditions on the capacitor voltages are different from zero (similarly to the discharge relaxation phase). The equation that describes the voltage response is Equation 3.4 where $I = 0$. Isolating the transient terms from the constant OCV one obtains

$$V(t) - V_{OC} = -V_1(0) \cdot e^{-\frac{t}{\tau_1}} - V_2(0) \cdot e^{-\frac{t}{\tau_2}} \tag{3.16}$$

where $V_1(0)$ and $V_2(0)$ are the polarization voltages accumulated across the capacitors during the charging phase (considering the residual voltage due to the previous discharge and relaxation steps)

$$\begin{cases} V_1(0) = -I_c \cdot R_1 \cdot (1 - e^{-\frac{T_c}{\tau_{1c}}}) + V_{1c}(0) \cdot e^{-\frac{T_c}{\tau_{1c}}} \\ V_2(0) = -I_c \cdot R_2 \cdot (1 - e^{-\frac{T_c}{\tau_{2c}}}) + V_{2c}(0) \cdot e^{-\frac{T_c}{\tau_{2c}}} \end{cases} \tag{3.17}$$

where $V_{1c}(0) = V_{1dr}(0) \cdot e^{-\frac{T_{dr}}{\tau_{1dr}}}$, $V_{2c}(0) = V_{2dr}(0) \cdot e^{-\frac{T_{dr}}{\tau_{2dr}}}$ are the voltages on the capacitors at the start of the charge phase, $I_c = |I| > 0$ is the charge pulse current amplitude, T_c is the duration of the charge pulse and τ_{1c}, τ_{2c} are the time constants from the charge phase.

The right side of Equation 3.16 can be fit by

$$y(t) = +a \cdot e^{-\frac{t}{\tau_1}} + b \cdot e^{-\frac{t}{\tau_2}} + c \tag{3.18}$$

where a and b represent the initial amplitudes of the polarization voltages at the moment relaxation begins, τ_1 and τ_2 the time constants of the charge relaxation phase and c is a constant offset term used to correct estimation errors in the OCV. The R, C parameters for the charge relaxation phase can be then obtained by doing

$$\begin{cases} a = I_c \cdot R_1 \cdot (1 - e^{-\frac{T_c}{\tau_{1c}}}) - V_{1c}(0) \cdot e^{-\frac{T_c}{\tau_{1c}}} \implies R_1 = \dfrac{a + V_{1c}(0) \cdot e^{-\frac{T_c}{\tau_{1c}}}}{I_c \cdot (1 - e^{-\frac{T_c}{\tau_{1c}}})} \\ \tau_1 = R_1 \cdot C_1 \implies C_1 = \dfrac{\tau_1}{R_1} \\ b = I_c \cdot R_2 \cdot (1 - e^{-\frac{T_c}{\tau_{2c}}}) - V_{2c}(0) \cdot e^{-\frac{T_c}{\tau_{2c}}} \implies R_2 = \dfrac{b + V_{2c}(0) \cdot e^{-\frac{T_c}{\tau_{2c}}}}{I_c \cdot (1 - e^{-\frac{T_c}{\tau_{2c}}})} \\ \tau_2 = R_2 \cdot C_2 \implies C_2 = \dfrac{\tau_2}{R_2} \end{cases} \tag{3.19}$$

The implementation in the code is shown in Script 3.6.

Script 3.6: Charge Relaxation Matlab Script

```
% Charge Relaxation
% Iterating the -10% SOC increments (variable j)
ChargeRelaxationdata=Data(starts(3+(j-1)*3):ends(3+(j-1)*3),:);
ChargeRelaxationArray{j}=ChargeRelaxationdata;

% Data initialization
V1_res_r=V1_res*exp(-Chargedata.('Time (s)')(end)/Cfit.tau1); % V1res(0)=V1c(0)*exp(-Tc/tau1c)
V2_res_r=V2_res*exp(-Chargedata.('Time (s)')(end)/Cfit.tau2); % V2res(0)=V2c(0)*exp(-Tc/tau2c)
InstantOCV=interp1(OCVdata.SOC, OCVdata.OCV, ChargeRelaxationdata.SOC(1), 'linear', 'extrap'); % OCV interpolation
ChargeRelaxationdata.('Voltage (V)')=ChargeRelaxationdata.('Voltage (V)')-InstantOCV; % V(t)-VOC
ChargeRelaxationdata.('Time (s)')=ChargeRelaxationdata.('Time (s)')-ChargeRelaxationdata.('Time (s)')(1); % Relative time

% Fitting
ft = fittype('+ a*exp(-x/tau1) + b*exp(-x/tau2) + c', ...
             'independent', 'x', ...
             'coefficients', {'a', 'tau1', 'b', 'tau2', 'c'});
opts = fitoptions(ft);
```

```
%[a, tau1, b, tau2]
opts.Lower=[1e-5, 0.05, 1e-5, 5, -1];
opts.Upper=[1.0, 5, 1.0, 200.0, +1];
opts.StartPoint=[0.05, 0.5, 0.05, 30.0, 0];
CRfit=fit(ChargeRelaxationdata.('Time (s)'), ChargeRelaxationdata.('Voltage (V)'), ft,
    opts);

% Extracting parameters and saving
R1data.R1ChargeRelaxation(j)=(CRfit.a+V1_res_r)/abs(Data.('Current (A)')(ends(2+(j-1)*3)
    +1))/(1-exp(-Chargedata.('Time (s)')(end)/Cfit.tau1)); % R1=(a+V1res(0))/Ic/(1-exp(-
    Tc/tau1c));
C1data.C1ChargeRelaxation(j)=CRfit.tau1/R1data.R1ChargeRelaxation(j); % C1=tau1/R1;
R2data.R2ChargeRelaxation(j)=(CRfit.b+V2_res_r)/abs(Data.('Current (A)')(ends(2+(j-1)*3)
    +1))/(1-exp(-Chargedata.('Time (s)')(end)/Cfit.tau2)); % R2=(b+V2res(0))/Ic/(1-exp(-
    Tc/tau2c));
C2data.C2ChargeRelaxation(j)=CRfit.tau2/R2data.R2ChargeRelaxation(j); % C2=tau2/R2;
adata.aChargeRelaxation(j)=CRfit.a;
bdata.bChargeRelaxation(j)=CRfit.b;
cdata.cChargeRelaxation(j)=CRfit.c;
tau1data.tau1ChargeRelaxation(j)=CRfit.tau1;
tau2data.tau2ChargeRelaxation(j)=CRfit.tau2;
```

Resulting Values

Figure 3.9 and 3.10 show how the script effectively fits data of the HPPC test pulses.

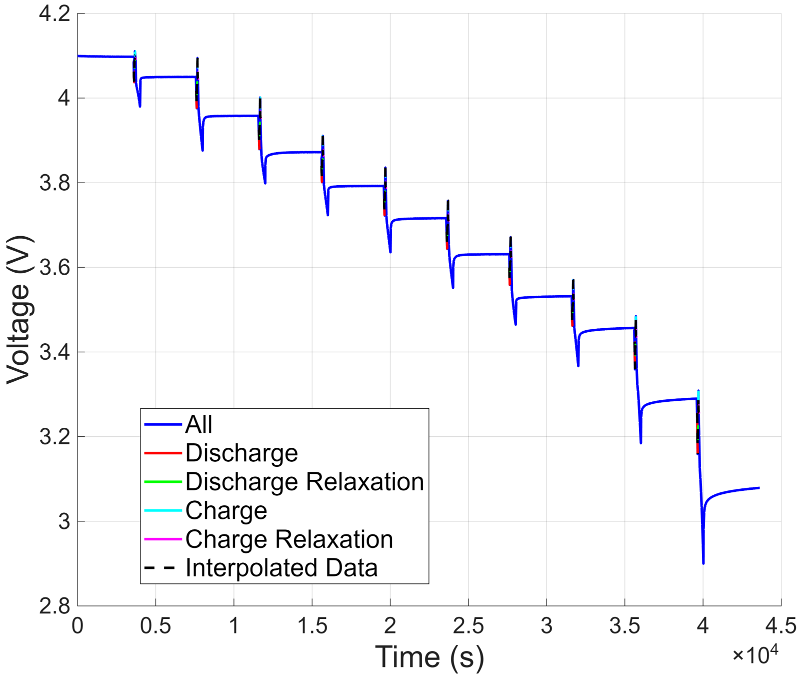

Figure 3.9: Voltage vs. Time

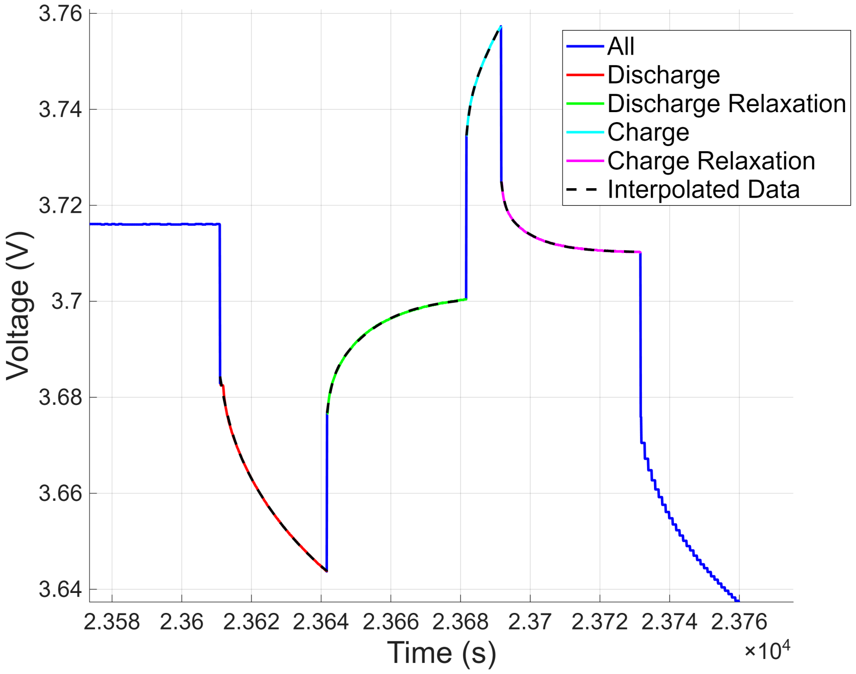

Figure 3.10: Voltage vs. Time - Zoom

The code for the plot in Figure 3.9 and 3.10 is shown in Script 3.7. The voltage respose is mathematically recalculated using the equations of the ECM and overlayed onto the raw test data. The voltage equations are:

Discharge Pulse

$$V_d = V_{OCV} + c - I_d \cdot R_0 - I_d \cdot R_1(1 - e^{-\frac{t}{\tau_1}}) - I_d \cdot R_2(1 - e^{-\frac{t}{\tau_2}}) \tag{3.20}$$

Discharge Relaxation

$$V_{dr} = V_{OCV} + c - I_d \cdot R_1 \cdot (1 - e^{-\frac{T_d}{\tau_{1d}}}) \cdot e^{-\frac{t}{\tau_1}} - I_d \cdot R_2 \cdot (1 - e^{-\frac{T_d}{\tau_{2d}}}) \cdot e^{-\frac{t}{\tau_2}} \tag{3.21}$$

Charge Pulse

$$\begin{aligned} V_c = V_{OCV} + c + I_c \cdot R_0 + I_c R_1 \left(1 - e^{-\frac{t}{\tau_1}}\right) - I_d R_1 (1 - e^{-\frac{T_d}{\tau_{1d}}}) \cdot e^{-\frac{T_{dr}}{\tau_{1dr}}} \cdot e^{-\frac{t}{\tau_1}} \\ + I_c R_2 \left(1 - e^{-\frac{t}{\tau_2}}\right) - I_d R_2 (1 - e^{-\frac{T_d}{\tau_{2d}}}) \cdot e^{-\frac{T_{dr}}{\tau_{2dr}}} \cdot e^{-\frac{t}{\tau_2}} \end{aligned} \tag{3.22}$$

Charge Relaxation

$$\begin{aligned} V_{cr} = V_{OCV} + c + \left[I_c \cdot R_1 \cdot (1 - e^{-\frac{T_c}{\tau_{1c}}}) - I_d R_1 (1 - e^{-\frac{T_d}{\tau_{1d}}}) \cdot e^{-\frac{T_{dr}}{\tau_{1dr}}} \cdot e^{-\frac{T_c}{\tau_{1c}}} \right] \cdot e^{-\frac{t}{\tau_1}} \\ + \left[I_c \cdot R_2 \cdot (1 - e^{-\frac{T_c}{\tau_{2c}}}) - I_d R_2 (1 - e^{-\frac{T_d}{\tau_{2d}}}) \cdot e^{-\frac{T_{dr}}{\tau_{2dr}}} \cdot e^{-\frac{T_c}{\tau_{2c}}} \right] \cdot e^{-\frac{t}{\tau_2}} \end{aligned} \tag{3.23}$$

This approach allows to immediately identify the goodness of the fit between the original and interpolated data.

Script 3.7: Time Response Fit Plotting Matlab Script

```
% Plot voltage different phases
figure;
hold on;
plota=plot(Data.('Time (s)'), Data.('Voltage (V)') ,'-b', 'LineWidth', 2, 'DisplayName', 'All');
for j=1:numSteps
    % Verification plot Discharge
    plotd=plot(DischargeArray{j}.('Time (s)'), DischargeArray{j}.('Voltage (V)') ,'-r', 'LineWidth', 2);
    Vocv=OCVdata.OCV(j);
    R0temp=R0data.R0Discharge(j);
    Id=abs(Data.('Current (A)')(ends(1+(j-1)*3)+1));
    R1temp=R1data.R1Discharge(j);
    R2temp=R2data.R2Discharge(j);
    t=DischargeArray{j}.('Time (s)')-DischargeArray{j}.('Time (s)')(1);
    tau1temp=tau1data.tau1Discharge(j);
    tau2temp=tau2data.tau2Discharge(j);
    ctemp=cdata.cDischarge(j);
    EstimatedVoltage = Vocv+ctemp-R0temp.*Id-R1temp.*Id.*(1-exp(-t./tau1temp))-R2temp.*Id.*(1-exp(-t./tau2temp));
    Vplot=plot(DischargeArray{j}.('Time (s)'), EstimatedVoltage, '--k', 'LineWidth', 2);
    % Verification plot Discharge Relaxation
    plotdr=plot(DischargeRelaxationArray{j}.('Time (s)'), DischargeRelaxationArray{j}.('Voltage (V)') ,'-g', 'LineWidth', 2);
    Vocv=interp1(OCVdata.SOC, OCVdata.OCV, DischargeRelaxationArray{j}.SOC(1), 'linear', 'extrap');
    Id=abs(Data.('Current (A)')(ends(1+(j-1)*3)+1));
    R1temp=R1data.R1DischargeRelaxation(j);
    R2temp=R2data.R2DischargeRelaxation(j);
    t=DischargeRelaxationArray{j}.('Time (s)')-DischargeRelaxationArray{j}.('Time (s)')(1);
    Td=DischargeArray{j}.('Time (s)')(end)-DischargeArray{j}.('Time (s)')(1);
    tau1temp=tau1data.tau1DischargeRelaxation(j);
    tau1prev=tau1data.tau1Discharge(j);
    tau2temp=tau2data.tau2DischargeRelaxation(j);
    tau2prev=tau2data.tau2Discharge(j);
    ctemp=cdata.cDischargeRelaxation(j);
    EstimatedVoltage = Vocv+ctemp-R1temp.*Id.*(1-exp(-Td/tau1prev)).*exp(-t./tau1temp)-R2temp.*Id.*(1-exp(-Td/tau2prev)).*exp(-t./tau2temp);
    plot(DischargeRelaxationArray{j}.('Time (s)'), EstimatedVoltage, '--k', 'LineWidth', 2);
    % Verification plot Charge
    plotc=plot(ChargeArray{j}.('Time (s)'), ChargeArray{j}.('Voltage (V)') ,'-c', 'LineWidth', 2);
```

```
    Vocv=interp1(OCVdata.SOC, OCVdata.OCV, ChargeArray{j}.SOC(1), 'linear', 'extrap');
    R0temp=R0data.R0Charge(j);
    Ic=abs(Data.('Current (A)')(ends(2+(j-1)*3)+1));
    R1temp=R1data.R1Charge(j);
    R2temp=R2data.R2Charge(j);
    t=ChargeArray{j}.('Time (s)')-ChargeArray{j}.('Time (s)')(1);
    tau1temp=tau1data.tau1Charge(j);
    tau2temp=tau2data.tau2Charge(j);
    V1temp=V1data.V1Charge(j);
    V2temp=V2data.V2Charge(j);
    ctemp=cdata.cCharge(j);
    EstimatedVoltage = Vocv+ctemp+R0temp.*Ic+R1temp.*Ic.*(1-exp(-t./tau1temp))+R2temp.*
        Ic.*(1-exp(-t./tau2temp))-V1temp.*exp(-t/tau1temp)-V2temp.*exp(-t/tau2temp);
    plot(ChargeArray{j}.('Time (s)'), EstimatedVoltage, '--k', 'LineWidth', 2);
    % Verification plot Charge Relaxation
    plotcr=plot(ChargeRelaxationArray{j}.('Time (s)'), ChargeRelaxationArray{j}.('
        Voltage (V)') ,'-m', 'LineWidth', 2);
    Vocv=interp1(OCVdata.SOC, OCVdata.OCV, ChargeRelaxationArray{j}.SOC(1), 'linear', '
        extrap');
    Ic=abs(Data.('Current (A)')(ends(2+(j-1)*3)+1));
    R1temp=R1data.R1ChargeRelaxation(j);
    R2temp=R2data.R2ChargeRelaxation(j);
    t=ChargeRelaxationArray{j}.('Time (s)')-ChargeRelaxationArray{j}.('Time (s)')(1);
    Tc=ChargeArray{j}.('Time (s)')(end)-ChargeArray{j}.('Time (s)')(1);
    tau1temp=tau1data.tau1ChargeRelaxation(j);
    tau1prev=tau1data.tau1Charge(j);
    tau2temp=tau2data.tau2ChargeRelaxation(j);
    tau2prev=tau2data.tau2Charge(j);
    V1temp=V1data.V1Charge(j);
    V2temp=V2data.V2Charge(j);
    ctemp=cdata.cChargeRelaxation(j);
    EstimatedVoltage = Vocv+ctemp+R1temp.*Ic.*(1-exp(-Tc/tau1prev)).*exp(-t./tau1temp)-
        V1temp.*exp(-Tc./tau1prev).*exp(-t./tau1temp)+R2temp.*Ic.*(1-exp(-Tc/tau2prev))
        .*exp(-t./tau2temp)-V2temp.*exp(-Tc./tau2prev).*exp(-t./tau2temp);
    plot(ChargeRelaxationArray{j}.('Time (s)'), EstimatedVoltage, '--k', 'LineWidth',2);
end
hold off;
xlabel('Time (s)');
ylabel('Voltage (V)');
title(['Voltage vs Time - Test',fields{i}], 'Interpreter','none');
legend([plota, plotd, plotdr, plotc, plotcr, Vplot], {'All','Discharge','Discharge
    Relaxation','Charge','Charge Relaxation','Interpolated Data'}, 'location', 'best')
grid on;
set(gcf,'Color','white');
end
```

The values obtained performing the parameter extraction are in Figures 3.11 - 3.15:

- R0 is quite constant across the entire SOC range, and increases only at very low SOC values (Figure 3.11). There is a good match ($\approx 0,1\times$ difference) between values extracted during discharge, discharge relaxation, charge and charge relaxation
- R1 is also quite constant and increasing only at low SOC (Figure 3.12). The error between the different fitting strategies is slightly larger ($\approx 1\times$ difference)
- C1 is quite uniform across the entire SOC range (Figure 3.13). Values obtained using the different methodologies are quite similar ($\approx 1\times$ difference)
- R2 also behaves similarly to the other resistive terms (Figure 3.14), but the error between the different values is much larger ($\approx 10\times$ difference)
- C2 is also quite constant on the entire SOC range (Figure 3.15), with the different values quite closely matched together ($\approx 1\times$ difference)

Table 3.2 summarizes the results obtained for the parameters of the ECM of Molicel P45B Li-ion battery cell at 30°C ambient temperature.

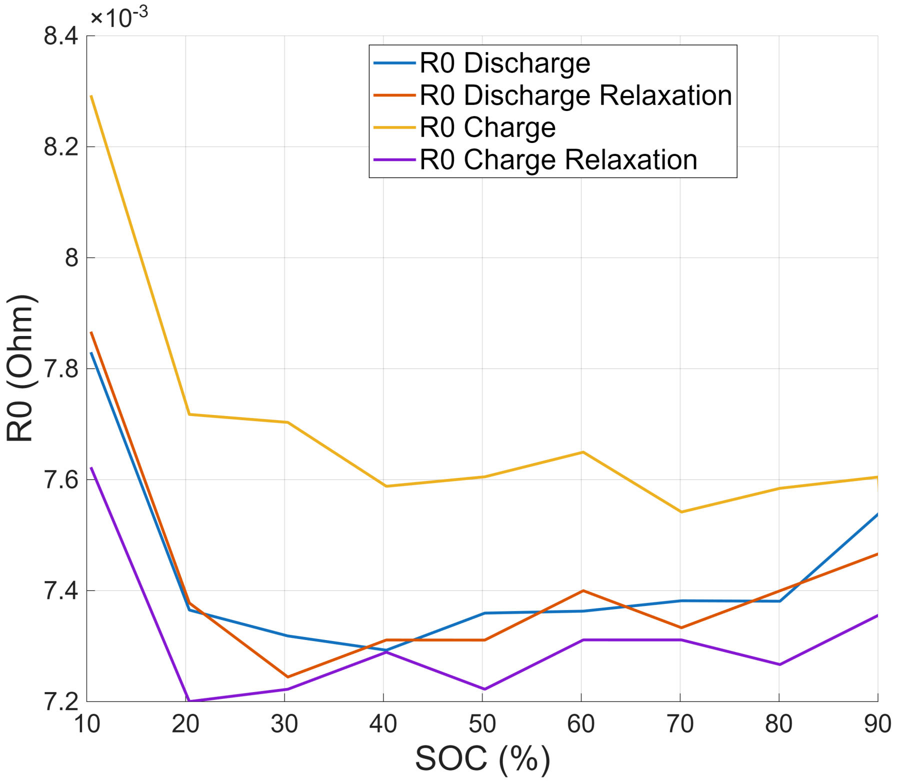

Figure 3.11: R0 vs. SOC

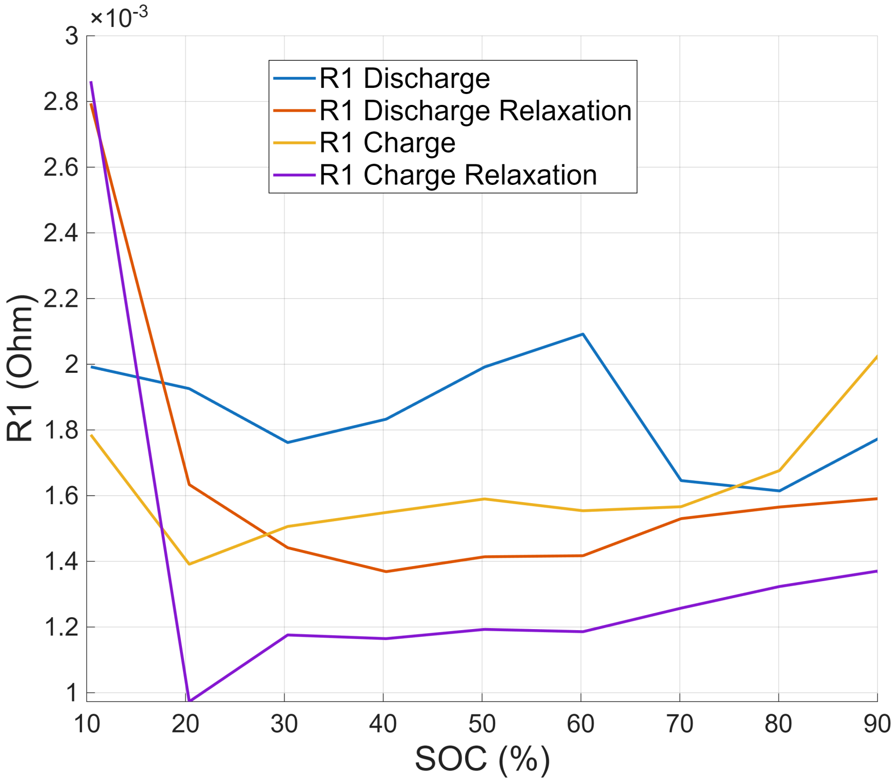

Figure 3.12: R1 vs. SOC

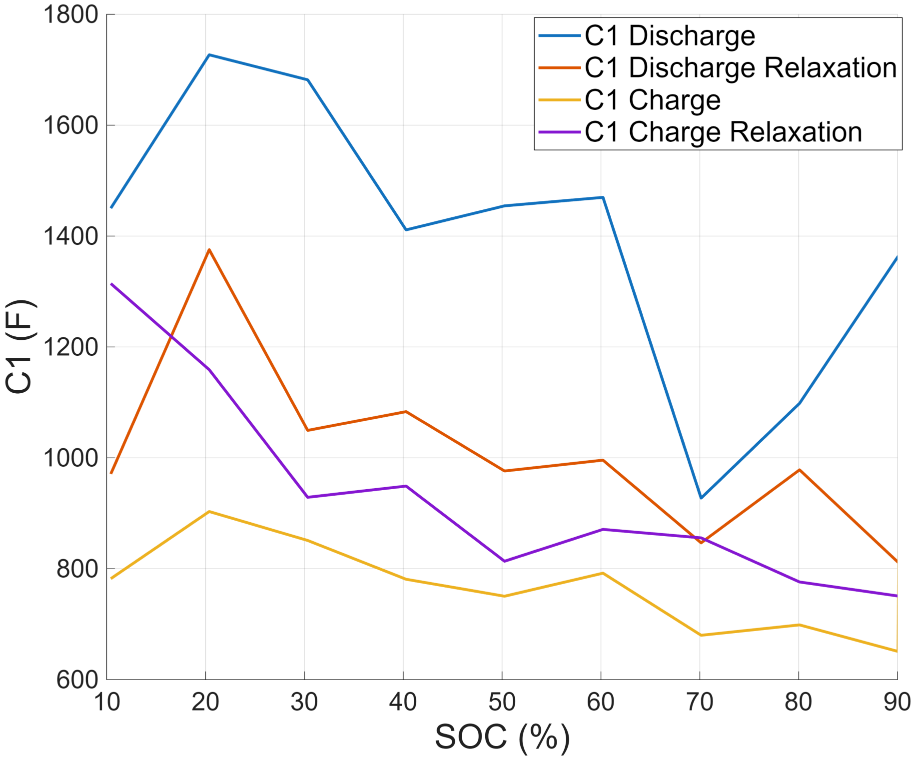

Figure 3.13: C1 vs. SOC

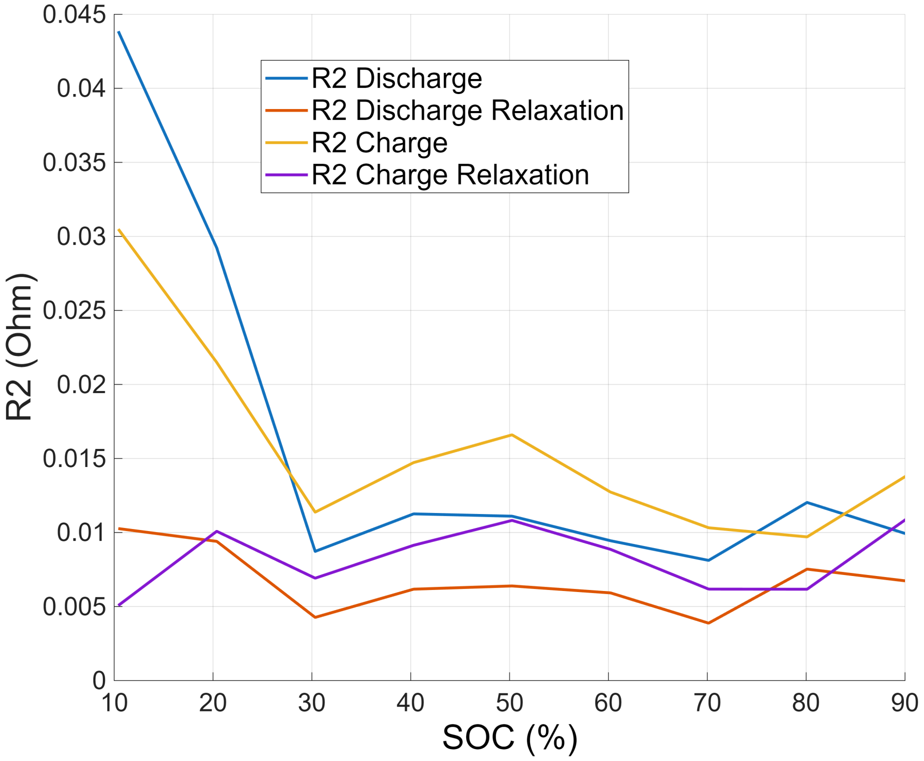

Figure 3.14: R2 vs. SOC

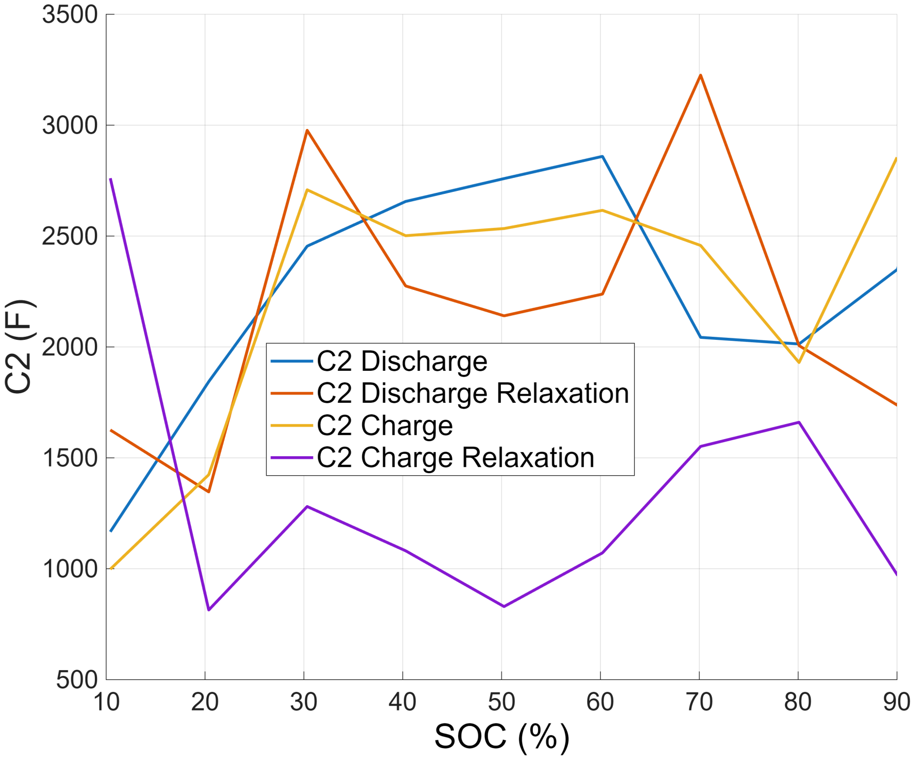

Figure 3.15: C2 vs. SOC

Table 3.2: HPPC Paramaters - Manual script results (fittype)

SOC	**90%**	**80%**	**70%**	**60%**	**50%**	**40%**	**30%**	**20%**	**10%**
OCV (V)	4,05	3,96	3,87	3,79	3,72	3,63	3,53	3,46	3,29
R0 D (mΩ)	7,54	7,38	7,38	7,36	7,36	7,29	7,32	7,37	7,83
R0 DR (mΩ)	7,47	7,4	7,33	7,4	7,31	7,31	7,24	7,38	7,87
R0 DA (mΩ)	7,5	7,39	7,36	7,38	7,34	7,3	7,28	7,37	7,85
R0 C (mΩ)	7,6	7,58	7,54	7,65	7,61	7,59	7,7	7,72	8,29
R0 CR (mΩ)	7,36	7,27	7,31	7,31	7,22	7,29	7,22	7,2	7,62
R0 CA (mΩ)	7,48	7,43	7,43	7,48	7,41	7,44	7,46	7,46	7,96
R1 D (mΩ)	1,77	1,61	1,65	2,09	1,99	1,83	1,76	1,93	1,99
R1 DR (mΩ)	1,59	1,57	1,53	1,42	1,41	1,37	1,44	1,63	2,79
R1 DA (mΩ)	1,68	1,59	1,59	1,75	1,7	1,6	1,6	1,78	2,39
R1 C (mΩ)	2,03	1,68	1,57	1,55	1,59	1,55	1,51	1,39	1,79
R1 CR (mΩ)	1,37	1,32	1,26	1,19	1,19	1,16	1,18	0,973	2,86
R1 CA (mΩ)	1,7	1,5	1,41	1,37	1,39	1,36	1,34	1,18	2,32
C1 D (F)	1360	1100	927	1470	1450	1410	1680	1730	1450
C1 DR (F)	812	978	847	996	976	1080	1050	1380	971
C1 DA (F)	1090	1040	887	1230	1220	1250	1370	1550	1210
C1 C (F)	651	699	680	792	751	781	851	903	782
C1 CR (F)	751	776	856	871	814	949	929	1160	1310
C1 CA (F)	701	737	768	832	782	865	890	1030	1050
R2 D (mΩ)	9,93	12	8,12	9,45	11,1	11,3	8,73	29,2	43,9
R2 DR (mΩ)	6,73	7,53	3,88	5,92	6,39	6,17	4,27	9,4	10,3
R2 DA (mΩ)	8,33	9,78	6	7,68	8,75	8,72	6,5	19,3	27,1
R2 C (mΩ)	13,8	9,7	10,3	12,7	16,6	14,7	11,4	21,5	30,5
R2 CR (mΩ)	10,9	6,17	6,18	8,86	10,8	9,14	6,92	10,1	5,07
R2 CA (mΩ)	12,3	7,94	8,25	10,8	13,7	11,9	9,15	15,8	17,8
C2 D (F)	2350	2010	2040	2860	2760	2660	2450	1840	1170
C2 DR (F)	1740	2010	3230	2240	2140	2280	2980	1350	1630
C2 DA (F)	2040	2010	2630	2550	2450	2470	2720	1600	1400
C2 C (F)	2860	1930	2460	2620	2530	2500	2710	1420	998
C2 CR (F)	970	1660	1550	1070	830	1080	1280	810	2760
C2 CA (F)	1920	1800	2010	1840	1680	1790	2000	1120	1880

Legend: **D**: Discharge; **C**: Charge; **DR**: Discharge Relaxation; **CR**: Charge Relaxation; **DA**: Discharge Average; **CA**: Charge Average

3.3 Results Validation

The results have been validated using an HPPC parameter estimation automated workflow [67] (Figure 3.16) available on Matlab's Simscape Battery extension since Matlab R2025a. It allows to automatically identify the HPPC pulse steps and extract the ECM parameters starting from the test data. The workflow is based on the *HPPCTest Object*, that imports raw test data (time, voltage, current, temperature, SOC) and automatically identifies, isolates, and tabulates the individual charge and discharge pulses. The advantage of this approach is, other that the extremely simple coding required, is the possibility to group multiple datasets (measured at different temperatures or current rates) in a single *HPPCTestSuite Object*, making data analysis and comparison much easier. The suite includes a set of useful commands for managing the test data, analyzing it, simulating it for validation and plotting the results. The package allows the selection of the circuit topology for the ECM and the fitting method. In this case, a second order (2RC) Thevenin circuit has obviously been chosen, and two different fitting methods have been tested (fminsearch and curvefit). The code is presented in Script 3.8.

Script 3.8: Automated Parameter Estimation Matlab Script

```
% Automated Parameter Estimation Workflow
% Input data preparation
hppcDataInput = Data(:, ["Time (s)", "Voltage (V)", "Current (A)"]);

% Using Matlab Integrated HPPC Tool (only from R2025)
hppcResult = hppcTest(hppcDataInput,...
    TimeVariable="Time (s)", ...
    VoltageVariable="Voltage (V)", ...
    CurrentVariable="Current (A)", ...
    TemperatureVariable="Temperature (C)", ...
    StateofChargeVariable="SOC", ...
    Capacity=DataNEWARE.(strcat(fields{i},'_NEWARE_xlsx')).('Pilot discharge capacity (
        Ah)')(1), ...
    InitialSOC=1);

% Remove Unwanted Pulses at SOC=1
removePulse(hppcResult,11);
removePulse(hppcResult,1);

% Save in Struct
HPPCAuto.(fields{i})=hppcResult;

% Display Summary
```

```
disp(hppcResult.TestSummary)

% Fit parameters
batteryEcmFM = fitECM(hppcResult, SegmentToFit="loadAndRelaxation", FittingMethod="
    fminsearch");
batteryEcmCF = fitECM(hppcResult, SegmentToFit="loadAndRelaxation", FittingMethod="
    curvefit");

% Display parameters
fprintf('Results auto method (fminsearch):');
disp(batteryEcmFM.ModelParameterTables);
fprintf('Results auto method (curvefit):');
disp(batteryEcmCF.ModelParameterTables);
```

The ECM parameters resulting from the automated approach, that have been used for the validation of the manually interpolated results, are shown in Figures 3.17 - 3.22. Comparing the results, one can see how the values obtained by the manual and automated scripts are of the same magnitude and generally quite close. One only remark is that, for reasons that have not been investigated, the automated approach provides values of R_0, R_1 and C_1 that are quite different from the others at 60 and 70% SOC (this seems unconsistent with all the other estimates, that are closely packed together).

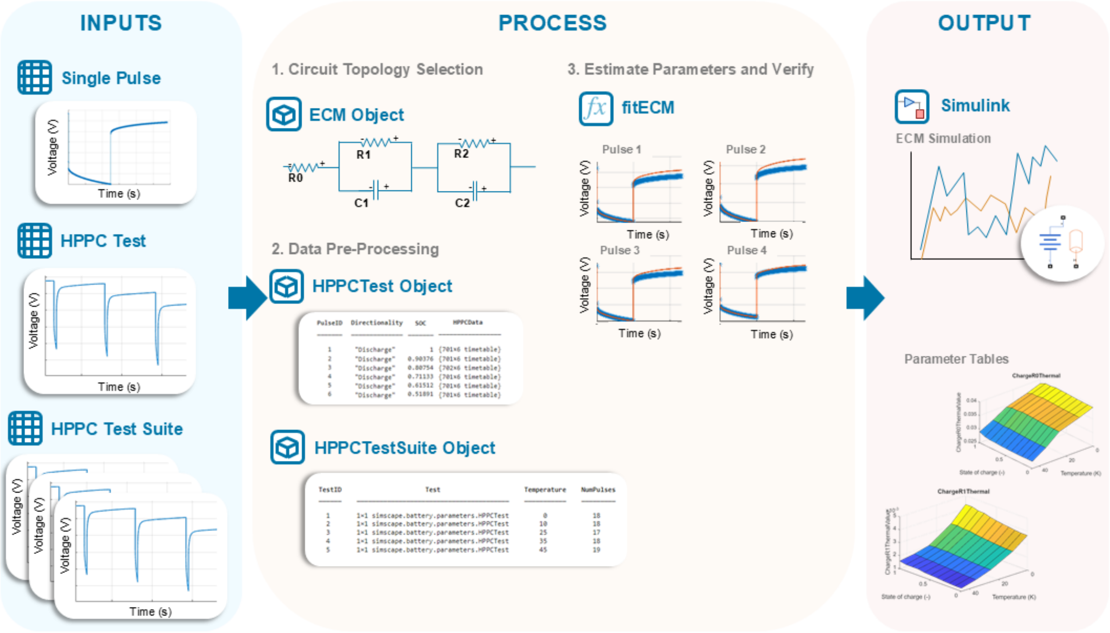

```
PulseID  Directionality    SOC       HPPCData
_______  ______________  _______  __________________

   1      "Discharge"          1  {701×6 timetable}
   2      "Discharge"    0.90376  {701×6 timetable}
   3      "Discharge"    0.80754  {702×6 timetable}
   4      "Discharge"    0.71133  {701×6 timetable}
   5      "Discharge"    0.61512  {701×6 timetable}
   6      "Discharge"    0.51891  {701×6 timetable}
```

```
TestID                  Test                     Temperature  NumPulses
______  _____________________________________  ___________  _________

  1     1×1 simscape.battery.parameters.HPPCTest        0          18
  2     1×1 simscape.battery.parameters.HPPCTest       10          18
  3     1×1 simscape.battery.parameters.HPPCTest       25          17
  4     1×1 simscape.battery.parameters.HPPCTest       35          18
  5     1×1 simscape.battery.parameters.HPPCTest       45          19
```

Figure 3.16: HPPC battery parameter estimation workflow [67]

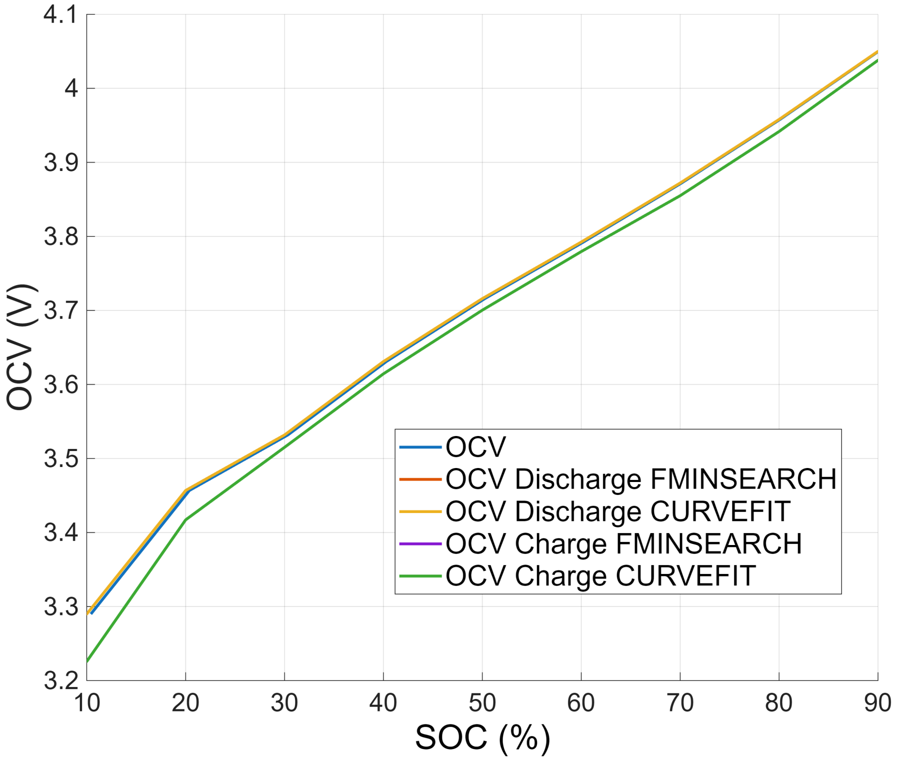

Figure 3.17: OCV vs. SOC Validation

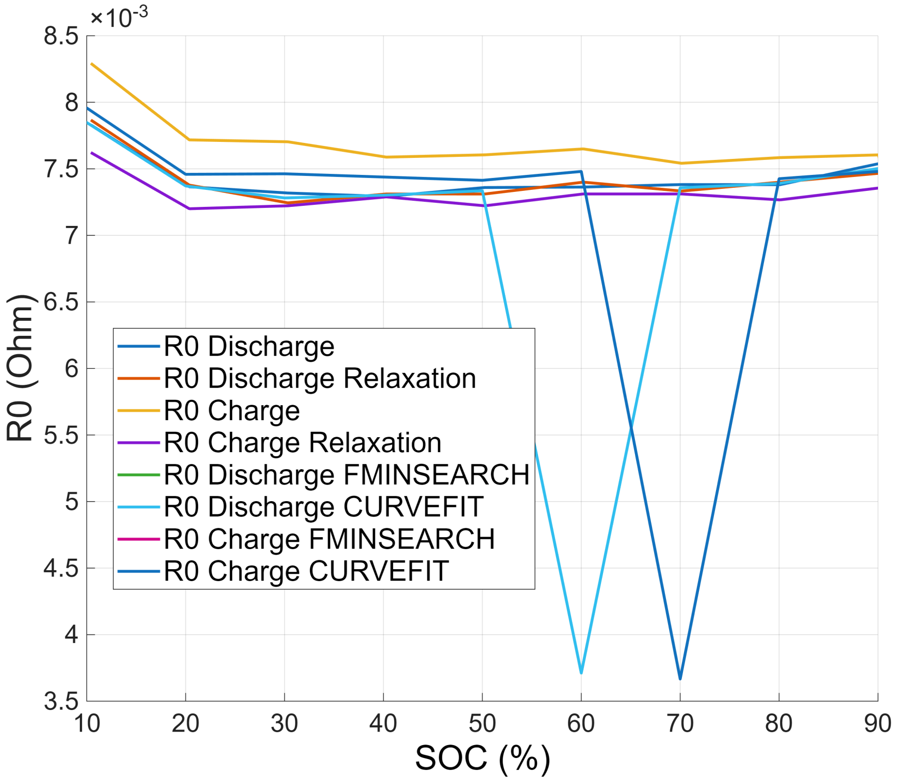

Figure 3.18: R0 vs. SOC Validation

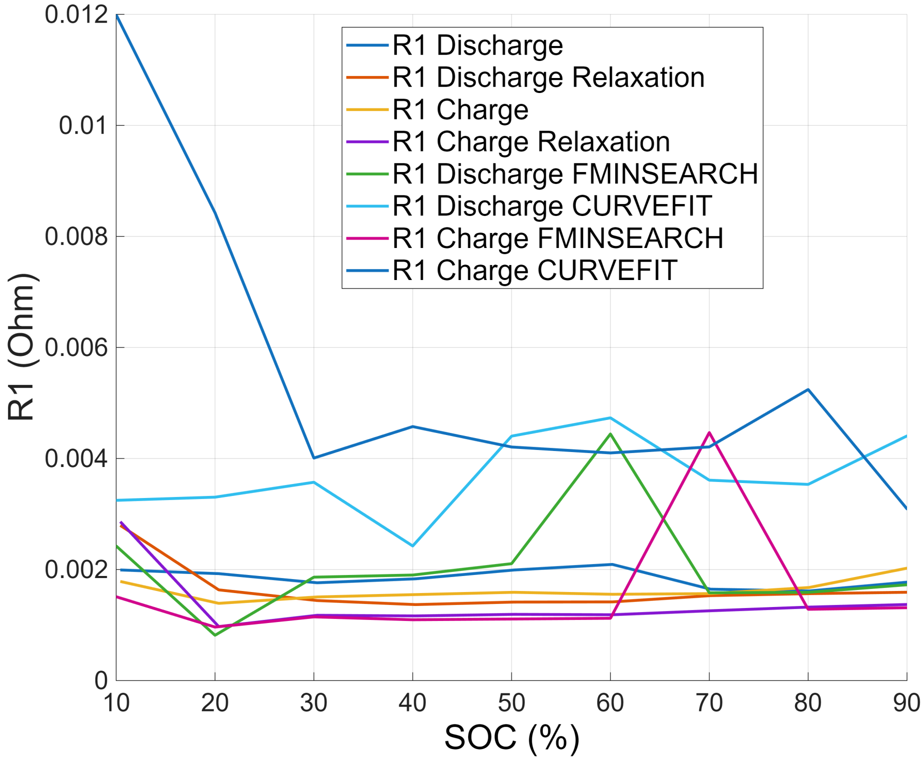

Figure 3.19: R1 vs. SOC Validation

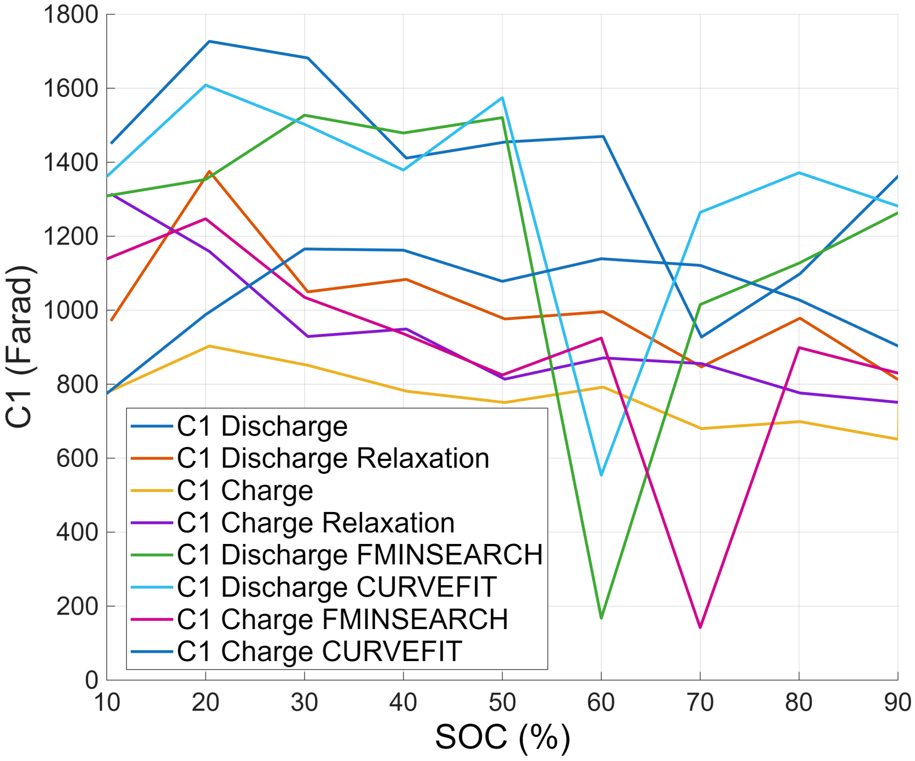

Figure 3.20: C1 vs. SOC Validation

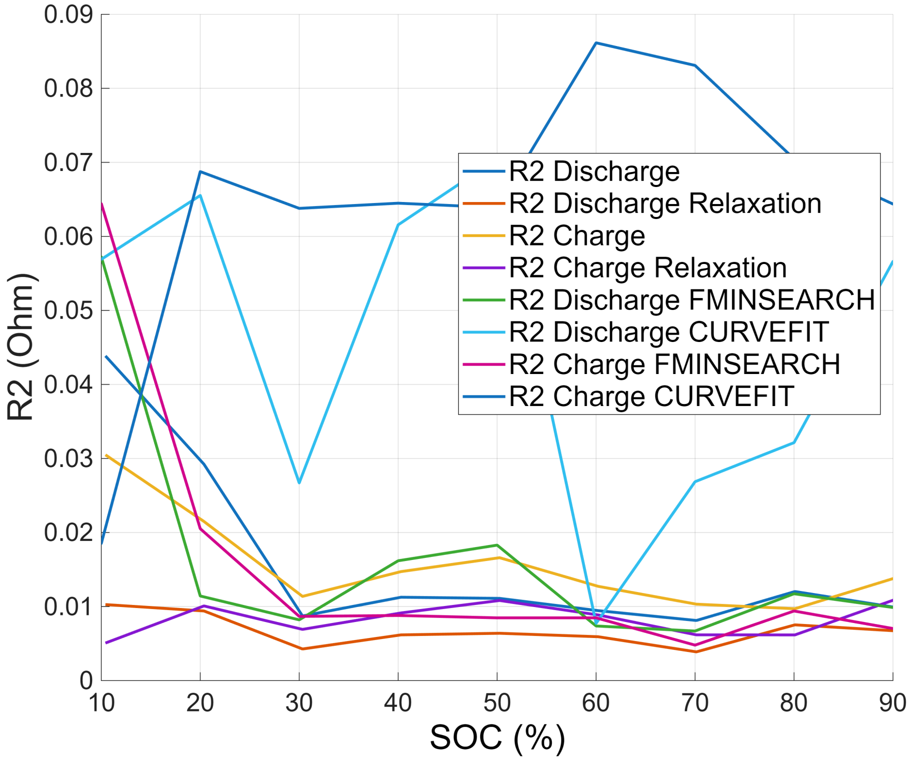

Figure 3.21: R2 vs. SOC Validation

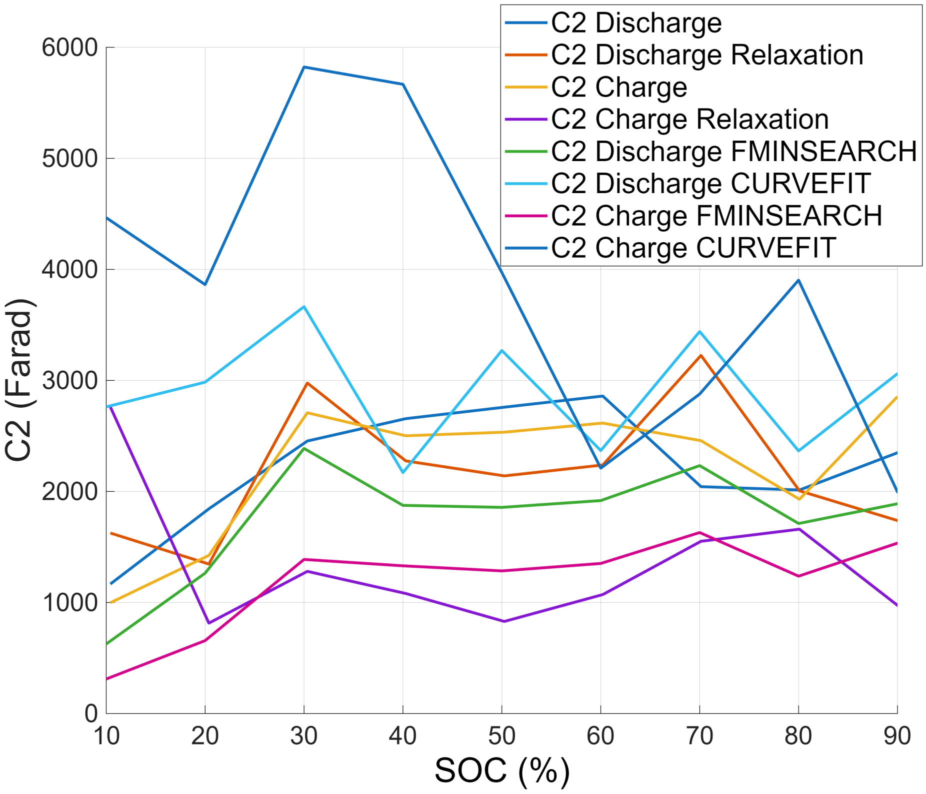

Figure 3.22: C2 vs. SOC Validation

Table 3.3: HPPC Parameters - Automated script results (fminsearch)

SOC	**90%**	**80%**	**70%**	**60%**	**50%**	**40%**	**30%**	**20%**	**10%**
OCV D (V)	4,05	3,96	3,87	3,79	3,72	3,63	3,53	3,46	3,29
OCV C (V)	4,04	3,94	3,85	3,78	3,7	3,61	3,52	3,42	3,23
R0 D (mΩ)	7,5	7,39	7,36	3,71	7,34	7,3	7,28	7,37	7,85
R0 C (mΩ)	7,48	7,43	3,67	7,48	7,41	7,44	7,46	7,46	7,96
R1 D (mΩ)	1,73	1,59	1,58	4,44	2,11	1,9	1,86	0,816	2,42
R1 C (mΩ)	1,31	1,28	4,47	1,12	1,11	1,1	1,15	0,964	1,51
C1 D (F)	1260	1130	1020	167	1520	1480	1530	1350	1310
C1 C (F)	830	899	142	925	825	936	1030	1250	1140
R2 D (mΩ)	9,87	11,7	6,69	7,37	18,3	16,2	8,2	11,4	57,2
R2 C (mΩ)	7,03	9,4	4,79	8,47	8,47	8,79	8,67	20,5	64,4
C2 D (F)	1890	1710	2230	1920	1860	1880	2390	1260	627
C2 C (F)	1540	1240	1630	1350	1280	1330	1390	657	311

Legend: **D**: Discharge; **C**: Charge

Table 3.4: HPPC Parameters - Automated script results (curvefit)

SOC	**90%**	**80%**	**70%**	**60%**	**50%**	**40%**	**30%**	**20%**	**10%**
OCV D (V)	4.05	3.96	3.87	3.79	3.72	3.63	3.53	3.46	3.29
OCV C (V)	4.04	3.94	3.85	3.78	3.7	3.61	3.52	3.42	3.23
R0 D (mΩ)	7.5	7.39	7.36	3.71	7.34	7.3	7.28	7.37	7.85
R0 C (mΩ)	7.48	7.43	3.67	7.48	7.41	7.44	7.46	7.46	7.96
R1 D (mΩ)	4.41	3.53	3.61	4.73	4.4	2.42	3.57	3.3	3.25
R1 C (mΩ)	3.09	5.24	4.21	4.1	4.21	4.57	4.01	8.43	12
C1 D (F)	1280	1370	1260	554	1570	1380	1500	1610	1360
C1 C (F)	903	1030	1120	1140	1080	1160	1170	988	775
R2 D (mΩ)	56.6	32.1	26.9	7.73	70.5	61.6	26.7	65.5	56.9
R2 C (mΩ)	64.4	70.5	83.1	86.1	63.9	64.5	63.8	68.8	18.5
C2 D (F)	3060	2370	3440	2370	3270	2170	3660	2980	2760
C2 C (F)	2000	3900	2880	2210	3970	5670	5820	3860	4470

Legend: **D**: Discharge; **C**: Charge

The HPPC Test suite also includes tools for plotting the time response of the automatically fitted parameters to the used test profile, that are summarized in Script 3.9. Figures 3.24 and 3.25 show the measured and simulated voltage response for the different pulses obtained with the command `plot(batteryEcm)`. Figure 3.23 shows the measured and simulated full HPPC test (the fminsearch fitting method has been chosen) obtained with the command `simulateHPPCTest(batteryEcm,hppcResult)`. One can notice how the quality of the fitting of this automated approach is actually quite poor. Thus, the automated approach is not going to be further investigated.

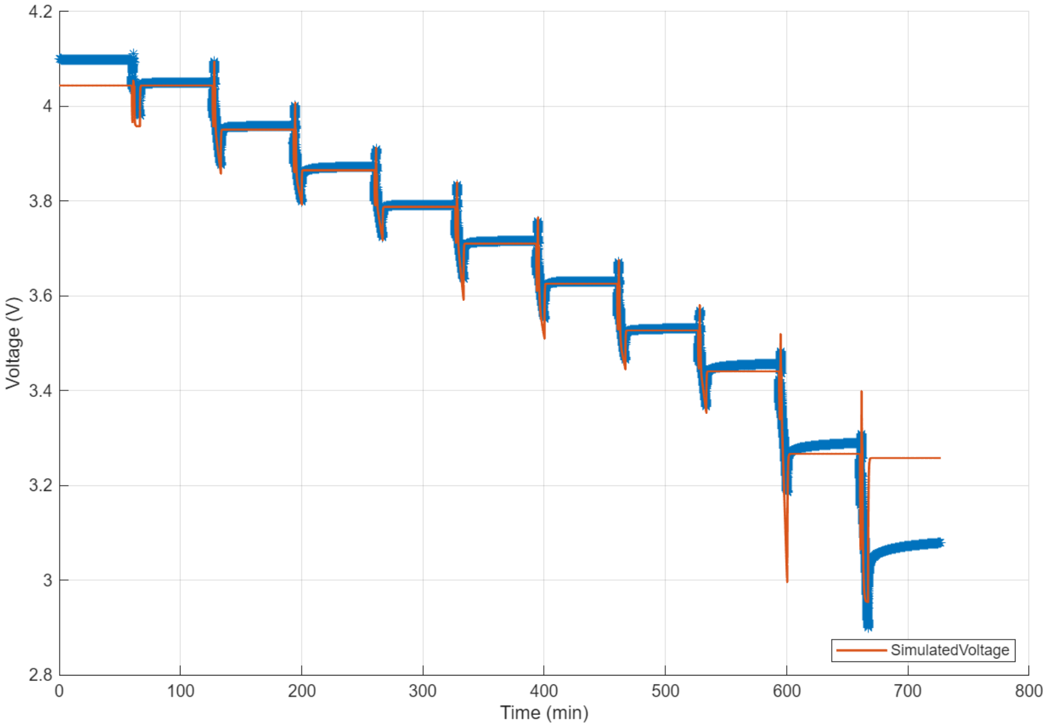

Figure 3.23: Voltage vs. Time - HPPC test simulation result

Script 3.9: Automated Parameter Results Plotting Matlab Script

```
% Automated Parameter Estimation Workflow Results Plotting
% Plot test and identified test points
plot(hppcResult);

% Plot HPPC pulse fit
plot(batteryEcmFM,1:18);
plot(batteryEcmCF,1:18);

% Plot HPPC test simulation
simulateHPPCTest(batteryEcmFM,hppcResult);
simulateHPPCTest(batteryEcmFM,hppcResult);
```

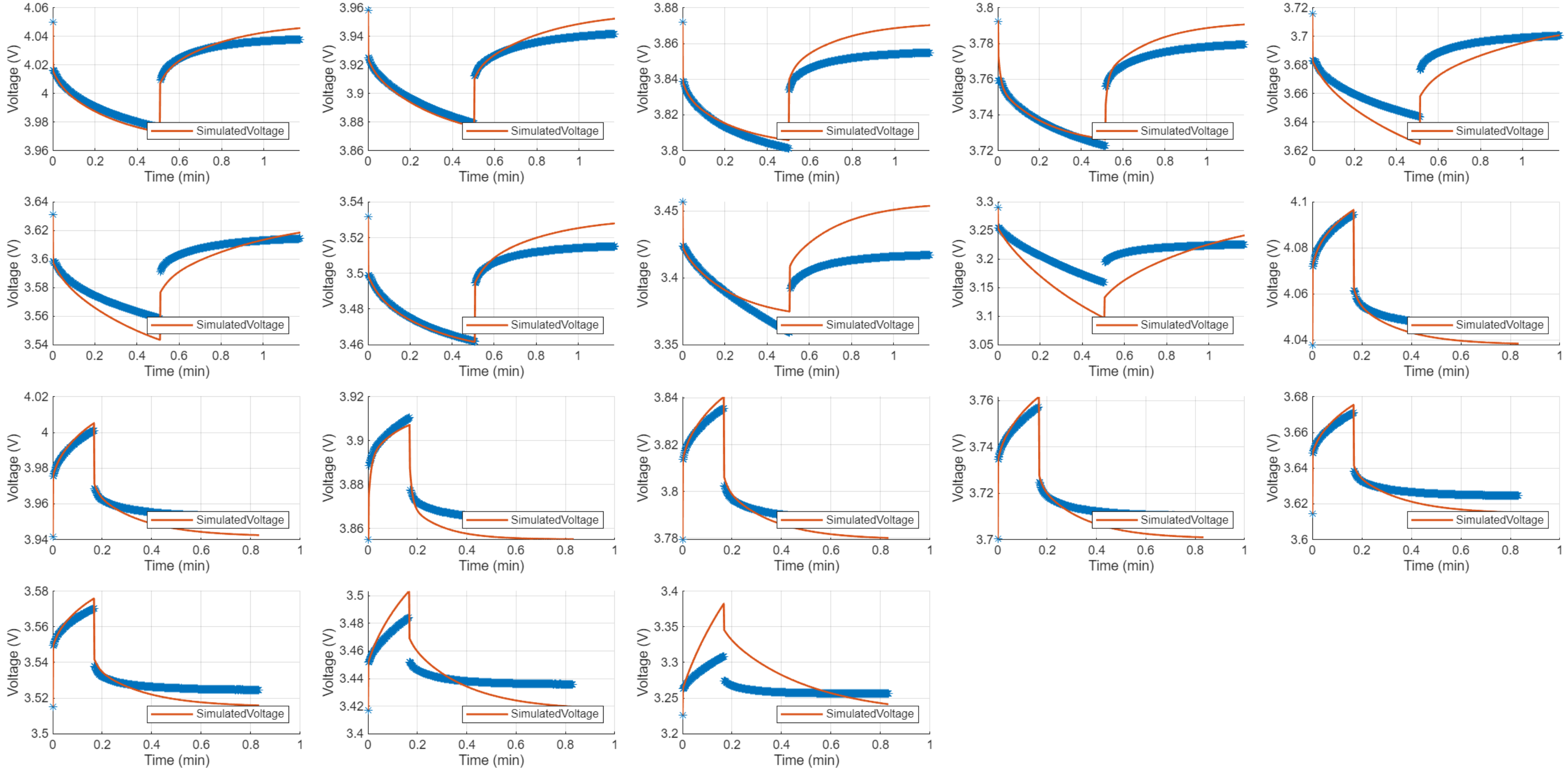

Figure 3.24: Voltage vs. Time - HPPC pulse fit - FMINSEARCH

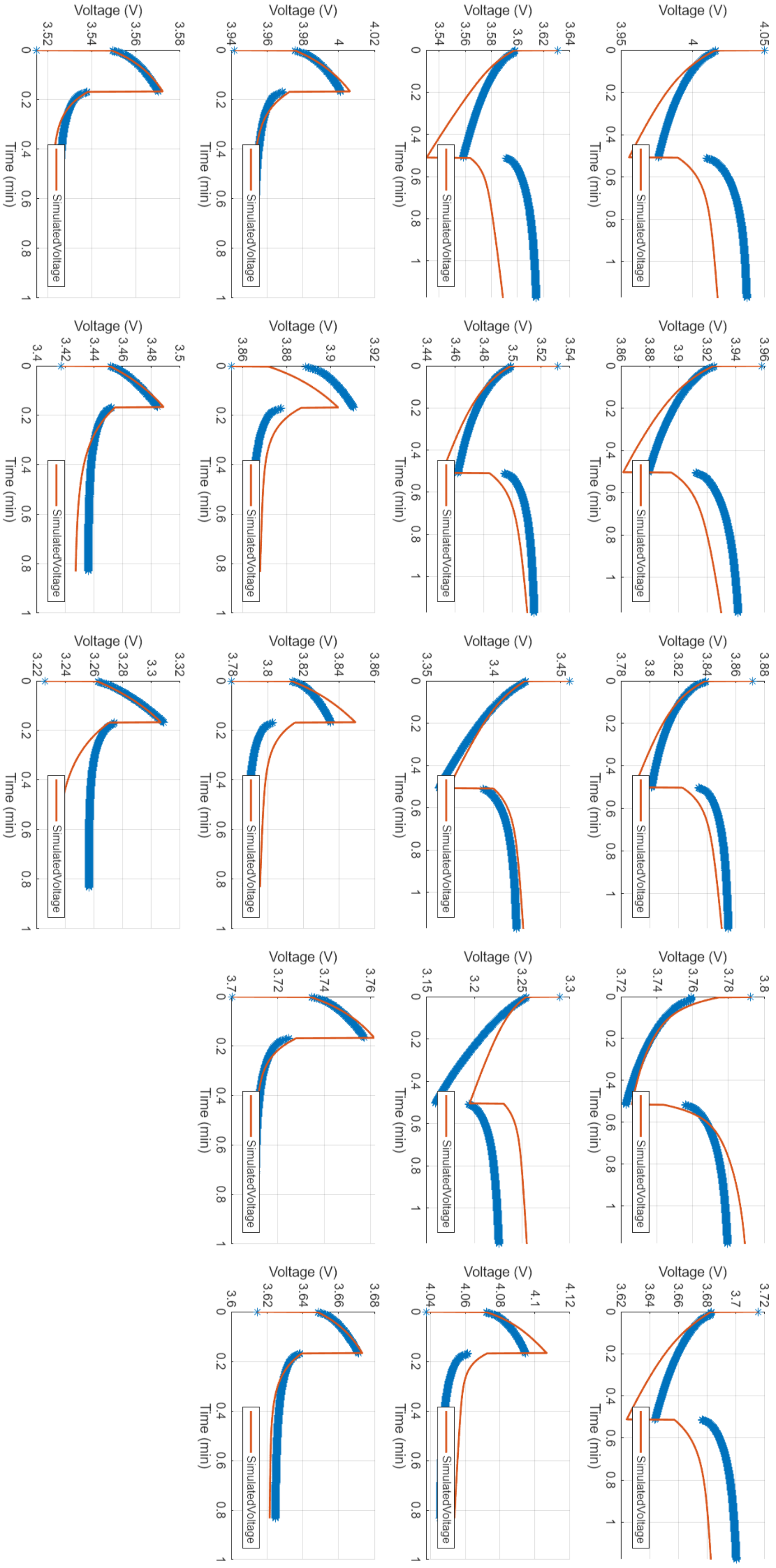

Figure 3.25: Voltage vs. Time - HPPC pulse fit - CURVEFIT

4

Thermal Characterization Approach and Results

This chapter focuses on the thermal characterization of Li-ion cells. It shows the testing results and describes the methodology that has been followed for the extraction of the thermal equivalent circuit parameters that will be used for deriving the thermal model of the battery cell.

4.1 Constant Current Discharge Results

Constant current discharge testing methodology has been introduced in Section 2.2.1. This testing approach, being characterized by uniform (and slow, especially al low C-rates) events, allows one to better characterize and extract thermal parameters. In fact, electrical and thermal phenomena typically have distinct time constants:

- the electrical time constant is dictated by the movement of electrons and lithium ions across the electrode/electrolyte interface. Thus, electrical time constants in a lithium-ion cell typically range from microseconds to seconds
- the thermal time constant is dictated by the physical vibration of atoms within the battery cell body, that is massive if compared to the electrons scale. So, thermal time constants in battery cells typically range from minutes to hours

For this reason, constant current tests are ideal for identification of thermal parameters, while fast current pulses are not.

Figure 4.1 shows the surface temperature profile measured during constant current discharge at different C-rates.

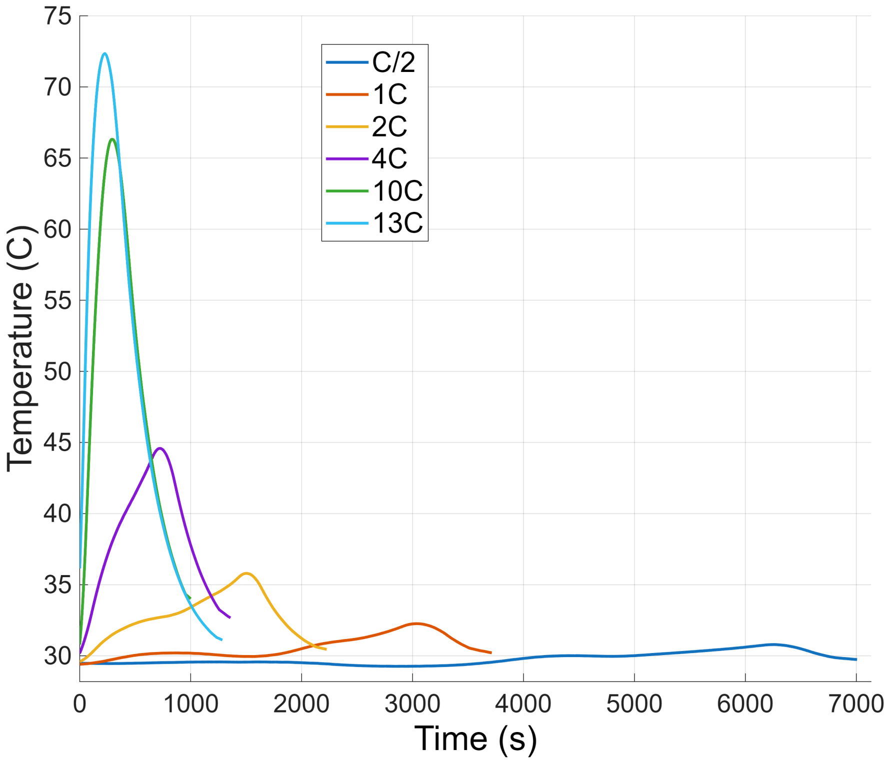

Figure 4.1: Temperature vs. Time (different discharge current rates)

4.1.1 Heat Generation Rate

As introduced in Section 1.1.4.8, heat generation from a battery cell is given by

$$\begin{aligned}\dot{Q} &= \dot{Q}_{irr} + \dot{Q}_{rev} \\ &= I(V_{OC} - V) - IT\frac{dV_{OC}}{dT} \qquad \text{for } I > 0 \text{ during discharging} \\ &= I(V - V_{OC}) + IT\frac{dV_{OC}}{dT} \qquad \text{for } I > 0 \text{ during charging} \end{aligned} \tag{4.1}$$

where V is the cell voltage (V_{OC} the open circuit voltage), I the current and T the temperature.

The heat balance equation, already defined in Equation 1.34 and written by expliciting the heat flux exchanged with the surroundings $\dot{Q}_{out}$, is

$$C_{th}\frac{dT}{dt} = \dot{Q} - \dot{Q}_{out} \tag{4.2}$$

where $C_{th} = m \cdot c$ is the thermal capacity, m is the cell mass and c the specific heat capacity.

In the tests carried out, the heat measured by the heat flux sensor represents $\dot{Q}_{out}$. In particular, Figure 4.2 shows the heat flux density measurement $\dot{Q}''_{out}$ for different discharge current rates, while Table 4.1 shows the corresponding heat transfer over the cell total surface area $A_{tot} = \pi dL + 2\pi \left(\frac{d}{2}\right)^2$, that is $\dot{Q}_{out} = \dot{Q}''_{out} \cdot A_{tot}$, where $d = 21\ mm$ is the cell diameter and $L = 70\ mm$ the cell height.

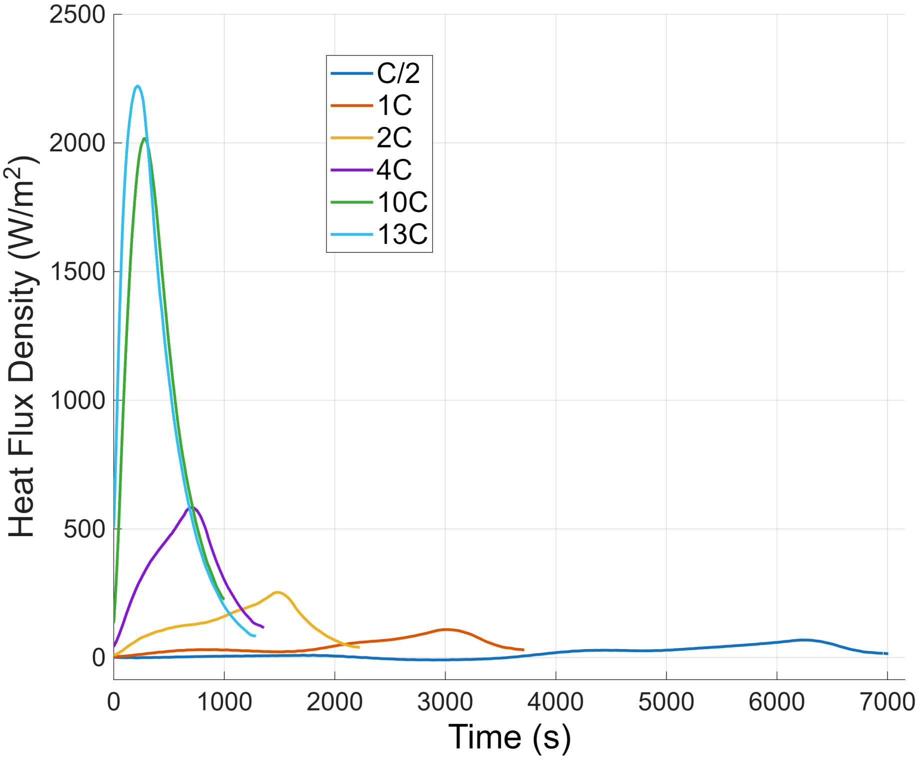

Figure 4.2: Heat Flux Density vs. Time (different discharge current rates)

4.1.2 Entropic Heat Coefficient (EHC) Estimation

The EHC has been extracted during the discharge phase. Since, as it can be seen in Equation 4.1, the irreversible heat scales with the square of the current while the reversible one is linear to it, the EHC can be derived with higher accuracy at low discharge currents (where the reversible heat is predominant). In this work, the lowest current rate available is C/2, but it is generally suggested to extrapolate it at lower current rates (i.e., C/10 or C/20) for higher accuracy.

Considering Equation 4.2, rearranging it expliciting the heat generation term in function of the others and combining it with Equation 4.1 one gets

$$\dot{Q} = C_{th}\frac{dT}{dt} + \dot{Q}_{out} = \dot{Q}_{irr} + \dot{Q}_{rev} \tag{4.3}$$

Table 4.1: Constant current discharge maximum heat flux values

C-rate	**Maximum Heat Flux Density** $\dot{Q}''_{out}$	**Maximum Heat Flux** $\dot{Q}_{out}$
C/2	72 W/m^2	0,38 W
1C	120 W/m^2	0,63 W
2C	250 W/m^2	1,4 W
4C	580 W/m^2	3,1 W
10C	1900 W/m^2	10 W
13C	2200 W/m^2	12 W

that yields

$$\dot{Q}_{rev} = C_{th}\frac{dT}{dt} + \dot{Q}_{out} - \dot{Q}_{irr} \tag{4.4}$$

where the irreversible (Joule) heat is determined as (for Neware $I > 0$ while charging)

$$\dot{Q}_{irr} = I \cdot (V - V_{OC}) \tag{4.5}$$

Note that the thermal capacity value C_{th} is the one obtained in Section 4.2.1, while the OCV is the one derived in Section 3.2.1.

Finally, the EHC can be retrieved by doing

$$\frac{dV_{OC}}{dT} = \frac{\dot{Q}_{rev}}{I \cdot T} \tag{4.6}$$

Script 4.1 shows the code written for performing the task. The EHC retrieved for the C/2 current rate discharge is plotted in Figure 4.3 and reported for clarity in Table 4.2, while Figure 4.4 represents the different heat components (total heat $\dot{Q}$, Joule heat $\dot{Q}_{irr}$ and entropic heat $\dot{Q}_{rev}$).

It is important to remind the meaning of the sign of the EHC:

- a positive EHC ($\frac{dV_{OC}}{dT} > 0$) indicates endothermic reversible heat generation during discharging ($\dot{Q}_{rev} < 0$), and exothermic during charging ($\dot{Q}_{rev} > 0$)
- a negative EHC ($\frac{dV_{OC}}{dT} < 0$) indicates exothermic reversible heat generation during discharging ($\dot{Q}_{rev} > 0$), and endothermic during charging ($\dot{Q}_{rev} < 0$)

In this example, the EHC is positive approximately in the 40-100% SOC range, and negative in the 0-20% one (apart from a small positive spike for SOC ranging between 0 and 5%).

For the sake of curiosity, the same data analysis has been performed at the 1C, 2C and 4C discharges (Figure 4.5). Even if for increasing current rate the noise on the final result should be higher, there looks to be a good correlation between the values obtained from the different discharge tests. Figure 4.6 shows how the diffferent heat contributions change for a higher current rate. As one can notice, while at C/2 the Joule and entropic heat have comparable magnitude, at 4C the Joule component is quite larger. This makes an accurate estimation of the EHC more difficult. For this reason, the C/2 values are the ones that are selected for the modelling phase.

Finally, it is important to point out the limits of this analysis:

- a precise calculation of the irreversible heat generation $\dot{Q}_{irr}$ relies on the accurate knowledge of the OCV. In this case, the OCV curve is the one derived during HPPC, and has a 10% SOC resolution. An OCV curve derived with a low current (i.e., C/20) would probably be more accurate
- additionally, as already discussed, the total heat flux $\dot{Q}$ has been measured during a C/2 discharge. Performing the measurement at low discharge currents would allow to better isolate the reversible (entropic) heat contribution
- finally, the estimation has been done only for a discharge process. The same could be done for charging, and the results may differ slightly due to hysteresis effects. The average of the two would provide a better estimate of the EHC

Table 4.2: EHC at different SOC values (discharge at C/2)

SOC	**EHC Value**
0%	0,25 mV/K
10%	-0,13 mV/K
20%	-0,085 mV/K
30%	-0,076 mV/K
40%	-0,029 mV/K
50%	0,19 mV/K
60%	0,19 mV/K
70%	0,085 mV/K
80%	0,060 mV/K
90%	0,048 mV/K
100%	0,084 mV/K

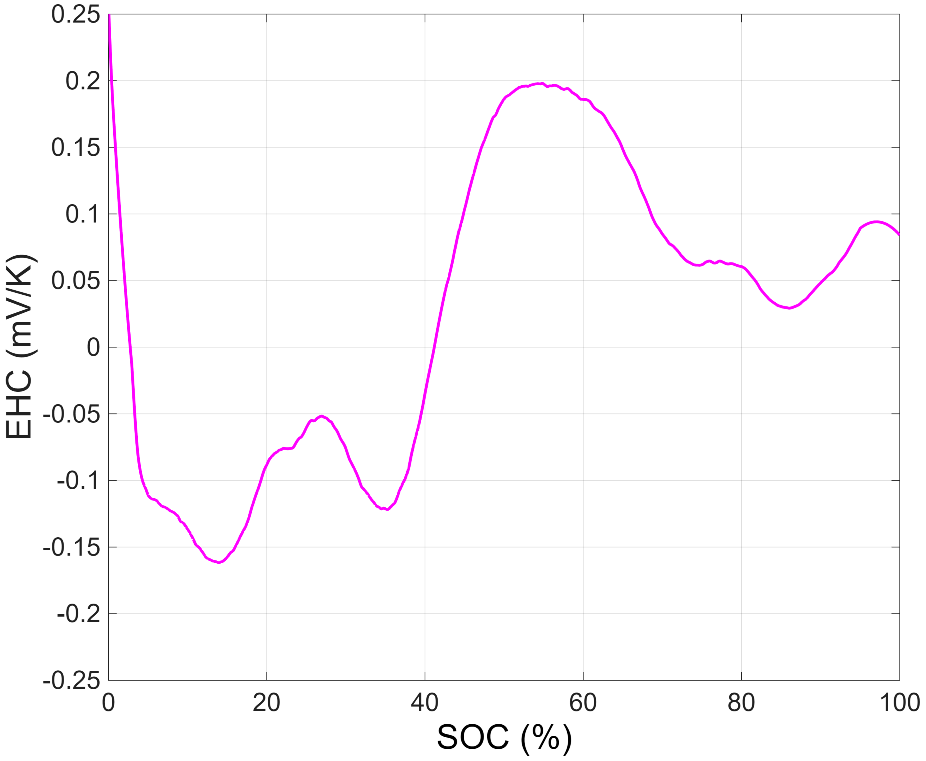

Figure 4.3: EHC vs. SOC (discharge at C/2)

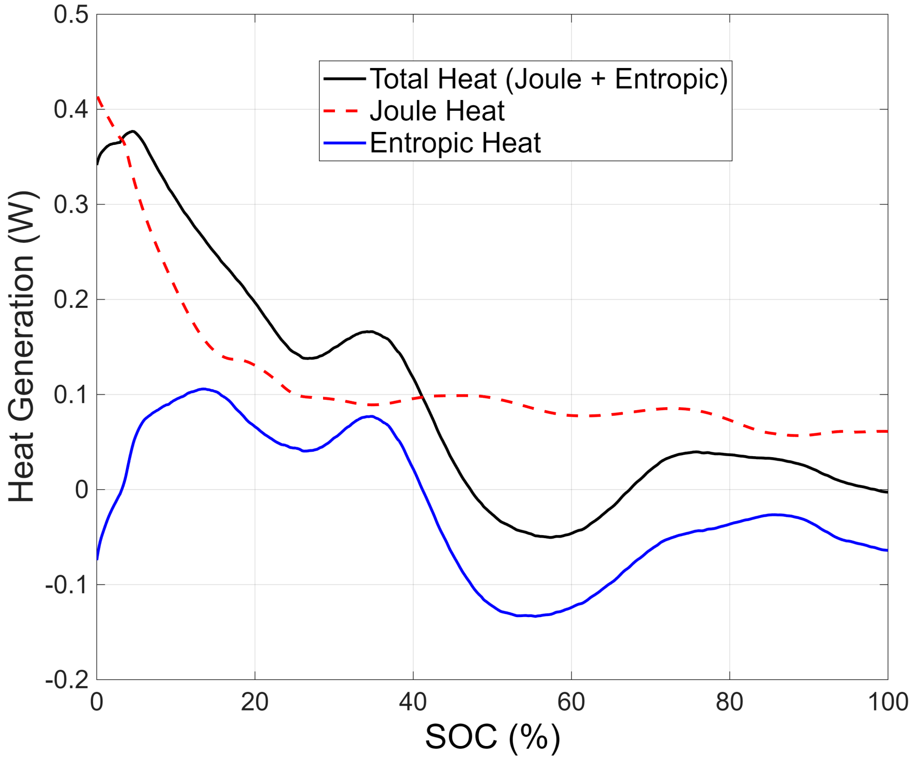

Figure 4.4: Heat Components vs. SOC (discharge at C/2)

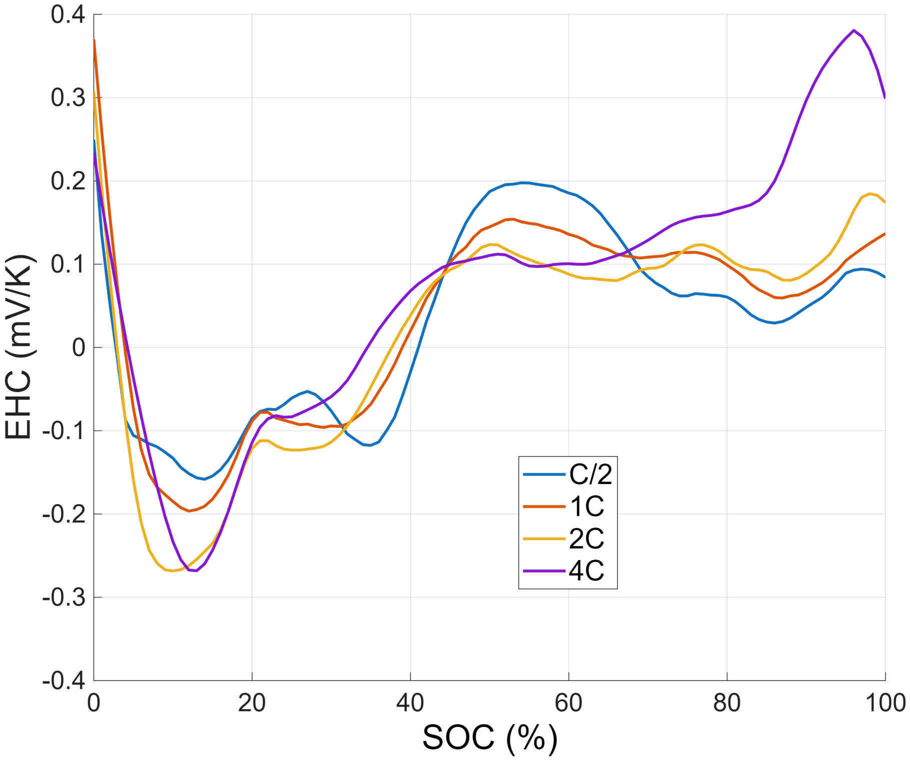

Figure 4.5: EHC vs. SOC (different discharge current rates)

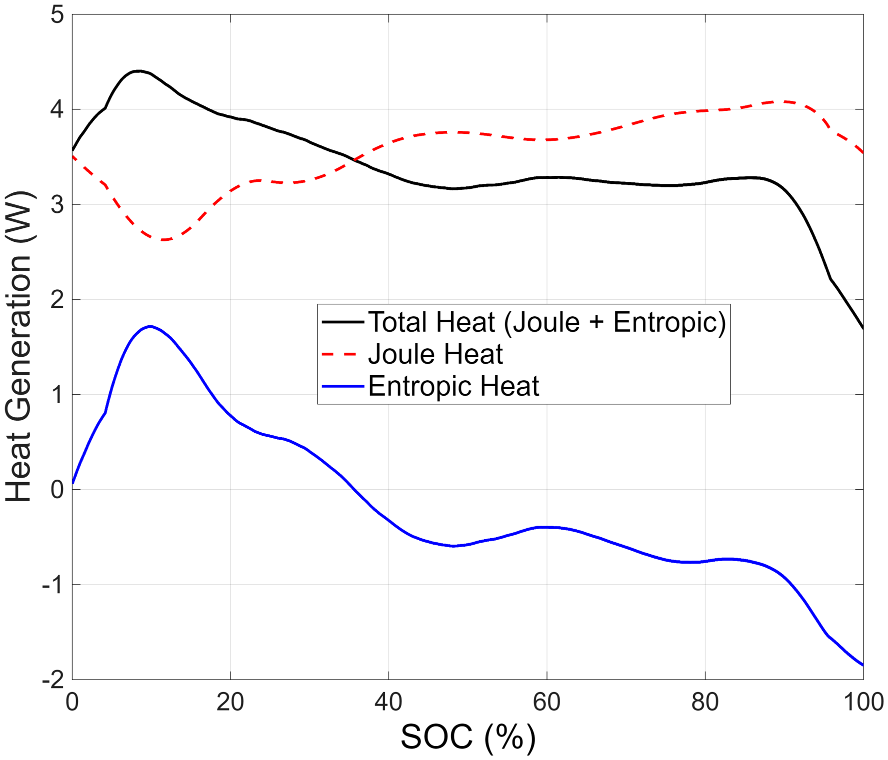

Figure 4.6: Heat Components vs. SOC (discharge at 4C)

Script 4.1: Entropic Heat Coefficient Matlab Script

```
% Entropic Heat Coefficient Estimation
% t: time vector (s)
% T: surface temperature vector (C)
% q: heat flux density vector measured by heat flux sensor (W/m^2)
% I: current vector (A)
% V: voltage vector (V)
% OCV: open circuit voltage vector (V)
% SOC: state of charge vector (%)

% Define Cell Parameters
A = pi*21*70*10^(-6)+2*pi*(21/2)^2*10^(-6);  % Surface area (m^2)
C_th = 63.266; % Thermal capacity (J/K)

% Calculate Total Heat Flux (W)
Q_out = q * A;

% Calculate the Temperature Gradient (dT/dt)
dT_dt = gradient(T, t);
dT_dt = filloutliers(dT_dt, 'clip', 'movmedian', 50); % Caps outliers using a moving
    median (avoids spikes)

% Calculate Total Heat Generation
Q_gen_tot = C_th .* dT_dt + Q_out;

% Calculate Irreversible Joule Heat
Q_joule = I .* (V - OCV);

% Isolate the Reversible (Entropic) Heat
Q_rev = Q_gen_tot - Q_joule;

% Calculate the Entropic Coefficient (dU/dT)
T_kelvin = T + 273.15;
dU_dT = Q_rev ./ (I .* T_kelvin);

% Plotting heat contributions
figure;
plot(SOC, Q_gen_tot, 'k-', 'LineWidth', 2, 'DisplayName', 'Total Heat (Joule + Entropic)
    ');
hold on;
plot(SOC, Q_joule, 'r--', 'LineWidth', 1.5, 'DisplayName', 'Joule Heat');
plot(SOC, Q_rev, 'b-', 'LineWidth', 1.5, 'DisplayName', 'Entropic Heat');
xlabel('SOC (%)');
ylabel('Heat Generation (W)');
legend('Location', 'best');
```

```
grid on;

% Plotting entropic coefficient
figure;
plot(SOC, dU_dT * 1000, 'm-', 'LineWidth', 2); % Multiplied by 1000 for mV/K
xlabel('SOC (%)');
ylabel('EHC (mV/K)');
grid on;
```

4.1.3 Thermal Conductivity Estimation

The radial thermal conductivity k_r is the only one that could be inferred from tests involving internal heating of the battery cell using current flow (direct heating, Section 1.2.2.3). It's quite difficult to determine the axial thermal conductivity k_z in this way, as this can be better determined using other methodologies, like heat guarding (Section 1.2.2.1). To determine the radial thermal conductivity, the following inverse heat problem approach, using a numerical optimizer coupled with an ODE solver, can be developed:

1. **Guess**: the optimizer guesses a random value for the internal (core) thermal resistance $R_{th,c}$, starting from a first realistic initial value
2. **Simulate**: the ODE solver calculates what the core and surface temperatures would be over a discharge process using those guessed parameters
3. **Compare**: the Sum of Squared Errors (SSE) between the simulated surface temperature and the measured experimental surface temperature is determined
4. **Iterate**: the guessed values are adjusted accordingly, and the simulation is run hundreds of times until the simulated values match the experimental ones
5. **Extract**: once the optimizer finds the optimal internal thermal resistance value $R_{th,c}$, the radial thermal conductivity k_r can be retrieved using Equation 1.41

This methodology has been trialled with scarse results, as the optimizer failed to converge to realistic thermal conductivity values. This is one of the reasons that led to the decision of adopting a first order thermal model (that doesn't account for thermal conductivity within the cell). The implementation of this approach and/or of a different characterization procedure to capture this parameter is thus left to the reader. Papers that go into the detail of radial thermal conductivity estimation for cylindrical Li-ion battery cells are [68, 40, 48, 51, 45, 36].

4.2 Hybrid Pulse Power Characterization (HPPC) Results

HPPC testing methodology has been introduced in Section 2.2.2. As introduced in Section 4.1, HPPC, being characterized by short current pulses, is not the best testing methodology to be used for thermal parameter identification. One could implement an HPPC-like testing approach based on using current pulses of opposit signs, but having timescales of minutes rather than seconds, and with sufficient resting time in between for reaching electrothermal equilibrium, allowing one to simultaneously identify both electrical and thermal parameters all in one go (but this is outside the scope of this thesis work). Thus, HPPC data is generally not useful for thermal purposes. In the context of this thesis work, data from the test steps preceding HPPC has been used for the estimation of specific heat capacity, but it is to point out that the procedure here proposed could be easily implemented in the constant current discharge tests, too.

4.2.1 Heat Capacity Estimation

Even if HPPC by itself is not useful for thermal characterization, the 1-hour rest phase between the pilot charge/discharge and subsequent steps has been used for characterizing the heat capacity. The reason why those instants have been chosen is since a long 1-hour rest phase has not been recorded anytime during other tests.

During a rest phase after a discharge event, the battery is cooling by exchanging heat with the environment, while no heat generation $\dot{Q}$ is occourring as $I = 0$. Considering Equation 4.2 we thus have that $\dot{Q} = 0$

$$C_{th}\frac{dT}{dt} = -\dot{Q}_{out} \tag{4.7}$$

By rearranging it to solve for $\dot{Q}_{out}$, we get the equation of a straight line ($y = mx$)

$$\dot{Q}_{out} = C_{th} \cdot \left(-\frac{dT}{dt}\right) \tag{4.8}$$

In the experiment, the heat flux leaving the cell is measured by the heat flux sensor. By scaling the specific heat flux $\dot{Q}''_{out}$ measured by the sensor over the entire cell surface area A one obtains an estimation of $\dot{Q}_{out}$. Thanks to the sensor temperature measurement, is is also possible to derive the temperature variation over time $\frac{dT}{dt}$. In this way one can characterize the thermal (or heat) capacity C_{th}.

In the context of this thesis, the approach followed is shown in Script 4.2. Data has been correlated using a linear regression algorithm, that fits a straight line to the observed data using an Ordinary Least Squares (OLS) approach (Figure 4.7). In particular, a straight line passing from the origin has been considered. The slope of the fitted line represents the thermal capacity of the battery cell. The specific heat capacity c is just derived by dividing the thermal capacity by the cell's mass $c = C_{th}/m$. As a final note, to isolate the effects of heat spreading within the battery cell (from the core to the surface), sufficient time has been awaited before performing the fit (only the final part of the rest phase has been considered). This allows to achieve a high quality fitting, having an R-squared really close to the unity ($R^2 > 0,99$).

The resulting value of heat capacity is $C_{th} = 63,3\ J/K$, that for a cell like the Molicel P45B, having a mass of $m = 0,070\ kg$ corresponds to a specific heat capacity of $c = 904\ J/(kg\ K)$.

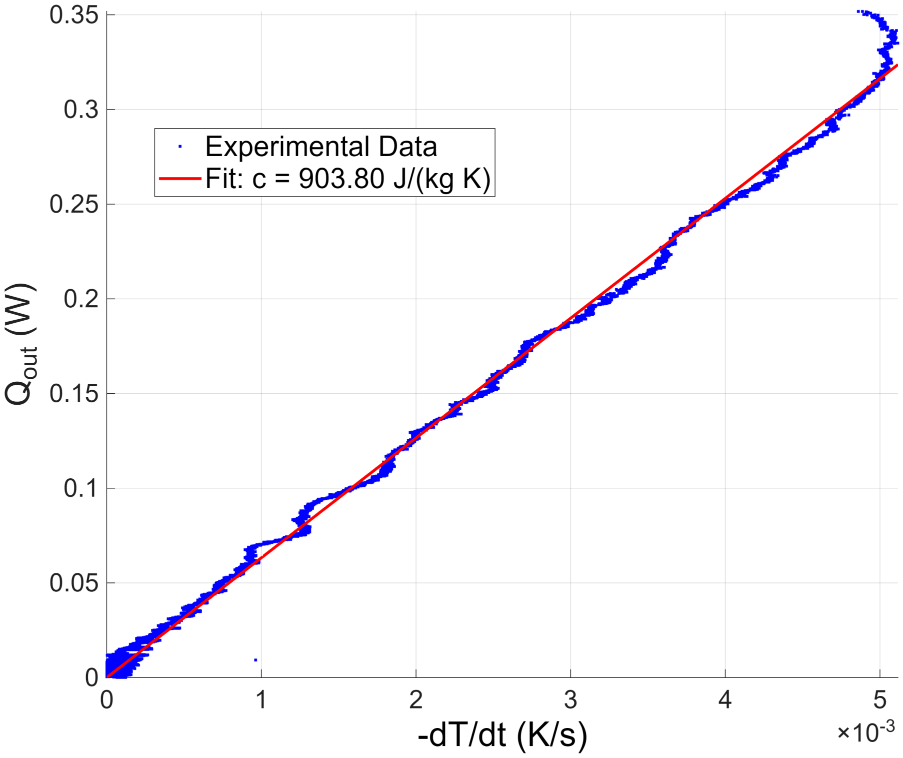

Figure 4.7: Heat capacity fitting

Script 4.2: Heat Capacity Estimation Matlab Script

```
% Specific Heat Capacity Estimation
% t: time vector (s)
% T: surface temperature vector (C)
% q: heat flux density vector measured by heat flux sensor (W/m^2)

% Define Cell Parameters
A = pi*21*70*10^(-6)+2*pi*(21/2)^2*10^(-6); % Surface Area (m)
m = 0.07; % Mass (kg)

% Calculate Total Heat Flux (W)
Q_out = q * A;

% Calculate the Temperature Derivative (dT/dt)
dTdt = gradient(T, t);

% Perform Zero-Intercept Linear Regression
mdl = fitlm(-dTdt, Q_out, 'Intercept', false);

% Extract the results
C_th = mdl.Coefficients.Estimate; % Heat capacity (slope of the curve)
c = C_th/m; % Specific heat capacity
Rsquared = mdl.Rsquared.Ordinary; % R squared

% Display the result in the command window
fprintf('Test %s \n', fields{i});
fprintf('Estimated Thermal Capacity (C_th) = %.2f J/K\n', C_th);
fprintf('Estimated Specific Heat Capacity (c) = %.2f J/(kg K)\n', c);
fprintf('R squared = %.2f \n', Rsquared);

% Visualize the Regression
figure;
scatter(-dTdt, Q_out, 'b.', 'DisplayName', 'Experimental Data');
hold on;
plot(-dTdt, C_th * (-dTdt), 'r-', 'LineWidth', 2, 'DisplayName', sprintf('Fit: c = %.2f
    J/(kg K)', c));
xlabel('-dT/dt(K/s)');
ylabel('{Q}_{out}(W)');
legend('Location', 'best');
grid on;
xlim([0 inf]);
ylim([0 inf]);
set(gcf,'Color','white');
```

4.3 Results Validation

Specific Heat Capacity

The typical specific heat capacities c for 21700 Li-ion cells generally range from 800 to 1100 $J/(kg\ K)$ (Table 4.3 shows the typical specific hest capacities for Li-ion battery cells from the literature). It is important to remark the following specific heat capacity characteristics:

- **Cell Chemistry**: the specific heat capacity changes for different chemistries, as different materials have different physical properties
- **Cell Format**: the specific heat capacity heavily depends on the cell format, which can be explained by the different mass fraction of the housing over the entire cell and different current collector geometry [32]
- **Temperature**: the specific heat capacity shows a strong, positive linear correlation with temperature (as the cell heats up, its specific heat capacity increases) [47, 32, 51, 35]
- **State of Charge**: the specific heat capacity is generally indipendent from the SOC [47, 32, 35]

In addition, [32] mentions that thermal capacity also depends on wether the entire cell (jelly roll and casing) or just the jelly roll is considered in the calculation, as the cell casing heavily influences the overall value (since the casing material has a lower specific heat capacity and a high mass ratio, it acts to lower the average specific heat of the entire cell), and founds that 912 $J/(kg\,K)$ is the specific heat capacity median value for cylindrical cells.

In any case, the retrieved value of specific heat capacity in this work ($c = 904\ J/(kgK)$, referring to the entire cell body) lays exactly in between the values obtained in the literature. The result has thus been considered as a valid outcome for battery thermal characterization.

Thermal Conductivity

Due to the spiral jelly roll construction of cylindrical Li-ion cells, the thermal conductivity is highly anisotropic. Heat flows much more easily along the layers (axial/in-plane) than across the multiple material interfaces (radial/through-plane). The typical thermal conductivities for 21700 Li-ion cells generally range from $0,2$ to 2 $W/(m\,K)$ for radial (through plane) k_r, and from 10 to 30 $W/(m\,K)$ for axial

Table 4.3: Specific heat capacities of Lithium-Ion cells

Reference	**Cell Format & Chemistry**	**Specific Heat Capacity** ($J \cdot kg^{-1} \cdot K^{-1}$)
Auch et al. [47]	21700 Cylindrical (NMC)	775
Auch et al. [47]	21700 Cylindrical (NCA)	821
Balkur et al. [43]	Prismatic (LFP)	1033–1055
Balkur et al. [43]	Pouch (NMC)	940–995
Bryden et al. [11]	26650 Cylindrical (NMC)	978
Bryden et al. [11]	26650 Cylindrical (LFP)	1169
Bryden et al. [11]	Pouch (NMC)	1182
Bryden et al. [11]	Prismatic (NMC)	1012
He et al. [46]	Prismatic (NMC)	1044
Murashko et al. [48]	26650 Cylindrical (LFP)	1115
Sheng et al. [51]	21700 Cylindrical (NMC)	967–1105
Steinhardt et al. [45]	18650 Cylindrical (NMC)	1002–1003
Steinhardt et al. [45]	21700 Cylindrical (NMC)	908–912
Yu et al. [35]	Cylindrical (NMC)	884–1016
Yu et al. [35]	Cylindrical (NMC)	892–1082

(in-plane) k_z (Table 4.4 reports the typical thermal conductivities for Li-ion battery cells from the literature). It is important to remark the following thermal conductivity characteristics:

- **Cell Chemistry**: the thermal conductivity changes for different chemistries, as different materials have different physical properties
- **Cell Format**: the cell format inherently affects the thermal conductivity, as different geometry, size and jelly roll arrangement significantly modify the thermal conduction properties [32]
- **Temperature**: the axial conductivity increases slightly with battery temperature, while for radial conductivity findings are mixed (it either slightly increases or decreases with temperature, but the dependence is not pronounced) [32, 51]
- **State of Charge**: both radial and axial thermal conductivities generally increase as the SOC increases [32, 35]

The thermal conductivity has not been characterized in this work. But, since the radial thermal conductivity was required for the calculation of the Biot number, a simplistic value of $k_r = 1\ W/(m\ K)$ has been considered.

Biot Number Verification

The entire thermal modelling in this works is fundamentally based on the lumped capacitance assumption. In fact, all the methodology described in Chapter 4 is

Table 4.4: Thermal conductivities of Lithium-Ion cells

Reference	**Cell Format & Chemistry**	**Thermal Conductivity** $(W \cdot m^{-1} \cdot K^{-1})$
Ahmed et al. [40]	26650 Cylindrical	0,39 (Radial)
Cailliez et al. [44]	Pouch (NMC)	1,22–1,37 (Through-plane)
Cailliez et al. [44]	Pouch (NMC)	19,4–20,7 (In-plane)
Jiang et al. [36]	18650 Cylindrical	2,14–2,87 (Radial)
Jiang et al. [36]	18650 Cylindrical	10,26–14,20 (Axial)
Kovachev et al. [69]	Pouch	0,55–0,80 (Through-plane)
Murashko et al. [48]	26650 Cylindrical (LFP)	0,45–0,49 (Radial)
Murashko et al. [48]	18650 Cylindrical (NCA)	0,65–0,90 (Radial)
Sheng et al. [51]	21700 Cylindrical (NMC)	1,14–1,19 (Radial)
Steinhardt et al. [45]	18650 Cylindrical (NMC)	1,22–1,30 (Radial)
Steinhardt et al. [45]	21700 Cylindrical (NMC)	1,24–1,36 (Radial)
Yu et al. [35]	18650 Cylindrical (NMC)	11,8–15,4 (Axial)
Yu et al. [35]	21700 Cylindrical (NMC)	12,6–16,7 (Axial)

based on a first order thermal ECM, that as shown in Section 1.3.2.2 is theoretically equivalent to a lumped capacitance model. The lumped capacitance assumption practically assumes that the temperature is uniform across the entire battery, and allows avoiding solving complex Partial Differential Equations (PDEs) in 3D space and solving a simple first order ODE instead. But for this approach to be physically correct, this assumption needs to be validated, and this is typically done calculating the Biot number. As already introduced in Section 1.3.2.1, if $Bi < 0,1$ heat conduction inside the battery is basically negligible (much faster) if compared to heat convection with the environment, and the temperature difference between the core and the surface can be ignored. The Matlab code that calculates the Biot number after thermal conductivity evaluation is reported in Script 4.3.

Script 4.3: Biot Number Verification Matlab Script

```
% Biot Number Verification
% Define Cell Parameters
L_c = 21/2*70/2/(21/2+70)*10^(-3); % Characteristic Length (m) = Volume/Surface
k = 1.0; % Radial Thermal Conductivity (W/m*K)
T_amb = T(end); % Ambient Temperature (C)

% Calculate the Convective Heat Transfer Coefficient (h)
delta_T = T - T_amb; % we calculate h when there is a meaningful temperature difference
valid_indices = delta_T > 1.0; % where the temperature difference is significant
h_instantaneous = q(valid_indices) ./ delta_T(valid_indices); % calculate h
h_avg = mean(h_instantaneous); % average value
```

```
% Calculate the Biot Number
Bi = (h_avg * L_c) / k;

% Calculate R_th
R_th = 1/(h_avg * A);

% Display Results
fprintf('Estimated Average h: %.2f W/(m^2 K)\n', h_avg);
fprintf('Calculated Biot Number (Bi): %.4f\n', Bi);
fprintf('Calculated Thermal Resistance (R_th): %.2f K/W \n', R_th);

if Bi < 0.1
    disp('Bi < 0.1: The lumped capacitance assumption is valid.');
else
    disp('Bi >= 0.1: The lumped capacitance assumption is NOT strictly valid.');
end
```

The calculated value of heat transfer coefficient is $h = 35,80\ W/(m^2\ K)$. This value is coherent with the tabulated heat transfer coefficient values for forced convection (the thermal chamber has two fans that continuously move the air inside). The Biot number value that has been retrieved is $Bi \approx 0,16$. The value is slightly above the $Bi = 0,1$ threshold, meaning that heat conduction in the cell is not really negligible, but still faster than the surrounding convection. Nevertheless, the first order lumped thermal model has been retained for this analysis. Transitioning to a higher-order spatial model would introduce new internal parameters ($C_{th,c}$, $C_{th,s}$, $R_{th,c}$) that, as mentioned alreay, are hard to estimate and risk mathematical overfitting without validation by measuring the real core temperature T_c. Because a Biot number of approximately $0,16$ corresponds to a temperature gradient error of less than 10%, the decision has been to proceed with a lumped capacitance model anyway.

The corresponding calculated value of external thermal resistance R_{th} according to Equation 1.37 is equal to

$$R_{th} = \frac{1}{h \cdot A_{tot}} = 5,26\ K/W \tag{4.9}$$

5

Model Development and Validation

This chapter presents the development and validation of the electrothermal model of the Li-ion battery cell in Matlab Simulink software.

5.1 Model Formulation

As introduced in Section 1.3.4 when discussing the model selection:

- the **electrical model** (Figure 5.1) is a Thevenin 2RC ECM, where the circuit components (resistors $R0$, $R1$ and $R2$, capacitors $C1$ and $C2$, voltage source V_{OC}) depend on the battery SOC. The SOC estimation is implemented by means of Coulomb counting (that is, integration of current over time), and the extracted value is used to update the instantaneous value of the circuit parameters

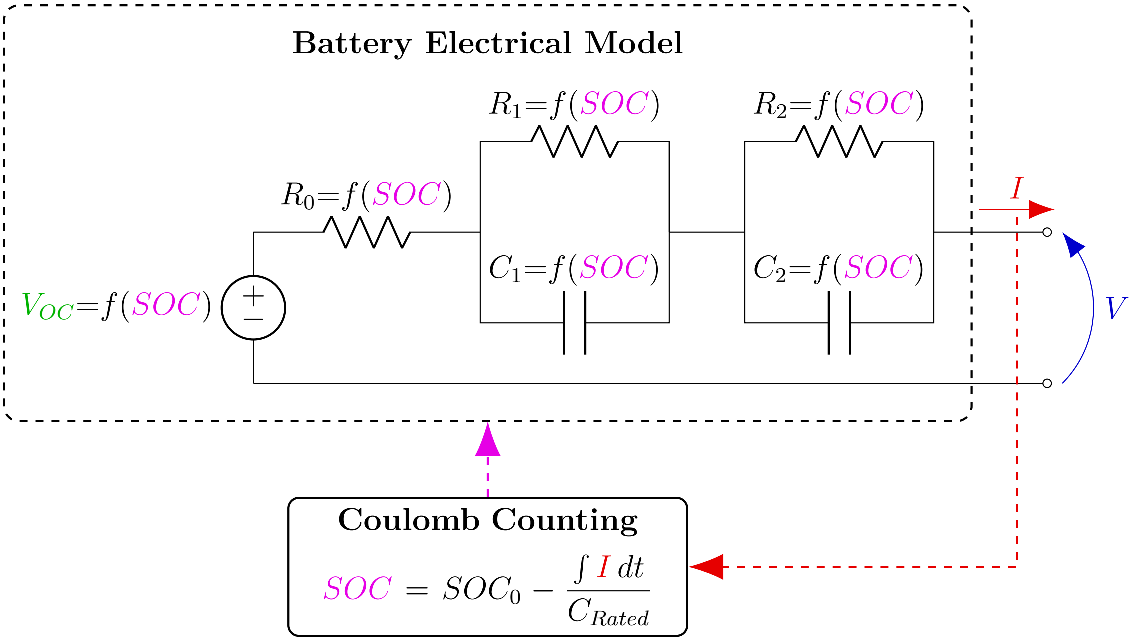

Figure 5.1: Electrical model formulation

- the **thermal model** (Figure 5.2) is a first order (1-state) thermal ECM, where the circut components (resistor R_{th}, capacitor C_{th}, voltage source T_a) are assumed to be constant. The thermal model calculates the internal heat generation $\dot{Q}$ from the instantaneous battery temperature T (obtained from the model itself) and the current I, voltage V and OCV provided by the electrical model

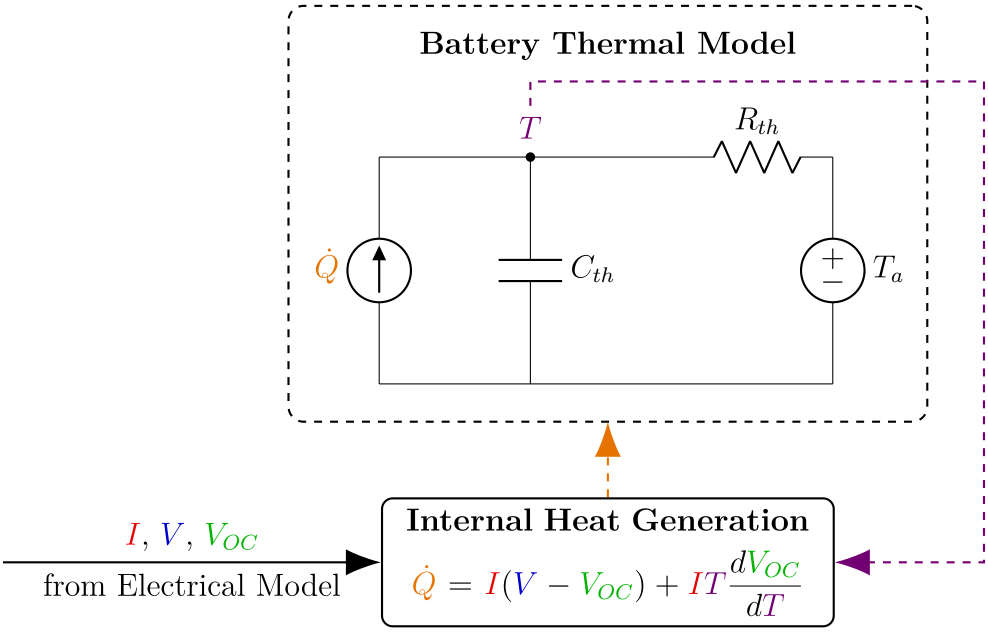

Figure 5.2: Thermal model formulation

- the **electrothermal coupling** (Figure 5.3) is a one-way coupling, as the electrical model quantities are used by the thermal model to estimate the battery temperature, but without further fedback to the electrical model to update the electrical circuit components

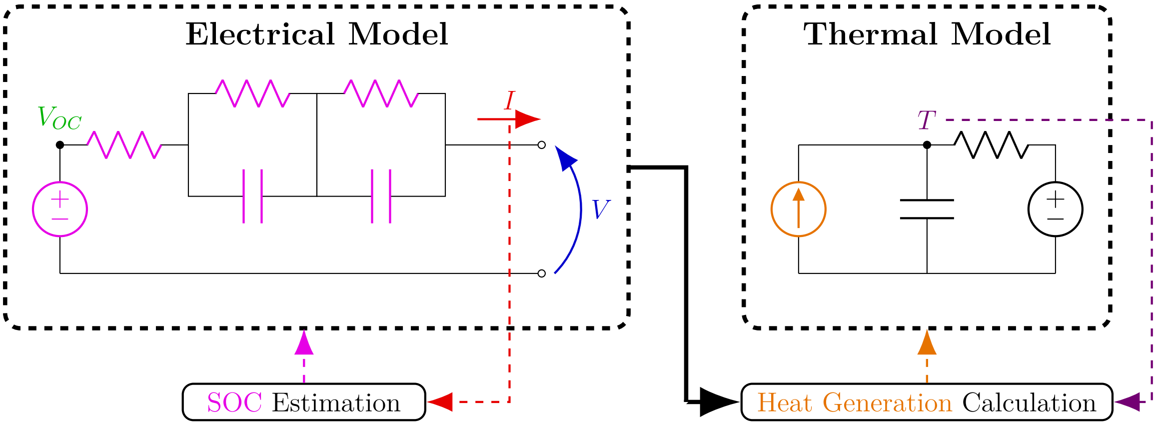

Figure 5.3: Electrothermal model coupling

5.2 Implementation in Simulation Environment

The model described in Section 5.1 has been implemented in the simulation software Matlab Simulink, in particular using the Simscape components library, a physical modelling toolbox used within Simulink that allows to model and simulate real-world physical systems using a graphical component-based approach.

5.2.1 Electrical Model

Figure 5.4 shows the electrical model implementation. The OCV is generated using a controlled voltage source, while the circuit elements (resistors R and capacitors C) are realised using variable resistors and capacitors blocks, where the values are read from lookup tables generated with the data obtained during characterization (more in Section 5.2.5). The current I flowing in the circuit is imposed by a controlled current source, and the current profile is the same to the one used during the testing phases at the bench described in Chapter 2. The terminal voltage V, that is the main output produced by the electrical model, is measured by a voltage sensor.

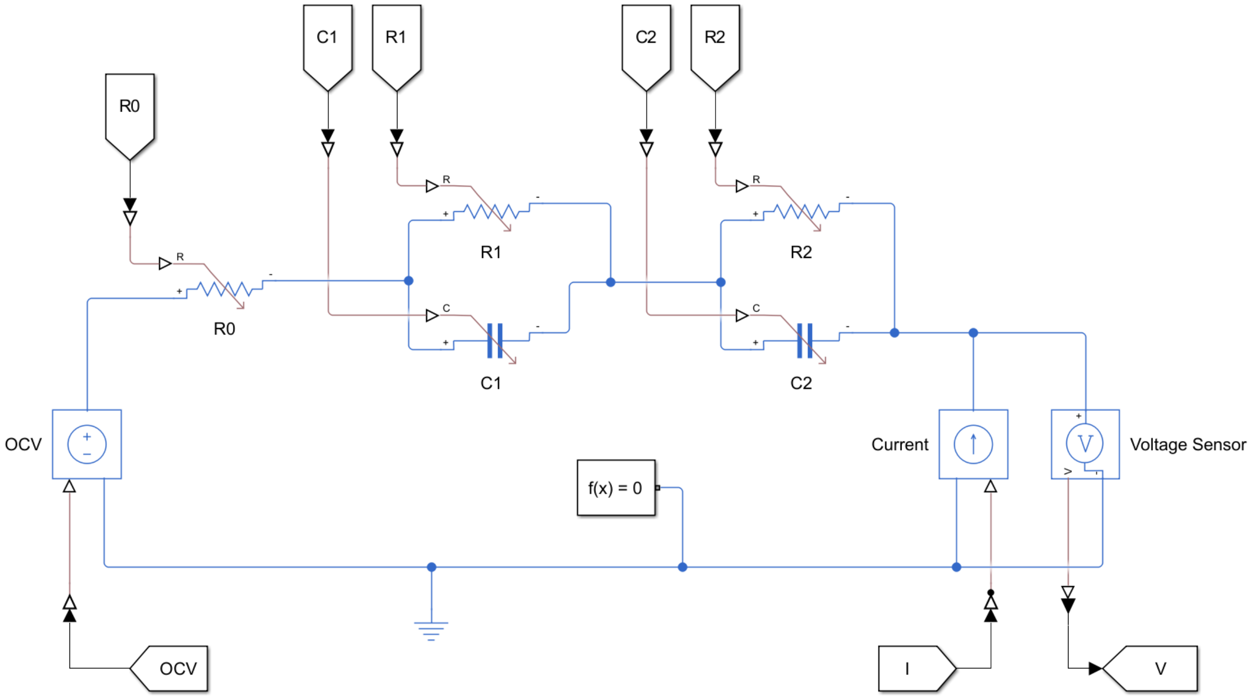

Figure 5.4: Electrical model implementation

5.2.2 State of Charge (SOC) Estimation

As already mentioned, the SOC is estimated by Coulomb counting. The SOC value is obtained using Equation 1.10

$$SOC = SOC_0 - \frac{\int I\,dt}{C_{Rated}} \tag{5.1}$$

where SOC_0 is the initial SOC (usually imposed to 100%, as the cell is assumed to be fully charged up to its upper voltage limit $V_{Upper,Limit}$), I is the current (coming from a variable containing the test current data) and C_{Rated} the rated capacity at that current rate (assumed, for simplicity, equal to the discharge capacity measured at the current value that most represents the test underway). The calculation blocks are reported in Figure 5.5.

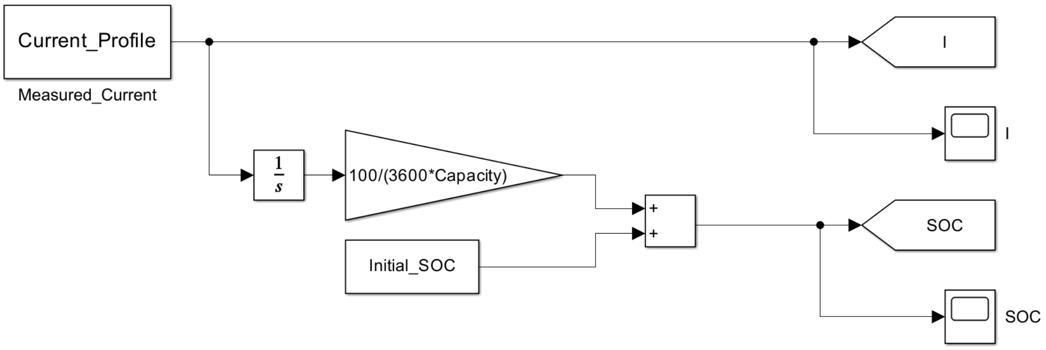

Figure 5.5: SOC estimation implementation

5.2.3 Thermal Model

Figure 5.6 shows the thermal model implementation. The internal heat generation value $\dot{Q}$, determined as per Section 5.2.4, is fed into a controlled heat flow rate surce, that imposes the heat flux running in the thermal circuit. The cell thermal capacity $C_{th} = m \cdot c$, where m is the cell mass and c the specific heat capacity, and the thermal resistance to ambient R_{th} are plugged in the respective thermal mass and thermal resistance blocks as model constants. The ambient temperature T_a is imposed using a controlled temperature source. The outputs of the thermal model are the surface temperature T and the heat flux to ambient $\dot{Q}_{out}$, and are measured using a temperature and heat flow rate sensor, respectively.

5.2.4 Internal Heat Generation Calculation

The internal heat generation is determined using Equation 4.1 for the case of $I > 0$ during charging, that is the current sign convention used by the Neware BTS. The

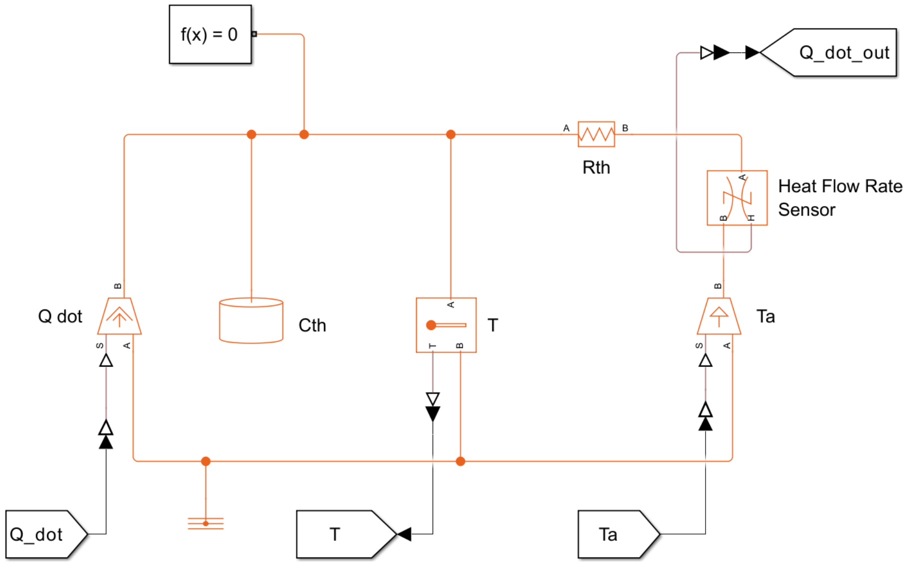

Figure 5.6: Thermal model implementation

irreversible and reversible components are separately calculated and then summed together (Figure 5.7)

$$\dot{Q} = I(V - V_{OC}) + IT\frac{dV_{OC}}{dT} \tag{5.2}$$

where T is the cell temperature provided by the thermal model, V is the cell voltage derived by the electrical model, I is the current, and the OCV and EHC are retrieved from the lookup tables of Section 5.2.5.

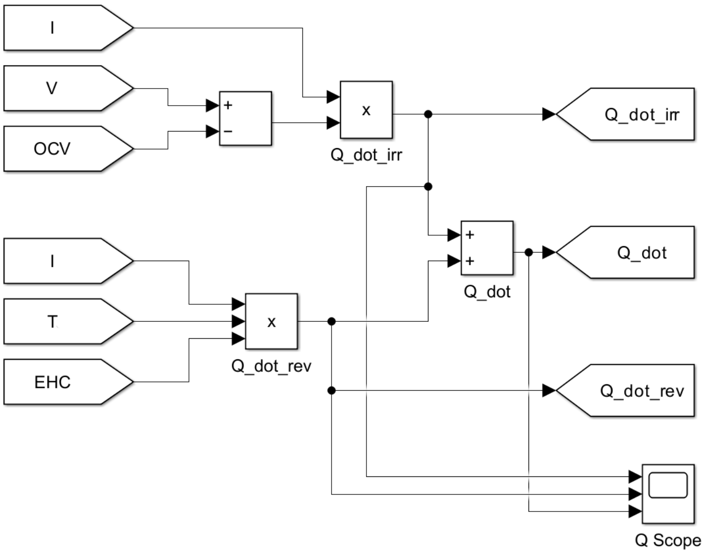

Figure 5.7: Heat generation implementation

5.2.5 Lookup Tables

The time-varying parameters of the model are computed using lookup tables in function of the real time estimation of the SOC:

- **OCV**: obtained from SOC using a 1D lookup table (Figure 5.8), using data from Section 3.2.1
- **EHC**: obtained from SOC using a 1D lookup table (Figure 5.9), using data from Section 4.1.2
- **RC**: obtained from SOC using two 1D lookup table, one for the discharge and one for the charge parameters. The R, C values are the ones retrieved during electrical characterization (from Table 3.2, where the charge and discharge averages between the pulse and relaxation steps have been considered). The charge/discharge profile is chosen by using a switch box, that selects the appropriate one depending on the current sign. Then, the signal is fed into a rate limiter, that limitis rising and falling rates of the quantities to avoid possible solver crashes. This approach is applied for all the R, C parameters (Figure 5.10)

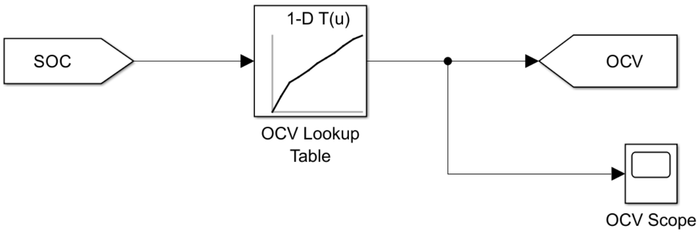

Figure 5.8: OCV lookup implementation

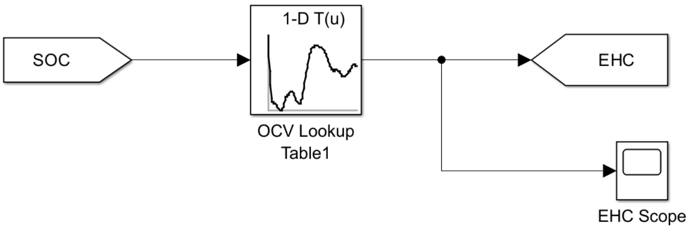

Figure 5.9: EHC lookup implementation

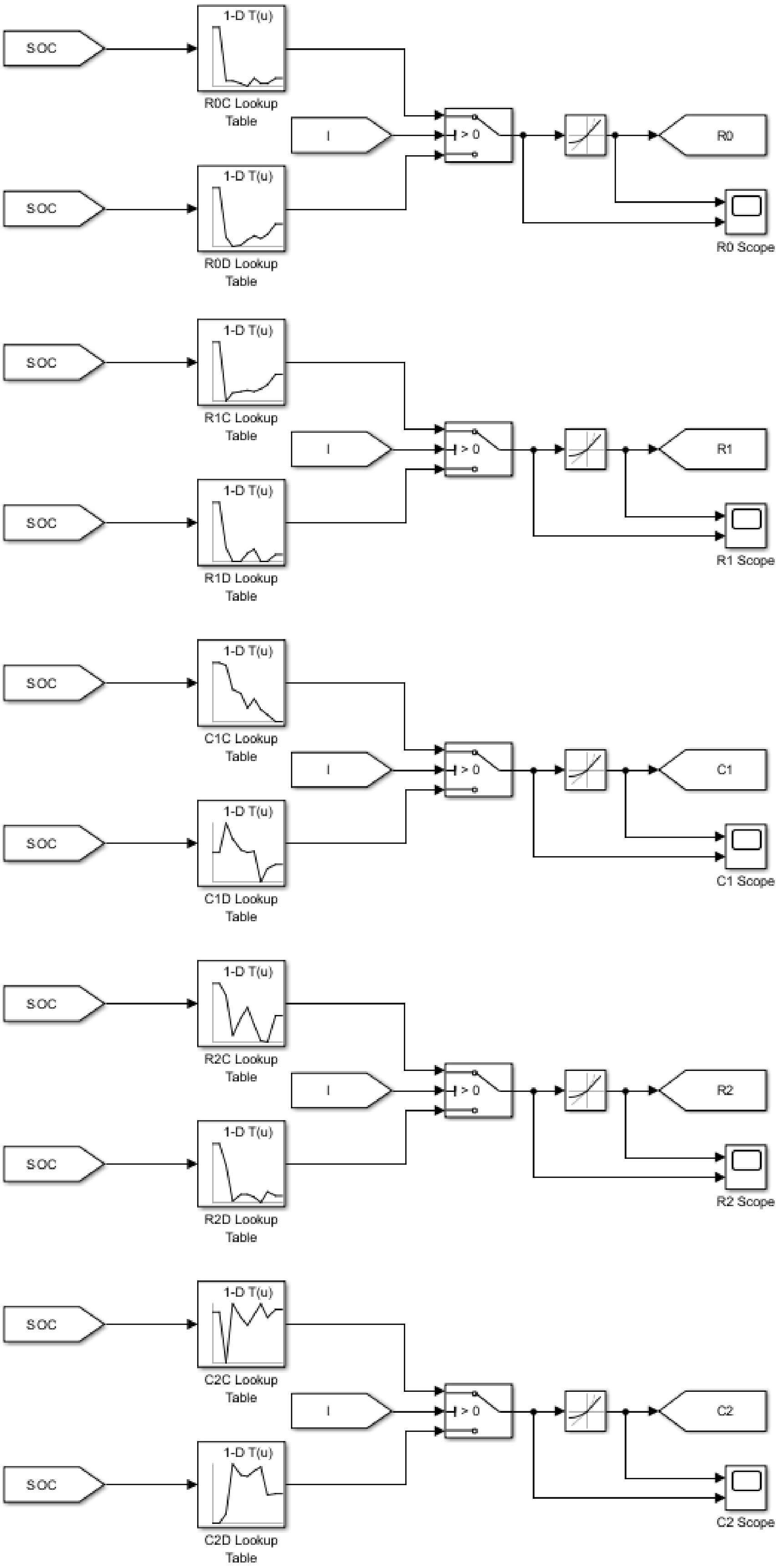

Figure 5.10: RC lookups implementation

It is important to remark that since the electrothermal characterization has been performed at a single temperature value (30 °C), the model parameters depend only on the SOC. More in general, the electrothermal model elements depend also on temperature, thus for a more complete and precise result one should use a 2D lookup table, integrating both the SOC and temperature dependency. For doing that, the characterization steps discussed in Chapters 3 and 4 should be repeated at different temperature values.

5.2.6 Parameters Setup

For the lookup tables to work, the parameters values have to be loaded in the workspace. For the purpose, a dedicated Matlab script, that loads the test data provided in the directory (the test current profile, and the voltage, temperature and heat flux for the comparison plots), the characterized parameters and other useful data has been developed (Script 5.1).

Script 5.1: Parameters Setup Matlab Script

```
% Battery parameters setup script
% Load data from .mat files
load('Current_Profile.mat');
load('Voltage_Profile.mat');
load('Temperature_Profile.mat');
load('Heat_Flux_Density_Profile.mat');

% Dynamically assign simulation time
t_end = Current_Profile.Time(end);

% Electrical data f(SOC)
SOC_vector = 0:10:100;
OCV = flip([4.1 4.05 3.96 3.87 3.79 3.72 3.63 3.53 3.46 3.29 3.07]); % V
R0D = flip([0.00750 0.00750 0.00739 0.00736 0.00738 0.00734 0.00730 0.00728 0.00737
    0.00785 0.00785]); % Ohm
R0C = flip([0.00748 0.00748 0.00743 0.00743 0.00748 0.00741 0.00744 0.00746 0.00746
    0.00796 0.00796]); % Ohm
R1D = flip([0.00168 0.00168 0.00159 0.00159 0.00175 0.00170 0.00160 0.00160 0.00178
    0.00239 0.00239]); % Ohm
R1C = flip([0.00170 0.00170 0.00150 0.00141 0.00137 0.00139 0.00136 0.00134 0.00118
    0.00232 0.00232]); % Ohm
C1D = flip([1087 1087 1038 887 1233 1215 1247 1366 1551 1211 1211]); % F
C1C = flip([701 701 737 768 832 782 865 890 1031 1048 1048]); % F
R2D = flip([0.0083 0.0083 0.0098 0.0060 0.0077 0.0087 0.0087 0.0065 0.0193 0.0271
    0.0271]); % Ohm
R2C = flip([0.01233 0.01233 0.00794 0.00825 0.01080 0.01371 0.01193 0.00915 0.01579
```

```
    0.01778 0.01778]); % Ohm
C2D = flip([2044 2044 2010 2634 2549 2450 2466 2716 1595 1396 1396]); % F
C2C = flip([1915 1915 1795 2005 1844 1682 1791 1995 1119 1880 1880]); % F

% Thermal data f(SOC)
SOC_vector_100 = 0:1:100;
ehc = [2.6e-04 1.4e-04 5.4e-05 -1.8e-05 -9.2e-05 -1.1e-04 -1.1e-04 -1.2e-04 -1.2e-04
    -1.3e-04 -1.4e-04 -1.5e-04 -1.5e-04 -1.6e-04 -1.6e-04 -1.6e-04 -1.5e-04 -1.4e-04
    -1.2e-04 -1.0e-04 -8.8e-05 -8.0e-05 -7.6e-05 -7.6e-05 -6.9e-05 -6.0e-05 -5.5e-05
    -5.2e-05 -5.6e-05 -6.4e-05 -7.6e-05 -9.0e-05 -1.0e-04 -1.1e-04 -1.2e-04 -1.2e-04
    -1.2e-04 -1.0e-04 -8.9e-05 -6.3e-05 -3.5e-05 -5.4e-06 2.6e-05 5.2e-05 8.0e-05 1.0e
    -04 1.3e-04 1.5e-04 1.6e-04 1.8e-04 1.9e-04 1.9e-04 1.9e-04 2.0e-04 2.0e-04 2.0e-04
    2.0e-04 2.0e-04 1.9e-04 1.9e-04 1.9e-04 1.8e-04 1.8e-04 1.7e-04 1.6e-04 1.5e-04 1.4e
    -04 1.2e-04 1.1e-04 9.4e-05 8.5e-05 7.7e-05 7.2e-05 6.5e-05 6.2e-05 6.2e-05 6.5e-05
    6.4e-05 6.3e-05 6.2e-05 6.0e-05 5.5e-05 4.8e-05 3.9e-05 3.4e-05 3.1e-05 2.9e-05 3.1e
    -05 3.5e-05 4.2e-05 4.8e-05 5.4e-05 6.0e-05 6.8e-05 7.8e-05 8.9e-05 9.3e-05 9.4e-05
    9.3e-05 9.0e-05 8.4e-05]; % V/K

% General data
Capacity = 4; % Ah
Mass = 0.07; % kg
Area = pi*21*70*10^(-6)+2*pi*(21/2)^2*10^(-6); % m^2
Specific_Capacity_th = 904; % J/(kg K)
Ambient_Resistance_th = 5.26; % K/W
%Ambient_Temperature = Temperature_Profile.Data(1); % C
Ambient_Temperature = 29.5; % C
%Initial_SOC = interp1(OCV, SOC_vector, Voltage_Profile.Data(1));
Initial_SOC = 100;
```

5.2.7 Output Processing

The simulated voltage, temperature and heat flux are then compared to the experimental ones in Figure 5.11. The two signals are sent in a scope block, that allows to represent them in the same figure, evaluate their difference and export the resulting plot. Since the measured heat flux input is the heat flux density $\dot{Q}''_{out}$, while the computed term is the total heat flux $\dot{Q}_{out}$, the experimental term is multiplied by the total surface area A, so that $\dot{Q}_{out} = \dot{Q}''_{out} \cdot A$. The temperature is converted from Kelvin to Celsius for the sake of clarity in the comparison diagram. Then, the absolute, relative and Root Mean Square (RMS) errors are calculated. Defining x as the experimentally measured (assumed to be true) value of the quantity, and $\hat{x}$ the simulated one, the expressions of the absolute E_{abs}, relative E_{rel}, and RMS error E_{RMS} are, respectively

$$E_{abs} = |\hat{x} - x| \tag{5.3}$$

$$E_{rel} = \frac{|\hat{x} - x|}{|x|} \tag{5.4}$$

$$E_{RMS} = \sqrt{\frac{1}{t} \int (\hat{x} - x)^2 \, dt} \tag{5.5}$$

The same error calculation strategy has been applied to all the three simulated quantitites (V, T and $\dot{Q}_{out}$). The block sheme implementation is reported for completeness in Figure 5.12. Note that a small constant ($1 \cdot 10^{-6}$) has been added to time t to avoid division by zero at the start of the simulation.

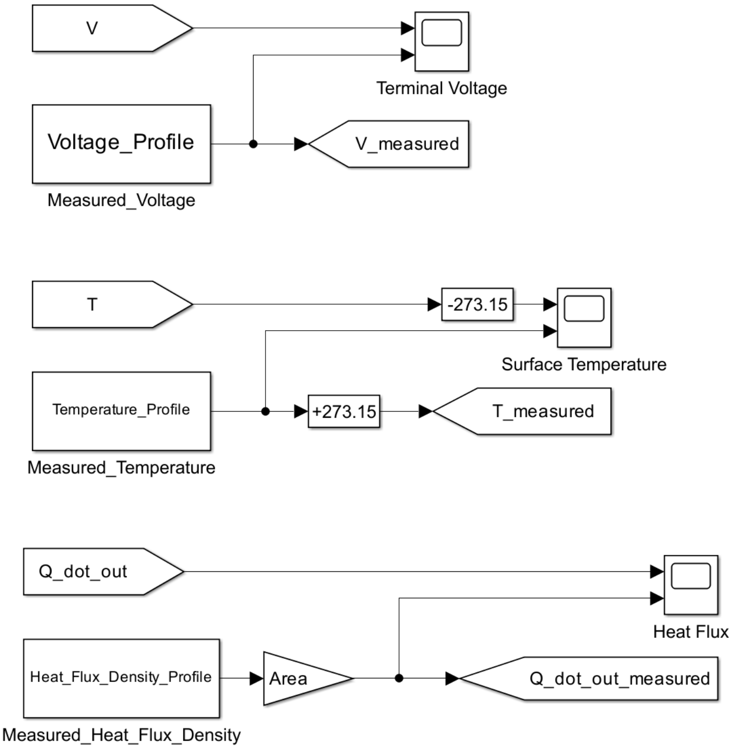

Figure 5.11: Results comparison implementation

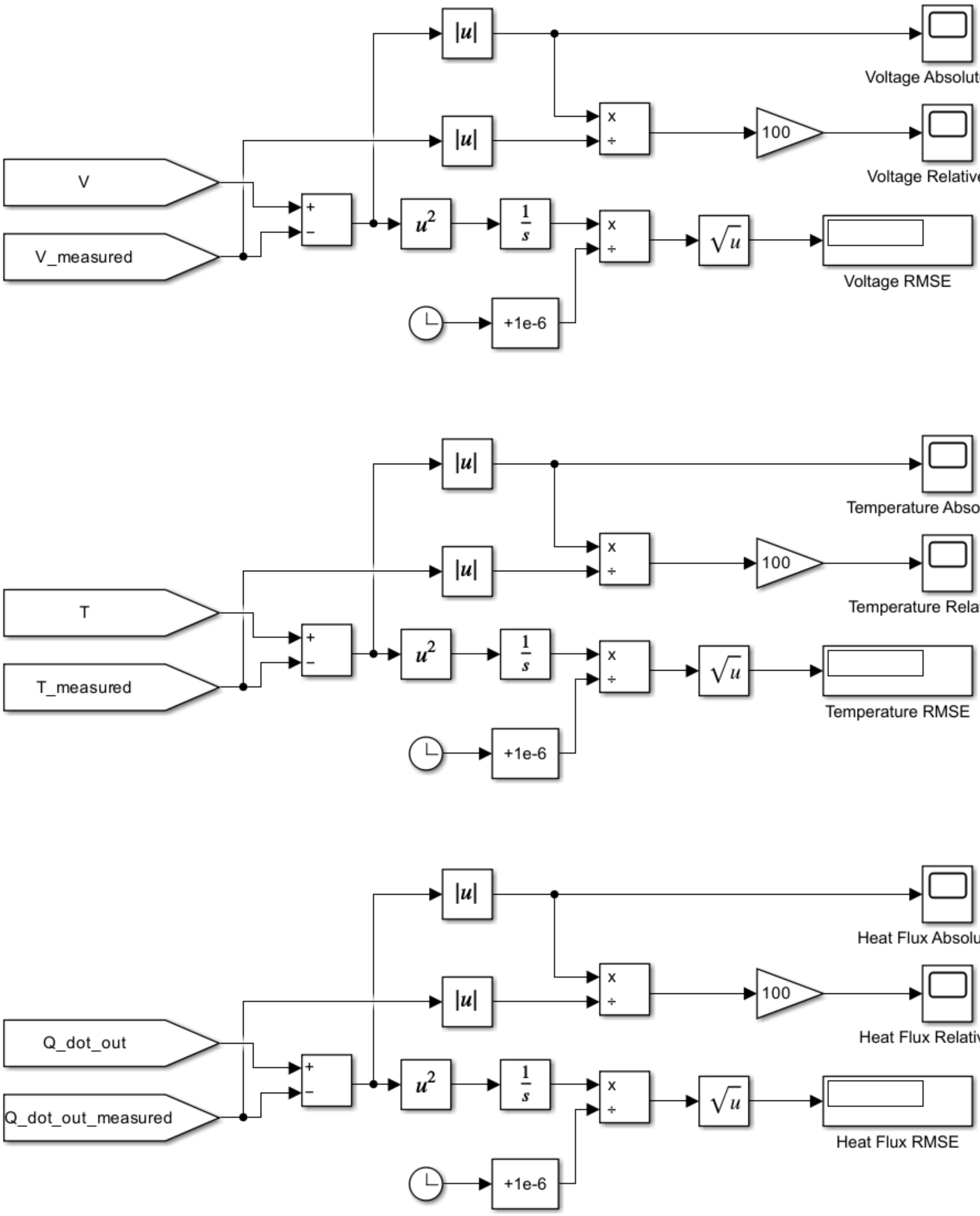

Figure 5.12: Error calculations implementation

5.3 Model Validation and Error Analysis

The model validation has been performed running two simulations (HPPC and Random Walk (RW)) and comparing the results with the experimental data.

5.3.1 Hybrid Pulse Power Characterization (HPPC) Simulation Results

To verify that the model is operational, the first test that has been simulated is an HPPC. In particular, due to reduced data availability, the same HPPC test that has been used for parameter extraction during electrothermal characterization has been selected. Thus, to avoid verifying the model on the same data it has been trained on, that would be an obvious case of data overfitting, this instance has been just used to verify that the model works, and not for assessing its accuracy. In Section 5.3.2 the model will be verified against a novel test profile, different from the one used during characterization.

The input current profile that has been provided to the model is presented in Figure 5.13. The resulting SOC staircase, showing the 10% SOC steps, is in Figure 5.14.

The following figures show the HPPC simulation results compared to the experimental data measured at the test bench:

- **Voltage**: Figure 5.15 compares the voltage profiles
- **Temperature**: Figure 5.17 compares the temperature profiles
- **Heat Flux**: Figure 5.18 compares the heat flux profiles (heat exchanged from the cell to the surrounding environment by convection)

At a first glance, the voltage prediction looks to be quite accurate, while the simulated temperature and heat flux are generally overestimated. The complete observations and final verdict on model performance is discussed in detail in Section 5.3.3.

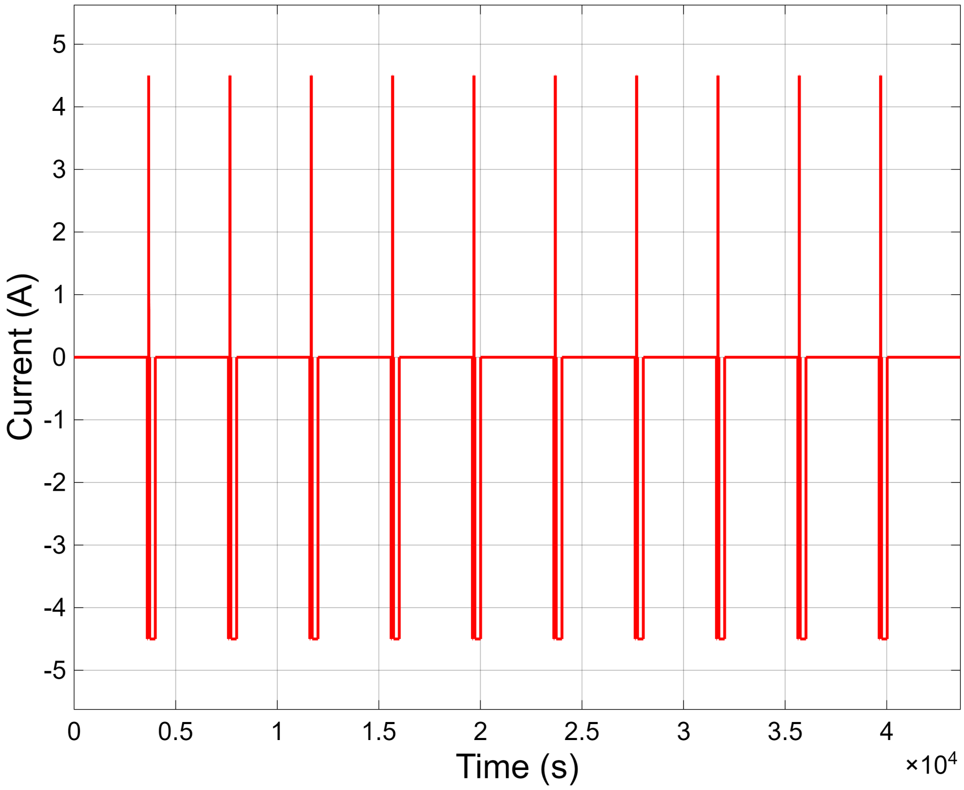

Figure 5.13: HPPC simulation - Current vs. Time

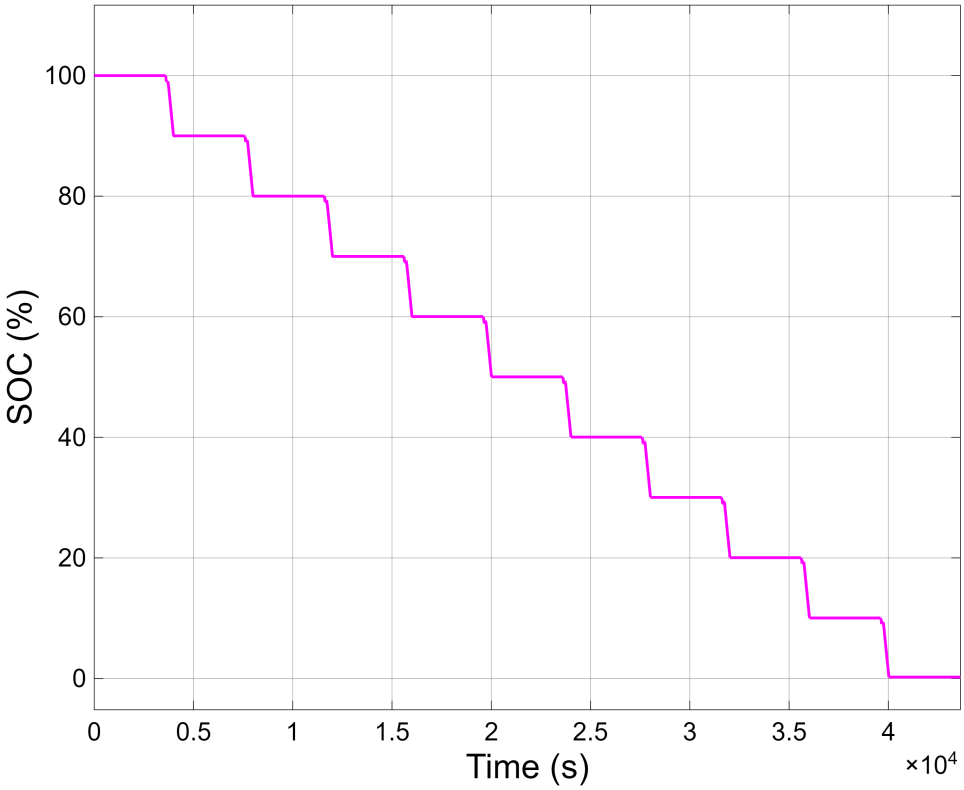

Figure 5.14: HPPC simulation - SOC vs. Time

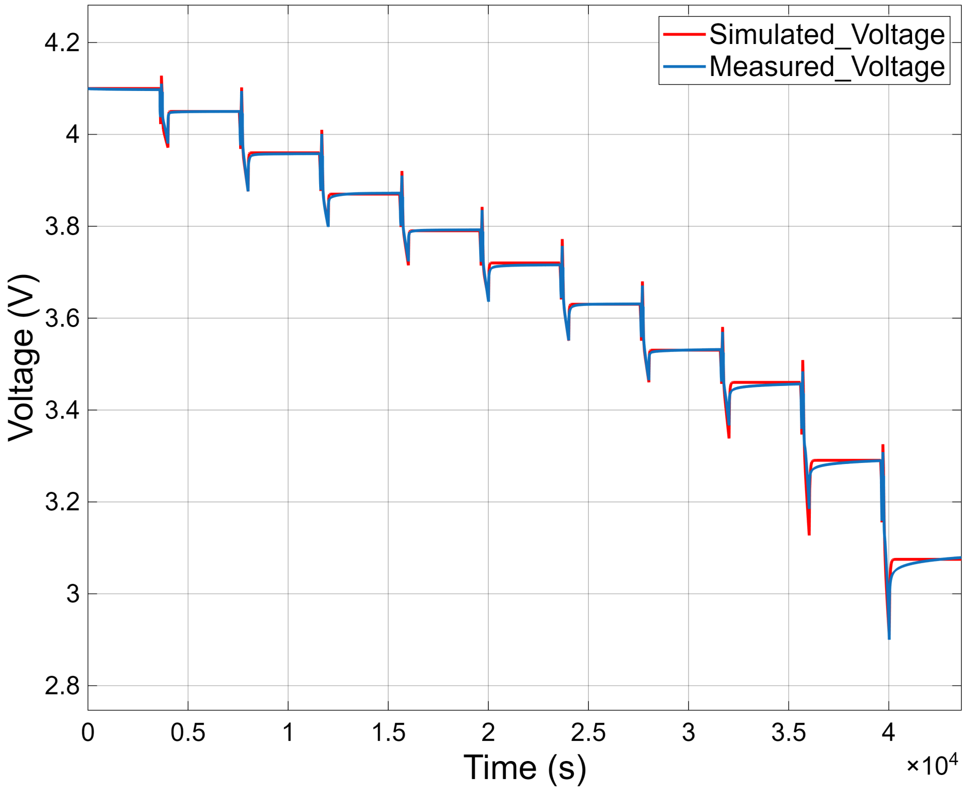

Figure 5.15: HPPC simulation - Voltage vs. Time

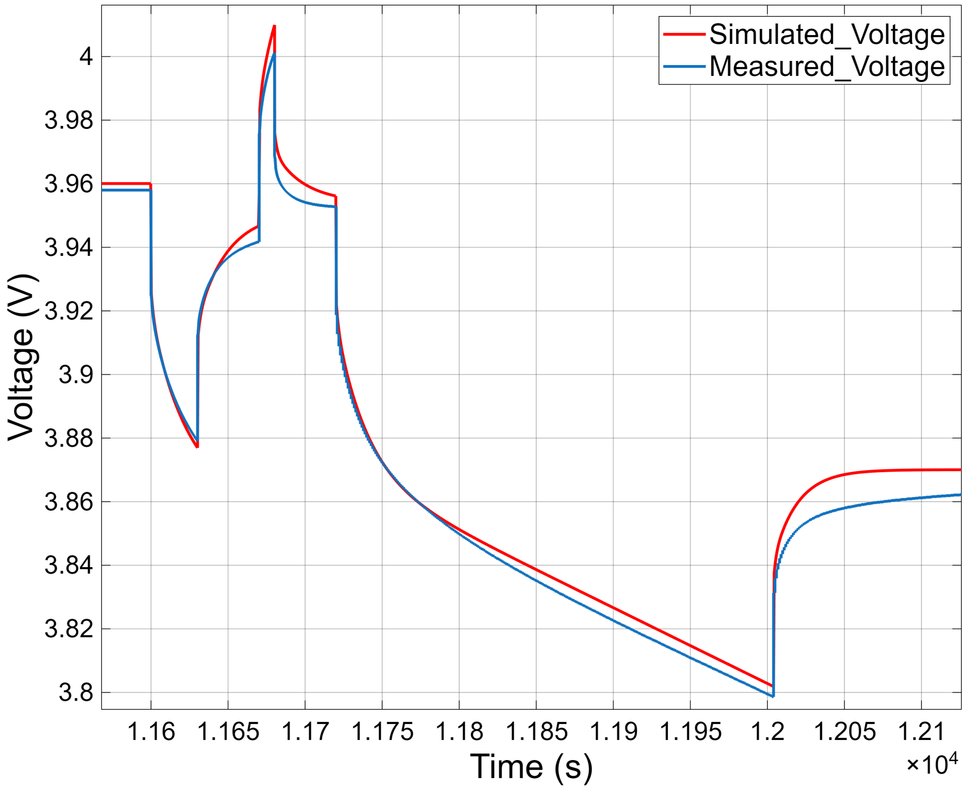

Figure 5.16: HPPC simulation - Voltage vs. Time - Zoom

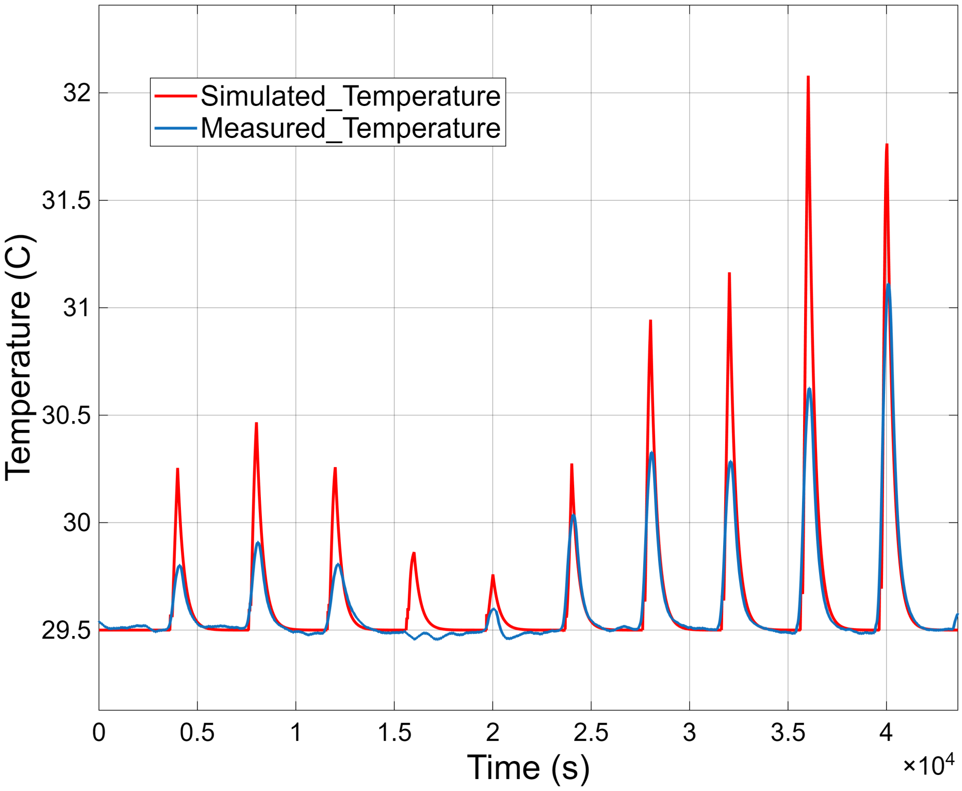

Figure 5.17: HPPC simulation - Temperature vs. Time

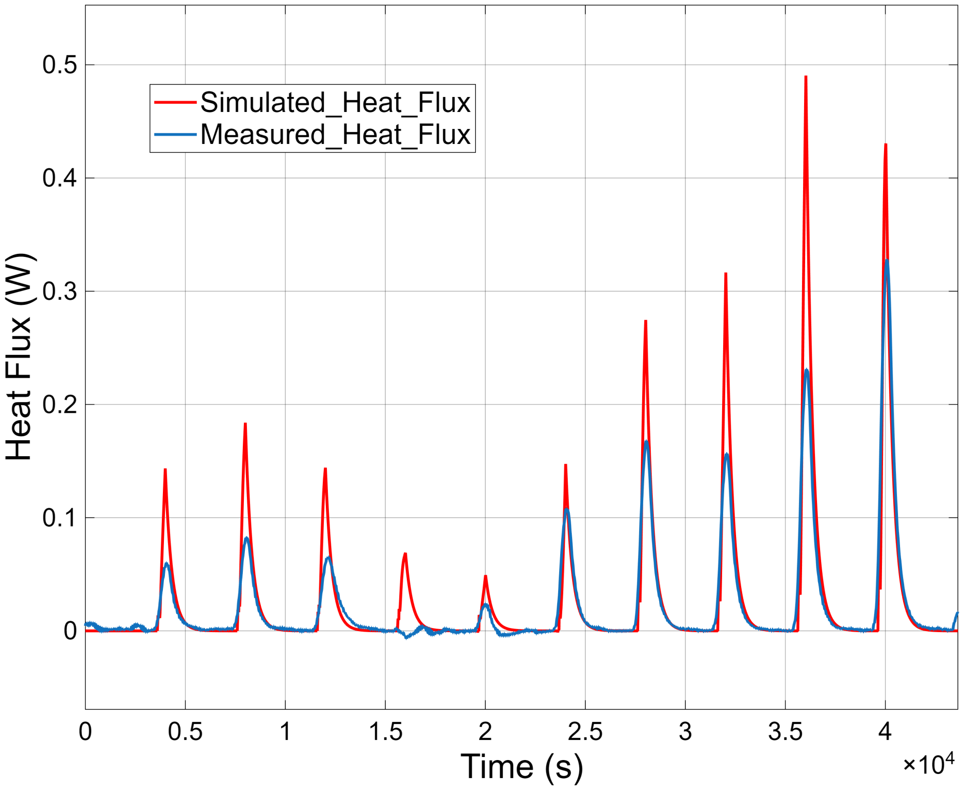

Figure 5.18: HPPC simulation - Heat Flux vs. Time

5.3.2 Random Walk (RW) Simulation Results

As introduced in Section 5.3.1, the RW test profile has been developed from scratch with the purpose of intensively testing the battery model performance on a novel test cycle including both high current discharge and charge pulses, hypothetically representing the operation of a battery powered EV on a demanding track, requiring both fast accelerations and subsequent energy regenerations while braking. In addition, being the test completely uncorrelated to the HPPC philosophy used for the characterization of the electrothermal model, this approach should potentially validate the model capability withouth any data overfitting. Table 5.1 shows the RW test implementation on the Neware BTS. Note that the charge current never exceeds the charge rate limit of 3C according to the datasheet (Table 2.1).

Table 5.1: Random walk test implementation

			Set Values		**Cut-off Limits**		
Id	**Step Name**	**Time**	**Voltage**	**Current**	**Voltage**	**Current**	**Notes**
1	Rest	00:01:00	-	-	-	-	
2	CC DChg	00:01:00	-	4,5 A	2,9 V	-	1C Discharge
3	CC Chg	00:00:20	-	4,5 A	4,1 V	-	1C Charge
4	Rest	00:00:10	-	-	-	-	
5	CC DChg	00:01:00	-	9 A	2,9 V	-	2C Discharge
6	CC Chg	00:00:20	-	9 A	4,1 V	-	2C Charge
7	Rest	00:00:10	-	-	-	-	
8	CC DChg	00:01:00	-	13,5 A	2,9 V	-	3C Discharge
9	CC Chg	00:00:20	-	13,5 A	4,1 V	-	3C Charge
10	Rest	00:00:10	-	-	-	-	
11	CC DChg	00:01:00	-	18 A	2,9 V	-	4C Discharge
12	CC Chg	00:00:20	-	13,5 A	4,1 V	-	3C Charge
13	Rest	00:00:10	-	-	-	-	
14	Cycle	-	-	-	-	-	Start step ID:2, Count:7
15	CC DChg	-	-	4,5 A	2,9 V	-	Final 1C Discharge
16	End	-	-	-	-	-	

The corresponding input current profile that has been provided to the model is presented in Figure 5.19. The resulting SOC behaviour is shown in Figure 5.20.

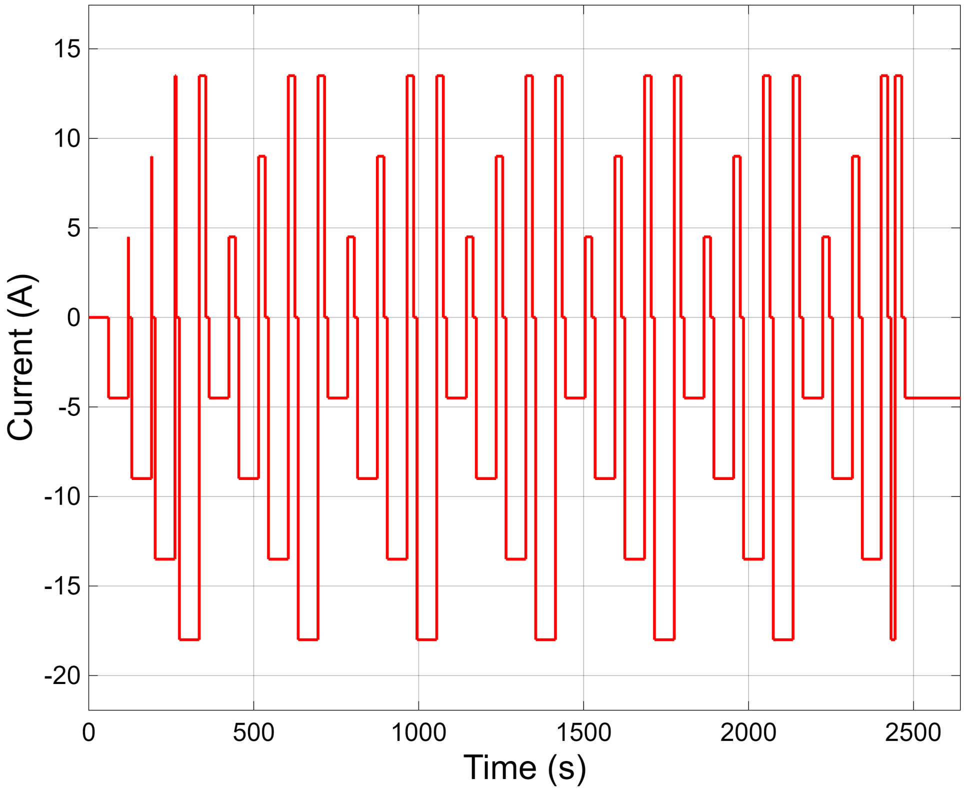

Figure 5.19: RW simulation - Current vs. Time

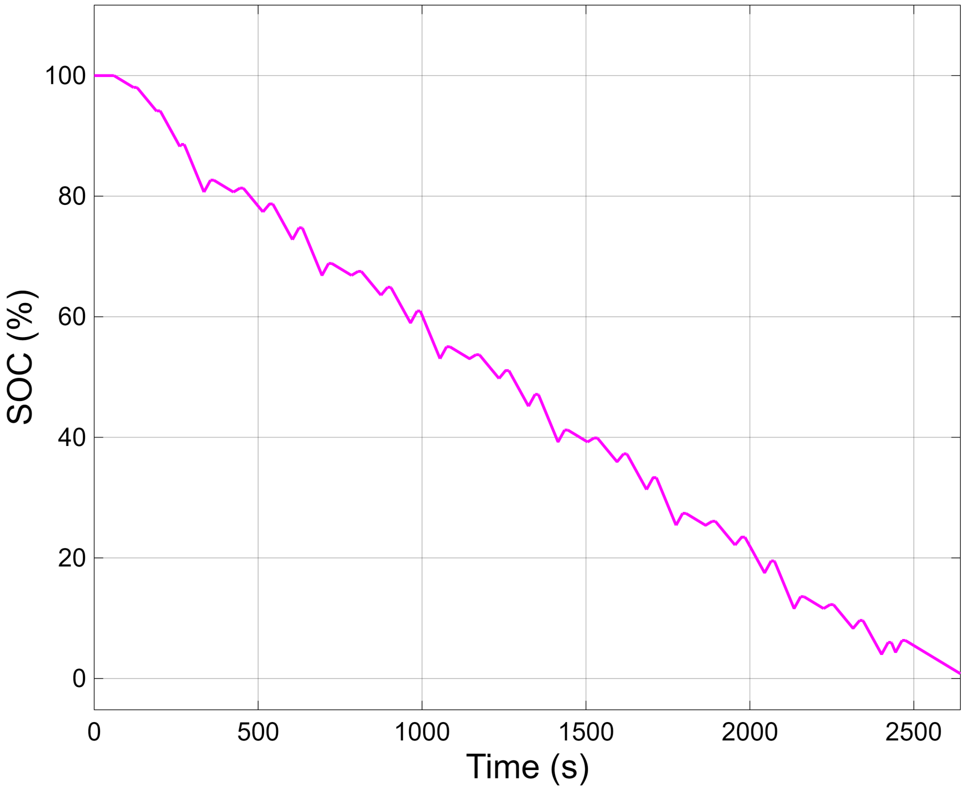

Figure 5.20: RW simulation - SOC vs. Time

The following figures show the RW simulation results compared to the experimental data measured at the test bench:

- **Heat Generation**: Figure 5.21 shows the evolution of heat generation terms $\dot{Q}_{irr}$, $\dot{Q}_{rev}$ and $\dot{Q} = \dot{Q}_{irr} + \dot{Q}_{rev}$ during the test. It can be seen that the irreversible heat generation is approximately one order of magnitude bigger than the reversible one, but that both contributions are generally not negligible for the calculation of the total heat generation $\dot{Q}$. One can notice how, for the same SOC, the term $\dot{Q}_{rev}$ changes sign between charging and discharging, while $\dot{Q}_{irr}$ sign always remains the same (positive)
- **Voltage**: Figure 5.22 shows the behaviour of voltage, while 5.23 the absolute voltage error of the simulated value against the measured
- **Temperature**: Figure 5.24 shows the behaviour of temperature, while 5.25 the absolute temperature error of the simulated value against the measured
- **Heat Flux**: Figure 5.26 shows the behaviour of heat flux, while 5.27 the absolute heat flux error of the simulated value against the measured

Similar considerations to the HPPC case apply. The complete observations and final verdict on model performance is discussed in detail in Section 5.3.3.

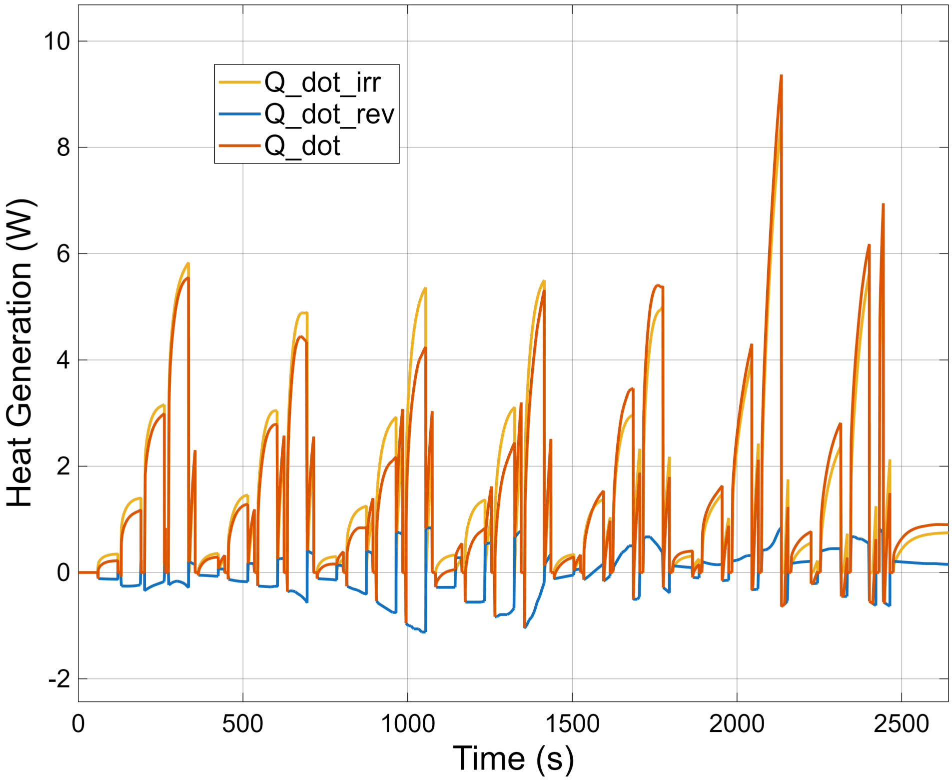

Figure 5.21: RW simulation - Heat Generation vs. Time

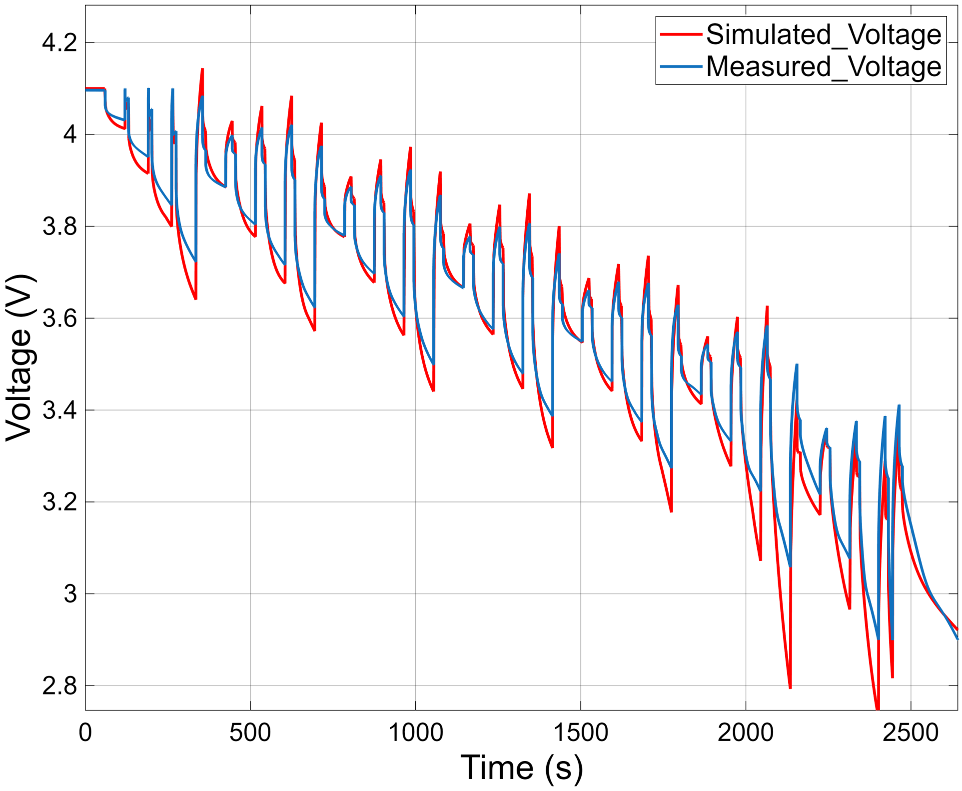

Figure 5.22: RW simulation - Voltage vs. Time

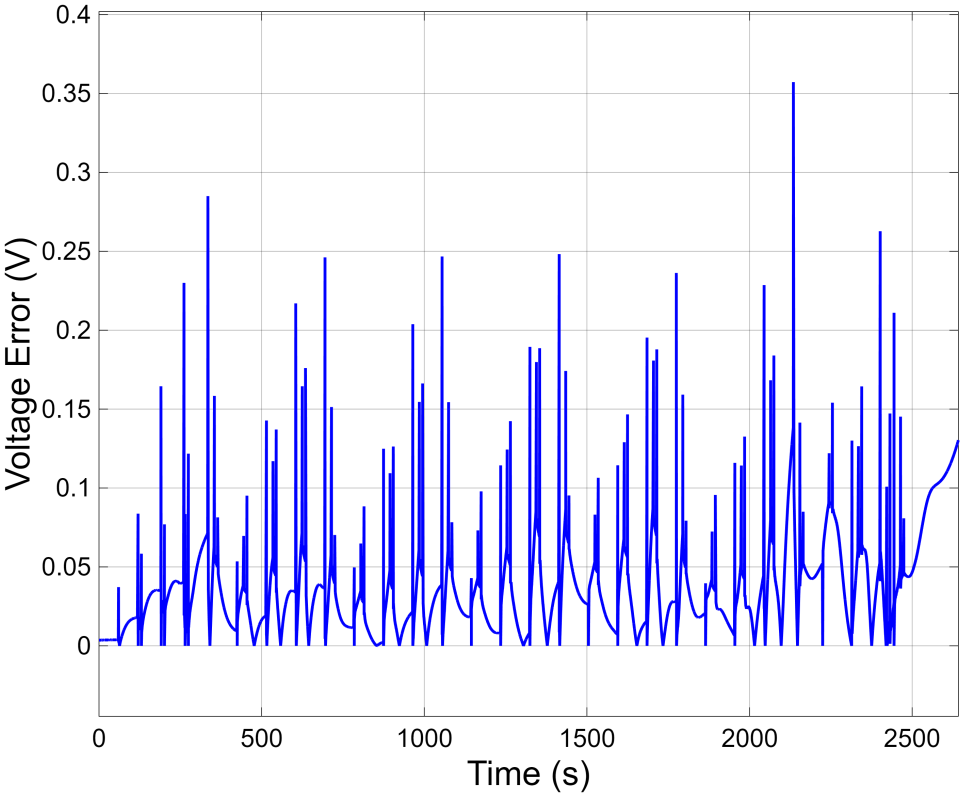

Figure 5.23: RW simulation - Voltage Error vs. Time

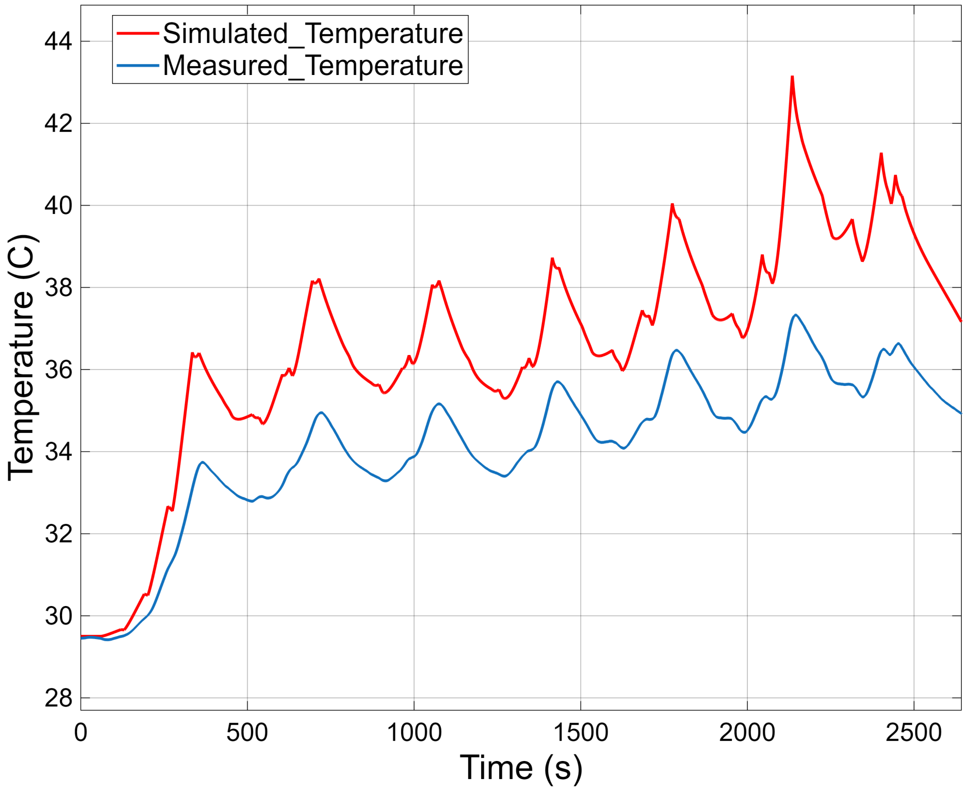

Figure 5.24: RW simulation - Temperature vs. Time

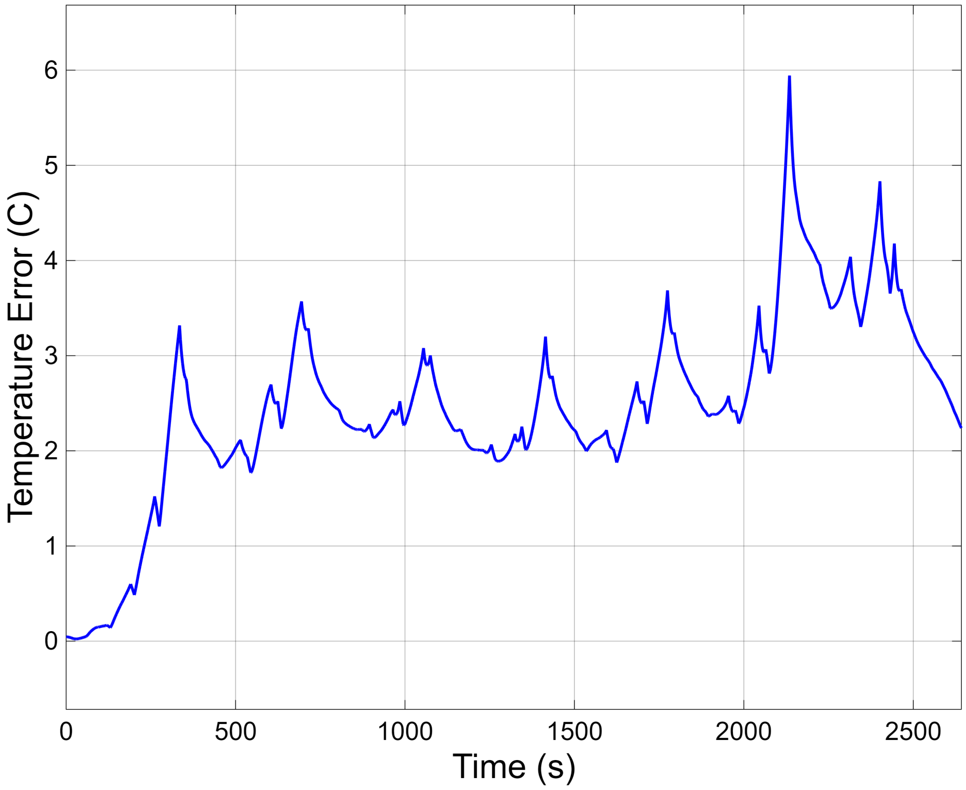

Figure 5.25: RW simulation - Temperature Error vs. Time

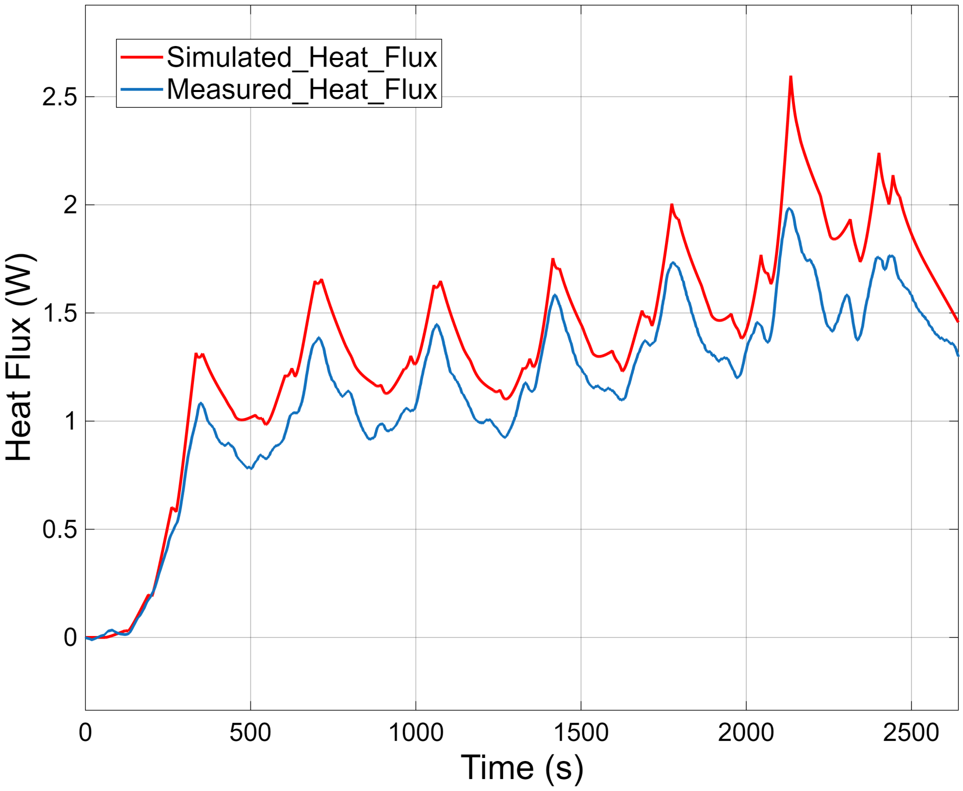

Figure 5.26: RW simulation - Heat Flux vs. Time

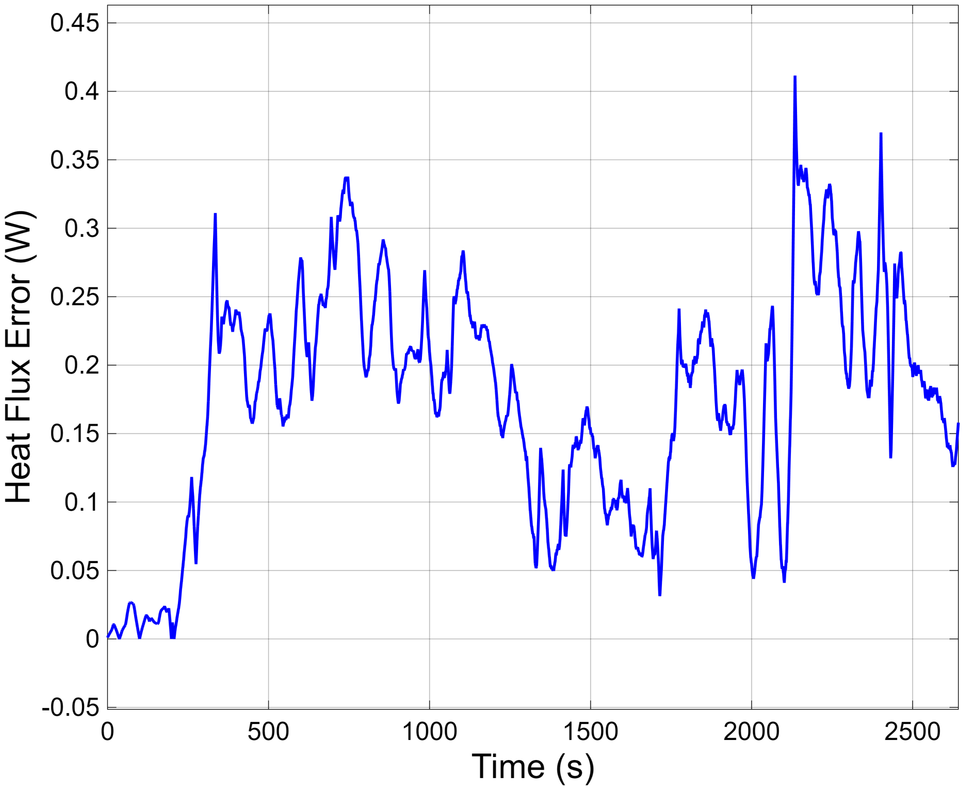

Figure 5.27: RW simulation - Heat Flux Error vs. Time

5.3.3 Model Results Analysis and Limitations

Table 5.2 shows the resulting absolute and RMS error achieved by the model during the HPPC and RW simulations.

Table 5.2: Model errors for HPPC and RW tests

Variable	**Metric**	**HPPC Test**	**RW Test**
Voltage	Maximum Absolute Error (V)	0,1	0,4
	RMS Error (V)	0,0076	0,045
Temperature	Maximum Absolute Error (°C)	1,5	6
	RMS Error (°C)	0,14	2,4
Heat Flux	Maximum Absolute Error (W)	0,3	0,4
	RMS Error (W)	0,025	0,20

Overall:

- the **electrical model** shows a good performance, that is well within the typical target RMS voltage error of 50 mV for standard automotive applications [20, 15, 14, 22]. More demanding systems, having stricter RMS voltage error requirements (< 10 mV), should consider more precise characterization approaches and/or advanced modelling strategies
- the **thermal model** shows a sufficient performance, that is sligthly outside the typical target RMS temperature error of 2 °C for standard automotive applications [43, 44, 8]. Anyway, the model presents capabilities in line with other first order models, and its accuracy has been proven to be suitable for optimization with a better tuning of the model parameters. For advanced applications, requiring sub degree RMS temperature error accuracy (< 1 °C), a second order or other more advanced characterization and modelling approaches should be considered

So, as a conclusion, the electrical model has reached the expectations that have been set at the start of this work (building a sufficiently accurate model that could be used as a starting point for an automotive grade system), while the thermal model requires some additional attention for maximising its potential and making it suitable for an automotive level solution.

The following observations on the validity of the results and limitations of the model have to be discussed:

- **Voltage**: Considering the HPPC test specifically, because the OCV breakpoints used to extract the characteristic curve (OCV vs. SOC) are exactly the same ones as those employed in the simulation, the steady-state error in the voltage trace is expectedly very small. Nevertheless, even considering this aspect, and the fact that the R and C parameters were derived from the same test, minor inconsistencies can still be observed in both the static and (more noticeably) the dynamic voltage behaviour (Figure 5.16). These errors, that at a first glance would seem unexpected, are potentially due to three reasons:

  1. **The OCV estimation is not precise**. In fact, when fitting the voltage curves (Section 3.2.2.3), a voltage offset correction parameter (named c) has been used to correct small OCV variations. This tiny offset has not been taken back into the OCV curve calculation and may lead to small OCV estimation errors. More in general, the true OCV knowledge is something that has been proven to be quite difficult to obtain by using only HPPC data, as the 10% SOC resolution and the absence of hysteresis information resulted to be a significant shortcoming of this approach

  2. **The fitted parameters are not exact**. During HPPC testing, the pulse duration, both during charge and discharge, is quite fast compared to the time constant of battery electrochemistry (the discharge and charge pulses last only 30 and 10 seconds respectively, while battery phenomeas can be much slower). This fundamentally limits the order of magnitude of the time constant that can be extrapolated from the battery physics. The slow dynamics of battery cells have time constants reaching a value of tenths (or hundreds) of seconds, and to accurately extract them, the test data must last for at least three to five times the lenght of the time constant. This leads to the general observation that (maybe) HPPC is not the best methodology for electrical ECM parameters extraction, or at the same time that a possible idea could be the one of trying to fit the voltage curve during the 10% SOC dicharge to retrieve further data

  3. **The model is not perfect**. The ECM equations assume that R and C are, for a given SOC and temperature, constant values. In reality, battery kinetics are governed by the Butler-Volmer equation (that describes the relationship between current and voltage overpotential, which is highly non-linear with respect to current especially at high current rates and cannot be approximated by Ohm's law as done in this work) and diffusion equations (which scale with the square root of time according to Fick's

laws of diffusion, and are not pure exponentials as it has been assumed). In addition, it is always important to remind that R and C do not actually exist inside the battery and are just mathematical fitting artifacts

Thus, the electrical model is far from exact, and even when run on the same data it has been derived from, it still produces some errors

- **Temperature**: Similar considerations can be applied to the thermal model, that is not perfect, and to its parameters, that are not exact, too. As expected with a first order lumped capacitance approach (as discussed in Section 4.3, in this case $Bi \approx 0.16$), the simulated temperature represents the bulk average of the cell rather than the localized surface casing. Consequently, the model exhibits a slight positive deviation (overestimation) compared to the experimental surface thermocouple data, as it inherently captures the higher thermal energy of the internal core without the physical conduction lag. In reality, since heat is generated inside the jelly roll, the core exhibits a higher temperature than the external casing. In this model, since the bulk average temperature is calculated, it is reasonable to have a simulated temperature higher than the experimentally measured one. For the same reason, due to the absence of the thermal lag from the inside to the outside of the cell for heat to flow through, the model also tends to slightly anticipate the temperature rise when compared to the experimental results

- **Heat Flux**: The same observations made for temperature apply (as the estimated temperature is higher, a higher heat flux is expected). In fact, the equation that governs the heat transfer is Newton's law of cooling

  $$\dot{Q} = h(T - T_a) \tag{5.6}$$

  and because the heat flux coefficient h and the ambient temperature T_a are constants, the heat flux $\dot{Q}$ just follows the same trend as temperature (slightly overestimating the heat transfer maximum value). Anyway, while the first order approach overestimates the instantaneous heat flux during the discharge phase, it does not violate conservation of energy, and the total heat exchanged should theoretically be the same

- **SOC**: As discussed multiple times within this thesis work, SOC estimation is a quite complex task. The sources of error in SOC estimation are multiple, and even a small inconsistency propagates to all the model parameters (R, C, OCV and EHC all depend on the SOC) causing considerable inaccuracies:

1. **The initial SOC estimation is not precise**. In this thesis work, the model has been always run starting from a fully charged battery condition (SOC=100%). In general, estimating the SOC from a generic starting point is possible by interpolating the OCV vs. SOC curve assuming that the battery is fully rested, but this condition rarely occours in real applications, and even in that case, the initial SOC estimation obtained using this method is quite poor

2. **The Coulomb counting method is not accurate**. Accumulated measuring errors and other drifts cause the SOC value estimation obtained by current integration to rapidly become massively incorrect. In particular, the battery rated capacity C_{Rated} (that is a fundamental part of Equation 5.1 used for SOC estimation) is far from a constant value and depends on multiple factors like current rate, temperature, current sign, and so on. Thus, in practice, Coulomb counting becomes unusable as soon as the simulation test profile complexity goes slightly above the one reached within this thesis work, and more complex approaches are required

As a matter of fact, in modern battery models more advanced SOC estimation tecniques are utilized, like Kalman filters (like Extended Kalman Filters (EKFs) and Unscented Kalman Filters (UKFs)), particle filters, adaptive H∞ filters, proportional-integral and sliding mode observers or even artificial neural networks [24, 20].

Conclusion

In this thesis, a complete overview of Li-ion cell electrothermal characterization has been presented. First, a complete analysis of the literature on the topic has been realised. Then, considering the available intrumentation, the different testing methodologies have been scrutinized, and the most appropriate have been selected and developed. The test programs have been defined from scratch according to the electrothermal characterization objectives, and the quantities of interest have been monitored with high accuracy using advanced mesuarement systems. The test results have been analysed in detail, developing a custom data elaboration script having a simple graphical user interface, allowing people less experienced in the topic to continue the characterization work with lower effort. The electrical and thermal parameters have been calculated exploiting basic physics principle, providing a holistic approach and paving the road for future developments in the research. Finally, the entire methodology has been validated by simulating the electrothermal model on a simulation software and verifying the accordance with experimental data.

Summary of contributions

- Analysis of the literature on the topic
- Implementation of a test methodology according to the characterization objectives and considering the available instrumentation
- Execution of the tests using a battery tester, DAQ system, and thermal chamber
- Study of the test results, developing data elaboration scripts and extracting equivalent circuit parameters
- Implementation of the most appropriate modelling strategies using advanced simulation software, validating the results against experimental data

Limitations

- HPPC showed its limits for the purpose of equivalent circuit parameters estimation, a different tetsing methodology could be considered for future testing
- The first order thermal model accuracy proved to be quite limited, more advanced characterization and modelling tecniques should be evaluated

Future work suggestions

- Analysis on full cell voltage range proposed by the manufacturer
- Performing characterization at different temperatures, implementing temperature dependency into the model
- Extrapolation of the thermal conductivity
- Implementation of more advanced SOC estimation algorithms
- Integration in the BMS and real world testing

A

Scripts Availability

The complete Matlab source code containing the full scripts developed for the characterization and simulation of Li-ion battery cells in this thesis are publicly available on GitHub. The repository includes the data it has been used for running the code and extracting the data, enabling anyone with the capability of reproducing (and possibly improving) the results discussed within this work.

The repository can be accessed at the following GitHub link:
`https://github.com/LTrussardi/Electrothermal-Characterization-of-Li-ion-Battery-Cells`
and a permanent archival version is available on Zenodo at:
`https://doi.org/10.5281/zenodo.18979940`

A brief guide on how to use the scripts is available in Appendix B.

B

Scripts Usage Guide

The repository where the scrips have been published is available in Appendix A.

This Appendix contains a brief guide on how to use the Matlab data analysis scripts and the Simulink model that have been developed as part of this thesis work.

Data Import for Matlab Scripts

First of all, the input data needs to be placed in a folder in the same directory as the Matlab file. The data should be exported according to the following procedure:

- For **Neware** data (voltages, currents, ...)
  Once the test is completed, export the data from Neware BTSDA software (orange icon) using these settings
  1. Export report
  2. Export type: “Customize report”
  3. Export format: “EXCEL”
  4. Export templateConfiguration: “DefaultTemplate”
  5. Click “Export”, a .xlsx file is produced
- For **Dewesoft** data (temperatures, heat fluxes, ...)
  Once the test is completed, export the data from DewesoftX software (starting from the Data file) using these settings
  1. Export type: “EXCEL”
  2. Select the channels you want to export
  3. Click “Export”

Then, data should be imported in the code. This can be done manually or automatically by the code:

- **Automatic import**: To automatically import data, select “Import” when the first window appears (different button for Neware and Dewesoft data), and follow the instructions
- **Manual import**: Otherwise, to manually import data, follow this procedure:
  - For **Neware** data (voltages, currents, ...)
    1. Import data using the Matlab “Import data” tool
    2. Select the Excel file containing the test data
    3. Select the “record” tab of the Excel sheet
    4. Set as output type “Table”
    5. Click on “Import selection”
    6. Close the “Import data” tool
  - For **Dewesoft** data (temperatures, heat fluxes, ...)
    1. Import data using the Matlab “Import data” tool
    2. Select the Excel file containing the test data
    3. Select the “Data1” tab of the Excel sheet
    4. Set as output type “Table”
    5. Click on “Import selection”
    6. Close the “Import data” tool

Constant Current Discharge Test Script

To start the script, run the *Cell_Testing_Data_Analysis_Code_LT_v9.m* file. The selection window in Figure B.1 will appear.

1) **Import NEWARE**: Automatic import of Neware data. Select one or more Neware data .xlsx files from the menu, the code will handle the import
2) **Import DEWESOFT**: Automatic import of Dewesoft data. Select one or more Dewesoft data .xlsx files from the menu, the code will handle the import
3) **Filter DEWESOFT**: Dewesoft data filtering using smoothdata to remove noise. Select one or more Dewesoft tables to filter from the menu, specify a filtering parameter (usually between 500 and 2000 works well), then a figure will appear showing the filtered data compared to the initial one. If happy with the result, confirm data overwriting clicking “Yes”, otherwise click “No” and repeat the procedure with a different filtering value
4) **Plot NEWARE VS Time (single test, multiple quantities)**: Plots one or more Neware quantities from a single test (e.g., current and voltage from the 1C discharge test). Select one Neware table from the menu, then select one or more quantities to plot. Finally, select the plotting style: “Single figure with subplots”, “Separate figures” or “Single plot with multiple axes” (the last option works well with up to two quantities, while the others can handle more)
5) **Plot DEWESOFT VS Time (single test, multiple quantities)**: Plots one or more Dewesoft quantities from a single test (e.g., temperature and heat flux density from the 1C discharge test). Select one Dewesoft table from the menu, then select one or more quantities to plot. Finally, select the plotting style: “Single figure with subplots”, “Separate figures” or “Single plot with multiple axes” (the last option works well with up to two quantities, while the others can handle more)
6) **Plot NEWARE VS Time (multiple tests, single quantity)**: Plots one Neware quantity from multiple tests (e.g., current from the 1C and 2C discharge tests). Select one or more Neware tables from the menu, then select one quantity to plot. The default plotting style is “Single figure, single plot”
7) **Plot DEWESOFT VS Time (multiple tests, single quantity)**: Plots one Dewesoft quantity from multiple tests (e.g., temperature from the 1C and 2C discharge tests). Select one or more Dewesoft tables from the menu, then select one quantity to plot. The default plotting style is “Single figure, single plot”

8) **Plot NEWARE and DEWESOFT VS Time (single test, multiple quantities)**: Merges Neware and Dewesoft data, allowing to plot one or more Neware and Dewesoft quantities from a single test together (e.g., current and temperature from the 1C discharge test). First, select one Neware table from the menu. then, select one Dewesoft table from the menu. After that, select one or more Neware quantities to plot. Afterwards, select one or more Dewesoft quantities to plot. Finally, select the plotting style: “Single figure with subplots”, “Separate figures” or “Single plot with multiple axes” (the last option works well with up to two quantities, while the others can handle more)

9) **Plot Discharge Voltage VS Capacity**: Plots the characteristic curve. Select one or more Neware tables from the menu. One figure will pop up with the final result

10) **Plot Voltage/Current Charging Phase**: Plots the voltage and current during charging. Select one Neware table from the menu. One figure will pop up with the final result. The default plotting style is “Single plot with multiple axes”

11) **Plot Voltage/Current Discharging Phase**: Plots the voltage and current during discharging. Select one Neware table from the menu. One figure will pop up with the final result. The default plotting style is “Single plot with multiple axes”

12) **Plot Temperature/Heat Flux Discharging Phase**: Plots the temperature and heat flux density during discharging. Select one data table from the menu. Two figures will pop up with the final result. The default plotting style is “Separate figures”

13) **Estimate Entropic Coefficient**: Estimates the EHC. Select one or more data tables from the menu. The script will provide figures containing the heat generation and EHC profiles. Remember to update the cell characteristics in the script (area, thermal capacity) if changed. The EHC data is then stored in the “ehc” variable and can be saved as a .mat file using the save command

14) **Export Data for SIMULINK**: Exports the voltage, current, temperature and heat flux traces to be used as inputs for the Simulink model. Select a table to export, the code will create .mat files containing the data

S) **Save Data to .mat files**: Saves the data stored in the DataNEWARE and DataDEWESOFT variables to two .mat files. Useful to avoid importing data every time (makes workflow faster)

L) **Load Data from .mat files**: Loads data from existing *DataNEWARE.mat* and *DataDEWESOFT.mat* files into the corresponding variables. Useful to avoid importing data every time (makes workflow faster)

C) **Close**: Closes the selection menu

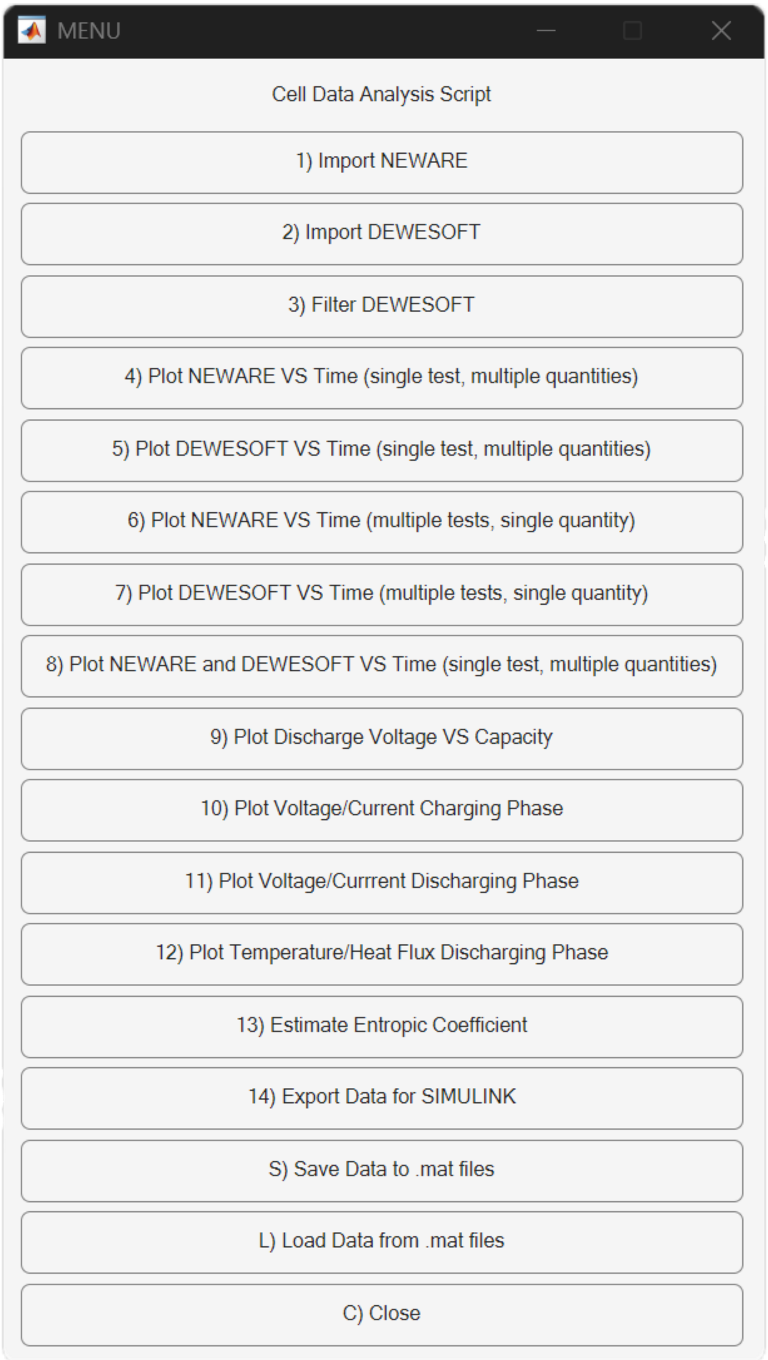

Figure B.1: Constant current discharge test script interface

HPPC Test Script

To start the script, run the *HPPC_Data_Analysis_Code_LT_v7.m* file. The selection window in Figure B.2 will appear.

1) **Import NEWARE**: Automatic import of Neware data. Select one or more Neware data .xlsx files from the menu, the code will handle the import

2) **Import DEWESOFT**: Automatic import of Dewesoft data. Select one or more Dewesoft data .xlsx files from the menu, the code will handle the import

3) **Filter DEWESOFT**: Dewesoft data filtering using smoothdata to remove noise. Select one or more Dewesoft tables to filter from the menu, specify a filtering parameter (usually between 500 and 2000 works well), then a figure will appear showing the filtered data compared to the initial one. If happy with the result, confirm data overwriting clicking “Yes”, otherwise click “No” and repeat the procedure with a different filtering value

4) **Plot NEWARE VS Time (single test, multiple quantities)**: Plots one or more Neware quantities from a single test (e.g., current and voltage from the 1C HPPC test). Select one Neware table from the menu, then select one or more quantities to plot. Finally, select the plotting style: “Single figure with subplots”, “Separate figures” or “Single plot with multiple axes” (the last option works well with up to two quantities, while the others can handle more)

5) **Plot DEWESOFT VS Time (single test, multiple quantities)**: Plots one or more Dewesoft quantities from a single test (e.g., temperature and heat flux density from the 1C HPPC test). Select one Dewesoft table from the menu, then select one or more quantities to plot. Finally, select the plotting style: “Single figure with subplots”, “Separate figures” or “Single plot with multiple axes” (the last option works well with up to two quantities, while the others can handle more)

6) **Plot NEWARE VS Time (multiple tests, single quantity)**: Plots one Neware quantity from multiple tests (e.g., current from two or more HPPC tests). Select one or more Neware tables from the menu, then select one quantity to plot. The default plotting style is “Single figure, single plot”

7) **Plot DEWESOFT VS Time (multiple tests, single quantity)**: Plots one Dewesoft quantity from multiple tests (e.g., temperature from two or more HPPC tests). Select one or more Dewesoft tables from the menu, then select one quantity to plot. The default plotting style is “Single figure, single plot”

8) **Plot NEWARE and DEWESOFT VS Time (single test, multiple quantities)**: Merges Neware and Dewesoft data, allowing to plot one or more Neware and Dewesoft quantities from a single test together (e.g., current and temperature from the 1C HPPC test). First, select one Neware table from the menu. then, select one Dewesoft table from the menu. After that, select one or more Neware quantities to plot. Afterwards, select one or more Dewesoft quantities to plot. Finally, select the plotting style: "Single figure with subplots" or "Separate figures"

9) **Create HPPC Data (MANUAL CODE)**: Elaborates the HPPC data following the approach described in Section 3.2. The script goes through all the HPPC tests in memory, and estimates the OCV and R, C parameters of the electrical ECM, providing the results as an output both in figures and in the command window. This part of the script uses the fit strategy developed in this thesis work

9E) **Export MANUAL Results to Excel file**: Exports the MANUAL results to an Excel file named *Exported_Battery_Params_MANUAL.xlsx*

10) **Create HPPC Data (MATLAB AUTO CODE)**: Elaborates the HPPC data following the approach described in Section 3.3. The script goes through all the HPPC tests in memory, and estimates the OCV and R, C parameters of the electrical ECM, providing the results as an output both in figures and in the command window. This part of the script uses the automated workflow proposed by Matlab in the Simscape Battery extension

10E) **Export AUTO Results to Excel file**: Exports the AUTO results to an Excel file named *Exported_Battery_Params_AUTO.xlsx*

11) **Compare HPPC Results**: Plots the MANUAL and AUTO results in common figures. Requires 9) and 10) to be run previously

12) **Estimate Heat Capacity**: Estimates the heat capacity. The script iterates through all the HPPC tests in memory and determines the thermal capacity and validates the result calculating the corresponding Biot number. Remember to update the cell characteristics in the script (area, mass, characteristic length, thermal conductivity) if changed

13) **Export Data for SIMULINK**: Exports the voltage, current, temperature and heat flux traces to be used as inputs for the Simulink model. Select a table to export, the code will create .mat files containing the data

S) **Save Data to .mat files**: Saves the data stored in the DataNEWARE and DataDEWESOFT variables to two .mat files. Useful to avoid importing data every time (makes workflow faster)

L) **Load Data from .mat files**: Loads data from existing *DataNEWARE.mat* and *DataDEWESOFT.mat* files into the corresponding variables. Useful to avoid importing data every time (makes workflow faster)

C) **Close**: Closes the selection menu

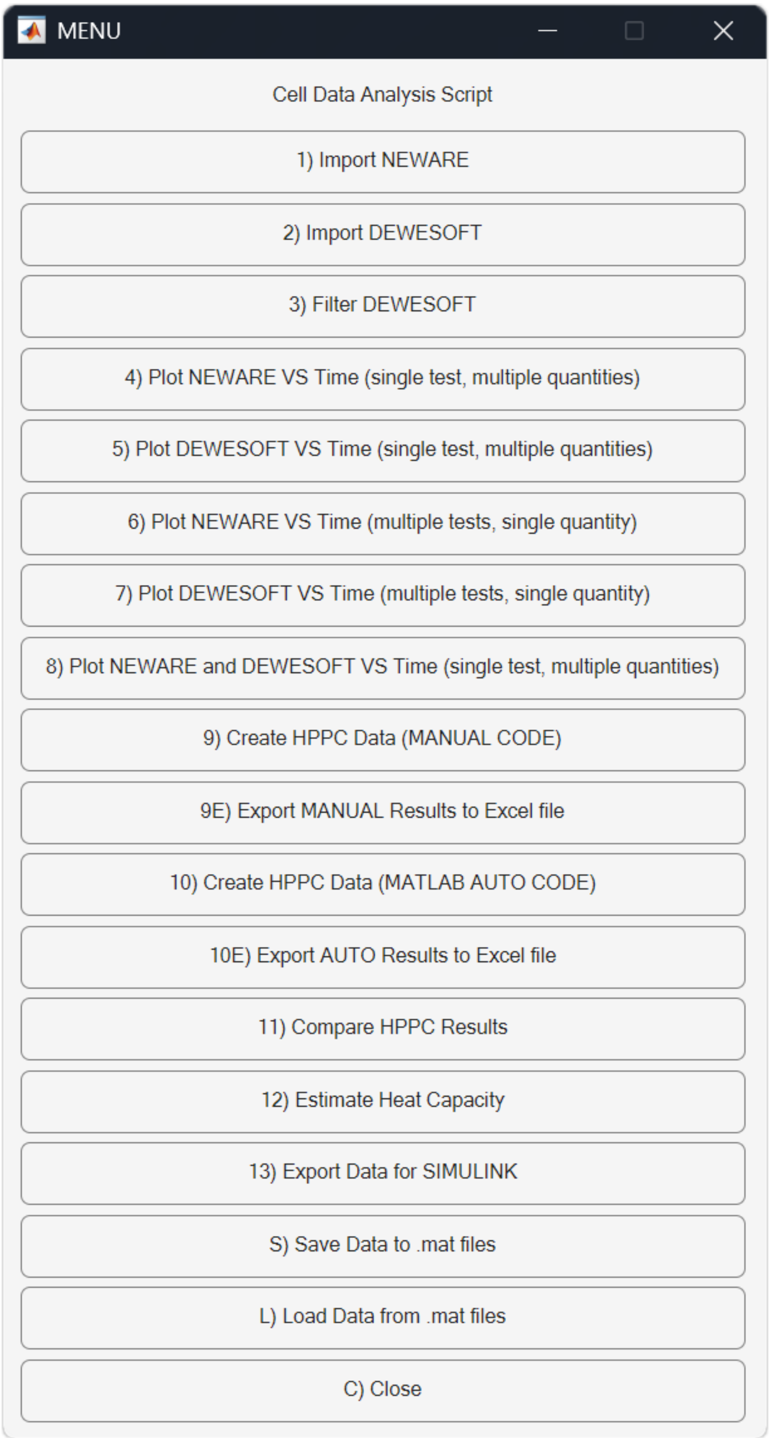

Figure B.2: HPPC test script interface

Random Walk Test Script

To start the script, run the *RW_Data_Analysis_Code_LT_v1.m* file. The selection window in Figure B.3 will appear.

1) **Import NEWARE**: Automatic import of Neware data. Select one or more Neware data .xlsx files from the menu, the code will handle the import

2) **Import DEWESOFT**: Automatic import of Dewesoft data. Select one or more Dewesoft data .xlsx files from the menu, the code will handle the import

3) **Filter DEWESOFT**: Dewesoft data filtering using smoothdata to remove noise. Select one or more Dewesoft tables to filter from the menu, specify a filtering parameter (usually between 500 and 2000 works well), then a figure will appear showing the filtered data compared to the initial one. If happy with the result, confirm data overwriting clicking “Yes”, otherwise click “No” and repeat the procedure with a different filtering value

4) **Plot NEWARE VS Time (single test, multiple quantities)**: Plots one or more Neware quantities from a single test (e.g., current and voltage from one RW test). Select one Neware table from the menu, then select one or more quantities to plot. Finally, select the plotting style: “Single figure with subplots”, “Separate figures” or “Single plot with multiple axes” (the last option works well with up to two quantities, while the others can handle more)

5) **Plot DEWESOFT VS Time (single test, multiple quantities)**: Plots one or more Dewesoft quantities from a single test (e.g., temperature and heat flux density from one RW test). Select one Dewesoft table from the menu, then select one or more quantities to plot. Finally, select the plotting style: “Single figure with subplots”, “Separate figures” or “Single plot with multiple axes” (the last option works well with up to two quantities, while the others can handle more)

6) **Plot NEWARE VS Time (multiple tests, single quantity)**: Plots one Neware quantity from multiple tests (e.g., current from two or more RW tests). Select one or more Neware tables from the menu, then select one quantity to plot. The default plotting style is “Single figure, single plot”

7) **Plot DEWESOFT VS Time (multiple tests, single quantity)**: Plots one Dewesoft quantity from multiple tests (e.g., temperature from two or more RW tests). Select one or more Dewesoft tables from the menu, then select one quantity to plot. The default plotting style is “Single figure, single plot”

8) **Plot NEWARE and DEWESOFT VS Time (single test, multiple quantities)**: Merges Neware and Dewesoft data, allowing to plot one or more Neware and Dewesoft quantities from a single test together (e.g., current and temperature from one RW test). First, select one Neware table from the menu. then, select one Dewesoft table from the menu. After that, select one or more Neware quantities to plot. Afterwards, select one or more Dewesoft quantities to plot. Finally, select the plotting style: “Single figure with subplots” or “Separate figures”

9) **Export Data for SIMULINK**: Exports the voltage, current, temperature and heat flux traces to be used as inputs for the Simulink model. Select a table to export, the code will create .mat files containing the data

S) **Save Data to .mat files**: Saves the data stored in the DataNEWARE and DataDEWESOFT variables to two .mat files. Useful to avoid importing data every time (makes workflow faster)

L) **Load Data from .mat files**: Loads data from existing *DataNEWARE.mat* and *DataDEWESOFT.mat* files into the corresponding variables. Useful to avoid importing data every time (makes workflow faster)

C) **Close**: Closes the selection menu

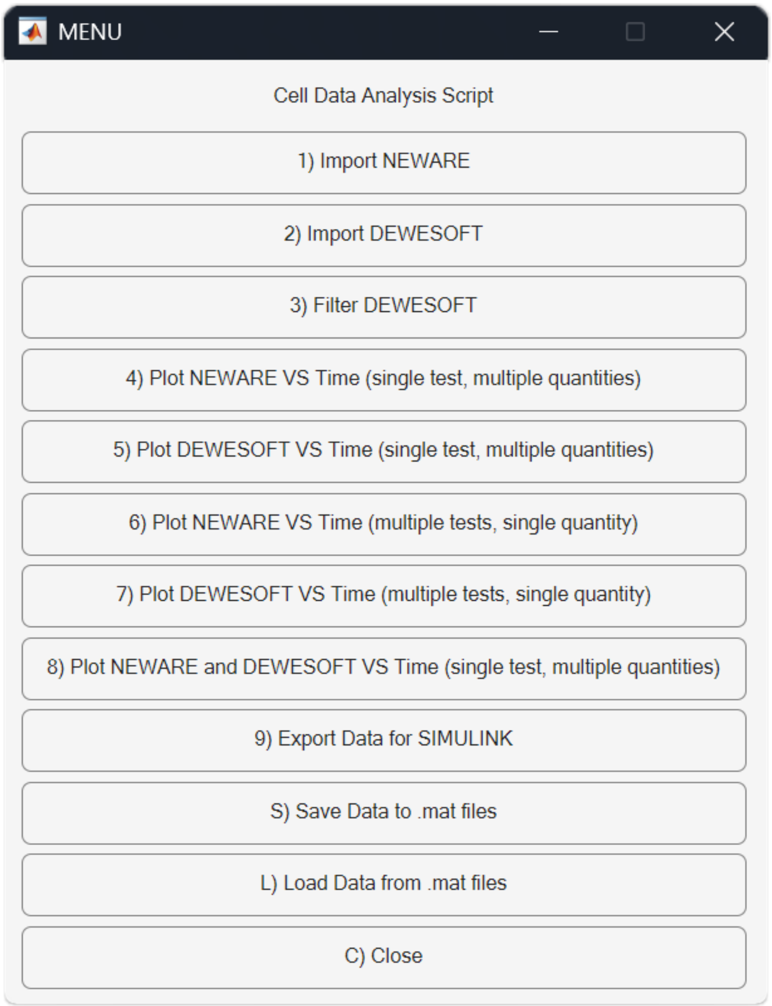

Figure B.3: Random walk tests script interface

Simulink Model

To open the model, run the *Battery_Electrothermal_Model_LT.slx* file. To load the model parameters in the workspace, run the *setup_battery_parameters.m* script (anyway, the model has the script set in its dependencies, so upon running the simulation it will automatically run the setup script, and if not in the right directory the user will be prompted with an error message). The inputs for the simulation, created by previous scripts, need to be provided in the same directory as the .slx file:

- Current profile: *Current_Profile.mat*
- Voltage profile: *Voltage_Profile.mat*
- Temperature profile: *Temperature_Profile.mat*
- Heat flux density profile: *Heat_Flux_Density_Profile.mat*

Once all the relative files have been prepared in the directory and the model has been opened, the simulation can be started clicking the “Run” button.

Bibliography

[1] Xuezhi Yang et al. “The Li-ion battery industry and its challenges”. In: *Nature Reviews Chemistry* (2025). DOI: `10.1038/s41570-025-00742-2`. URL: `https://www.nature.com/articles/s41570-025-00742-2`.

[2] Battery University. *BU-205: Types of Lithium-ion*. URL: `https://batteryuniversity.com/article/bu-205-types-of-lithium-ion` (visited on 2026-01-13).

[3] Battery University. *BU-216: Summary Table of Lithium-based Batteries*. URL: `https://batteryuniversity.com/article/bu-216-summary-table-of-lithium-based-batteries` (visited on 2026-01-13).

[4] G. Zubi et al. “The lithium-ion battery: State of the art and future perspectives”. In: *Renewable and Sustainable Energy Reviews* (2018). DOI: `10.1016/j.rser.2018.03.002`.

[5] BatteryDesign.net. *Battery Design: From Chemistry to Pack*. URL: `https://www.batterydesign.net/` (visited on 2026-01-15).

[6] Richtek Technology Corporation. *Li-ion Battery and Gauge Introduction*. Application Note AN024. Richtek Technology Corporation. URL: `https://www.richtek.com/Design%20Support/Technical%20Document/AN024` (visited on 2026-01-16).

[7] Takumi Yamanaka et al. “Multi-Physics Equivalent Circuit Models for a Cooling System of a Lithium Ion Battery Pack”. In: *Batteries* (2020). DOI: `10.3390/batteries6030044`.

[8] Xinfan Lin et al. “A lumped-parameter electro-thermal model for cylindrical batteries”. In: *Journal of Power Sources* (2014). DOI: `10.1016/j.jpowsour.2014.01.097`.

[9] Sumukh Surya et al. “Smart Core and Surface Temperature Estimation Techniques for Health-Conscious Lithium-Ion Battery Management Systems: A Model-to-Model Comparison”. In: *Energies* (2022). DOI: `10.3390/en15020623`. URL: `https://www.mdpi.com/1996-1073/15/2/623`.

[10] N.P. Williams et al. “Experimental determination of the entropic heat coefficient of a lithium-ion cell through immersion in a dielectric fluid”. In: *Applied Thermal Engineering* (2025). DOI: `https://doi.org/10.1016/j.applthermaleng.2024.124597`. URL: `https://www.sciencedirect.com/science/article/pii/S1359431124022658`.

[11] Thomas S. Bryden et al. “Methodology to determine the heat capacity of lithium-ion cells”. In: *Journal of Power Sources* (2018). DOI: `10.1016/j.jpowsour.2018.05.084`.

[12] Mohammad Shahjalal, Yashraj Tripathy, and Muhammad Sheikh. “Investigation on thermal performance analysis of a pouch Li-ion battery under various drive cycle profiles”. In: *Journal of Energy Storage* (2023). DOI: `10.1016/j.est.2023.108977`.

[13] Kaiyuan Li and King Jet Tseng. “Energy efficiency of lithium-ion battery used as energy storage devices in micro-grid”. In: *IECON 2015 - 41st Annual Conference of the IEEE Industrial Electronics Society*. 2015. DOI: `10.1109/IECON.2015.7392923`.

[14] Nicolò Zatta et al. “Holistic Testing and Characterization of Commercial 18650 Lithium-Ion Cells”. In: *Batteries* (2024). DOI: `10.3390/batteries10070248`.

[15] Davide Cittanti et al. “Modeling Li-Ion Batteries for Automotive Application: a Trade-Off between Accuracy and Complexity”. In: *2017 International Conference of Electrical and Electronic Technologies for Automotive (EETA)*. Torino, Italy, 2017. DOI: `10.23919/EETA.2017.7993213`.

[16] Raul Octavian Nemes et al. “Parameters identification using experimental measurements for equivalent circuit Lithium-Ion cell models”. In: *2019 11th International Symposium on Advanced Topics in Electrical Engineering (ATEE)*. Bucharest, Romania, 2019. DOI: `10.1109/ATEE.2019.8723659`.

[17] Jinghua Sun and Josef Kainz. “Optimization of hybrid pulse power characterization profile for equivalent circuit model parameter identification of Li-ion battery based on Taguchi method”. In: *Journal of Energy Storage* (2023). DOI: `10.1016/j.est.2023.108034`.

[18] Gary Hunt. *FreedomCAR Battery Test Manual For Power-Assist Hybrid Electric Vehicles*. DOE/ID-11069. Idaho National Engineering and Environmental Laboratory, 2003.

[19] Jon P. Christophersen. *Battery Test Manual For Electric Vehicles*. INL/EXT-15-34184 Revision 3. Idaho National Laboratory, 2015. URL: `http://www.inl.gov`.

[20] Shrisha Balkur. "Electro-Thermal modelling of LFP Prismatic cell with SOC estimation model". Master's Thesis. Gothenburg, Sweden: Chalmers University of Technology, 2020.

[21] Rares Catalin Nacu and Daniel Fodorean. "Lithium-Ion Cell Characterization, Using Hybrid Current Pulses, for Subsequent Battery Simulation in Mobility Applications". In: *Processes* (2022). DOI: `10.3390/pr10102108`.

[22] Leonardo Pasquali. "State of Charge and parameter estimation for a 48V Lithium-Ion battery based on temperature dependent second-order RC model". Master's Thesis. Torino, Italy: Politecnico di Torino, 2022.

[23] Tadeusz Białoń et al. "HPPC Test Methodology Using LFP Battery Cell Identification Tests as an Example". In: *Energies* (2023). DOI: `10.3390/en16176239`.

[24] Ruoyu Xu. "Lithium-ion battery modeling and SoC estimation". Master's Thesis. Stockholm, Sweden: KTH Royal Institute of Technology, 2023.

[25] Witold Maranda. "Capacity Degradation of Lead-acid Batteries Under Variable-depth Cycling Operation in Photovoltaic System". In: 2015. DOI: `10.1109/MIXDES.2015.7208584`.

[26] Suguna Thanagasundram et al. "A Cell Level Model for Battery Simulation". In: *European Electric Vehicle Congress*. Brussels, Belgium, 2012.

[27] W. Weppner and R. A. Huggins. "Determination of the Kinetic Parameters of Mixed-Conducting Electrodes and Application to the System Li_3Sb". In: *Journal of The Electrochemical Society* (1977). DOI: `10.1149/1.2133112`. URL: `https://doi.org/10.1149/1.2133112`.

[28] Jaeyoung Kim et al. "Principles and Applications of Galvanostatic Intermittent Titration Technique for Lithium-ion Batteries". In: *J. Electrochem. Sci. Technol* (2022). DOI: `10.33961/jecst.2021.00836`. URL: `http://jecst.org/journal/view.php?number=409`.

[29] Initial Energy Science and Technology (IEST) Co., Ltd. *Entering Electrochemistry | GITT Analyzes The Diffusion Kinetics Of Lithium Batteries*. URL: `https://iestbattery.com/case/gitt-analyzes-batteries-diffusion-kinetics/` (visited on 2025-01-20).

[30] Alexandros Ch. Lazanas and Mamas I. Prodromidis. "Electrochemical Impedance Spectroscopy - A Tutorial". In: *ACS Measurement Science Au* (2023). DOI: `10.1021/acsmeasuresciau.2c00070`. URL: `https://doi.org/10.1021/acsmeasuresciau.2c00070`.

[31] Marco Grossi and Bruno Riccò. "Electrical impedance spectroscopy (EIS) for biological analysis and food characterization: a review". In: *Journal of*

Sensors and Sensor Systems (2017). URL: `https://api.semanticscholar.org/CorpusID:54071288`.

[32] Marco Steinhardt. “Experimental Investigation of the Thermal Conductivity through the Layers of the Electrode-Separator Stack in Lithium-Ion Cells”. Doctoral dissertation. Technischen Universität München, 2022.

[33] D. Kim, S. Lee, and I. Yang. “Verification of thermal conductivity measurements using guarded hot plate and heat flow meter methods”. In: *Journal of the Korean Physical Society* (2021). DOI: `10.1007/s40042-021-00177-0`.

[34] Marco Steinhardt et al. “Thermal conductivity inside prismatic lithium-ion cells with dependencies on temperature and external compression pressure”. In: *Journal of Energy Storage* (2020). DOI: `10.1016/j.est.2020.101680`.

[35] Hong Yu et al. “Thermal parameters of cylindrical power batteries: Quasi-steady state heat guarding measurement and thermal management strategies”. In: *Applied Thermal Engineering* (2023). DOI: `10.1016/j.applthermaleng.2023.120959`.

[36] Yihang Jiang et al. “Axial and radial thermal conductivity measurement of 18,650 Lithium-ion battery”. In: *Journal of Energy Storage* (2023). DOI: `10.1016/j.est.2023.108516`.

[37] Alastair Hales and James Bulman. “A Standardised Potentiometric Method for the Effective Parameterisation of Reversible Heating in a Lithium-Ion Cell”. In: *Journal of The Electrochemical Society* (2024). DOI: `10.1149/1945-7111/ad4918`. URL: `https://doi.org/10.1149/1945-7111/ad4918`.

[38] Akram Eddahech, Olivier Briat, and Jean-Michel Vinassa. “Thermal characterization of a high-power lithium-ion battery: Potentiometric and calorimetric measurement of entropy changes”. In: *Energy* (2013). DOI: `https://doi.org/10.1016/j.energy.2013.09.028`. URL: `https://www.sciencedirect.com/science/article/pii/S0360544213007792`.

[39] Boxia Lei et al. “Experimental Analysis of Thermal Runaway in 18650 Cylindrical Li-Ion Cells Using an Accelerating Rate Calorimeter”. In: *Batteries* (2017). DOI: `10.3390/batteries3020014`. URL: `https://www.mdpi.com/2313-0105/3/2/14`.

[40] Muhammad B. Ahmed, Salwa Shaik, and Ankur Jain. “Measurement of radial thermal conductivity of a cylinder using a time-varying heat flux method”. In: *International Journal of Thermal Sciences* (2018). DOI: `10.1016/j.ijthermalsci.2018.03.008`.

[41] Cedric Kirst, Juan Ramos Zayas, and Jan Singer. “Measurement approaches for Thermal Impedance Spectroscopy of Li-ion batteries”. In: *Journal of Power*

Sources (2023). DOI: https://doi.org/10.1016/j.jpowsour.2023.233020. URL: https://www.sciencedirect.com/science/article/pii/S0378775323003956.

[42] Evgenij Barsoukov, Jee Hwan Jang, and Hosull Lee. "Thermal impedance spectroscopy for Li-ion batteries using heat-pulse response analysis". In: *Journal of Power Sources* (2002). DOI: https://doi.org/10.1016/S0378-7753(02)00080-0. URL: https://www.sciencedirect.com/science/article/pii/S0378775302000800.

[43] Shrisha Balkur et al. "A cost and time effective novel methodology to determine specific heat capacity of lithium-ion cells". In: *Journal of Power Sources* (2021). DOI: 10.1016/j.jpowsour.2021.229981.

[44] Sylvain Cailliez, David Chalet, and Philippe Mannessiez. "Simultaneous identification of the heat capacity and the anisotropic thermal conductivities of a Li-ion pouch cell by a non-destructive analytical approach". In: *Journal of Power Sources* (2022). DOI: 10.1016/j.jpowsour.2022.231751.

[45] Marco Steinhardt et al. "Low-effort determination of heat capacity and thermal conductivity for cylindrical 18650 and 21700 lithium-ion cells". In: *Journal of Energy Storage* (2021). DOI: 10.1016/j.est.2021.103065.

[46] Jiacheng He et al. "A novel methodology to determine the specific heat capacity of lithium-ion batteries". In: *Journal of Power Sources* (2022). DOI: 10.1016/j.jpowsour.2021.230869.

[47] Marcus Auch, Timo Kuthada, and Andreas Wagner. "Simple experimental method to determine the specific heat capacity of cylindrical Lithium-Ion-Battery cells". In: *Applied Thermal Engineering* (2023). DOI: 10.1016/j.applthermaleng.2023.121212.

[48] K. A. Murashko, J. Pyrhönen, and J. Jokiniemi. "Determination of the through-plane thermal conductivity and specific heat capacity of a Li-ion cylindrical cell". In: *International Journal of Heat and Mass Transfer* (2020). DOI: 10.1016/j.ijheatmasstransfer.2020.120330.

[49] Yunkun Chu, Naxin Cui, and Kailong Liu. "Nonlinear modeling and SOC estimation of lithium-ion batteries based on block-oriented structures". In: *Energy* (2025). DOI: https://doi.org/10.1016/j.energy.2024.134273. URL: https://www.sciencedirect.com/science/article/pii/S0360544224040519.

[50] Hartmut Hinz. "Comparison of Lithium-Ion Battery Models for Simulating Storage Systems in Distributed Power Generation". In: *Inventions* (2019). DOI: 10.3390/inventions4030041. URL: https://www.mdpi.com/2411-5134/4/3/41.

[51] Lei Sheng et al. “Quasi steady state method to measure thermophysical parameters of cylindrical lithium ion batteries”. In: *Journal of Power Sources* (2021). DOI: `10.1016/j.jpowsour.2020.229342`.

[52] Zhongfu Zhou, Paul Holland, and Petar Igic. “Compact thermal model of a three-phase IGBT inverter power module”. In: 2008. DOI: `10.1109/ICMEL.2008.4559249`.

[53] Jiuchun Jiang et al. “A reduced low-temperature electro-thermal coupled model for lithium-ion batteries”. In: *Applied Energy* (2016). DOI: `https://doi.org/10.1016/j.apenergy.2016.05.153`. URL: `https://www.sciencedirect.com/science/article/pii/S0306261916307668`.

[54] Andrea Trivella et al. “Joint non-invasive identification of an electrochemical and thermal model for an ultra high-power Li-ion pouch cell”. In: *Control Engineering Practice* (2025). DOI: `https://doi.org/10.1016/j.conengprac.2024.106228`. URL: `https://www.sciencedirect.com/science/article/pii/S0967066124003873`.

[55] Ashkan Pirooz, Joeri Van Mierlo, and Maitane Berecibar. “3D Thermal and 1D Electro-Thermal Model Coupling Framework for Lithium-Ion Battery Cells in Automotive Industry Platforms”. In: *2021 IEEE Vehicle Power and Propulsion Conference (VPPC)*. 2021. DOI: `10.1109/VPPC53923.2021.9699116`.

[56] Robyn Jackey et al. “Battery Model Parameter Estimation Using a Layered Technique: An Example Using a Lithium Iron Phosphate Cell”. In: *SAE Technical Paper 2013-01-1547*. SAE International, 2013. DOI: `10.4271/2013-01-1547`.

[57] Nicolò Federico Quattromini et al. “Experimental investigation of Li-ion cylindrical cell thermal response through heat flux measurement”. In: *2025 IEEE International Workshop on Metrology for Automotive (MetroAutomotive)*. IEEE, 2025. ISBN: 979-8-3315-0202-7. DOI: `10.1109/METROAUTOMOTIVE64646.2025.11119261`.

[58] E-One Moli Energy Corp. *Product Data Sheet: Model INR-21700-P45B MOLICEL Lithium-Ion Rechargeable Battery*. Molicel. URL: `https://www.molicel.com/wp-content/uploads/INR21700P45B_1.2_Product-Data-Sheet-of-INR-21700-P45B-80109.pdf` (visited on 2026-02-02).

[59] Hukx. *FHF05 series heat flux sensors*. Hukx Sensor Technology. URL: `https://www.hukx.com/products/fhf05-series-heat-flux-sensors` (visited on 2026-02-02).

[60] Phoenix Contact. *VS-09-ST-DSUB/10-MPT-0,5 - D-SUB contact insert (1688379)*. Phoenix Contact GmbH & Co. KG. URL: `https :`

//www.phoenixcontact.com/en-pc/products/d-sub-contact-insert-vs-09-st-dsub-10-mpt-05-1688379 (visited on 2026-02-03).

[61] Dewesoft. *DSI Adapters Technical Specifications*. Dewesoft d.o.o. URL: `https://dewesoft.com/products/dsi-adapters/tech-specs` (visited on 2026-02-03).

[62] Pico Technology. *Thermocouple type K SE030*. Pico Technology Ltd. URL: `https://www.picotech.com/accessories/type-k-thermocouple/thermocouple-type-k-glass-fibre-2-m` (visited on 2026-02-02).

[63] Dewesoft. *DEWE-43A Technical Specifications*. Dewesoft d.o.o. URL: `https://dewesoft.com/products/dewe-43/tech-specs` (visited on 2026-02-02).

[64] Neware. *BTS-4008-5V20A-A Battery Testing System Datasheet*. Neware Co., Ltd. 2024. URL: `https://www.neware.ltd`.

[65] MSL s.r.l. *New Evolution Thermo / New Evolution Clima: Evolution Series Technical Information*. MSL s.r.l. 2020. URL: `http://www.mslitaly.eu`.

[66] TechLanz. *Battery RC Model Parameter Estimation from HPPC Test Data*. URL: `https://www.linkedin.com/pulse/battery-rc-model-parameter-estimation-from-hppc-test-data-part-2-n0v9f/` (visited on 2026-02-16).

[67] The MathWorks, Inc. *Hybrid Pulse Power Characterization (HPPC) Parameter Estimation*. MATLAB & Simulink. URL: `https://it.mathworks.com/help/simscape-battery/ug/hppc-parameter-estimation-workflow.html` (visited on 2026-02-19).

[68] S. J. Drake et al. “Measurement of anisotropic thermophysical properties of cylindrical Li-ion cells”. In: *Journal of Power Sources* (2014). DOI: `10.1016/j.jpowsour.2013.11.107`.

[69] Georgi Kovachev et al. “Thermal Conductivity in Aged Li-Ion Cells under Various Compression Conditions and State-of-Charge”. In: *Batteries* (2021). DOI: `10.3390/batteries7030042`.

«There are too many of us in this little island. We spend half our time trying not to tread on one another's feet. And we try, equally desperately, to express ourselves, to be people, not just "the holder of this card". Utopia is not Subtopia. Freedom must be physical, as well as mental and spiritual, and it is axiomatic that freedom of any kind decreases with density. The "concentration" camp is the final example. Ten hours away there is Canada, into one of whose lakes England could be dropped, and it has a population only twice that of one of England's towns. I do not think that youth is going to be satisfied much longer with four walls and flights of theory; nor with the carefully edited pornography that the theorists are content to see handed out to it as a substitute for air and space. Youth is both keen and generous, and it is getting bored stiff.

Intellectual adventure by itself is not enough. Sanity is largely a matter of humility, and nobody can be either humble or sane who imagines that by an exertion of intellect alone he can find all the answers. Intellect is an essential tool, but the situation so constantly outruns its best endeavours that, without trust—in what, exactly, it does not seem to matter, so that it be both beneficent and external—there would soon be madness or collapse.

In shelter, one may never learn this. In the furnaces of human hate and misery, one may be scorched in the process. Great natural forces are the surest and kindest teachers. A gale at sea presents a majesty and a beauty that require no formula or liturgy to make them real, and impresses very quickly upon anyone who is out in it the limits of his own strength and of his own intelligence. To be forcibly made aware of these limits is the true shrift; for then there is nothing left, and the blank can only be filled by trust—which is also love and reverence—if a man is to remain master of himself and be at peace.

The strong tides ebb and flow. If they have given me any certainty it is this: that I have known no heaven lovelier than this natural world, and that to have been next to it, even for a moment, is to have worshipped and to have been alive.»

— **Anthony Bridges**, *Scapa Ferry*